



**Development and performance analysis of
autonomous catalytic micropumps**

by

Ali Afshar Farniya

Doctoral Thesis

Doctoral Program in Materials Science

Directed by Dr. Maria Jose Esplandiu Egido

Department of Chemistry

Faculty of Science

May 2014

This report, manuscript is presented by Mr. Ali Afshar Farniya to obtain the Doctor degree

Memòria presentada per aspirar al Grau de Doctor per Ali Afshar Farniya

Vist i plau

Maria Jose Esplandiu Egado, Tenured CSIC Researcher at the Catalan Institute of Nanoscience and Nanotechnology (ICN2) and Associate Professor at the Autonomous University of Barcelona

CERTIFIES

That Mr. Ali Afshar Farniya, has done the present thesis entitled “Development and performance analysis of autonomous catalytic micropump”s under her supervision

Dr. Maria Jose Esplandiu Egado

Bellaterra, 3rd April 2014

Acknowledgements

This doctoral Thesis has been done with the support from the European Union (ERC-carbonNEMS Project), the Spanish government (200960I065, FIS2009-11284, MAT2012-31338), and the Catalan government (AGAUR, SGR).

Summary

One of the main challenges in the engineering of nanomachines, besides the difficulties to fabricate complex nanometric objects, is how to power them. The application of external fields is a common and easy way to actuate relatively large machines. However, when the size of the machines becomes smaller, the transfer of power from the macroscopic scale to the nanoscale becomes problematic. Therefore, the development of fully autonomous nanoscale systems which can self-generate their required power is very desirable. Biological systems are the source of numerous examples of natural micro/nanoscale autonomous motors. The conversion of chemical energy into directional motion is the key point behind the high efficient nanofactory of biomolecular machines. Therefore there is a high interest to create novel artificial machines which can self-propel and perform autonomous activities in a similar way the impressive molecular machinery does in living organisms. Many research activities have recently focused on chemically powered motors and micropumps based on the local self-generation of gradients.

The present research work deals with the catalytic micropump concept which was reported for the first time in 2005. A catalytic micropump is an active system which has the capability of triggering electrohydrodynamic phenomena due to an (electro)chemical reaction taken place on a micro/nano bimetallic structure. Although catalytic devices have been the subject of previous reports in which their nanotechnological applications have started to be demonstrated, the mechanism of the chemo-mechanical actuation has been less studied. That is in part due to the complex interrelation between the catalytic reactions and the electrohydrodynamic phenomena. As a consequence there is still a number of intriguing questions that require further investigation for establishing the role played by the different processes and for achieving a better understanding of the mechanism behind them. Therefore, the research was focused on the full characterization of the chemomechanical actuation and the understanding of the main physicochemical factors governing the operating mechanism of Au-Pt bimetallic micropumps in presence of hydrogen peroxide fuel. The investigations were supported not only by experimental findings but also by numerical simulations. These fundamental studies are of high importance not only for catalytic micropumps but also for other autonomous micro/nano swimmers or active self-propelled colloids. The studies were also extended to other bimetallic structures (Au-Ag, Au-Ru, Au-Rh, Cu-Ag, Cu-Ni, Ni-Ru and Ni-Ag) and to semiconductor/metallic structures (p-doped Si/Pt, n-doped Si/Pt) to evaluate their potentialities as catalytic micropumps in presence of the same chemical fuel. In the last case photoactivation of the catalytic reactions can be accomplished which provides an added value to these pumps as novel photochemical-electrohydrodynamic switches. These achievements can open new and promising research activities in the field of catalytic actuators and nanomotors. The thesis work also describes one of the potential applications of these active devices which is related to the autonomous material guiding and self-assembly on particular locations of a sample. That allows fabricating nanostructured surfaces in an autonomous way with potential nanotechnological impact in a wide range of fields.

Resumen

Uno de los principales retos de la ingeniería de nanomotores, además de las dificultades para fabricar objetos nanométricos complejos, es cómo proveerles de energía para que funcionen. La aplicación de campos externos es una forma común y fácil de impulsar motores relativamente grandes. Sin embargo, cuando el tamaño de los motores se hace más pequeño, la transferencia de energía desde la escala macroscópica a la nanoescala se vuelve más problemática. Por lo tanto, el desarrollo de sistemas a nivel de la nanoescala totalmente autónomos que puedan generar su propia energía para poder autopropulsarse es muy deseable. Los sistemas biológicos ofrecen numerosos ejemplos de micro/nano motores autónomos. El punto clave detrás de la eficiente maquinaria biológica es la conversión de energía química en movimiento direccional. Por lo tanto existe un alto interés en crear nuevos motores artificiales que puedan auto-impulsarse y realizar actividades autónomas de forma similar a la impresionante maquinaria molecular de los organismos vivos. Recientemente se ha comenzado una intensa actividad científica en el desarrollo de motores y sistemas de bombeo propulsados químicamente en base a la auto-generación local de gradientes.

El presente trabajo de investigación trata sobre el concepto de microsistemas de bombeo catalítico que fue reportado por primera vez en 2005. Un microsistema de bombeo catalítico es un sistema activo que tiene la capacidad de inducir fenómenos electrohidrodinámicos a partir de una reacción (electro)química sobre una micro/nano estructura bimetálica. Aunque los dispositivos catalíticos han sido objeto de investigaciones anteriores en el que sus aplicaciones nanotecnológicas han comenzado a demostrarse, el mecanismo de actuación quimio-mecánica ha sido menos estudiado. Esto es en parte debido a la compleja interrelación que existe entre las reacciones catalíticas y los fenómenos electro-hidrodinámicos. Como consecuencia de ello todavía hay una serie de preguntas sin resolver que requieren mayor investigación para establecer el rol desempeñado por los diferentes procesos y lograr una mejor comprensión del mecanismo detrás de ellos. Por lo tanto, en esta tesis doctoral se ha realizado una caracterización exhaustiva de la actuación quimio-mecánica para entender los principales factores fisicoquímicos que regulan el mecanismo de funcionamiento de microbombas bimetálicas de Au- Pt en presencia de peróxido de hidrógeno como combustible. Las investigaciones han sido solventadas no sólo con resultados experimentales sino también con simulaciones numéricas. Estos estudios fundamentales son relevantes no sólo para estos sistemas de bombes catalíticos, sino también para micro/nanomotores o nanorobots suspendidos en fluidos o coloides activos autopropulsados. Los estudios se han extendido también a otras estructuras bimetálicas (Au- Ag , Au- Ru , Au -Rh , Cu - Ag , Cu - Ni, Ni- Ru y Ni- Ag) y a dispositivos semiconductores/metálicos (Si dopado p / Pt , Si dopado n / Pt) con la idea de evaluar sus potencialidades como sistemas de bombeo catalítico en presencia del mismo combustible químico. En el caso de los sistemas metal/semiconductor su funcionamiento se basa en la fotoactivación de reacciones catalíticas, lo que proporciona un valor añadido a estas bombas y permite el desarrollo de nuevos interruptores foto-electrohidrodinámicos. Estos logros pueden abrir nuevas y prometedoras líneas de investigación en el campo de los actuadores y nanomotores catalíticos. El trabajo de tesis describe también una de las posibles aplicaciones de estos dispositivos activos que está relacionada con el transporte y depósito de materia en lugares específicos de un sustrato guiado por los fenómenos electrohidrodinámicos locales. Eso permite fabricar superficies nanoestructuradas de forma autónoma con un gran impacto nanotecnológico en una amplia gama de campos.

Table of Contents

| | |
|--|----|
| Chapter 1 | 1 |
| 1.1 The concept of catalytic motion..... | 2 |
| 1.2 Bimetallic catalytic micropumps | 8 |
| Chapter 2 | 17 |
| 2.1 Scope of work..... | 18 |
| 2.2 Research Goals..... | 18 |
| 2.3 Incoming chapters | 19 |
| Chapter 3 | 22 |
| 3.1 Electrokinetics | 23 |
| 3.2 Concepts and Governing equations | 23 |
| 3.3 Poisson's equation..... | 24 |
| 3.4 Electric double layer | 25 |
| 3.5 Electrochemical kinetics at the metal interface..... | 33 |
| 3.6 Nernst–Planck Equation | 35 |
| 3.7 Governing equation for the fluid motion | 37 |
| 3.7. a Continuity equation | 37 |
| 3.7.b Navier–Stokes equation..... | 38 |
| 3.8 Electro-osmosis | 40 |
| 3.9 Electrophoresis..... | 42 |
| 3.10. Full electrokinetic equations..... | 46 |
| Chapter 4 | 52 |
| Introduction | 53 |
| 4.1 Device fabrication | 54 |
| 4.1.1 Metal deposition | 55 |
| 4.1.2 Lithography | 58 |
| 4.1.3 Cleaning processes | 59 |
| 4.1.4 Fabrication sequences | 60 |
| 4.2 Characterization | 66 |
| 4.2.1 Optical microscopy | 66 |
| 4.2.2 Confocal fluorescence microscopy | 67 |
| 4.2.3 X-ray photoelectron spectroscopy (XPS)..... | 68 |
| 4.2.4 Atomic force microscopy (AFM) | 69 |
| 4.2.5 Zeta potential measurement..... | 69 |

| | |
|---|-----|
| 4.2.6 TAFEL plot measurement..... | 70 |
| 4.2.7 pH measurement..... | 71 |
| Chapter 5..... | 74 |
| Introduction..... | 75 |
| 5.1 Activation of Au-Pt catalytic micropumps | 75 |
| 5.1.a X-ray photoelectron spectroscopy (XPS) | 76 |
| 5.1.b TAFEL plot measurement..... | 78 |
| 5.1.c Proton concentration imaging on activated devices | 80 |
| 5.2 Zeta potential of the surfaces | 84 |
| 5.3 Studying the activated Au-Pt devices..... | 87 |
| 5.3.a Quasi-neutral particles (P°) | 87 |
| 5.3.b Positively charged particles (P^{+})..... | 90 |
| 5.3.c Negatively charged particles (P^{-})..... | 95 |
| 5.4 Electric field and fluid flow around Au-Pt devices | 95 |
| 5.6 simulations..... | 100 |
| 5.5.1 Results and Discussion..... | 102 |
| 5.6 Conclusions..... | 111 |
| Chapter 6..... | 113 |
| Introduction..... | 114 |
| 6.1 Pattern formation with negatively charged particles..... | 114 |
| 6.2 Sequential stages in the patterning process..... | 116 |
| 6.2.a Electrostatic repulsion | 117 |
| 6.2.b Clustering formation outside the repulsive band | 119 |
| 6.2.c Cluster transportation to the Pt disk edge | 121 |
| 6.2.d Silica crystallization..... | 128 |
| 6.3 Pattern formation on Pt-Au system | 131 |
| 6.4 Pattern formation with positively charged particles..... | 132 |
| Conclusions..... | 133 |
| Chapter 7..... | 136 |
| Introduction..... | 137 |
| 7.1. TAFEL plot measurements | 137 |
| 7.2 X-Y Bimetallic micropumps | 138 |
| 7.2.1 Au-Ru Devices..... | 140 |
| 7.2.2 Ni-Cu Devices..... | 144 |

| | |
|---|-----|
| 7.2.3 Cu-Ni Devices..... | 145 |
| 7.2.4 Au-Rh Devices..... | 146 |
| 7.2.5 Ni-Ru Devices | 149 |
| 7.2.6 Ni-Ag Devices..... | 151 |
| 7.2.7 Cu-Ag..... | 155 |
| 7.2.8 Au-Ag | 156 |
| Conclusion | 159 |
| Chapter 8..... | 162 |
| 8.1 Primary experiments | 163 |
| 8.2 Effect of different parameters on the electrohydrodynamic process..... | 165 |
| 8.2a Effect of adding hydrogen peroxide | 165 |
| 8.2b Effect of light intensity..... | 170 |
| 8.2c Effect of the salt concentration | 171 |
| 8.2d Effect of the silicon substrate type..... | 172 |
| 8.2d Effect of replacing the platinum layer by gold | 174 |
| 8.2e Effect of the plasma treatment..... | 175 |
| 8.3 Conclusion..... | 176 |
| Chapter 9..... | 178 |
| 9.1 Methodology..... | 179 |
| 9.2 Results and Discussion..... | 180 |
| 9.2a Effect of the substrate surface potential | 180 |
| Effect of the salt or other extra ions: concentration, diffusion coefficients and charge .. | 186 |
| Effect of the rate constants of the anode and cathode | 191 |
| Effect of the hydrogen peroxide and the bulk proton concentration..... | 197 |
| Effect of the geometry: size of the cathode and anode | 199 |
| Conclusions..... | 203 |
| Chapter 10..... | 205 |
| Conclusions..... | 206 |
| Outlook..... | 208 |
| Appendixes | 210 |
| Appendix 4.1 : Ru and Rh voltammograms | 211 |
| Appendix 4.2: Measuring particle velocity toward disk center as a function of radial distance | 214 |
| Appendix 4.3: Derivation of Appendix 4.2-Equation 9..... | 220 |

| | |
|---|-----|
| Appendix 3.4: Calculation of particle radial velocity..... | 222 |
| Appendix 3.5 Fluorescence confocal microscopy- Calculation..... | 224 |
| Appendix 4.6 Surface zeta potential measurement | 229 |
| Appendix 5.1 : A guideline to TAFEL plots | 232 |
| Appendix 6.1 configuration of adjoining clusters | 235 |

Chapter 1

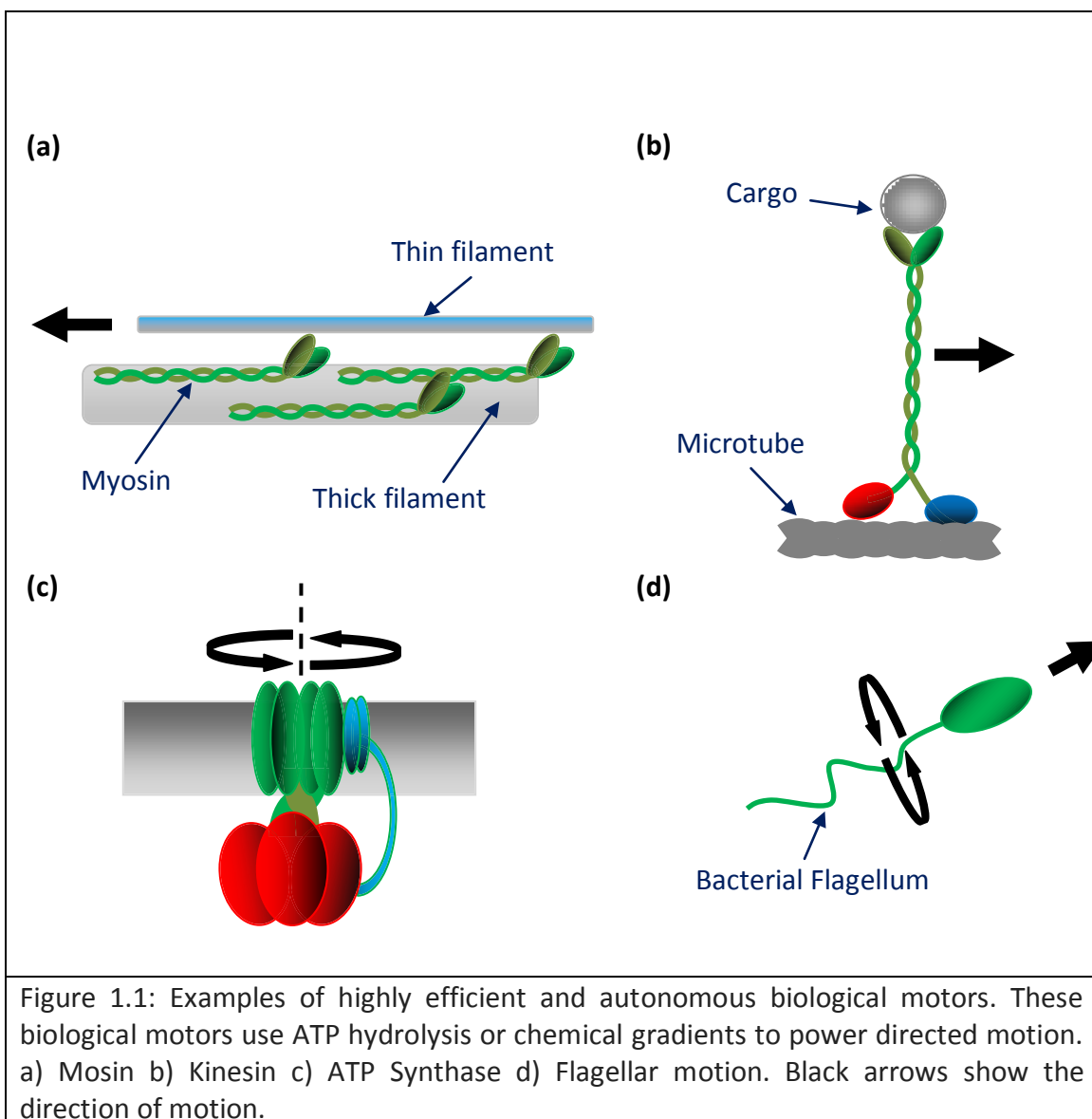
1.1 The concept of catalytic motion

Besides the difficulties to fabricate structurally complex nanometric objects, the main challenge in nanomachines is the strategies to power them. Applying external fields such as electromagnetic field is an easy way to actuate the relatively large machines. When the size of the machines become smaller, the transfer of power from the macroscopic length to the nanoscale one becomes problematic [1, 2].

Therefore, the development of fully autonomous nanoscale systems which can self-generate their required power is very desirable. Moreover, autonomous motion is the first step to have nano- and micromotors which are capable of multi-task functions. The emergence of collective behaviors like dynamic self-assembly, swarming, etc., is also another aspect related with the self-generation of motion which has recently brought a lot of research interest in the field of nano- and micromotors [3-19].

Biological systems are the source of numerous examples of natural micro/nanoscale autonomous motors [20-23]. The conversion of chemical energy into directional motion is the key point behind the high efficient nanofactory of biomolecular machines which are responsible of controlling cell activity. Some of the fascinating examples of chemically powered machines in nature are illustrated in figure 1.1. For instance, myosin (figure 1.1 a) and kinesin (figure 1.1 b) are protein-based linear motors which take advantage of the hydrolysis of Adenosine-5'-TrisPhosphate (ATP) to generate force to walk on protein filaments (actin or microtubule filaments) [24-28]. These motors are responsible of the muscle contraction and the transport of cellular cargo respectively. The ATP synthase (figure 1.1 c) is a rotary transmembrane protein machine which uses a proton gradient across the membrane to rotate. The rotational energy is used to add phosphate ions to Adenosine-5'-DiPhosphate (ADP) to make ATP [29, 30].

Rotary motors power the swimming of the bacteria. These motors like flagellums use the stored energy of proton gradients to rotate [31, 32]. The corkscrew-like motion is very efficient self-propulsion mode in the nanoscale environment dominated by viscous forces.



Nano-engineering aims at creating novel artificial machines which can be self-propelled and perform autonomous activities in a similar way the impressive molecular machinery does in the vivo organisms [33-41]. The research activities have recently focused on chemically powered motors and micropumps based on the local self-generation of gradients [1,2,42-52].

One of the most inspirational researches was the earlier work of the Whitesides group¹ [53]. It was shown that a millimeter scale polymeric disc with a Pt patch at one end could move autonomously at the air/ H_2O_2 solution interface.

¹ Whitesides research group, Prof. George M. Whitesides, Harvard University
Website: <http://gmwgroup.harvard.edu/index.php>

The structure was propelled by a bubble-recoil mechanism. The platinum patch converted the H_2O_2 into oxygen gas which propelled the entire structure forward. Result of this research triggered strong efforts to scale down such concept to the nano/micro scale.

The groups of Sen² and Mallouk³ at Pennsylvania state university demonstrated the proof of concept at smaller scales in 2004 [54, 55]. They showed that catalytic reactions can be used to drive axial movement of metallic nano-objects. The first structure was template-electroplated grown bimetallic Au-Pt nanorods with diameters between 200-400 nm and 1-2 μm in length. The bimetallic nanomotors moved at speeds of about $10 \mu m s^{-1}$. The catalytic decomposition of H_2O_2 on the bimetallic structure, was also the reason behind the movement but in this case without oxygen bubble formation (figure 1.2 a). [56]

The asymmetry either in the motor composition, shape or in the surface reactions is an important issue to design catalytic micromotors. Two different metal segments in the bimetallic nanomotors induce chemical reaction asymmetry. This asymmetry causes a gradient along the nanomotor which generates axial forces. [1]

Enhancing the motor speed, controlling the direction of motion and designing novel functional catalytic systems became new research goals. Changing the conductivity of bimetallic nanorods with the addition of carbon nanotubes on the Pt segment, using metal alloys in the metals, mixing other chemical fuels (based on hydrazine), increasing temperature and the surface area were done to enhance the nanomotor speed [57-62].

It was possible to achieve speeds up to $200 \mu m.s^{-1}$ (around 60 body length per second) competing with the fastest bacteria driven by flagellum [63]. In some cases, a better control on the motor direction was improved by the incorporation of magnetic segments in the nanorods and using external magnetic fields [1,51, 55, 64-68].

Novel catalytic systems were designed with carbon fiber and nanotube motors modified with redox enzymes catalyzed by the glucose decomposition [69, 70]. Regarding the geometry, new nanomotor designs like microgears and colloidal Janus microparticles (Au-Ag, SiO_2 -Pt, Al-Ga, Al-Pd), were introduced [42, 71-76].

Schmidt 's group⁴ innovated catalytic motors and developed the tubular microjet engines (a tube with a platinum coating in the inner wall) driven by bubble recoil provided by the oxygen production due to the hydrogen peroxide decomposition [51, 68, 77-80].

Figure 1.2 b shows schematically the microjet engine with conical shape. The asymmetry of the tube causes its motion in one direction. These tubular engines which are bigger than the bimetallic nanorods, could reach speeds as high as $10 mm.s^{-1}$ (Equal to 200-275 body length per second) [80, 84].

² The Sen Group, Prof. Ayusman Sen, Pennsylvania State University
Website: <http://research.chem.psu.edu/axsgroup/index.html>

³Mallouk research group, Prof. Thomas E. Mallouk, Pennsylvania State University
Website: <http://research.chem.psu.edu/mallouk/>

⁴ Institute for Integrative Nanosciences (IIN), Prof. Oliver G. Schmidt, The Leibniz Institute for Solid State and Materials Research Dresden (IFW Dresden)
Website: <http://www.ifw-dresden.de/de/institute/iin/>

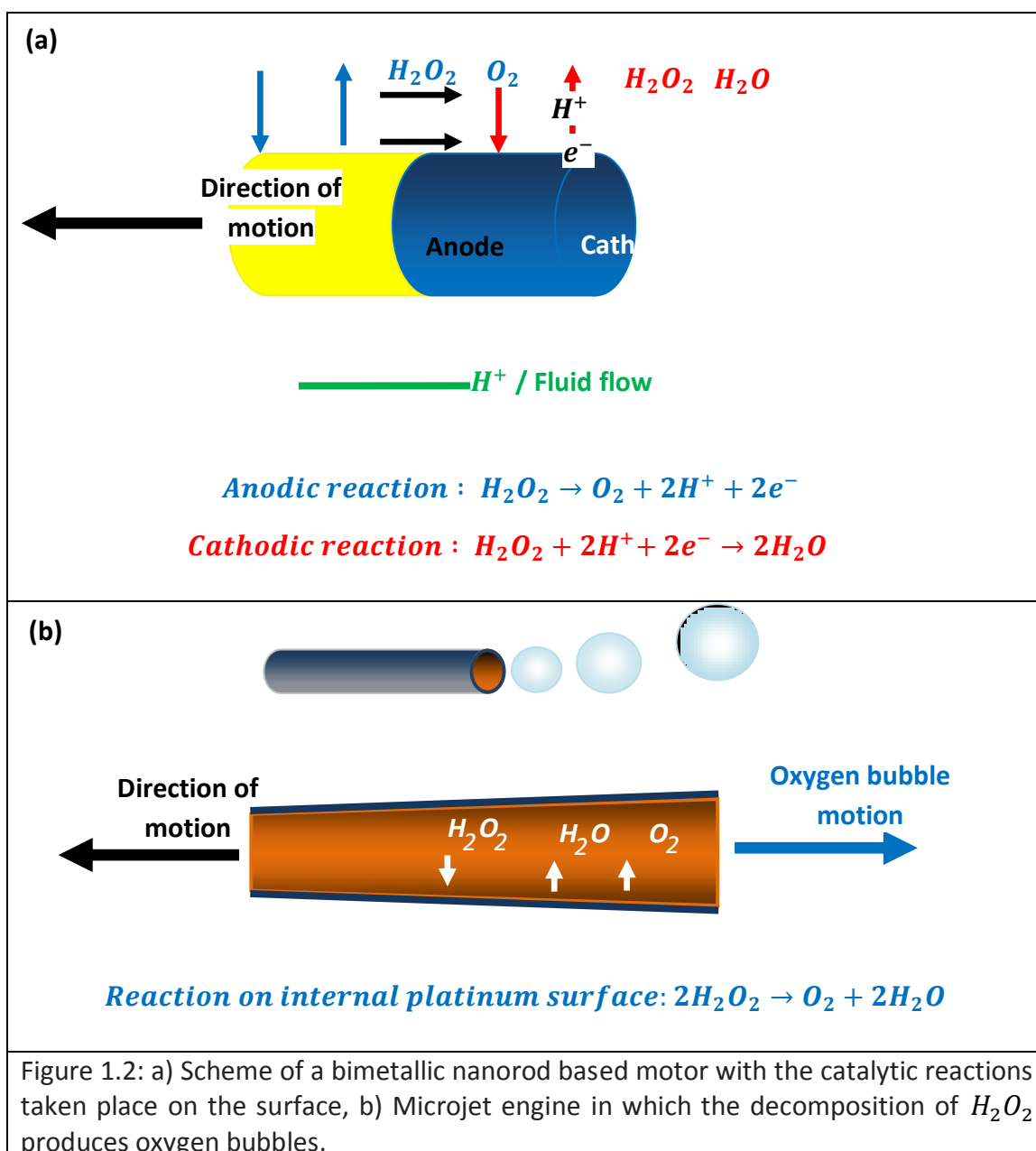
Another kind of catalytic microjets with similar principles was presented by Wang 's group⁵ [81-83]. The speed of these motors was faster than any bacteria and any other known autonomous synthetic microengine. The speed reached about 375 body length per second [63].

Catalytic microjets show impressive functionalities which make them qualified for being applied in drug delivery, robotics, fluidics, nano and micro electromechanical systems (NEMS/MEMs), environmental remediation, etc. [1, 2, 47-52, 85-87]. The swimming objects can be applied to pick up, transport and release cargo [65, 84, 89-96]. Selective capture and transport of biological proteins, and their controlled release was reported [97-98]. In a similar way, these swimming objects were used to isolate cancer cells, bacteria and nucleic acid from complex biological mixtures [99-101].

Moreover, the motors were employed for sensing purposes [102, 103]. Wang et al. developed the concept of motion-based sensing and it was exploited for sensitive detection of DNA and bacterial ribosomal RNA [103].

In some cases, it was possible to observe that motors can follow a corkscrew-like trajectory, which allows drilling and penetrating tissues [94].

⁵ Laboratory for Nanobioelectronics, Prof. Joseph Wang, University California San Diego (UCSD)
Website: <http://joewang.ucsd.edu/>



Although artificial micro/nano motors with impressive speed and functionalities have been developed, energy efficiency⁶ of these catalytic systems is rather too low in comparison with the biological counterparts [1]. In order to design efficient catalytic motors, it is very important to understand the principles and mechanisms governing the motion in the micrometer and nanometer regimes. The major motion mechanisms of micro/nano motors are based on self-electrophoresis, self-diffusiophoresis, dynamic interfacial tension or bubble recoil [1, 44, 52, 56, 54].

Depending on the size, shape, material, chemical fuel composition and concentration one of the mechanisms can become dominant over the others. For instance, the microjets (microtubes) have large enough platinum surface to let the oxygen bubbles

⁶ Energy efficiency is defined as the mechanical power output divided by the overall energy input.

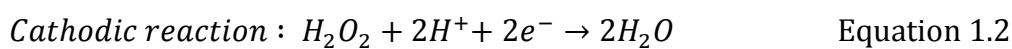
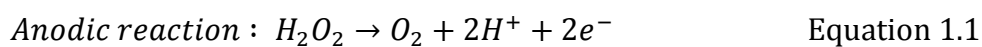
nucleate and grow. The detachment of the bubbles causes generation of the recoil force which explains the main propulsion mechanism in such system [51, 77].

In contrast to motors which operate based on electrokinetics, microjets have the advantage to operate in salt-rich environment. In the case of bimetallic nanorods, it has been more difficult to determine which mechanisms is the dominant one. The bubble recoil mechanism is omitted from the list of candidates because no nucleation of bubbles was observed. The groups of Sen and Mallouk proposed an interfacial tension mechanism for the axial motion of Pt-Au nanorods based on analysis of reaction rates, drag forces and interfacial energies [54]. The basic idea of this model is that the oxygen generated in the reaction disrupts the hydrogen bonding locally, lowering the interfacial tension energy between the aqueous solution and the gas coated nanorod. The rod moves in one direction because of a net axial force generated due to the oxygen gradient. The same groups also took into the consideration the possibility of diffusiophoresis due to an oxygen gradient. However, they predicted a diffusiophoretic velocity much smaller than the observed one [44].

However it was also found that the catalytic actuation was sensitive to the ionic strength of the fluid [46] and it was also disrupted if an insulating segment was inserted between the bimetallic structures [69]

These findings suggested that an electrokinetic mechanism with self-generation of electric fields at the fluid was more appropriate to explain the experimental observations [43, 44, 49, 56]. In this model, a proton gradient is established along the bimetallic rod because of the asymmetric reaction of H_2O_2 at the two metallic surfaces according to equations 1.1 and 1.2.

As a consequence of such proton gradient, an electric field and a fluid flow emerge. These two phenomena push the rod to move in one direction. This process has been addressed as self-electrophoresis since it deals with charged rods⁷ immersed in a self-induced field.



Although the electrokinetic process could be considered as the more accepted propulsion scheme for bimetallic structures, still a lot of work is pending to go deep in the experimental and theoretical details of the process. That is not an easy task given the complexity of the chemomechanical actuation which involves the coupled

⁷ Generally bimetallic rods are negatively charged.

phenomena of (electro) chemical reactions, electrostatics, mass transport and fluid motion.

In this line, some theoretical studies are trying to clarify the complex interrelation between the catalytic reactions and the electro-hydrodynamics phenomena by solving the governing equations of Poisson (electrostatics), Nernst-Planck (species transportation) and Navier-Stokes (fluid motion) with different approximations [104-107]. However a systematic analysis of the different parameters involved in the chemomechanical actuation is still missing.

1.2 Bimetallic catalytic micropumps

In 2005, the bimetallic catalytic micropump was introduced as an alternative concept for generating fluid flow in an autonomous way and it was reported by the same research group⁸ which pioneered the development of bimetallic catalytic nanomotors [46,108,109].

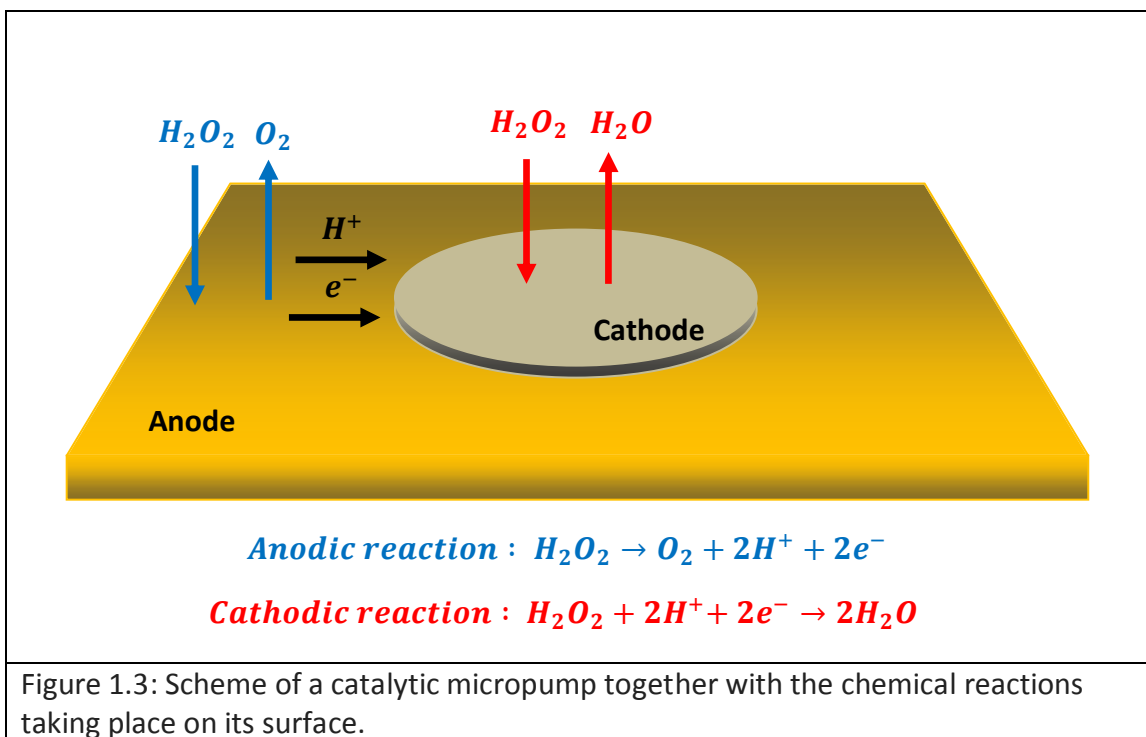
Applying external pressure, electric field, thermal gradient or concentration gradient are traditional methods for pumping fluids. The catalytic micropump is a stationary heterogeneous structure which has ability to gain energy autonomously from the environment to generate a local flow. Both bimetallic catalytic nanomotors and micropumps can share the same electrokinetic actuation process⁹. In the case of the catalytic nanomotors, the chemical reactions induce body forces that make the object move with respect to the surrounding fluid. In the catalytic micropumps which are immobilized structures on a substrate, the chemical reactions generate fluid motion with respect to the substrate surface.

Similar to the catalytic nanomotor, the process is based on the oxidation and reduction of chemical fuel (hydrogen peroxide) at two different metallic regions acting as anode and cathode, respectively. The H_2O_2 molecules decompose on both anode and cathode surface in the same way as mentioned before (equation 1.1 and equation 1.2). [1,108, 109]

Overall, there is a net flux of protons (H^+) from the anode (where protons are produced) to the cathode (where they are consumed). The electric field generated in this process is believed to induce the flow of the liquid through electro-osmosis. [108,109]

⁸ The Sen Group, Prof. Ayusman Sen, Pennsylvania State University
Website: <http://research.chem.psu.edu/axsgroup/index.html>

⁹ The electrokinetic process becomes dominant in a catalytic pump if bubble formation is minimized. That can be accomplished in low concentrations of chemical fuel and restricting the exposed surface area of the bimetallic structures.



The catalytic micropump made of Au-Ag was taken as a model for studying the electric field and fluid flow in combination with colloidal tracers [108-111]. After Au-Ag catalytic system, another bimetallic catalytic micropump based on a palladium disk on a gold surface was characterized. Instead of H_2O_2 , the new catalytic micropump worked with either Hydrazine (N_2H_4) or asym-N, N-dimethylhydrazine ($N_2Me_2H_2$) [24,112].

Surprisingly and despite being the pioneer composition of autonomous bimetallic motors, there was no study on Au-Pt catalytic micropumps (with the exception of a report on interdigitated Pt-Au electrodes [46]).

Recent designs also include polymeric micropumps based on the concept of diffusiophoresis in a non-electrolyte fluid. The pump consists of a polymer film that depolymerizes to release soluble monomeric products when exposed to a specific species or light. Products formed as a result of the depolymerization reaction create a concentration gradient that pumps fluids. [113]

Although there are different possibilities with catalytic pumps, this dissertation will deal with bimetallic catalytic pumps actuated by the electrokinetic process. Beyond their potential applications, these pumps are ideal candidates for understanding the chemical actuation mechanism. As mentioned before, this is an issue of high interest given the complex interrelation and the poor understanding of the processes involved in the actuation mechanism and the lack of a systematic studies from the experimental and theoretical point of view [109].

Indeed, catalytic pumps comprise an attractive model system for this kind of studies since their actuation can be probed in combination with differently charged particle tracers [108, 109]. New effective experimental methods could be more easily

implemented to comprehend and spatially quantify the parameters involved in such coupled processes. Moreover catalytic pumps profit from the advantage that are better defined and controlled from the point of view of electrode shape, size, surface chemical composition and roughness which are also important aspects affecting the catalytic motion and not so easy to control in free-suspending nanomotors. At the same time they are also a very convenient system to address it theoretically.

Moreover and beyond catalytic pumps and motors, the scientific knowledge that can be acquired might have important repercussions on other related topics. It should not be forgotten that the actuation mechanism is based on electrochemical processes at the liquid-surface interface of spatially heterogeneous electrodes. Therefore it can have a lot in common with the physics of basic electrochemical systems [114], corrosion processes [115], energy related devices (such as batteries and fuel cells)[116,117], ion-exchange membranes [118, 119], and biological systems (such as biomembranes and ion pumps)[120].

References

- [1] W. Wang, W. Duan, S. Ahmed, T.E. Mallouk, A. Sen, "Small power: Autonomous nano- and micromotors propelled by self-generated gradients", *Nano Today*, vol 8, pp. 531-554, 2013.
- [2] Y. Wang, "Powered motion at micro/nanoscale and controlled interactions between catalytic motors", PhD dissertation, 2009, Pennsylvania State University.
- [3] C. András, T. Vicsek, "Collective of interacting self-propelled particles", *Physica A*, vol. 281, pp. 17-29, 2000.
- [4] V. Schaller, C. Weber, C. Semmrich, E. Frey, A.R. Bausch, "Polar patterns of driven filaments", *Nature*, vol. 467, pp. 73-77, 2010.
- [5] S. Köhler, V. Schaller, A.R. Bausch, "Structure formation in active networks", *Nature Materials*, vol. 10, pp. 462-468, 2011.
- [6] I. Theurkauff, C. Cottin-Bizonne, J. Palacci, C. Ybert, L. Bocquet, "Dynamic clustering in active colloidal suspensions with chemical signalling", *Physical Review Letters*, vol 108, 268303, 2012.
- [7] F.D.C. Farrell, M.C. Marchetti, D. Marenduzzo, J. Tailleur, "Pattern formation in self-propelled particles with density-dependent motility", *Physical Review Letters*, vol. 108, 248101, 2012.
- [8] A. Bricard, J.B. Caussin, N. Desreumaux, O. Dauchot, D. Bartolo, "Emergence of macroscopic directed motion in populations of motile colloids", *Nature*, vol. 503, pp. 95-98, 2013.
- [9] J. Palacci, S. Sacanna, A.P. Steinberg, D.J. Pine, P.M. Chaikin, "Living crystals of light – activated colloidal surfers", *Science*, vol. 339, pp. 936-940, 2013.
- [10] B.M. Mognetti, A. Saric, S. Angioletti-Uberti, A. Cacciuto, C. Valeriani, D. Frenkel, "Living clusters and crystals from low-density suspensions of active colloids", *Physical Review Letters*, vol. 111, 245702, 2013.
- [11] M.P. Brenner, L.S. Levitov, E.O. Budrene, "Physical mechanisms for chemotactic pattern formation by bacteria", *Biophysical Journal*, vol. 74, pp. 1677-1693, 1998.
- [12] M. Ibele, T.E. Mallouk, A. Sen, "Schooling behavior of light-powered autonomous micromotors in water", *Angewandte Chemie International Edition*, vol. 48, pp. 3308-3312, 2009.
- [13] Y. Hong, D. Velegol, N. Chaturvedi, A. Sen, "Biomimetic behavior of synthetic particles: from microscopic randomness to microscopic control", *Physical Chemistry Chemical Physics*, vol. 12, pp.1423-1435, 2010.

- [14] Y. Hong, M. Diaz, U.M. Córdova-Figueroa, A. Sen, "Light-driven titanium dioxide based reversible microfireworks and micromotor/micropump systems", *Advanced Functional Materials*, vol. 20, pp. 1-9, 2010.
- [15] W. Duan, M. Ibele, R. Liu, A. Sen, "Motion analysis of light-powered autonomous silver chloride nanomotors", *European Physical Journal E*, vol. 35, pp. 77, 2012.
- [16] J. Yan, M. Bloom, S.C. Bae, E. Luitjen, S. Granick, "Linking synchronization to self-assembly using magnetic Janus colloids", *Nature*, vol. 491, pp. 578-581, 2012.
- [17] A.A. Solovev, S. Sanchez, O.G. Schmidt, "Collective behavior of self-propelled catalytic micromotors", *Nanoscale*, vol. 5, pp. 1284-1293, 2013.
- [18] W. Duan, R. Liu, A. Sen, "Transition between collective behaviors of micromotors in response to different stimuli", *Journal of the American Chemical Society*, vol. 135, pp. 1280-1273, 2013.
- [19] W. Wang, W. Duan, A. Sen, T.E. Mallouk, "Catalytically powered dynamic assembly of rod-shaped nanomotors and passive tracer particles", *Proceedings of the National Academic of Science USA*, vol. 110, pp. 17744-17749, 2013.
- [20] J. Howard, "Molecular motors: structural adaptations to cellular functions", *Nature*, vol. 389, pp. 561-567, 1997.
- [21] M. Gross, "Travels to the Nanoworld: miniature machinery in nature and nanotechnology", Plenum, New York, 1999.
- [22] M. G. L. van den Heuvel and C. Dekker, "Motor proteins at work for nanotechnology", *Science*, vol. 317, pp. 333-336, 2007.
- [23] M. Stephen, "Life as a Nanoscale Phenomenon", *Angewandte Chemie International Edition*, vol. 47, pp. 5306-5320, 2008.
- [24] D.A. Fletcher, R.D. Mullins, "Cell mechanics and the cytoskeleton", *Nature*, vol. 463, pp. 485-492, 2010.
- [25] M.J. Tyska, D.M. Warshaw, "The myosin power stroke", *Cell Motility and the Cytoskeleton*, vol. 51, pp. 1-15, 2002.
- [26] J. Menetrey, P. Llinas, M. Mukherjee, H.L. Sweeney, A. Houdusse, "The structural basis for the large powerstroke of myosin VI", *Cell*, vol. 131, pp. 300-308, 2007.
- [27] R.D. Vale, "The molecular motor toolbox for intracellular transport", *Cell*, vol. 112, pp. 467-480, 2003.
- [28] C.V. Sindelar, K.H. Downing, "An atomic-level mechanism for activation of the kinesin molecular motors", *Proceedings of the National Academy of Science U S A*, vol. 107, pp. 4111-4116, 2010.
- [29] P.D. Boyer, "A research journey with ATP synthase", *Journal of Biological Chemistry*, vol. 277, pp. 39045-39061, 2002.
- [30] R.K. Nakamoto, J.A.B. Scanlon, M.K. Al-Shawi, "The Rotary Mechanism of the ATP Synthase", *Arch. Biochem. Biophys.*, vol. 476, pp. 43-80, 2008.
- [31] M. Silverman, M. Simon, "Flagellar rotation and the mechanism of bacterial motility". *Nature*, vol. 249, pp. 73-74, 1974.
- [32] T. Atsumi, L. McCarter, Y. Imae, "Polar and lateral flagellar motors of marine *Vibrio* are driven by different ion-motive forces", *Nature*, vol. 355, pp. 182-184, 1992.
- [33] K. Kinbara and T. Aida, "Toward Intelligent Molecular Machines: Directed Motions of Biological and Artificial Molecules and Assemblies," *Chemical Reviews*, vol. 105, pp. 1377-1400, 2005.
- [34] C. Bustamante, D. Keller, and G. Oster, "The Physics of Molecular Motors†," *Accounts of Chemical Research*, vol. 34, pp. 412-420, 2001.
- [35] R. Ballardini, V. Balzani, A. Credi, M. T. Gandolfi, and M. Venturi, "Artificial Molecular-Level Machines: Which Energy To Make Them Work?," *Accounts of Chemical Research*, vol. 34, pp. 445-455, 2001.

- [36] J. F. Stoddart, "Molecular Machines," *Accounts of Chemical Research*, vol. 34, pp. 410-411, 2001.
- [37] B. L. Feringa, "In Control of Motion: From Molecular Switches to Molecular Motors," *Accounts of Chemical Research*, vol. 34, pp. 504-513, 2001.
- [38] "Molecular Machines Special Issue!, *Accounts of Chemical Research*, vol. 34, pp. 409-409, 2001.
- [39] V. Balzani, A. Credi, and M. Venturi, *Molecular Devices and Machines: Concepts and Perspectives for the Nanoworld*: Wiley, 2008.
- [40] T. R. Kelly and V. Balzani, *Molecular Machines*: Springer, 2005.
- [41] J. P. Sauvage, *Molecular Machines and Motors*: Springer, 2001.
- [42] S. J. Ebbens and J. R. Howse, "In pursuit of propulsion at the nanoscale," *Soft Matter*, vol. 6, pp. 726-738, 2010.
- [43] W. F. Paxton, S. Sundararajan, T. E. Mallouk, and A. Sen, "Chemical Locomotion," *Angewandte Chemie International Edition*, vol. 45, pp. 5420-5429, 2006.
- [44] W. F. Paxton, A. Sen, and T. E. Mallouk, "Motility of Catalytic Nanoparticles through Self-Generated Forces," *Chemistry – A European Journal*, vol. 11, pp. 6462-6470, 2005.
- [45] S. Sánchez and M. Pumera, "Nanorobots: The Ultimate Wireless Self-Propelled Sensing and Actuating Devices," *Chemistry – An Asian Journal*, vol. 4, pp. 1402-1410, 2009.
- [46] W. F. Paxton, P. T. Baker, T. R. Kline, Y. Wang, T. E. Mallouk, and A. Sen, "Catalytically Induced Electrokinetics for Motors and Micropumps," *Journal of the American Chemical Society*, vol. 128, pp. 14881-14888, 2006.
- [47] G.A. Ozin, I. Manners, S. Fournier-Bidoz, A. Arsenault, "Dream Nanomachines", *Advanced Materials*, vol. 17, pp. 3011-3018, 2005.
- [48] J. Wang, "Can Man-Made Nanomachines Compete with Nature Biomotors?," *ACS Nano*, vol. 3, pp. 4-9, 2009.
- [49] M. Pumera, "Electrochemically powered self-propelled electrophoretic nanosubmarines", *Nanoscale*, vol. 2, pp. 1643-1649, 2010.
- [50] J. Wang, K.M. Manesh, "Motion Control at the Nanoscale", *Small*, vol. 6, pp. 338-345, 2010.
- [51] Y. Mei, A.A. Solovev, S. Sanchez, O.G. Schmidt, "Rolled-up nanotech on polymers: from basic perception to self-propelled catalytic microengines", *Chemical Society Reviews*, vol. 40, pp. 2109-2119, 2011.
- [52] S. Sengupta, M.E. Ibele, A. Sen, "Fantastic Voyage: Designing Self-Powered Nanorobots" *Angewandte Chemie International Edition*, vol. 51, pp. 8434-8445, 2012.
- [53] R. F. Ismagilov, A. Schwartz, N. Bowden, G. M. Whitesides, Autonomous Movement and Self-Assembly, *Angewandte Chemie International Edition*, vol. 41, pp. 652 – 654, 2002.
- [54] W. F. Paxton, K. C. Kistler, C. C. Olmeda, A. Sen, S. K. St. Angelo, Y. Cao, *et al.*, "Catalytic Nanomotors: Autonomous Movement of Striped Nanorods", *Journal of the American Chemical Society*, vol. 126, pp. 13424-13431, 2004.
- [55] T. R. Kline, W. F. Paxton, T. E. Mallouk, and A. Sen, "Catalytic Nanomotors: Remote-Controlled Autonomous Movement of Striped Metallic Nanorods", *Angewandte Chemie International Edition*, vol. 44, pp. 754-756, 2005.
- [56] Y. Wang, R. M. Hernandez, D. J. Bartlett, J. M. Bingham, T. R. Kline, A. Sen, *et al.*, "Bipolar Electrochemical Mechanism for the Propulsion of Catalytic Nanomotors in Hydrogen Peroxide Solutions", *Langmuir*, vol. 22, pp. 10451-10456, 2006.
- [57] U. K. Demirok, R. Laocharoensuk, K. M. Manesh, J. Wang, "Ultrafast catalytic alloy nanomotor", *Angewandte Chemie International Edition*, vol. 47, pp. 9349 – 9351, 2008.
- [58] R. Laocharoensuk, J. Burdick, J. Wang, "CNT-induced acceleration of catalytic nanomotors", *ACS Nano*, vol. 2, pp. 1069 – 1075, 2008.

- [59] N.S. Zacharia, Z.S. Sadeq, G.A. Ozin, "Enhanced speed of bimetallic nanorod motors by surface roughening", *Chemical Communications*, pp. 5856—5858, 2009.
- [60] S. Balasubramanian, D. Kagan, K. M. Manesh, P. Calvo-Marzal, G.-U. Flechsig, J. Wang, "Thermal modulation of nanomotor movement", *Small*, vol. 5, pp. 1569 – 1574, 2009.
- [61] P. Calvo-Marzal, K. M. Manesh, D. Kagan, S. Balasubramanian, M. Cardona, G.-U. Flechsig, J. Posner, J. Wang, "Electrochemically triggered motion of nanomotors", *Chemical Communications*, pp. 4509 – 4511, 2009.
- [62] S. Sattayasamitsathit, W. Gao, P. Calvo-Marzal, K. M. Manesh, J. Wang, "Simplified cost-effective preparation of high performance Ag-Pt nanowire motors", *ChemPhysChem*, vol. 11, pp. 2802 – 2805, 2010.
- [63] W. Gao, S. Sattayasamitsathit, J. Wang, "Catalytically propelled micro-/nanomotors: how fast can they move?", *Chemical Records*, vol. 12, pp. 224—231, 2012.
- [64] P. Dhar, Y.Y. Cao, T. Kline, P. Pal, C. Swayne, T.M. Fischer, B. Miller, T.E. Mallouk, A. Sen, T.H. Johansen, "Autonomously moving local nanoprobe in heterogeneous magnetic fields", *Journal of Physical Chemistry C*, vol. 111, pp. 3607—3613, 2007.
- [65] J. Burdick, R. Laocharoensuk, P. M. Wheat, J. D. Posner, and J. Wang, "Synthetic Nanomotors in Microchannel Networks: Directional Microchip Motion and Controlled Manipulation of Cargo", *Journal of the American Chemical Society*, vol. 130, pp. 8164-8165, 2008.
- [66] N. Chaturvedi, Y. Hong, A. Sen, D. Velegol, "Magnetic enhancement of phototaxing catalytic motors", *Langmuir*, vol. 26, pp. 6308—6313, 2010.
- [67] W. Gao, K. M. Manesh, J. Hua, S. Sattayasamitsathit, and J. Wang, "Hybrid Nanomotor: A Catalytically/Magnetically Powered Adaptive Nanowire Swimmer," *Small*, vol. 7, pp. 2047-2051, 2011.
- [68] A. A. Solovev, Y. Mei, E. Bermúdez Ureña, G. Huang, and O. G. Schmidt, "Catalytic Microtubular Jet Engines Self-Propelled by Accumulated Gas Bubbles," *Small*, vol. 5, pp. 1688-1692, 2009.
- [69] N. Mano, A. Heller, "Bioelectrochemical propulsion", *Journal of the American Chemical Society*, vol. 127, pp. 11574-11575, 2005.
- [70] D. Pantorotto, W.R. Browne, B.L. Feringa, "Autonomous propulsion of carbon nanotubes powered by a multienzyme ensemble", *Chemical Communications*, pp. 1533-1535, 2008.
- [71] J.M. Catchmark, S. Subramanian, A. Sen, "Directed rotational motion of microscale objects using artificial tension gradients continually generated via catalytic reactions", *Small*, vol. 1, pp. 202-206, 2005.
- [72] J.G. Gibbs, Y.P. Zhao, "Design and characterization of rotational multicomponent catalytic nanomotors", *Small*, vol. 5, pp. 2304-2308, 2009.
- [73] J. R. Howse, R. A. L. Jones, A. J. Ryan, T. Gough, R. Vafabakhsh, R. Golestanian, "Self-motile colloidal particles: from directed propulsion to random walk", *Physical Review Letters*, vol. 99, 048102, 2007.
- [74] P.M. Wheat, N.A. Marine, J.L. Moran, J.D. Posner, "Rapid fabrication of bimetallic spherical motors", *Langmuir*, vol. 26, 13052—13055, 2010.
- [75] W. Gao, A. Pei, J. Wang, "Water-driven micromotors", *ACS Nano*, vol. 6, 8432-8438, 2012.
- [76] W. Gao, M. D'Agostino, V. Garcia-Gradilla, J. Orozco, J. Wang, *Small*, vol. 9, pp.467-471, 2013.
- [77] A.A. Solovev, Y.F. Mei, E. Bermudez Ureña, G.S. Huang, O.G. Schmidt, "Catalytic Microtubular jet engines self-propelled by accumulated gas bubbles", *Small*, vol. 5, pp. 1688-1692, 2009.
- [78] A. A. Solovev, S. Sanchez, Y. Mei, and O. G. Schmidt, "Tunable catalytic tubular micro-pumps operating at low concentrations of hydrogen peroxide", *Physical Chemistry Chemical Physics*, vol. 13, pp. 10131-10135, 2011.

- [79] S. Sanchez, A.A. Solovev, S.M. Harazim, O.G. Schmidt, "Microbots swimming in the flowing streams of microfluidic channels", *Journal of the American Chemical Society*, vol.133, pp. 701-703, 2011.
- [80] S. Sanchez, A.N. Ananth, V.M. Fomin, M. Viehrig, O.G. Schmidt, "Superfast motion of catalytic microjet engines at physiological temperature", *Journal of the American Chemical Society*, vol. 133, pp. 14860-14863, 2011.
- [81] K. M. Manesh, M. Cardona, R. Yuan, M. Clark, D. Kagan, S. Balasubramanian, J. Wang, "Template-assisted fabrication of salt-independent catalytic tubular microengines", *ACS Nano*, vol. 4, pp. 1799 – 1804, 2010.
- [82] W. Gao, S. Sattayasamitsathit, J. Orozco, J. Wang, "Highly efficient catalytic microengines: template electrosynthesis of bilayer polyaniline-platinum conical microtubes", *Journal of the American Chemical Society*, vol. 133, pp. 11862-11864, 2011.
- [83] G. Huang, J. Wang, Y. Mei, "Material considerations and locomotive capability in catalytic tubular microengines", *Journal of Material Chemistry*, vol. 22, pp. 6519-6525, 2012.
- [84] A. A. Solovev, S. Sanchez, M. Pumera, Y. F. Mei, O. G. Schmidt, "Magnetic control of tubular catalytic microbots for the transport, assembly and delivery of micro-objects", *Advanced Functional Materials*, vol. 20, pp. 2430-2435, 2010.
- [85] J. Wang, W. Gao, "Nano/microscale motors: biomedical opportunities and challenges", *ACS Nano*, vol. 6, pp. 5745-5751, 2012
- [86] M. Guix, J. Orozco, M. Garcia, W. Gao, S. Sattayasamitsathit, A. Merkoci, A. Escarpa, J. Wang, "Superhydrophobic alkanethiol-coated microsubmarines for effective removal of oil", *ACS Nano*, vol. 6, pp. 4445-4451, 2012.
- [87] L. Soler, V. Magdanz, V.M. Fomin, S. Sanchez, O.G. Schmidt, "Self-propelled micromotors for cleaning polluted water", *ACS Nano*, vol. 7, pp. 9611-9620, 2013.
- [88] J. Orozco, V. Garcia-Gradilla, M. D'Agostino, W. Gao, A. Cortes, J. Wang, "Artificial enzyme-powered microfish for water-quality testing", *ACS Nano*, vol. 7, pp. 818-824, 2013.
- [89] S. Sundararajan, P. E. Lammert, A. W. Zudans, V. H. Crespi, and A. Sen, "Catalytic Motors for Transport of Colloidal Cargo", *Nano Letters*, vol. 8, pp. 1271-1276, 2008.
- [90] S. Sundararajan, S. Sengupta, M. E. Ibele, and A. Sen, "Drop-Off of Colloidal Cargo Transported by Catalytic Pt–Au Nanomotors via Photochemical Stimuli", *Small*, vol. 6, pp. 1479-1482, 2010.
- [91] D. Kagan, R. Laocharoensuk, M. Zimmerman, C. Clawson, D. Balasubramanian, D. Kong, D. Bishop, S. Sattayasamitsathit, L.F. Zhang, J. Wang, "Rapid delivery of drug carriers propelled and navigated by catalytic nanoshuttles", *Small*, vol. 6, pp. 2741-2747, 2010
- [92] S. Sanchez, A.A. Solovev, S. Schulze, O.G. Schmidt, "Controlled manipulation of multiple cells using catalytic microbots", *Chemical Communications*, vol. 47, pp. 698-700, 2011.
- [93] E.J. Smith, W. Xi, D. Makarov, I. Monch, S. Harazim, V.A.B. Quinones, C.K. Schmidt, Y.F. Mei, S. Sanchez, O.G. Schmidt, "Lab-in-a-tube: ultracompact components for on-chip capture and detection of individual micro/nanoorganisms", *Lab on a Chip*, vol. 12, pp. 1917-1931, 2012.
- [94] A. A. Solovev, W. Xi, D. H. Gracias, S. M. Harazim, C. Deneke, S. Sanchez, *et al.*, "Self-Propelled Nanotools", *ACS Nano*, vol. 6, pp. 1751-1756, 2012.
- [95] L. Baraban, M. Tasinkevych, M.N. Popescu, S. Sanchez, S. Dietrich, O.G. Schmidt, "transport of cargo by catalytic Janus micro-motors", *Soft Matter*, vol 8, pp.48-52, 2012.
- [96] J. Wang, "Cargo-towing synthetic nanoachines: towards active transport microchip devices", *Lab on a chip*, vol. 12, pp. 1944-1950, 2012.

- [97] J. Orozco, S. Campuzano, D. Kagan, M. Zhou, W. Gao, J. Wang, "Dynamic isolation and unloading of target proteins by aptamer -modified microtransporters", *Analytical Chemistry*, vol. 83, pp. 7962 – 7969, 2011.
- [98] M. Garcia, J. Orozco, M. Guix, W. Gao, S. Sattayasamitsathit, A. Escarpa, A. Merkoci, J. Wang, "Micromotor-based lab-on-chip immunoassays", *Nanoscale*, vol. 5, pp. 1325-1331, 2013.
- [99] S. Campuzano, J. Orozco, D. Kagan, M. Guix, W. Gao, S. Sattayasamitsathit, J.C. Claussen, A. Merkoci, J. Wang, "Bacterial isolation by lectin-modified microengines", *Nano Letters*, vol. 12, pp. 396-401, 2012.
- [100] D. Kagan, S. Campuzano, S. Balasubramanian, F. Kuralay, G. Flechsig, J. Wang, "Functionalized micromachines for selective and rapid isolation of nucleic acid targets from complex samples", *Nano Letters*, vol. 11, pp. 2083-2087, 2011.
- [101] S. Balasubramanian, D. Kagan, C.M. Hu, Campuzano, M.J. Lobo-Castañon, N. Lim, Y. Dae, M. Kang, L. Zimmerman, J. Zhang, J. Wang, "Micromachine enables capture and isolation of cancer cells in complex media", *Angewandte Chemie International Edition*, vol. 50, pp. 4161--4164, 2011.
- [102] D. Kagan, P. Calvo-Marzal, S. Balasubramanian, S. Sattayasamitsathit, K. M. Manesh, G.-U. Flechsig, J. Wang, "Chemical sensing based on catalytic nanomotors: motion-based detection of trace silver", *Journal of the American Chemical Society*, vol. 131, 12082 – 12083, 2009.
- [103] J. Wu, D. Balasubramanian, D. Kagan, K.M. Manesh, S. Campuzano, J. Wang, "Motion-based DNA detection using catalytic nanomotors", *Nature Communications*, vol. 1, 36, 2010.
- [104] J. L. Moran, P. M. Wheat, and J. D. Posner, "Locomotion of electrocatalytic nanomotors due to reaction induced charge autoelectrophoresis", *Physical Review E*, vol. 81, p. 065302, 2010.
- [105] J. L. Moran and J. D. Posner, "Electrokinetic locomotion due to reaction-induced charge auto-electrophoresis", *Journal of Fluid Mechanics*, vol. 680, pp. 31-66, 2011.
- [106] E. Yariv, "Electrokinetic self-propulsion by inhomogeneous surface kinetics," *Proceedings of the Royal Society A: Mathematical, Physical and Engineering Science*, vol. 467, pp. 1645-1664, 2011.
- [107] B. Sabass and U. Seifert, "Nonlinear, electrocatalytic swimming in the presence of salt," *The Journal of Chemical Physics*, vol. 136, 214507, 2012.
- [108] T. R. Kline, W. F. Paxton, Y. Wang, D. Velegol, T. E. Mallouk, and A. Sen, "Catalytic Micropumps: Microscopic Convective Fluid Flow and Pattern Formation", *Journal of the American Chemical Society*, vol. 127, pp. 17150-17151, 2005.
- [109] T. R. Kline, J. Iwata, P. E. Lammert, T. E. Mallouk, A. Sen, and D. Velegol, "Catalytically Driven Colloidal Patterning and Transport", *The Journal of Physical Chemistry B*, vol. 110, pp. 24513-24521, 2006.
- [110] J. Zhang and J. Catchmark, "A catalytically powered electrokinetic lens: toward channelless microfluidics," *Microfluidics and Nanofluidics*, vol. 10, pp. 1147-1151, 2011.
- [111] S. Subramanian and J. M. Catchmark, "Control of Catalytically Generated Electroosmotic Fluid Flow through Surface Zeta Potential Engineering," *The Journal of Physical Chemistry C*, vol. 111, pp. 11959-11964, 2007.
- [112] M. E. Ibele, Y. Wang, T. R. Kline, T. E. Mallouk, and A. Sen, "Hydrazine Fuels for Bimetallic Catalytic Microfluidic Pumping," *Journal of the American Chemical Society*, vol. 129, pp. 7762-7763, 2007.
- [113] H. Zhang, K. Yeung, J. S. Robbins, R. A. Pavlick, M. Wu, R. Liu, *et al.*, "Self-Powered Microscale Pumps Based on Analyte-Initiated Depolymerization Reactions," *Angewandte Chemie International Edition*, vol. 51, pp. 2400-2404, 2012.

- [114] M. Z. Bazant, M. S. Kilic, B. D. Storey, and A. Ajdari, "Towards an understanding of induced-charge electrokinetics at large applied voltages in concentrated solutions," *Advances in Colloid and Interface Science*, vol. 152, pp. 48-88, 2009.
- [115] J.M. Sykes, Y. Xu, "Electrochemical studies of galvanic action beneath organic coatings", *Progress in organic coatings*, vol. 74, pp. 320-325, 2012.
- [116] W. A. Braff, M. Z. Bazant, and C. R. Buie, "Membrane-less hydrogen bromine flow battery," *Nature communications*, vol. 4, 2013.
- [117] V. E. Brunini, Y.-M. Chiang, and W. C. Carter, "Modeling the hydrodynamic and electrochemical efficiency of semi-solid flow batteries," *Electrochimica Acta*, vol. 69, pp. 301-307, 2012.
- [118] R. Kwak, V. S. Pham, K. M. Lim, and J. Han, "Shear flow of an electrically charged fluid by ion concentration polarization: Scaling laws for electroconvective vortices," *Physical Review Letters*, vol. 110, 114501, 2013.
- [119] R. Kwak, G. Guan, W. K. Peng, and J. Han, "Microscale electrodialysis: Concentration profiling and vortex visualization," *Desalination*, vol. 308, pp. 138-146, 2013.
- [120] H. Dong, R. Nie, X. Hou, P. Wang, J. Yue, and L. Jiang, "Assembly of FOF1-ATPase into solid state nanoporous membrane," *Chemical Communications*, vol. 47, pp. 3102-3104, 2011.

Chapter 2

This chapter presents the scope of the work, research goals, road map and summary of incoming chapters.

2.1 Scope of work

This research deals with the catalytic micropump concept which was reported for the first time in 2005 [1]. As described in chapter 1 a catalytic micropump is an active system which has the capability of triggering electrohydrodynamics [2-4] phenomena due to catalytic reactions acting as chemical fuel [1, 5]. Although catalytic devices have been the subject of previous reports in which their nanotechnological applications have started to be demonstrated, the mechanism of the chemo-mechanical actuation has been less studied. That is in part due to the complex interrelation between the catalytic reactions and the electro-hydrodynamics phenomena. As a consequence there is still a number of ill-defined parameters that require further investigation for establishing the role played by the different process and for achieving a better understanding of the mechanism behind. Therefore, the research was focused on the full characterization of the chemomechanical actuation and the understanding of the main physicochemical factors governing the operating mechanism on Au-Pt bimetallic micropumps in presence of hydrogen peroxide fuel. These fundamental studies are of big importance not only for catalytic micropumps but also for other autonomous swimmers or active colloids. The studies were also extended to other bimetallic structures (Au-Ag, Au-Ru, Au-Rh, Cu-Ag, Cu-Ni, Ni-Ru and Ni-Ag) and to semiconductor/metallic structures (p-doped Si/Pt, n-doped Si/Pt) to evaluate their potential for being used as catalytic micropump in presence of the same chemical fuel. In the last case photoactivation of the catalytic reactions can be achieved which provides an added value to these pumps as potential photo-electrohydrodynamic switches. The thesis work also describes a potential application of these active devices in guiding colloidal self-assembly on particular locations of a sample. That allows fabricating nanostructured surfaces in an autonomous way with nanotechnological impact in a wide range of fields.

2.2 Research Goals

There were four main goals:

- I. **Understanding the physical details of the chemochemical mechanism behind bimetallic catalytic micropump using as a model system Au-Pt in hydrogen peroxide solution.**

In this part it was evaluated the influence of the surface chemistry of the bimetallic structures on the electrocatalytic reactions. In this context, surface pretreatment procedures were tested to enhance the electrochemical activity. The full characterization of the electrohydrodynamic parameters was followed up by using two independent techniques based on charged tracers (electric field, electrical potential and fluid velocity) and on fluorescence techniques (for mapping the distribution profile of the more relevant chemical species responsible of triggering the catalytic actuation).

- II. **Implementation of simulations based on finite elements to support experimental data.**

A comprehensive and systematic numerical analysis of the different parameters involved in the function of catalytic devices was performed. The simulations not only reproduced the experimental results but also shed light on the whole catalytic

scenario and provided clues of how to design more efficient catalytic actuators by discriminating the main factors affecting the chemomechanical mechanism.

III. Proposing alternative catalytic micropumps based on other bimetallic or semiconductor/metallic structures.

In this part it was put forth a series of bimetallic couples that can also trigger the catalytic mechanism in presence of hydrogen peroxide. Electrochemical techniques based on TAFEL measurements have become a powerful tool to predict the combination of metals with capabilities of setting-up the electrohydrodynamic process. It was also tested the combination of semiconductor and metal couples in which the catalytic actuation can be additionally turned on with light.

IV. Studying the self-generated electrohydrodynamic process to guide colloidal self – assembly as a potential application of these devices.

In this section it was used a Au-Pt catalytic pump to demonstrate guided colloidal self-assembly as a potential application of these active devices. It was evaluated the effect of the self-generated electrohydrodynamic forces, the zeta potential of the colloids and the surface treatment to locally pattern a surface.

In order to achieve the research goals, a research plan, so called road map, was considered. Figure 2.1 shows the work flow of the research.

2.3 Incoming chapters

Besides the introduction and this chapter, in which it has been covered the state of the art of the research in artificial swimmers/micropumps and outlined the research motivation and goals of the thesis, respectively, the dissertation contains seven more chapters.

Chapter 3 includes essential pieces of information about electrohydrodynamics to provide proper background. Experimental activities, device fabrication and characterization are described at chapter 4 in detail. Chapter 5 provides results and discussion of the model system Pt-Au together with the finite numerical simulations that have aided to set a physical and chemical comprehensive vision of the chemomechanical actuation. Chapter 6 comprises the evaluation of the electrohydrodynamic performance of alternative bimetallic structures and chapter 7 addresses semiconductor/metallic structures as catalytic pumps with the added value of being photoactivated. Chapter 8 describes a potential application of the chemomechanical actuation: autonomous guided self-assembly which allows to preferentially pattern regions of a sample. Finally, chapter 9 outlines general conclusions together with the perspectives of active devices.

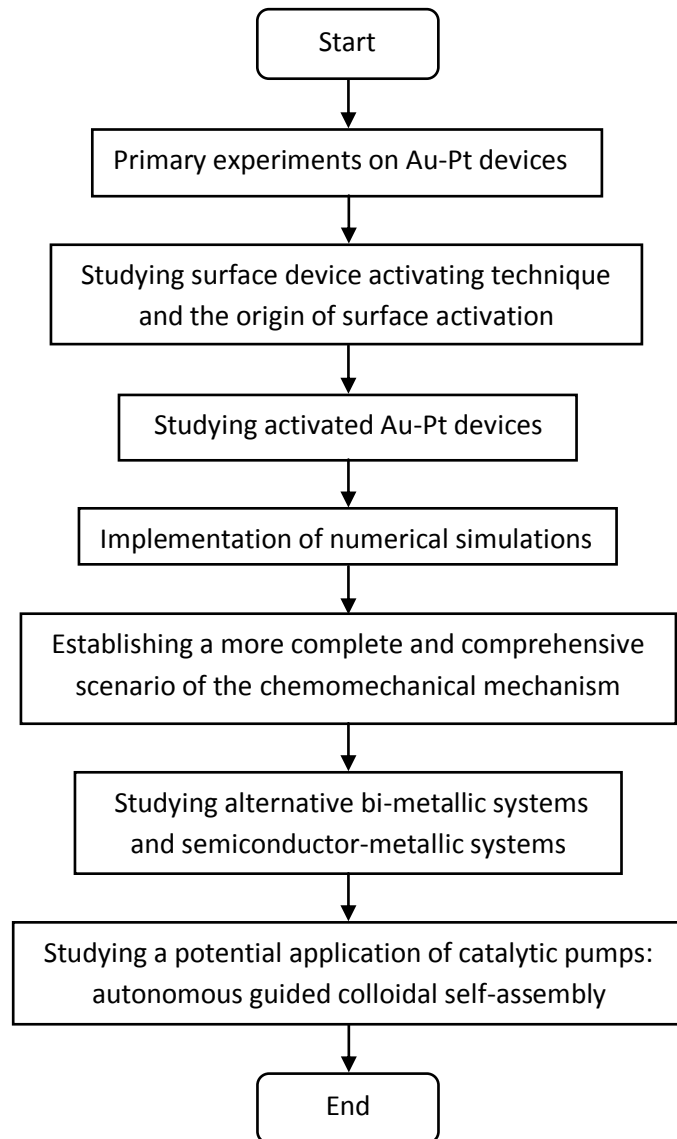


Figure 2.1: The work flow of the research

References

- [1] T. R. Kline, W. F. Paxton, Y. Wang, D. Velegol, T. E. Mallouk, and A. Sen, "Catalytic micropumps: microscopic convective fluid flow and pattern formation," *Journal of the American Chemical Society*, vol. 127, pp. 17150-17151, 2005.
- [2] A. Castellanos and I. C. f. M. Sciences, *Electrohydrodynamics*: Springer, 1998.
- [3] A. Ramos, *Electrokinetics and Electrohydrodynamics in Microsystems*: SpringerWienNewYork, 2011.
- [4] J. Russell and R. Cohn, *Electrohydrodynamics*: Book on Demand, 2012.
- [5] M. E. Ibele, Y. Wang, T. R. Kline, T. E. Mallouk, and A. Sen, "Hydrazine Fuels for Bimetallic Catalytic Microfluidic Pumping," *Journal of the American Chemical Society*, vol. 129, pp. 7762-7763, 2007/06/01 2007.

Chapter 3

In this chapter, a brief review of electrokinetics phenomena, the related concepts (surface charge, electric double layer and zeta potential) and governing equations which are essential to understand the future chapters will be presented. As mentioned previously, the electrokinetic phenomenon depends on the interaction of a complex set of interrelated variables and parameters. Therefore to thoroughly address this issue from an experimental or theoretical point of view is a difficult task

3.1 Electrokinetics

Electrokinetic generally covers all those phenomena involving tangential fluid motion adjacent to charged surfaces as a consequence of an external force (e.g. electric force, gravitational force, etc.) [1-5]. Among the many types of phenomena that can be described as electrokinetic processes the more commonly encountered are: electrophoresis, electroosmosis, streaming potential and sedimentation potential [1-4].

Electrokinetics has been widely applied in microsystems [1-3], microfluidics and nanofluidics [2, 4-6], tissue engineering [7-9], drug delivery [6, 10, 11], chromatography [12, 13], remediation of soils and control of hazardous wastes [6, 14, 15] etc. It is also a very important tool in biological methods for separation and analysis of macromolecules (DNA, RNA and proteins) and their fragments, based on their size and charge [16].

In this chapter, electrophoresis and electro-osmosis will be reviewed since they are the mainly two electrokinetic phenomena behind the catalytic pumps.

3.2 Concepts and Governing equations

Electrokinetic phenomena are described by the governing equations in fluid mechanics and transport phenomena [4, 6, 17, 18]. In this chapter, a complete derivation of the governing equations will not be provided. It will be only outlined the main equations which are necessary to explain the movement of liquid at the interface of the catalytic pump and the movement of charged colloidal particles¹⁰ due to electro-osmosis and electrophoresis.

In view that the systems are based on charged interfaces, it will be first addressed the Poisson equation as the main equation of the electrostatics and then the double layer concept will be developed. Since the catalytic pumps exhibit non-static double layer conditions due to the electrochemical reactions taken place at the double layer interface, the concept of electrochemical current at the interface will be discussed. The importance of this topic stems from the fact that electrochemical current at the

¹⁰ Rigid spherical colloidal particles are taken as a model system to describe the governing equations

interface is the source of asymmetrically charged species generation which plays a crucial role in the electrokinetic process. Then, it will be discussed the set of equations related with the transport of species and fluid flow. Finally the chapter will be finished with a more detailed discussion of the electrophoresis and electro-osmosis processes.

Therefore the main equations of interest are:

- a. Poisson equation
- b. Nernst-Planck equation
- c. Continuity equation
- d. Navier-Stokes equation

It is assumed that the electrolyte contains N species. For i^{th} specie in the solution, the following parameters are defined:

n_i : Number concentration of i^{th} species [m^{-3}]

$n_{i\infty}$: Number concentration of i^{th} species in bulk solution [m^{-3}]

M_i : Molar mass of i^{th} species [$kg. (k mol)^{-1}$]

z_i : Valence of the i^{th} ionic species including appropriate sign

D_i : Diffusion coefficient of i^{th} specie [$m^2. s^{-1}$]

ρ_i : Density of i^{th} specie [$kg. m^{-3}$]

3.3 Poisson's equation

It is an important electrostatic equation which is derived from Gauss's law. The Poisson's equation relates the electric potential (ψ) which is a scalar function to dielectric constant (or relative permittivity) of medium (ϵ_r) and the free volumetric charge density (ρ_f) in a dielectric medium. If the \mathbf{E} is electric field generated by electric charge distributed in dielectric medium, ψ is the generated potential (equation 3.1). [6, 17, 19]

$$\mathbf{E} = -\nabla\psi \quad \text{Equation 3.1}$$

Poisson's equation for electric potential in the electrolyte is [6, 19]:

$$\nabla^2\psi = -\frac{\rho_f}{\epsilon_r\epsilon_0} \quad \text{Equation 3.2}$$

ρ_f : Free volumetric charge density [$C \cdot m^{-3}$]

ϵ_r : Relative permittivity of medium (Dimensionless)

ϵ_0 : Free space permittivity (8.854187×10^{-12} [$F \cdot m^{-1}$])

The free volumetric charge density ρ_f is the charge density of any charge which is not generated because of polarization¹¹. For instance, ions in the solution, ions embedded in the dielectric material and electrons on conductor material are categorized under free charges. [6]

When studying a solution containing N charged species, ρ_f can be written by equation 3.3 to cover the existence of all ions distributed in electrolyte. [6, 19]

$$\rho_f = \sum_{i=1}^N e \cdot z_i n_i \quad \text{Equation 3.3}$$

e : Magnitude of the elementary charge on an electron [1.602×10^{-19} C]

It is essential to mention that the concentration and type of ions in the electrolyte may affect the permittivity of the electrolyte [20].

3.4 Electric double layer

When a solid object is brought into contact with an aqueous solution¹², the arrangement of anions and cations in the solution change over a finite volume around the solid. Due to the interaction between surface charge of the solid and ions in the solution, the counter-ions¹³ surround the solid surface simultaneously. These counter-ions compensate the surface charge in order to keep electro-neutrality in the system. As the distance from the solid surface increases, the concentration of the counter-ions decreases up to reach their concentration in bulk fluid. In contrast to counter-ions, the concentration of the co-ions¹⁴ increases up to reach the co-ion concentration in bulk solution with increasing distances from the surface. The volume in which the new ion

¹¹ Free charge density is not the total charge density . Total charge density of system is the sum of polarization charge density and the free charge density.

¹² The most important liquid to build a double layer is water. Because of its high dielectric constant water is a good solvent for ions. For this reason most surfaces in water are charged.

¹³ Ions in the solution with sign which is opposite of charge of solid surface are counter-ions.

¹⁴ Ions in the solution with sign which is same as charge of solid surface are co-ions.

distribution in the solution is formed around the solid is so called **electric double layer (EDL)**¹⁵. [6, 18, 19, 21, 22]

Regardless of its generating mechanism, the existence of surface charge on the solid surface causes an electric double layer. Although different mechanisms in different systems may generate surface charge¹⁶ [18, 23-25], there are three major reasons which explain the existence of surface charge in aqueous medium:

- a. Dissociation or ionization of chemical groups on the surface
- b. Adsorption of ions or molecules from the solution
- c. Application of an electric field between a surface and a counter-electrode

In the absence of adsorption of specific ions or molecules from the solution or an external electric field, ionization of acidic or basic groups¹⁷ is the most common way of obtaining surface charge. The ionization of acidic or basic groups depends on the pH of the solution. Generally, acid groups release hydronium ions (H_3O^+) into the solution and the solid surface gets negative charge. In case of basic groups, the groups incorporate protons and the surface becomes positively charged. [26-28]

Two examples which are relevant to this research¹⁸ are polystyrene bead functionalized with amidine group ($-NH_2$)¹⁹ and silica beads. For amidine-functionalized polystyrene beads, hydronium ions protonate amidine groups and change it to $[-NH_3^+]$. So the particle surface obtains positive charge [25].

In the case of silica beads, the silanol groups ($[-Si - OH]$) at silica-water interface are quite acidic and tend to be dissociated $[-Si - O^-]$ providing a negative charge to the silica surface [29, 30]. However this negative charge can be modified to a more neutral one if the pH of the medium is considerably decreased.

Double-layer theory emerged in the middle of nineteenth century. Helmholtz proposed the concept and described a model of Double-layer formation on an interface for the first time [31].

¹⁵ The term of "double" is applied traditionally. There is no essential relation between the term of "double" and number of layers in an applied model.

¹⁶ For instance; preferential adsorption of ions in solution, adsorption-desorption of lattice ions for silver iodide, direct dissociation or ionization of surface groups, Charge-defective lattice: isomorphous substitution for minerals etc.

¹⁷ It is valid only for groups which have ability to be dissociated or ionized in the solution.

¹⁸ These particles were applied as the tracers.

¹⁹ In this thesis, we will refer to amidine in its more simple formula $RC(=NH)NH_2$. We do not know the exact substituents that can have the $-NH_2$ group in the functionalized polystyrene beads

Primary proposed models considered one layer for electric double layer. One-layer models like Constant-Capacitance Model (CCM) and Diffuse-Layer Model (DLM), were not comprehensive enough to explain phenomena like ion pairs formation between charge surface group and ions in solution, electro neutrality condition and surface charge variation with ionic strength. Therefore models with more layers were developed to explain additional features. [21, 32-37]

For further reading, the most highlighted models are mentioned in the table 3.1.

| Number of Layers | Model | Reference |
|------------------|--|-----------------|
| 1 | Constant-Capacitance Model (CCM) | [21, 32-41] |
| | Diffuse-Layer Model (DLM) | [21, 32-37] |
| 2 | Extended Constant Capacitance Model (ECCM) | [21, 42-46] |
| | 1-pK Stern-layer Model | [21, 47-51] |
| 3 | 1-pK Triple Layer Model (1-pK TLM) ²⁰ | [21, 52-54] |
| | 2-pK Triple Layer Model (2-pK TLM) | [21, 52-56] |
| | Triple Plane Model (TPM) | [21, 51, 57-61] |
| 4 | Four Layer Model (FLM) | [21, 61-64] |

A developed triple layer model (TLM)²¹ is described in this chapter based on references [18, 19, 65]. Figure 3.1 shows schematically the ion distribution and potential distribution in the electric double layer. To explain the model easily, five planes parallel to the solid surface (plane A, B, C, D and E) are defined.

In this model, the electric double layer has two major parts:

- 1- Compact layer²² (space between plane A and C)
- 2- Diffuse layer²³ (space between plane C and E)

Plane C is boundary between compact and diffuse layers. The compact layer comprises ions which are directly adsorbed to the surface and which are immobile. It is divided into two regions:

²⁰ 1-pK 2-pK are two approaches to evaluate protonation mechanisms. For more information: József Tóth, "Adsorption: Theory, Modeling, and Analysis", Volume 107 of Surfactant Science Series, CRC Press, 2002

²¹ It is the triple layer model (2-pK inter/ outer shell).

²² Compact layer may be addressed as *Stern layer*, *inner part of double layer* or *dense part of double layer* (comprises the inner and outer layer).

²³ Diffuse layer may be addressed as *diffuse part of double layer*.

- a. Inner layer(space between plane A and B)
- b. Outer layer(space between plane B and C)

Plane A is the solid surface. The surface charge of the solid is located in this plane. The charge is the so called *titratable* charge. **Plane B**, referred as inner Helmholtz plane (IHP), separates inner layer and outer layer of the compact layer. The locus of the inner layer contains solvent molecules and other ions that are said to be specifically adsorbed. Normally these ions have lost part of their hydration layer or their ionic atmosphere²⁴. The distance of this plane from the surface is in the order of an atomic radius. **Plane C** is the outer Helmholtz plane (OHP) which is the boundary between diffuse layer and compact layer. At the plane C, there are ions, which have less electrostatic interaction with charged solid surface and contain their solvation layer. Those electrostatic interactions are not powerful enough to move the ions into the plane B but the ions and their ionic atmosphere are immobile and bounded to the solid surface. It is assumed that there is no ion between plane B and C. **Plane E** is boundary of electric double layer and bulk solution. The space between the plane C and E is the *diffuse layer*. [18, 19, 65]. **Plane D** which is located in the diffuse layer is the so called slip plane²⁵. It is boundary between the immobile and mobile ions. All ions placed between the solid surface and **plane D** are immobile. The potential at the slip plane is the zeta potential (ζ). Zeta potential is an important concept in electrokinetics, colloidal and interfacial science.

The main feature of diffuse layer is the spatial distribution of co-ions and counter-ions on it. As the potential over the diffuse layer decreases, the concentration of counter-ions decreases. At the same situation, the concentration of co-ions increases. Distribution of ions over the diffuse layer in the equilibrium condition is estimated with the Boltzmann distribution²⁶ (equation 3.4). Distribution of i^{th} specie over the diffuse layer depends on the potential (ψ), temperature, the concentration on the bulk and ion's valence number. [18, 19, 65]

²⁴ In this research, the electrolyte is water-based. Therefore, understanding of hydration process (solvation process) which deals with ion- water molecules interaction is important. Hydration process keeps the ions in the solution. When an ion entered to the water, local electric field generated by the ion polarizes the water molecules locally. Polarized water molecules orient themselves around the ions. This polarized region is so called *ionic atmosphere*. The ion and its ion atmosphere move together.

²⁵ Slip plane may be addressed as *shear plane* or *slipping plane*.

²⁶ Boltzmann distribution is valid when equation $\nabla\eta_i = 0$. η_i is electrochemical potential of i^{th} specie.

$$n_i = n_{i\infty} \cdot \exp\left(-\frac{ez_i}{k_B T} \psi\right) \quad \text{Equation 3.4}$$

According to equations 3.3 and 3.4, free volume charge density (ρ_f) is:

$$\rho_f = \sum_{i=1}^N \left[e \cdot z_i \cdot n_{i\infty} \exp\left(-\frac{ez_i}{k_B T} \psi\right) \right] \quad \text{Equation 3.5}$$

So, the Poisson equation (equation 3.2) for the system is:

$$\nabla^2 \psi = -\frac{1}{\epsilon_r \epsilon_0} \sum_{i=1}^N \left[e \cdot z_i \cdot n_{i\infty} \exp\left(-\frac{ez_i}{k_B T} \psi\right) \right] \quad \text{Equation 3.6}$$

The equation 3.6 is Boltzmann - Poisson equation [18, 19, 65]. It shows the relation between potential and the ion type and concentration in the electrolyte. Thickness of diffuse layer or the Debye length (κ^{-1})²⁷ is [18, 19, 65]:

$$\kappa^{-1} = \sqrt{\epsilon_r \epsilon_0 k_B T} \left[\sum_{i=1}^N e^2 z_i^2 n_{i\infty} \right]^{-\frac{1}{2}} \quad \text{Equation 3.7}$$

There is an interesting relation between the Debye length and the *ionic strength* (I) of the solution. The ionic strength of the solution is defined as [66]:

$$I = \frac{N_A}{2} \cdot \sum_{i=1}^N z_i^2 n_{i\infty} \quad \text{Equation 3.8}$$

Considering equations 3.7 and 3.8:

²⁷ The Debye length may be addressed as *Debye-Huckel parameter*.

$$\kappa^{-1} = \sqrt{\frac{N_A \epsilon_r \epsilon_0 k_B T}{2e^2 I}}$$

Equation 3.9

Equation 3.9 shows that the Debye length strongly depends on the temperature, permittivity and the ionic strength of the solution and not on the solid surface properties. Increasing the ionic strength of the liquid or decreasing temperature decreases the diffuse layer thickness [4].

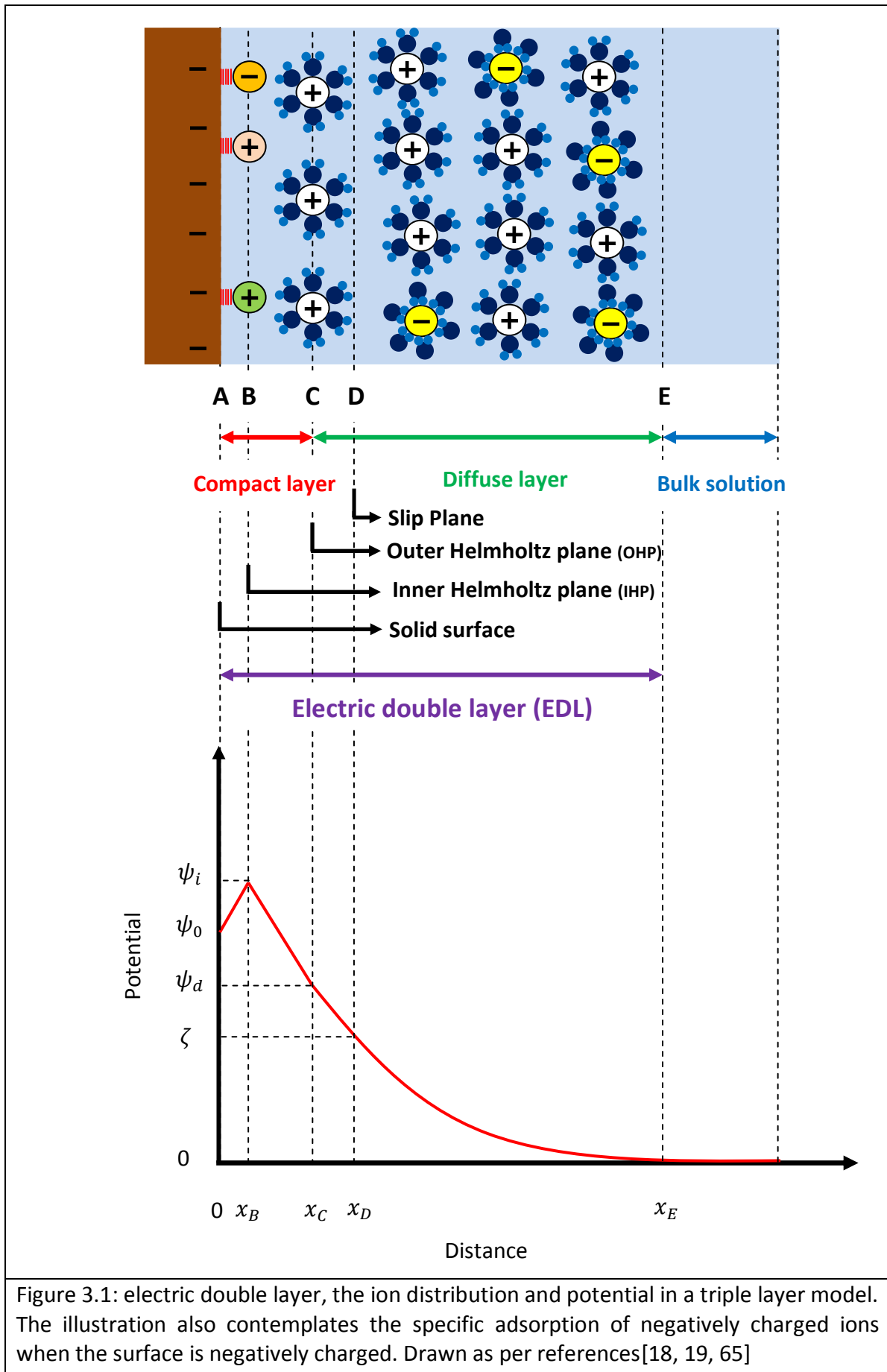


Figure 3.1: electric double layer, the ion distribution and potential in a triple layer model. The illustration also contemplates the specific adsorption of negatively charged ions when the surface is negatively charged. Drawn as per references[18, 19, 65]

As a principle, the electroneutrality of the system is preserved. Therefore, the overall charge over the electric double layer and the solid surface should be equal to zero. Considering the charge on the solid surface (plane A), Helmholtz plane (plane B) and over the diffuse layer (between planes C and E) as Q_0 , Q_i and Q_d respectively, then the overall charge in the system should be [18, 19, 65]:

$$Q_0 + Q_i + Q_d = 0 \quad \text{Equation 3.10}$$

If the charge density of solid surface (plane A) and inner Helmholtz plane (plane B) are σ_0 and σ_i respectively, the equation 3.10 becomes:

$$\sigma_0 + \sigma_i + \int_{x=x_C}^{x=x_E} \rho_f dx = 0 \quad \text{Equation 3.11}$$

x_C : Distance from solid surface to the plane C [m]

x_E : Distance from solid surface to the plane E [m]

Considering equation 3.5 for ρ_f at equilibrium, equation 3.11 becomes:

$$\sigma_0 + \sigma_i + \int_{x=x_C}^{x=x_E} \left(\sum_{i=1}^N \left[e \cdot z_i \cdot n_{i\infty} \exp\left(-\frac{e z_i}{k_B T} \psi\right) \right] \right) dx = 0 \quad \text{Equation 3.12}$$

The potential over the diffuse layer depends on the position from the solid surface. So, the relation between charge density on different planes and free charges on the solution is not so simple.

The potential distribution over the electric double layer is an important topic. The potential at solid surface (plane A), inner Helmholtz plane (plane B), outer Helmholtz plane (plane C) and diffuse layer are ψ_0, ψ_i, ψ_d and ψ respectively. Surface charge on the solid generates the surface potential (ψ_0) which attracts counter-ions and repulses co-ions of the solution. If the space between solid surface and inner Helmholtz plane (planes A and B) is assumed as an ion-free zone, the space between two charged surfaces is considered as a capacitor²⁸ with capacitance equal to C_1 . Similarly for the space between

²⁸ Based on charge neutrality equation, the charge on the solid surface (plane A) is equal to total charge over distance between inner Helmholtz plane (plane B) and plane E with opposite sign. This is why it can be considered as a capacitor.

inner and outer Helmholtz plane (planes B and C), C_2 is defined as the capacitance. The potential distribution over double layer (figure 3.1) is described with following equations [18, 19, 65]:

$$\psi_0 - \psi_i = \frac{\sigma_o}{C_1} \quad \text{Equation 3.13}$$

$$\psi_i - \psi_d = \frac{\sigma_o + \sigma_i}{C_2} \quad \text{Equation 3.14}$$

σ_o : Charge density of the solid surface (plane A) [$C.m^{-2}$]

σ_i : Charge density of the plane B [$C.m^{-2}$]

Regarding the potential distribution over diffuse layer (ψ), the resolution of equation 3.6 with proper boundary conditions and assumptions, provides the potential profile. The potential is considered as zero at the plane E and bulk solution. [18, 19, 65]

3.5 Electrochemical kinetics at the metal interface

The electrochemical reaction and kinetics at a surface is an added ingredient of the electrokinetic process in the special case of catalytic systems. As mentioned in the introduction, the process is based on the oxidation and reduction of chemical species on heterogeneous electrodes. This redox process generates the charged species which trigger the electrokinetic process. The reaction current depends on the local electric potential at the interface, concentrations of reactant species and the rate constants of the electrodes. The kinetic process is described by the Butler–Volmer formalism incorporating the Frumkin correction [67]. The oxidation and reduction equations at the anode (equation 3.15) and cathode (equation 3.16) can be represented by:



R_A : Reduced form of the redox couple in anode

R_C : Reduced form of the redox couple in cathode

O_A : Oxidized form of the redox couple in anode

O_C : Oxidized form of the redox couple in cathode

n : Number of electrons participated in the reaction

The Frumkin-corrected Butler–Volmer equation for the oxidation (equation 3.17) and reduction (equation 3.18) at the anode and cathode respectively are:

$$j_A = k_A \cdot C_{R_A} \cdot \exp\left(\frac{(1 - \alpha) \cdot n \cdot F \cdot \Delta\psi_i}{RT}\right) \quad \text{Equation 3.17}$$

$$j_C = -k_C \cdot C_{O_C} \cdot \exp\left(-\frac{\alpha \cdot n \cdot F \cdot \Delta\psi_i}{RT}\right) \quad \text{Equation 3.18}$$

j_A : The electrochemical current density for the oxidation

j_C : The electrochemical current density for the reduction

k_A : Effective rate constants for the oxidation

k_C : Effective rate constants for the reduction

C_{R_A} : The respective concentrations of reactants for the oxidation

C_{O_C} : The respective concentrations of reactants for the reduction

α : A dimensionless number between 0 and 1

$\Delta\psi_i$: The electrode potential drop at the Stern layer (compact layer) of the double layer.

α Coefficient is a dimensionless number which describes the symmetry of the activation energy barrier for the reaction.

. For simplicity, only the forward reactions are considered. The potential drop across the compact Stern layer scales with the ratio between the Stern layer length (λ_s), the

Debye length (λ_D or κ^{-1}) and with the zeta potential of the substrate (ζ_w) according to the equations 3.19 and 3.20. [67]

$$\Delta\psi_i = \zeta_w - \psi \quad \text{Equation 3.19}$$

$$\Delta\psi_i \propto \frac{\lambda_s}{\lambda_D} \zeta_w \quad \text{Equation 3.20}$$

ψ : The total potential drop at the metal electrode

In the case of very low salt concentrations in the electrolyte:

$$\frac{\lambda_s}{\lambda_D} \ll 1 \quad \text{Equation 3.21}$$

The $\Delta\psi_i$ would be very small (below the millivolts) and the potential at the surface becomes approximately equal to the zeta potential [67]. Under such circumstances, the electrochemical current of protons at the anode and cathode becomes independent of the potential and proportional to the concentration of the reactants:

$$j_A = k_A \cdot C_{RA} \quad \text{Equation 3.22}$$

$$j_C = -k_C \cdot C_{OC} \quad \text{Equation 3.23}$$

3.6 Nernst–Planck Equation

Another important topic in electrokinetic systems is the movement or mass transfer of ions. Movement of ions occurs by convection, diffusion and migration due to *external forces* (\mathbf{F}_{EXT}). To quantify the movement of i^{th} specie in the solution, the *number concentration flux* (\mathbf{j}_i) is defined as number of i^{th} species crossing control volume per second [6, 18, 19, 68, 69]:

$$\mathbf{j}_i = n_i \mathbf{v}_i \quad \text{Equation 3.24}$$

\mathbf{j}_i : Number concentration flux [$m^{-2} \cdot s^{-1}$]

\mathbf{v}_i : Velocity field of i^{th} species

Convection, diffusion and migration due to external forces contribute in the total number concentration flux. It can be written as superposition of the number concentration flux due to convection ($\mathbf{j}_{i,C}$), diffusion ($\mathbf{j}_{i,D}$) and an external force ($\mathbf{j}_{i,M}$) [6, 68]:

$$\mathbf{j}_i = \mathbf{j}_{i,C} + \mathbf{j}_{i,D} + \mathbf{j}_{i,M} \quad \text{Equation 3.25}$$

For low concentration i^{th} specie solution, \mathbf{j}_i is [6, 68]:

$$\mathbf{j}_i = n_i \mathbf{u} - D_i \nabla n_i - \frac{n_i}{k_B T} D_i \mathbf{F}_{EXT} \quad \text{Equation 3.26}$$

\mathbf{u} : Velocity vector of bulk fluid

k_B : Boltzmann constant [$1.3806 \times 10^{-23} \text{ J K}^{-1}$]

T : Temperature [K]

In electrokinetics, the electric force can be considered as an external force. If electric field (\mathbf{E}) forces i^{th} species to migrate, the relevant electric force (\mathbf{F}_{EXT}) on i^{th} specie is [6, 68]:

$$\mathbf{F}_{EXT} = -e z_i \nabla \psi \quad \text{Equation 3.27}$$

Substituting equation 3.27 in equation 3.26 provides the Nernst–Planck equation [6, 18, 19, 68]:

$$\mathbf{j}_i = n_i \mathbf{u} - D_i \nabla n_i - \frac{e n_i z_i}{k_B T} D_i \nabla \psi \quad \text{Equation 3.28}$$

Considering equations 3.24 and 3.28, the relation between velocity field of i^{th} specie (\mathbf{v}_i) and the velocity field of bulk fluid (\mathbf{u}) is:

$$\mathbf{v}_i = \mathbf{u} - \frac{D_i \nabla n_i}{n_i} - \frac{e z_i}{k_B T} D_i \nabla \psi \quad \text{Equation 3.29}$$

For steady state conditions without chemical reaction the combination of mass conservation equation (equation 3.36) and equation 3.29 gives:

$$\nabla \left[n_i \mathbf{u} - D_i \nabla n_i - \frac{e n_i z_i}{k_B T} D_i \nabla \psi \right] = 0 \quad \text{Equation 3.30}$$

3.7 Governing equation for the fluid motion

Continuity equation and Navier–Stokes equation are the governing equation for the fluid motion.

3.7. a Continuity equation

Mass conservation in a fluid system is a fundamental law. Generally, the rate of mass accumulating within a control volume²⁹ is the difference between the entering and leaving mass into the control volume (equation 3.31). The continuity equation connects the fluid velocity vector in the system (\mathbf{u}) to the fluid density rate. [6, 17-19, 70]

It is written as follow:

$$\frac{\partial \rho}{\partial t} = -\nabla(\rho \mathbf{u}) \quad \text{Equation 3.31}$$

ρ : Fluid density [$kg \cdot m^{-3}$]

t : Time [s]

It is the *mass conservation law* or *continuity equation*. In case of time independent fluid density or steady state system, the rate of mass enters in control volume is equal to the rate of mass leaves of the control volume. [6, 18, 19, 70]

So, the equation 3.31 is changed to:

²⁹ Control volume is the finite volume on which the principles can be applied.

$$\nabla \mathbf{u} = 0 \quad \text{Equation 3.32}$$

Besides single compound systems, continuity equation is valid for multi-compound systems. If there are several species in a multi-compound system, continuity equation can be written for i^{th} specie [6, 18, 19]:

$$\frac{\partial \rho_i}{\partial t} = -\nabla(\rho_i \mathbf{v}_i) + R_i \quad \text{Equation 3.33}$$

\mathbf{v}_i : Fluid velocity vector of i^{th} specie

R_i : Source term of i^{th} specie [$kg \cdot m^{-3} \cdot s^{-1}$]

Source term (R_i) is the production rate of i^{th} specie due to chemical reaction per unit volume. In case of steady state, the equation 3.3 becomes [6, 19]:

$$\nabla(\rho_i \mathbf{v}_i) = 0 \quad \text{Equation 3.34}$$

The density of i^{th} specie can be defined as [6]:

$$\rho_i = \frac{n_i M_i N_A^{-1}}{1000} \quad \text{Equation 3.35}$$

N_A : Avogadro number ($6.02214 \times 10^{23} [mol^{-1}]$)

Incorporating equation 3.35 on equation 3.34 provides:

$$\nabla(n_i \mathbf{v}_i) = 0 \quad \text{Equation 3.36}$$

3.7.b Navier-Stokes equation

Navier–Stokes equation deals with conservation of momentum in the fluid motion. It is derived from Newton's second law of motion which explains momentum conservation [6, 17, 19, 68, 70, 71].

Gravity force ($\mathbf{f}_{gravity}$), pressure force ($\mathbf{f}_{pressure}$), viscosity force ($\mathbf{f}_{viscosity}$) and any other forces imposed to the fluid (body forces, \mathbf{f}_b), may push the fluid to flow and accelerate. As per Newton's second law, the relation between forces and generated acceleration (\mathbf{a}) is:

$$\mathbf{f}_{gravity} + \mathbf{f}_{pressure} + \mathbf{f}_{viscosity} + \mathbf{f}_b = m\mathbf{a} \quad \text{Equation 3.37}$$

Where m is mass of the fluid which is under the forces. The \mathbf{f}_b represents a generic force like electric force or centrifugal force. Navier–Stokes equation in vector form for homogeneous, incompressible, low Reynolds number³⁰, Newtonian fluid³¹ with constant viscosity is [6, 17, 19]:

$$\rho \frac{\partial \mathbf{u}}{\partial t} + \rho \mathbf{u} \nabla \mathbf{u} = -\nabla P + \eta \nabla^2 \mathbf{u} + \rho \mathbf{g} + \mathbf{f}_b \quad \text{Equation 3.38}$$

\mathbf{u} : Velocity vector in the system

P : Fluid pressure [N. m⁻²]

\mathbf{g} : Acceleration due to gravity

η : Fluid viscosity [Pa.s]

\mathbf{f}_b : Any other body force per unit volume [F. m⁻³]

Besides gravity, pressure and viscosity forces which always affect the fluid, electric force are considered body forces in the electrokinetic problems. Existence of electric field (\mathbf{E}) generates electric force (\mathbf{f}_E) per unit volume [6, 17]:

$$\mathbf{f}_E = \rho_f \mathbf{E} - \frac{1}{2} \mathbf{E} \cdot \mathbf{E} \nabla \varepsilon + \frac{1}{2} \nabla \left[\left(\rho \frac{\partial \varepsilon}{\partial \rho} \right)_T \mathbf{E} \cdot \mathbf{E} \right] \quad \text{Equation 3.39}$$

ε : Permittivity of the fluid [F.m⁻¹]

ρ : Density of the fluid [kg.m⁻³]

T : Temperature [K]

If the liquid permittivity is constant, \mathbf{f}_E is

$$\mathbf{f}_E = \rho_f \mathbf{E} \quad \text{Equation 3.40}$$

Considering equation 3.1, the electric force is:

$$\mathbf{f}_E = -\rho_f \nabla \psi \quad \text{Equation 3.41}$$

³⁰ Reynolds number is a dimensionless quantity defined as the ratio of inertial forces to viscous forces and consequently quantifies the relative importance of these two types of forces. Low Reynold numbers (such as in in this case, $Re_e < 10$) means that the viscous forces are important, an effect that becomes very important for nano-objects.

³¹ Newtonian liquid is a liquid which it's viscosity is constant for a fixed temperature and pressure.

Incorporating equation 3.41 into the Navier–Stokes equation (equation 3.38):

$$\rho \frac{\partial \mathbf{u}}{\partial t} + \rho \mathbf{u} \nabla \mathbf{u} = -\nabla P + \eta \nabla^2 \mathbf{u} + \rho \mathbf{g} - \rho_f \nabla \psi \quad \text{Equation 3.42}$$

In steady state, equation 3.32 is valid. So, the Navier–Stokes equation is:

$$-\nabla P + \eta \nabla^2 \mathbf{u} + \rho \mathbf{g} - \rho_f \nabla \psi = 0 \quad \text{Equation 3.43}$$

If the $\rho \mathbf{g}$ is considered as a negligible term, the equation 3.43 becomes:

$$-\nabla P + \eta \nabla^2 \mathbf{u} - \rho_f \nabla \psi = 0 \quad \text{Equation 3.44}$$

3.8 Electro-osmosis

Electro-osmosis is the relevant electrokinetic phenomenon for describing the chemomechanical actuation in catalytic pumps. It comprises the motion of the non-electroneutral liquid at the electric double layer of a charged solid surface due to an electric field. As previously mentioned, the formation of the double layer comprises the appearance of a diffuse layer which is a non-zero charge density solution. An applied electric field parallel to the solid surface forces the ions to move. The motion of ions drags the liquid and causes a bulk fluid motion. [17, 18, 69]

Unlike pressure-driven flow, electro-osmotic flow depends on an electric double layer formation. Electro-osmotic velocity is derived by integrating Navier Stokes equation in presence of an electrical force and considering Poisson equation [69]. Depending on the distance from the solid surface, there are two different profiles for the electro-osmotic velocity, one taken place in the electric double layer and the other in the bulk liquid (figure 3.2) If the electric field is assumed constant in the double layer, the velocity will depend on the Coulomb force acting on the ions of the electric double layer and on the viscose drag at the solid surface. Fluid velocity in electric double layer (\mathbf{u}_{eo-EDL}) is [69]:

$$\mathbf{u}_{eo-EDL} = \frac{\varepsilon_r \varepsilon_0}{\eta} (\psi - \zeta_s) \mathbf{E} \quad \text{Equation 3.45}$$

ϵ_r : Relative permittivity of medium (Dimensionless)

ϵ_0 : Free space permittivity ($8.854187 \times 10^{-12} \text{ F.m}^{-1}$)

ζ_s : Zeta potential of the solid surface [V]

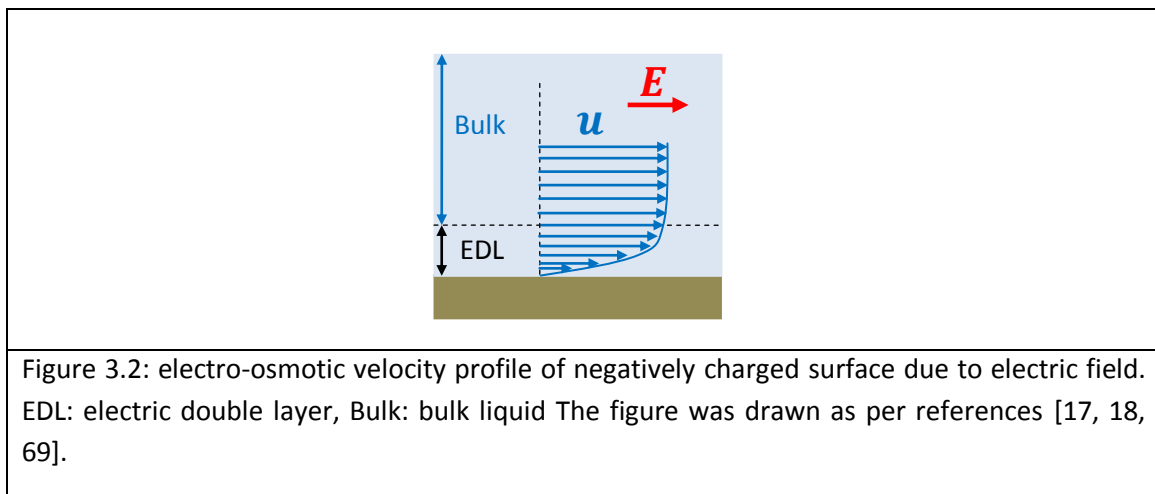
ψ : Potential at electric double layer [V]

η : Fluid viscosity [Pa.s]

Over a distance range from the solid surface ($x = 0$) to the end of the diffuse layer ($x = \kappa^{-1}$)³², the velocity is not constant. It depends on the potential distribution at the electric double layer. The velocity increases as the distance from the surface is incremented from zero at the solid surface up to $x = \kappa^{-1}$. [69]

In bulk liquid, the velocity is constant if the electric field remains constant [17, 18, 69]. The velocity at bulk liquid ($\mathbf{u}_{eo-Bulk}$) is:

$$\mathbf{u}_{eo-Bulk} = -\frac{\epsilon_r \epsilon_0 \zeta_s}{\eta} \mathbf{E} \quad \text{Equation 3.46}$$



³² κ^{-1} : the Debye length of the electric double layer

3.9 Electrophoresis

The electrophoresis deals with the movement of charged colloidal particles relative to the liquid due to an electric field. The charged particle³³ starts moving due to the generated electrostatic force (F_E) (equation 3.47). The electrostatic force depends on the particle charge and the electric field [18, 19, 65]:

$$F_E = Q_s E \quad \text{Equation 3.47}$$

Q_s : Particle charge [C]

As soon as the particle starts to move under the influence of the electrical force, a viscous force exerted by the liquid in the opposite direction tends to retard the particle. The velocity of the particle is the so called electrophoretic velocity (V_e). The force in the opposite direction is the fluid drag force (F_s), Stokes' drag force, [18, 19, 65]:

$$F_s = -6\pi\eta a V_e \quad \text{Equation 3.48}$$

η : Viscosity of medium [$kg.s^{-1}.m^{-1}$]

a : Particle radius [m]

In steady state condition the particle moves at constant velocity and the relation between the two opposite forces (Stokes' drag and electrostatic force) acting on the system, is as follows [18, 19, 65]:

$$F_s + F_E = 0 \quad \text{Equation 3.49}$$

Equation 3.49 is an important equation to analyze the electrophoretic motion of the spherical particle. One of the most useful parameters to analyze the electrokinetic phenomenon is the electrophoretic mobility (μ_e). It is defined as the generated electrophoretic velocity per unit of applied electric field. Equations 3.50 and 3.51 show the relation between the applied electric field and the electrophoretic velocity. [18, 19, 65]

$$V_e = \mu_e E \quad \text{Equation 3.50}$$

³³ It is considered that the particle is not conductive. It causes no field-induced potential distribution. Also, the particle has dielectric permittivity lower than dispersion medium. Uniform zeta potential is another important assumption in this theory. Regarding the medium properties, η and ϵ_r are considered uniform all over the medium.

$$\mu_e = \frac{|V_e|}{|E|} \quad \text{Equation 3.51}$$

Depending on the assumptions for solving the governing equations, there are six major analytical approximations of mobility (Smoluchowski, Hückel, Henry, Ohshima, O'Brien-White and Ohshima-Healy-White approaches) which cover different κa ³⁴ versus μ_e area [19].

Let's select the Henry equation as a more general equation. It meets the requirements to cover the proposed models which will be explained in following chapters. Derivation of Henry equation was explained in references [18, 19]. Equations 3.52 and 3.53 show the mobility and electrophoretic velocity based on Henry's model respectively. [18, 19, 65]

$$\mu_e = \frac{\varepsilon_r \varepsilon_0 \zeta_p}{\eta} f(\kappa a) \quad \text{Equation 3.52}$$

$$V_e = \frac{\varepsilon_r \varepsilon_0 \zeta_p}{\eta} f(\kappa a) E \quad \text{Equation 3.53}$$

ε_r : Relative permittivity of the medium (Dimensionless)

ε_0 : Free space permittivity (8.854187×10^{-12} [F.m⁻¹])

ζ_p : Zeta potential of the particle [V]

η : Viscosity of the medium [kg.s⁻¹. m⁻¹]

$f(\kappa a)$: Henry function

The $f(\kappa a)$ is the *Henry function* which is a function of sphere radius (a) and the reciprocal of Debye length (κ). It covers any κa values for any sphere [18, 19, 65]:

$$f(\kappa a) = \frac{2}{3} + \frac{1}{24}(\kappa a)^2 - \frac{5}{72}(\kappa a)^3 - \frac{1}{144}(\kappa a)^4 + \frac{1}{144}(\kappa a)^5 + \frac{1}{12}(\kappa a)^4 e^{\kappa a} \left(1 - \frac{(\kappa a)^2}{12}\right) E_1(\kappa a) \quad \text{Equation 3.54}$$

Where $E_1(\kappa a)$ is:

³⁴ κa is the ratio of Particle radius to the Debye length of the particle in the solution.

$$E_1(\kappa a) = \int_{\kappa a}^{\infty} \frac{e^{-t}}{t} dt \quad \text{Equation 3.55}$$

According to equation 3.53, the velocity of colloidal sphere depends on the Debye length, radius, and zeta potential of the particle, viscosity and relative permittivity of the medium.

Although the Henry function covers wide range of κa values, it assumes that the potential distribution in the double layer around the charged colloid remains unchanged during electrophoresis. That is valid for low zeta potential particles. The potential distribution remains stable and the double layer is spherically symmetrical at low zeta potential (figure 3.3 a1). For particles with high zeta potential, the applied electric field changes the potential distribution and the geometry of the double layer becomes more asymmetric (figure 3.3 a2). This polarization of the electric double layer of the particle during electrophoretic migration is the so called relaxation effect. Therefore Henry function is not valid when relaxation effect occurs. [18, 19] When the spherical particle is subjected to an electric field, a distortion of the electric field is produced around the particle parallel to the surface (figure 3.3 b1 and b2). The electric field strength becomes higher in the region near particle surface. For the particle with thick double layer as compared with its radius ($a \ll \kappa^{-1}$), most of the ions in double layer are under undistorted (original) electric field (figure 3.3 b1). For this case, the Henry function is equal to $\frac{2}{3}$. In this limited case the Henry equation is reduced to the Debye-Huckel one.

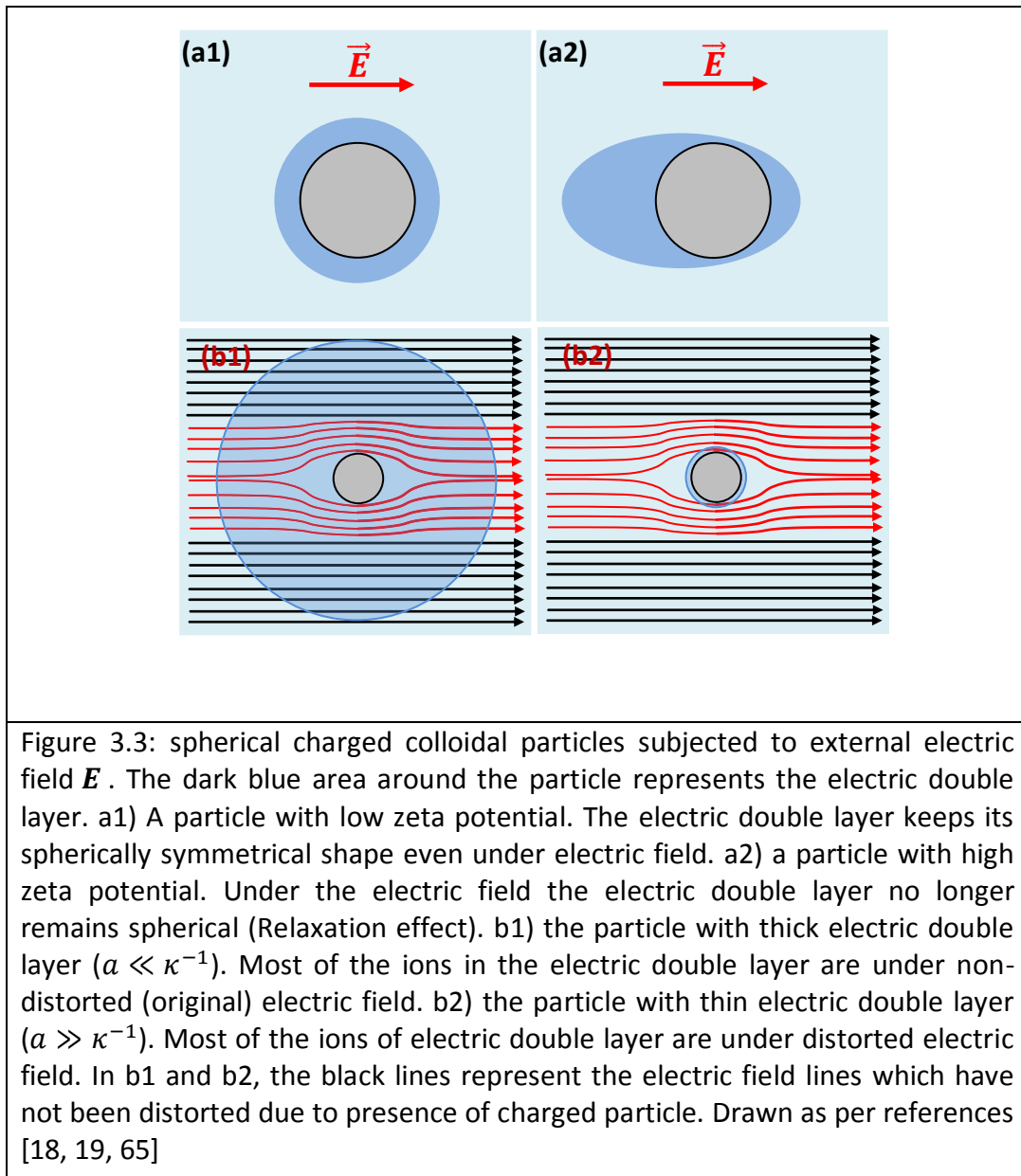
$$\mathbf{V}_e = \frac{2\varepsilon_r \varepsilon_0 \zeta_p}{3\eta} \mathbf{E} \quad \text{Equation 3.56}$$

if the double layer is very thin ($a \gg \kappa^{-1}$), the distorted electric field affects most of the ions in double layer (figure 3.3 b2). In this case, the output of Henry function is equal to one and the expression is reduced to the so called Smoluchowski equation. [18, 19]

$$\mathbf{V}_e = \frac{\varepsilon_r \varepsilon_0 \zeta_p}{\eta} \mathbf{E} \quad \text{Equation 3.57}$$

In this thesis work, it has been used particles with radius bigger than the particle's Debye length. Therefore, the electrophoretic mobility which will be used in further chapters is the Smoluchowski equation [18, 19, 65]:

$$\mu_e = \frac{\varepsilon_r \varepsilon_0 \zeta_p}{\eta} \quad \text{Equation 3.58}$$



Other mobility expressions were achieved In order to have a mobility equation which covers arbitrary zeta potential. Solving the electrokinetic equations for spherical particle provides analytic approximations such as the works made by Ohshima, O'Brien- White and Ohshima-Healy-White. [19, 72]

3.10. Full electrokinetic equations

Summarizing, in order to analyze the electro-osmotic flow at a surface or the electrophoretic motion of the particles, the governing equations which cover mass and momentum conservation, fluid motion, transport of ions (ionic fluids), interaction of charged particle with an electric field and electric double layer formation should be solved together. Table 3.2 covers the governing equations which should be solved together with boundary conditions depending on the system:

| Table 3.2 : governing equations for analyzing electrophoretic motion of the colloidal particle | |
|---|---|
| Mathematical form | Description |
| $\nabla^2 \psi = -\frac{\rho_f}{\epsilon \epsilon_0}$ | Poisson's equation (equation 3.2): connecting the electric potential to charge distribution in the system |
| $\nabla \left[n_i \mathbf{u} - D_i \nabla n_i - \frac{e n_i z_i}{k_B T} D_i \nabla \psi \right] = 0$ | Nernst–Planck Equation (equation 3.30): describing ionic mass transfer |
| $\mathbf{v}_i = \mathbf{u} - \frac{D_i \nabla n_i}{n_i} - \frac{e z_i}{k_B T} D_i \nabla \psi$ $i = 1, 2, 3, \dots, N$ | Equation 3.29: connecting velocity vector of bulk fluid and Velocity vector of species |
| $-\nabla P + \mu \nabla^2 \mathbf{u} - \rho_f \nabla \psi = 0$ | Navier–Stokes equation (equation 3.44): describing momentum conservation in the system |
| $\nabla \mathbf{u} = 0$ | Continuity equation (equation 3.32): describing mass conservation and fluid flow in the system |
| $\nabla (n_i \mathbf{v}_i) = 0$ | Continuity equation (equation 3.36): describing mass conservation and ionic flow in the system |

In the particular case of the catalytic systems studied in this work, an additional governing equation should be added as mentioned previously. That is the electrochemical current at the interface according to the electrochemical reactions taken place on the bimetallic structures. That equation plays a crucial role to switch on the electrokinetic process.

References:

- [1] A. Ramos, *Electrokinetics and Electrohydrodynamics in Microsystems*: SpringerWienNewYork, 2011.
- [2] S. Kakaç, B. Kosoy, D. Li, and A. Pramuanjaroenkij, *Microfluidics Based Microsystems: Fundamentals and Applications*: Springer, 2010.
- [3] M. U. Kopp, H. J. Crabtree, and A. Manz, "Developments in technology and applications of microsystems," *Current Opinion in Chemical Biology*, vol. 1, pp. 410-419, 10// 1997.
- [4] D. Li, *Electrokinetics In Microfluidics*: Academic, 2004.
- [5] H. C. Chang and L. Y. Yeo, *Electrokinetically-Driven Microfluidics and Nanofluidics*: Cambridge University Press, 2010.
- [6] J. H. Masliyah and S. Bhattacharjee, *Electrokinetic and Colloid Transport Phenomena*: Wiley, 2006.
- [7] S. R. Tully-Dartez and L. T. University, *Applied Electrokinetics for Tissue Engineering Applications*: Louisiana Tech University, 2009.
- [8] A. Sebastian, A.-M. Buckle, and G. H. Markx, "Tissue engineering with electric fields: Immobilization of mammalian cells in multilayer aggregates using dielectrophoresis," *Biotechnology and Bioengineering*, vol. 98, pp. 694-700, 2007.
- [9] G. H. Markx, "The use of electric fields in tissue engineering," *Organogenesis*, vol. 4, pp. 11-17, 2008.
- [10] L. Chen, J. Choo, and B. Yan, "The microfabricated electrokinetic pump: a potential promising drug delivery technique," *Expert Opinion on Drug Delivery*, vol. 4, pp. 119-129, 2007.
- [11] A. J. Chung, D. Kim, and D. Erickson, "Electrokinetic microfluidic devices for rapid, low power drug delivery in autonomous microsystems," *Lab on a Chip*, vol. 8, pp. 330-338, 2008.
- [12] U. Pyell, *Electrokinetic Chromatography: Theory, Instrumentation and Applications*: Wiley, 2007.
- [13] S. Terabe, "Electrokinetic chromatography: An interface between electrophoresis and chromatography," *TrAC Trends in Analytical Chemistry*, vol. 8, pp. 129-134, 4// 1989.
- [14] K. R. Reddy and C. Cameselle, *Electrochemical Remediation Technologies for Polluted Soils, Sediments and Groundwater*: Wiley, 2009.
- [15] D. L. Wise, *Remediation Engineering of Contaminated Soils*: Taylor & Francis, 2000.
- [16] M. R. Wilkins, C. Pasquali, R. D. Appel, K. Ou, O. Golaz, J.-C. Sanchez, et al., "From proteins to proteomes: large scale protein identification by two-dimensional electrophoresis and amino acid analysis," *Nature Biotechnology*, vol. 14, pp. 61-65, 1996.

- [17] G. Karniadakis, A. Beskok, and N. Aluru, *Microflows and Nanoflows: Fundamentals and Simulation*: Springer, 2006.
- [18] A. V. Delgado, *Interfacial Electrokinetics and Electrophoresis*: Taylor & Francis, 2001.
- [19] H. Ohshima, *Theory of Colloid And Interfacial Electric Phenomena*: Elsevier Academic Press, 2006.
- [20] H. Morgan and N. G. Green, *AC Electrokinetics: Colloids and Nanoparticles: Research Studies Press Limited*, 2003.
- [21] J. Tóth, *Adsorption: Theory, Modeling, and Analysis* Volume 107 of *Surfactant Science Series*: CRC Press, 2002.
- [22] H. J. Butt, K. Graf, and M. Kappl, *Physics and Chemistry of Interfaces*: Wiley, 2006.
- [23] Á. V. Delgado, *Interfacial Electrokinetics and Electrophoresis*: Marcel Dekker, 2002.
- [24] D. H. Everett, *Basic principles of colloid science*: Royal Society of Chemistry, 1988.
- [25] M. Stamm, *Polymer Surfaces and Interfaces: Characterization, Modification and Applications*: Springer London, Limited, 2008.
- [26] A. J. Milling, *Surface Characterization Methods: Principles, Techniques, and Applications*: Taylor & Francis, 1999.
- [27] J. Gregory, *Particles in Water: Properties and Processes*: Taylor & Francis, 2004.
- [28] X. Jia, J. Gregory, and R. Williams, *Particle Deposition & Aggregation: Measurement, Modelling and Simulation*: Elsevier Science, 1998.
- [29] E. Papirer, *Adsorption on Silica Surfaces*: Taylor & Francis, 2000.
- [30] H. E. Bergna and W. O. Roberts, *Colloidal Silica: Fundamentals and Applications*: Taylor & Francis, 2005.
- [31] B. Damaskin and O. Petrii, "Historical development of theories of the electrochemical double layer," *Journal of Solid State Electrochemistry*, vol. 15, pp. 1317-1334, 2011/07/01 2011.
- [32] J. Havlin, J. S. Jacobsen, and A. S. Agronomy, *SSSA Special Publication Series: Soil Science Society of America*, 1994.
- [33] B. Merkel, B. Planer-Friedrich, and D. K. Nordstrom, *Groundwater Geochemistry: A Practical Guide to Modeling of Natural and Contaminated Aquatic Systems*: Springer, 2008.
- [34] H. M. Selim, *Competitive Sorption and Transport of Heavy Metals in Soils and Geological Media*: Taylor & Francis, 2012.
- [35] H. Bradl, *Heavy Metals in the Environment: Origin, Interaction and Remediation: Origin, Interaction and Remediation*: Elsevier Science, 2005.

- [36] J. Lutzenkirchen, *Surface Complexation Modelling*: Elsevier Science, 2006.
- [37] J. Lützenkirchen, "The Constant Capacitance Model and Variable Ionic Strength: An Evaluation of Possible Applications and Applicability," *Journal of Colloid and Interface Science*, vol. 217, pp. 8-18, 1999.
- [38] P. W. Schindler, B. Fürst, R. Dick, and P. U. Wolf, "Ligand properties of surface silanol groups. I. surface complex formation with Fe³⁺, Cu²⁺, Cd²⁺, and Pb²⁺," *Journal of Colloid and Interface Science*, vol. 55, pp. 469-475, 1976.
- [39] P. W. Schindler and H. Gamsjäger, "Acid — base reactions of the TiO₂ (Anatase) — water interface and the point of zero charge of TiO₂ suspensions," *Kolloid-Zeitschrift und Zeitschrift für Polymere*, vol. 250, pp. 759-763, 1972/07/01 1972.
- [40] W. Stumm, R. Kummert, and L. Sigg, "A ligand-exchange model for the adsorption of inorganic and organic-ligands at hydrous oxide interfaces," *Croatica Chemica Acta*, vol. 53, pp. 291-312, 1980.
- [41] W. Stumm, C. P. Huang, and S. R. Jenkins, "Specific Chemical Interactions Affecting the Stability of Dispersed Systems," *Croat. Chem. Acta* vol. 42, pp. 223-245 1970.
- [42] J.-F. Boily and J. B. Fein, "Adsorption of Pb(II) and benzenecarboxylates onto corundum," *Chemical Geology*, vol. 148, pp. 157-175, 1998.
- [43] Y. S. Hwang and J. J. Lenhart, "Surface complexation modeling of dual-mode adsorption of organic acids: Phthalic acid adsorption onto hematite," *Journal of Colloid and Interface Science*, vol. 336, pp. 200-207, 2009.
- [44] J. Ikhsan, B. B. Johnson, J. D. Wells, and M. J. Angove, "Adsorption of aspartic acid on kaolinite," *Journal of Colloid and Interface Science*, vol. 273, pp. 1-5, 2004.
- [45] J. Ikhsan, J. D. Wells, B. B. Johnson, and M. J. Angove, "The effect of aspartic acid on the binding of transition metals to kaolinite," *Journal of Colloid and Interface Science*, vol. 273, pp. 6-13, 2004.
- [46] J. Ikhsan, J. D. Wells, B. B. Johnson, and M. J. Angove, "Surface complexation modeling of the sorption of Zn(II) by montmorillonite," *Colloids and Surfaces A: Physicochemical and Engineering Aspects*, vol. 252, pp. 33-41, 2005.
- [47] W. B. S. de Lint, N. E. Benes, A. P. Higler, and H. Verweij, "Derivation of adsorption parameters for nanofiltration membranes using a 1-pK Basic Stern model," *Desalination*, vol. 145, pp. 87-95, 2002.
- [48] M. Gunnarsson, A.-M. Jakobsson, S. Ekberg, Y. Albinsson, and E. Ahlberg, "Sorption Studies of Cobalt(II) on Colloidal Hematite Using Potentiometry and Radioactive Tracer Technique," *Journal of Colloid and Interface Science*, vol. 231, pp. 326-336, 2000.
- [49] M. Gunnarsson, M. Rasmusson, S. Wall, E. Ahlberg, and J. Ennis, "Electroacoustic and Potentiometric Studies of the Hematite/Water Interface," *Journal of Colloid and Interface Science*, vol. 240, pp. 448-458, 2001.

- [50] I. Heidmann, I. Christl, and R. Kretzschmar, "Sorption of Cu and Pb to kaolinite-fulvic acid colloids: Assessment of sorbent interactions," *Geochimica et Cosmochimica Acta*, vol. 69, pp. 1675-1686, 2005.
- [51] R. Weerasooriya, B. Dharmasena, and D. Aluthpatabendi, "Copper–gibbsite interactions: an application of 1-pK surface complexation model," *Colloids and Surfaces A: Physicochemical and Engineering Aspects*, vol. 170, pp. 65-77, 2000.
- [52] W. Piasecki, "Determination of the parameters for the 1-pK triple-layer model of ion adsorption onto oxides from known parameter values for the 2-pK TLM," *Journal of Colloid and Interface Science*, vol. 302, pp. 389-395, 2006.
- [53] J. Lützenkirchen, "Comparison of 1-pK and 2-pK Versions of Surface Complexation Theory by the Goodness of Fit in Describing Surface Charge Data of (Hydr)oxides," *Environmental Science & Technology*, vol. 32, pp. 3149-3154, 1998/10/01 1998.
- [54] W. Piasecki, W. Rudziński, and R. Charmas, "1-pK and 2-pK Protonation Models in the Theoretical Description of Simple Ion Adsorption at the Oxide/Electrolyte Interface: A Comparative Study of the Behavior of the Surface Charge, the Individual Isotherms of Ions, and the Accompanying Electrokinetic Effects," *The Journal of Physical Chemistry B*, vol. 105, pp. 9755-9771, 2001/10/01 2001.
- [55] J. Sonnefeld, "On the influence of background electrolyte concentration on the position of the isoelectric point and the point of zero charge," *Colloids and Surfaces A: Physicochemical and Engineering Aspects*, vol. 190, pp. 179-183, 2001.
- [56] W. Rudziński, R. Charmas, and W. Piasecki, "Searching for Thermodynamic Relations in Ion Adsorption at Oxide/Electrolyte Interfaces Studied by Using the 2-pK Protonation Model," *Langmuir*, vol. 15, pp. 8553-8557, 1999/12/01 1999.
- [57] R. Weerasooriya and H. J. Tobschall, "Mechanistic modeling of chromate adsorption onto goethite," *Colloids and Surfaces A: Physicochemical and Engineering Aspects*, vol. 162, pp. 167-175, 2000.
- [58] C. Jing, X. Meng, S. Liu, S. Baidas, R. Patraju, C. Christodoulatos, et al., "Surface complexation of organic arsenic on nanocrystalline titanium oxide," *Journal of Colloid and Interface Science*, vol. 290, pp. 14-21, 2005.
- [59] J. P. Gustafsson, "Modelling competitive anion adsorption on oxide minerals and an allophane-containing soil," *European Journal of Soil Science*, vol. 52, pp. 639-653, 2001.
- [60] R. Weerasooriya, H. K. D. K. Wijesekara, and A. Bandara, "Surface complexation modeling of cadmium adsorption on gibbsite," *Colloids and Surfaces A: Physicochemical and Engineering Aspects*, vol. 207, pp. 13-24, 2002.
- [61] R. Charmas, "Four-Layer Complexation Model for Ion Adsorption at Energetically Heterogeneous Metal Oxide/Electrolyte Interfaces," *Langmuir*, vol. 15, pp. 5635-5648, 1999/08/01 1999.

- [62] R. Charmas, "Calorimetric Effects of Simple Ion Adsorption at the Metal Oxide/Electrolyte Interfaces: An Analysis Based on the Four Layer Complexation Model," *Langmuir*, vol. 14, pp. 6179-6191, 1998/10/01 1998.
- [63] R. Charmas and W. Piasecki, "Four-Layer Complexation Model for Ion Adsorption at Electrolyte/Oxide Interface: Interrelations of Model Parameters," *Langmuir*, vol. 12, pp. 5458-5465, 1996/01/01 1996.
- [64] R. Charmas, W. Piasecki, and W. Rudzinski, "Four Layer Complexation Model for Ion Adsorption at Electrolyte/Oxide Interface: Theoretical Foundations," *Langmuir*, vol. 11, pp. 3199-3210, 1995/08/01 1995.
- [65] J. P. Hsu and A. M. Spasic, *Interfacial Electroviscoelasticity and Electrophoresis*: CRC Press/Taylor & Francis, 2009.
- [66] H. Freiser and M. Freiser, *Concepts & Calculations in Analytical Chemistry, Second Edition, Featuring the Use of Excel*: Taylor & Francis, 1992.
- [67] J. L. Moran and J. D. Posner, "Electrokinetic locomotion due to reaction-induced charge auto-electrophoresis," *J. Fluid Mech*, vol. 680, pp. 31-66, 2011.
- [68] K. Kontturi, L. Murtoimäki, and J. A. Manzanares, *Ionic Transport Processes : in Electrochemistry and Membrane Science*: in *Electrochemistry and Membrane Science*: OUP Oxford, 2008.
- [69] B. Kirby, *Micro- and Nanoscale Fluid Mechanics: Transport in Microfluidic Devices*: Cambridge University Press, 2010.
- [70] C. Kleinstreuer, *Modern Fluid Dynamics: Basic Theory and Selected Applications in Macro- and Micro-Fluidics*: Springer, 2009.
- [71] P. G. Drazin, N. Riley, and L. M. Society, *The Navier-Stokes Equations: A Classification of Flows and Exact Solutions*: Cambridge University Press, 2006.
- [72] H. Ohshima, T. W. Healy, and L. R. White, "Approximate analytic expressions for the electrophoretic mobility of spherical colloidal particles and the conductivity of their dilute suspensions," *Journal of the Chemical Society, Faraday Transactions 2: Molecular and Chemical Physics*, vol. 79, pp. 1613-1628, 1983.

Chapter 4

Introduction

The Research plan and related work flow were briefly described in the chapter 2. In order to implement the plan, large number of devices were designed, fabricated and subjected to optical and confocal fluorescence microscopy. This chapter covers the experimental activities related to device fabrication and characterization.

Primary experiments were performed to understand the fluid pumping mechanism in Au-Pt devices³⁵. Devices were fabricated with electron beam lithography and electron beam evaporation and cleaned with typical organic solvents (acetone and isopropanol) prior to evaluate the device performance. Charged beads, as tracing agents, were used to observe the interaction of them with fluid flow and electric field self-generated at the devices in hydrogen peroxide aqueous solutions. Au-Pt devices mounted either in microfluid channels or channel-less systems, were inspected by optical microscopy. Under these conditions it was not possible to observe either direction movement of tracking beads or pattern formation.

According to the previous results, it was considered that the devices would require activation before optical microscopy. Therefore, finding activating agent(s) and activating method(s) became the first research priority. Since the chemomechanical process is based on a catalysis process, it was proposed that surface contamination and surface chemistry could cause devices not to actuate. Consequently, removing surface contamination and modifying its surface chemistry were possible solutions. Besides taking proper measures to prevent surface contamination during fabrication, a cleaning method, cleaning process C₅ (table 4.3), including both wet and dry type of cleaning processes, were selected to treat samples before testing. The cleaning could successfully activate the Au-Pt devices. Meaningful and directional motion of charged beads and pattern formation around the devices were observed on such pretreated devices. The charged beads- device interactions were completely reproducible. After finding a proper activating method, the studies continued on two lines of work:

- a. Studying the activated Au-Pt devices
- b. Studying origin of the activation

Optical microscopy of activated Au-Pt devices provided the backbone to the research. The devices were exposed to the low concentration hydrogen peroxide solution in presence of differently charged tracing beads.

Tracking beads were spherical particles which were positively charged (P^+), negatively charged (P^-) or quasi-neutral charged (P^0). Interaction between device and differently charged beads helps to understand spatial variation of fluid flow and electric field around the device. Au-Pt devices (a platinum disk³⁶ (thickness: 50 nm, diameter: 10 μm – 100 μm) deposited on gold surface (thickness: 50 nm, minimum Area: 40,000 μm^2)), were fabricated by procedure F1 (table 4.5). Cleaning process C₅ was taking as activating step. In order to avoid PMMA (polymethymethacrylate) from fabrication, to decrease the fabrication steps and to increase device fabrication speed, an alternative method based on Stencil lithography,

³⁵ Device design : Platinum disks (Thickness: 50 nm , Diameter: 10 μm -100 μm) on gold-coated surface

³⁶ In some cases, other geometries like rectangles, squares and triangles were tried.

procedure F2 (table 4.6), was also applied. Devices fabricated as per either F1 or F2 procedure, were subjected to process C₅.

Inspection of the device performance but integrated in PDMS (Poly (dimethylsiloxane)) fluidic channels (a widely used material in microfluidics [1-4]) was also considered. Although difficulties with fluid flow control were overcome successfully, the experiments were not successful at all. Mounting the sample on fluidic experiment setup contaminates the sample and it is not possible to apply the cleaning process again. Therefore, a simple channel-less experimental setup was selected to perform further experiments.

It is very important to understand the surface modification caused by the cleaning process. Although the cleaning process C₅ removes organic contamination and residual PMMA from the surface [5-8], accurate study was required to evaluate its effect on the surface chemistry and electrochemical behavior of the metallic surfaces. That was accomplished by X-ray photoelectron spectroscopy and TAFEL plot measurement respectively.

A key element of the research was fluorescence confocal microscopy to evaluate proton concentration variation around activated Au-Pt devices when exposed to hydrogen peroxide solution.

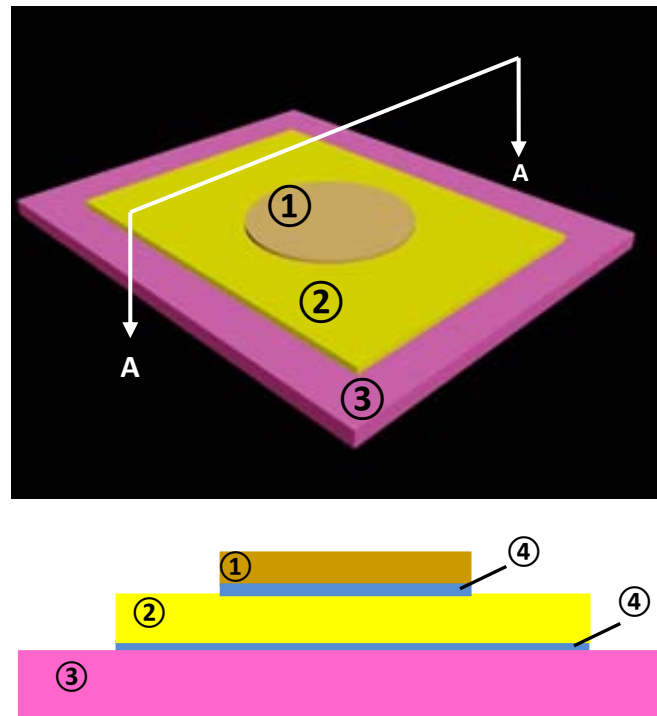
Analysis and interpretation of the experimental data led to propose a mechanism to explain micropumping. After proposing a model, some computer simulations were done to understand more about the micropumping phenomenon.

In order to explore alternative X-Y bi-metallic devices for microfluidic pumping, the electrochemical properties of copper (Cu), silver (Ag), Ruthenium (Ru), Rhodium (Rh) and Nickel (Ni) were studied with TAFEL plot measurements. TAFEL analysis allowed finding the proper bi-metallic combinations (Pt-Au, Au-Ag, Au-Ru, Au-Rh, Cu-Ag, Cu-Ni, Ni-Cu, Ni-Ru and Ni-Ag systems) to perform further experiments.

Besides bi-metallic systems, semiconductor-metal structures (p-doped Si/Pt, n-doped Si/Pt) were fabricated as per procedure F4 (table 4.8) and examined to evaluate their potential for being used as catalytic micropump in presence of hydrogen peroxide.

4.1 Device fabrication

In this part, the device design, applied techniques (lithography and metal deposition), cleaning processes and fabrication sequences are described briefly. As illustrated in figure 4.1, General design of a device for X-Y bi-metallic system was mainly a disk deposited on a substrate made of element X. The element Y had a thickness of 50 nm and diameters between 10 μm and 100 μm . Element X had a thickness of 50 nm and a minimum area of 40,000 μm^2 . In case on the semiconductor-metal systems, X is the silicon substrate and Y is the metallic layer. Therefore one step metal deposition meets the requirements.



A-A Cross section

| | Material | Geometry | Thickness | Other information |
|---|---------------|----------|-------------------|-------------------------------------|
| ① | Element Y | Disk | 50 nm | Diameter:10-100 μm |
| ② | Element X | Square | 50 nm | Minimum area: 40000 μm^2 |
| ③ | Silicon wafer | Square | 550 μm | Minimum area: 1 cm^2 |
| ④ | Chromium | Square | 6 nm | Same as layer made of X |
| | | Disk | 6 nm | Same as layer made of Y |

Figure 4.1: device design. Figures were not drawn on scale

4.1.1 Metal deposition

Metal deposition was done with two methods: electron beam evaporation [9-12] and electroplating [13-15].

4.1.1.a Electron beam evaporation

An electron beam evaporator (AJA Model: ATC ORION 8-E UHV³⁷) was used to deposit gold (Au), chromium (Cr), silver (Ag), platinum (Pt), nickel (Ni) and copper (Cu)³⁸ with 8 kV as

³⁷ AJA International, INC Website: <http://www.ajaint.com>

accelerating voltage under chamber pressure less than 10^{-7} Torr. Before depositing any Au, Ag, Pt, Ni or Cu layer, a 6 nm thick chromium interlayer was deposited to promote adhesion between coating and the substrate[16,17]. Deposition rate and layer thickness were controlled with a quartz crystal sensor connected to a thin film controller (INFICON Model: Inficon XTC/3M)³⁹. Deposition rate was $0.2 \pm 0.1 \text{ \AA} \cdot \text{s}^{-1}$ for chromium and $1.2 \pm 0.1 \text{ \AA} \cdot \text{s}^{-1}$ for the rest of the metals.

4.1.1.b Electroplating

Electroplating was selected to deposit ruthenium (Ru) and rhodium (Rh) layers at room temperature. An Electrochemical workstation Model: CH 660D⁴⁰ controlled by CHI software Ver.10.21, was the electroplating process controller.

As shown in the experimental setup (figure 4.2), sample was set as working electrode and two other electrodes, a platinum wire as counter electrode and an Ag/AgCl/KCl reference electrode were used to complete the setup. All electrodes were in contact with an electrolyte droplet. The setup was used to fabricate 10 μm -50 μm disks of Ru and Rh on conductive metals (gold and nickel) as illustrated in fabrication method F3 (table 4.7). The electroplating was performed on PMMA-coated samples which were pre-patterned in disk shape structures with e-beam lithography. PMMA layer acts as a protecting mask and restricts interface between electrolyte and conductive metal surface to the disk openings. Consequently, metal deposition occurs only on the disk openings. Equation 4.1 and equation 4.2 show the reactions of Ru and Rh bulk deposition respectively. After running electroplating, the sample was rinsed with deionized water⁴¹, dried with nitrogen gun and subjected to cleaning process C2 (Table 4.3)



Regarding the key parameters of electroplating, it was essential to adjust cathodic potential (E_p) and electroplating time to deposit uniform layers avoiding hydrogen bubble generation due to reduction of hydrogen ions (cathodic reaction) [18].

³⁸ For all the elements, consumable materials were in the form of Pellets (diameter: 3 mm length: 6 mm) with 99.99% purity. Supplier: NEYCO Website: <http://www.neyco.fr>

³⁹ INFICON Inc. Website: <http://www.inficon.com>

⁴⁰ CH Instruments, Inc. website : www.chinstruments.com

⁴¹ Specification: 18.2 M Ω .cm at 25°C , 4PPB, Purified by Milli-Q Integral water purification system Merck Millipore Website: <http://www.millipore.co>

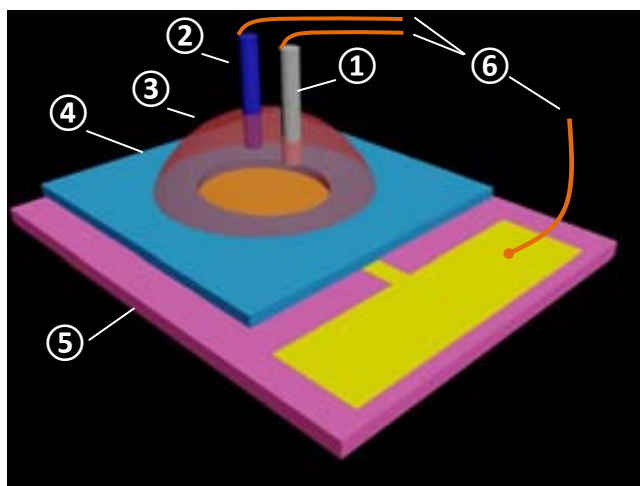


Figure 4.2: Experimental setup for electroplating. ① Reference electrode ② Platinum counter electrode ③ Electrolyte droplet on an opening ④ PMMA layer ⑤ Sample (table 4.7 – F3.4) ⑥ contacts to the electrochemical workstation

For each element, the cathodic deposition potential (E_p) against Ag/AgCl/KCl reference electrode was extracted from cyclic voltammetry [19-21]. Cyclic voltammetry of Ru and Rh are evaluated in Appendix 4.1. After finding E_p values for each element, electroplating time was experimentally determined. Each electroplating process was monitored by performing chronocoulometry [21,22] which evaluates the evolution of the charge of the deposited material as a function of time. Cyclic voltammetry and chronocoulometry were done with the same instrument and experimental setup. The thickness and chemical composition of the deposited layer were determined with atomic force microscopy and X-ray photoelectron spectroscopy respectively. Table 4.1 contains the electrolyte and relative pH, cathodic Potential (E_p) against Ag/AgCl/KCl reference electrode, electroplating time, , thickness, roughness (R_a) and chemical composition of each deposited layer.

Table 4.1: Electroplating parameters for Ruthenium, Rhodium and Nickel layer: electrolyte, pH , cathodic Potential (E_P) against Ag/AgCl/KCl reference electrode, electroplating time, Electrolyte, layer thickness, roughness (R_a) and chemical composition

| Element | Electrolyte ⁴² | pH | E_P [V] | Time [s] | Deposited layer | | |
|---------|---|----|-----------|----------|-----------------|------------|------------------|
| | | | | | Thickness[nm] | R_a [nm] | Oxide percentage |
| Ru | $RuCl_3 \cdot xH_2O$: 10mM KCl : 0.50 M | 6 | -0.85 | 120 | 101±5 | 0.67±0.1 | < 5% |
| Rh | $RhCl_3 \cdot xH_2O$: 5mM KCl : 0.50 M | 6 | -0.40 | 60 | 81±8 | 0.80±0.2 | < 5% |

4.1.2 Lithography

Two lithography techniques, electron beam lithography [23-25] and Stencil lithography [26-29], were applied during device fabrication.

4.1.2.a Electron beam lithography

Standard electron beam lithography was done with a Raith Pionner⁴³. Samples were spin-coated with PMMA 950⁴⁴ as described (table 4.2). Lithography was done at 10 kV acceleration voltage and with $130 \frac{\mu C}{cm^2}$ exposure dose. Developing solution was a 1:3 mixture of Methyl isobutyl ketone (MIBK) to Isopropyl alcohol (IPA)⁴⁵. Developing process included: immersing the sample in developing solution bath for 90 seconds, immersing the sample in isopropyl alcohol bath for 30 seconds and nitrogen drying.

⁴² $RuCl_3 \cdot xH_2O$ (Ruthenium (III) chloride hydrate, Degree of hydration ≤ 1 , Ru content: 40.00-49.00%), $RhCl_3 \cdot xH_2O$ (Rhodium(III) chloride hydrate, Rh content 38-40%), KCl (Potassium chloride, Purity: $\geq 99.0\%$),

Supplier: Sigma-Aldrich Co. LLC. Website: <http://www.sigmaaldrich.com>

⁴³ Raith GmbH Website: <http://www.raith.com>

⁴⁴ Poly(methyl methacrylate) 950 ($C_5O_2 H_8$)_n Supplier: MicroChem Corp Website: <http://www.microchem.com>

⁴⁵ Methyl isobutyl ketone ($(CH_3)_2CHCH_2C$), Isopropyl alcohol ($(CH_3)_2CHOH$) Supplier: Sigma-Aldrich Ltd. <http://www.sigmaaldrich.com>

Lift-off for samples subjected to metal deposition with either e-beam evaporation or electroplating, consisted in immersing the samples in acetone⁴⁶ bath for 30 minutes, followed by isopropyl alcohol bath for 10 minutes and nitrogen drying.

Table 4.2: Spin coating procedure

| No. | Activity |
|-----|--|
| 1 | PMMA 950 spin coating with a WS-400-BZ-6NPP/LITE spin coater ⁴⁷ Program: 30 seconds at 1500 rpm ⁴⁸ followed by 30 seconds at 3000 rpm |
| 2 | Sample baking with hot plate ⁴⁹ at 150°C for 120 seconds |
| 3 | Repeating activity No.1 |
| 4 | Repeating activity No.2 |
| 5 | Repeating activity No.1 |
| 6 | Sample baking with hot plat at 150°C for 15 minutes |

4.1.2.b Stencil lithography

In order to minimize residual contaminants, Stencil lithography was selected to provide a PMMA-free device fabrication. In this technique, Stencil masks with 30 μm and 50 μm diameter openings allowed depositing metallic disks with e-beam evaporation.

4.1.3 Cleaning processes

Table 4.3 shows different sample cleaning processes during fabrication:

⁴⁶ Acetone ((CH₃)₂CO) Supplier: Honeywell Specialty Chemicals Seelze GmbH Website: <http://honeywell.com>

⁴⁷ Supplier: Laurell Technologies Corporation Website: <http://www.laurell.com>

⁴⁸ rpm : rounds per minute

⁴⁹ Hot plate model: PLACTRONIC -6155100, Supplier: JP SELECTA S.A. Website: <http://www.grupo-selected.com>

Table 4.3: Cleaning processes

| No. | Purpose | Description |
|-----|--|--|
| C1 | Silicon wafer cleaning | <ol style="list-style-type: none"> 1. Ultrasonic⁵⁰ acetone bath for 15 minutes 2. Ultrasonic isopropyl alcohol bath for 15 minutes 3. Nitrogen Drying |
| C2 | General cleaning | <ol style="list-style-type: none"> 1. Acetone bath for 5 minutes 2. Isopropyl alcohol for 5 minutes 3. Nitrogen Drying |
| C3 | Piranha treatment | <ol style="list-style-type: none"> 1. Piranha solution (1:3 mixture of hydrogen peroxide and sulfuric acid⁵¹) bath for 30 minutes 2. Rinsing samples with deionized water 3. Ultrasonic isopropyl alcohol bath for 5 minutes 4. Nitrogen Drying |
| C4 | Plasma cleaning ⁵² for cleaning and activating Au-Pt device | Plasma power : 500 W Oxygen flow rate: 50 SCCM ⁵³ Time : one minute |
| C5 | Piranha and plasma treatment | <ol style="list-style-type: none"> 1. C3 process 2. C4 process |

4.1.4 Fabrication sequences

Generally, three fabrication methods were designed, implemented and modified to cover all X-Y bi-metallic or semiconductor–metal systems studied in this research. Table 4.4 shows the method applied for each system. Method F1, F2,F3 and F4 are related to tables 4.5, 4.6, 4.7 and 4.8 which show the major steps of fabrication respectively. Regarding the substrate material, insulating silicon oxide substrates with 1 μm oxide thickness were used for all devices. For semiconductor- metal systems, n-type and p-type silicon wafers were selected⁵⁴.

All samples were cleaned following procedure C1 (table 4.3).

⁵⁰ Economic Ultrasonic Cleaner - Elmasonic Model: E300H, Ultrasound frequency: 37 kHz, Website: Laval Lab Inc. <http://www.lavallab.com>

⁵¹ Hydrogen peroxide (H_2O_2) wt 30% , sulfuric acid (H_2SO_4) 98% Supplier: Sigma-Aldrich Ltd. <http://www.sigmaaldrich.com>

⁵² Tepla 300E Microwave Plasma Etcher Manufacturer: PVA TEPLA AG Website: <http://www.pvateplaamerica.com>

⁵³ SCCM : Standard cubic centimeters per minute

⁵⁴ Specification: Polished prime wafers, n-type (dopant: Arsenic) p-type (dopant: Boron) , Diameter :100mm,Thickness: 500-550[μm] Cemat Silicon S.A. Website: <http://www.cematsil.com>

In fabrication step F2.2 (Table 4.6) and F3.2 (Table 4.7), homemade aluminum stencil lithography masks were fabricated and applied to restrict the area subjected to metal deposition with e-beam evaporation.

Table 4.4: fabrication method(s) for X-Y bi-metallic and n-doped or p-doped Si/Pt systems

| No. | system | Method(s) |
|-----|--------------------------------|-----------|
| 1 | Au-Pt | F1 / F2 |
| 2 | Au-Ag | F2 |
| 3 | Au-Rh | F3 |
| 4 | Au-Ru | F3 |
| 5 | Cu-Ag | F2 |
| 6 | Cu-Ni | F2 |
| 7 | Ni-Cu | F2 |
| 8 | Ni-Ru | F3 |
| 9 | Ni-Ag | F2 |
| 10 | Pt-Au | F1 |
| 11 | (p-doped Si/Pt, n-doped Si/Pt) | F4 |

Table 4.5: Fabrication for X-Y bi-metallic device – Method No. F1

Figures were not drawn on scale

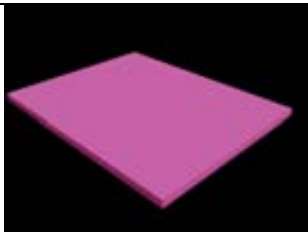
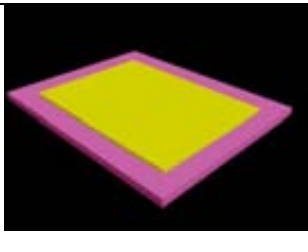
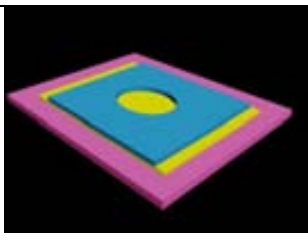
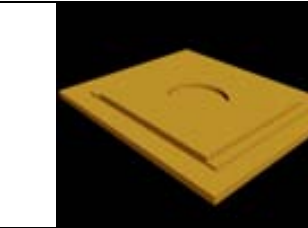
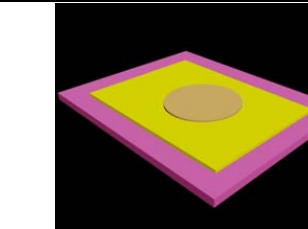
| Step No. | Activity | Schematics illustration of device after each step |
|----------|--|--|
| F1.1 | Silicon wafer cleaning Process C1 (table 4.3) |  |
| F1.2 | Deposition of element X (Thickness: 50 nm) |  |
| F1.3 | Patterning with E-beam lithography |  |
| F1.4 | Deposition of element Y (Thickness: 50 nm) |  |
| F1.5 | Lift-off |  |
| F1.6 | Sample Cleaning: Process C2 (Table 4.3) Process C5 (Table 4.3) | N/A |

Table 4.6: Fabrication for X-Y bi-metallic device – Method No. F2

Figures were not drawn on scale

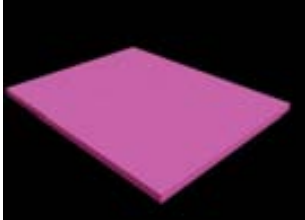
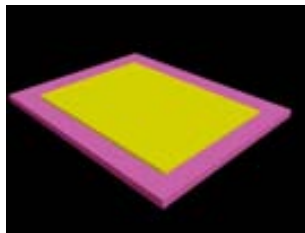
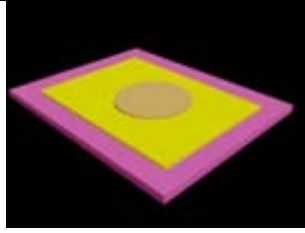
| Step No. | Activity | Schematics illustration of device after each step |
|----------|--|--|
| F2.1 | Silicon wafer cleaning Process C1 (table 4.3) |  |
| F2.2 | Deposition of element X (Thickness: 50 nm) |  |
| F2.3 | Stencil lithography - E-beam deposition of element Y (Thickness: 50 nm) |  |
| F2.4 | Sample cleaning: A. Process C2 (Table 4.3) B. Process C5 (Table 4.3) only for Au-Pt devices | N/A |

Table 4.7: Fabrication for X-Y bi-metallic device – Method No. F3

Figures were not drawn on scale

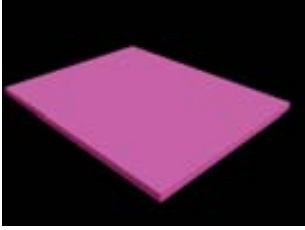
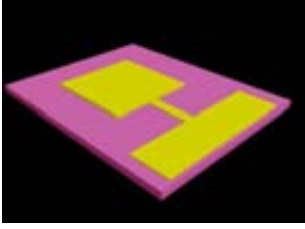
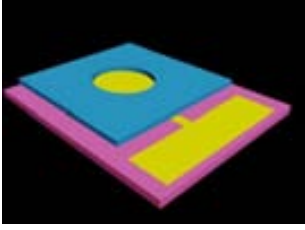
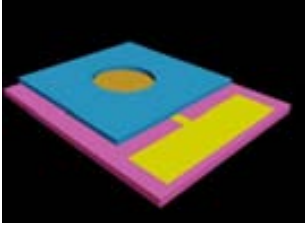
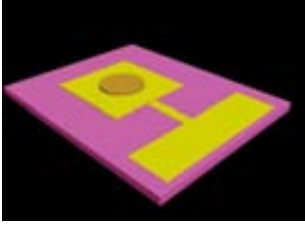
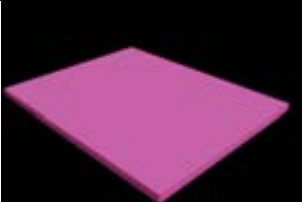
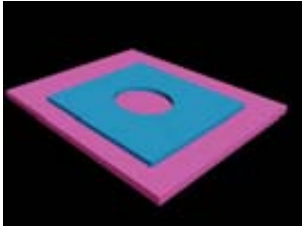
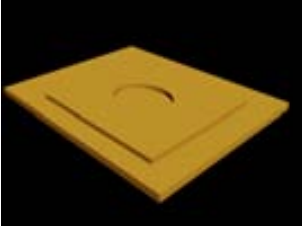
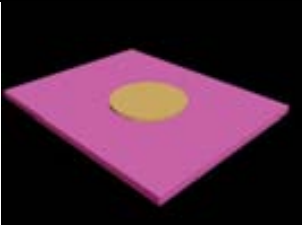
| Step No. | Activity | Schematics illustration of device after each step |
|----------|--|--|
| F3.1 | Silicon wafer cleaning Process C1 (table 4.3) |  |
| F3.2 | Stencil lithography - electron beam metal deposition of element X (Thickness: 50 nm) |  |
| F3.4 | Patterning with E-beam lithography for element Y |  |
| F3.5 | Deposition of element Y with electroplating |  |
| F3.6 | Lift-off |  |
| F3.7 | Sample Cleaning: Process C2 (Table 4.3) | N/A |

Table 4.8: Fabrication for p-doped Si/Pt, n-doped Si/Pt device – Method No. F4

Figures were not drawn on scale

| Step No. | Activity | Schematics illustration of device after each step |
|----------|--|--|
| F4.1 | Silicon wafer cleaning Process C1 (table 4.3) |  |
| F4.2 | Patterning with E-beam lithography |  |
| F4.4 | Deposition of platinum (Thickness: 50 nm) |  |
| F4.5 | Lift-off |  |
| F4.6 | Sample cleaning: Process C2 (Table 4.3) or Process C4 (Table 4.3) | N/A |

4.2 Characterization

Different characterization methods were selected to evaluate the properties of charged particles, the fabrication quality and performance of the devices.

4.2.1 Optical microscopy

A BX51M Olympus microscope equipped with a Olympus UC30 digital camera⁵⁵ and long working distance objectives (Magnification: 5X, 10X, 20X, 50X and 100X), was used to perform the experiments. As shown in figure 4.3, a microfluidic Channel-less setup was employed to study the particle- device interaction. 1 wt % Hydrogen peroxide solution⁵⁶ including particles was confined in the space restricted by the silicon wafer, spacer (well diameter: 9 mm Depth: 0.12 mm⁵⁷) and cover glass (shape size: 22 mm x22 mm Thickness: 0.15 ± 0.01 mm⁵⁸). After pouring solution on the device, the wafer was immediately capped with a thin glass cover. The event was recorded at 5 frames per second rate.

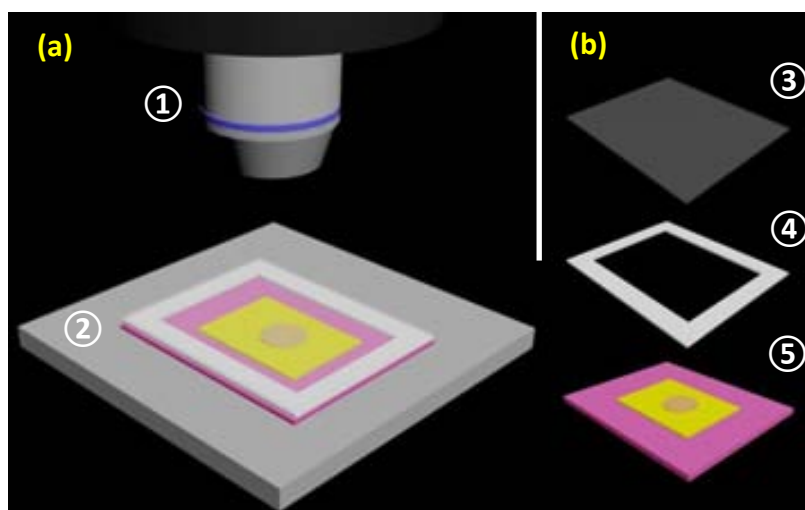


Figure 4.3 : Experimental setup for optical microscopy a) assembled view of the sample b) exploded view. ①Microscope objective ②Microscope stage ③Cover glass ④Spacer ⑤Sample

Precise measurement of particle velocity provides important data for further calculations. Movies recorded with the optical microscope, were subjected to image processing in order to track moving particles. The movie was converted to a batch of image files. Image files were processed with DiaTrack software⁵⁹ (Ver. 3.03). After processing the raw data, radial velocity of

⁵⁵ Olympus España S.A.U. Website: <http://www.olympus.es>

⁵⁶ The solution was prepared in carefully cleaned safe seal microcentrifuge tubes supplier: Bioscience Inc . Website: <http://www.sorbio.com>

⁵⁷ Life Technologies Corporation Website: <http://www.invitrogen.com>

⁵⁸ Sigma-Aldrich Co. LLC. Website: <http://www.sigmaaldrich.com>

⁵⁹ Semasopht Websith: <http://www.Semasopht.com>

particles toward the device center (disk center) as a function of distance from disk center, was reported. Appendix 4.2, 4.3 and 4.4 contain details of particle tracking and velocity calculation.

4.2.2 Confocal fluorescence microscopy

A TSC SP5 Leica⁶⁰ confocal microscope, equipped with an AOBS system (Acousto-optical Beam splitter) and with different wavelength range of laser beam sources was employed to image spatial concentration of protons. Pyranine (8-hydroxypyrene-1,3,6-trisulfonic acid, trisodium salt) which is a water soluble and pH-sensitive fluorescent dye [30-32], was selected⁶¹ to study the samples (figure 4.4).

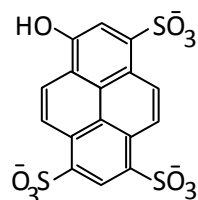


Figure 4.4 : Pyranine (8-hydroxypyrene-1,3,6-trisulfonic acid, trisodium salt) [30-32]

Au-Pt devices were exposed to water solution (without hydrogen peroxide) and 1% hydrogen peroxide solution in presence of 5 μM of Pyranine⁶². Samples were excited with 405 nm and 458 nm laser beams as illustrated in Figure 4.5. Emission spectrum was acquired in the frequency range of 480 nm – 580 nm. Appendix 4.5 contains the details of calibration and data processing.

⁶⁰ Leica Microsystems GmbH website: <http://www.leica-microsystems.com>

⁶¹ Primary experiments for selecting proper fluorescence dyes were done. Apart from pyranine, Oregon green 488, Lyso Sensor DND-160, Rhodamine and SNARF-4F were evaluated. Some of them could not meet the research requirements of high quality and reliable imaging of proton gradients, other dyes were rejected because the confocal set-up did not have available the specific excitation lasers.

⁶² Supplier: Life Technologies Corporation Website: <http://www.invitrogen.com>

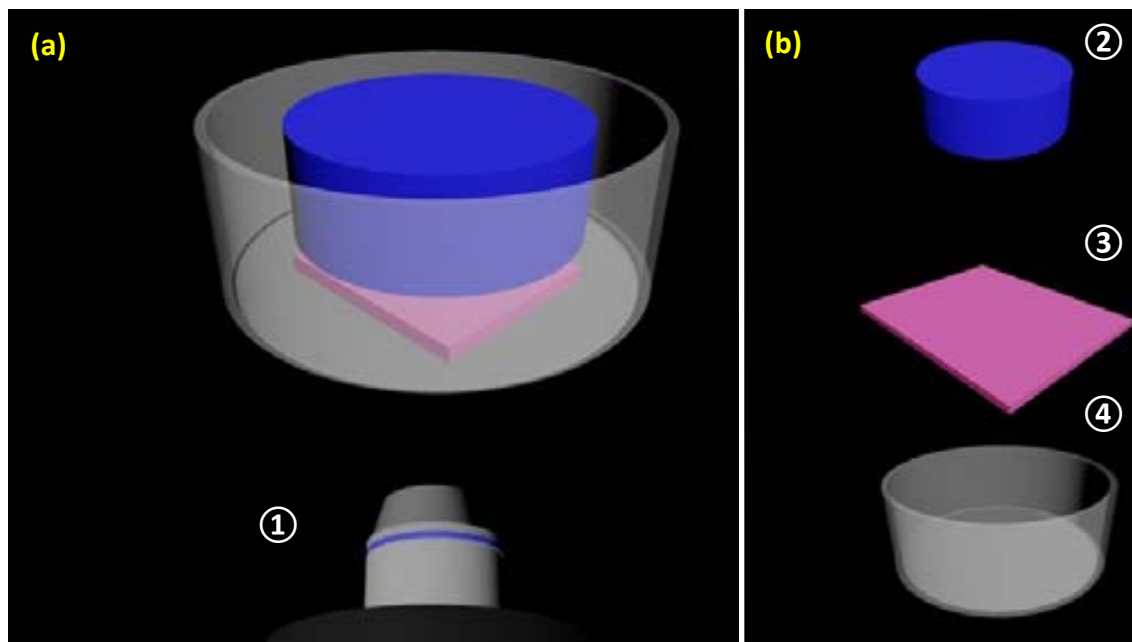


Figure 4.5 : Experimental setup for Confocal fluorescence microscopy a) assembled view of the sample b) exploded view . ① Microscope objective ② Polytetrafluoroethylene (PTFE) cylinder (it acts as sample holder.) ③ Sample (device is in front of the objective.) ④ Special liquid container

4.2.3 X-ray photoelectron spectroscopy (XPS)

X-ray photoelectron spectroscopy was selected as quantitative method to analyze chemical surface composition[33-35].

Sample size was 30 mm ×30 mm. A Perkin Elmer PHI 5500 Electron Spectroscopy for Chemical Analysis (ESCA)⁶³ was applied to perform X-ray photoelectron spectroscopy in ultra-high vacuum chamber (Pressure : 10^{-9} Torr). The machine had the capability to evaluate the entire periodic table except hydrogen and helium. The spectrometer was calibrated with $3d_{5/2}$ peak of the Silver⁶⁴. Excitation x-ray source was aluminum k_{α} radiation ($h\nu = 1486.6$ eV). Analysis depth was 10 nm. Data analysis was done with Multipak Physical Electronics v8.2B software⁶⁵.

⁶³ Perkin Elmer Physical Electronics division Website: [www http://www.perkinelmer.com](http://www.perkinelmer.com)

⁶⁴ Binding energy (BE) of 3d shell state of silver with quantum number $j = \frac{5}{2}$, was 368.3 eV on full width at half maximum (FWHM) equals to 0.68 eV .

⁶⁵ Physical Electronics, Inc Website: [http://www. http://www.phi.com](http://www.physical-electronics.com)

4.2.4 Atomic force microscopy (AFM)

Atomic force microscopy [36-38] was selected to measure the layer thickness and roughness (arithmetic average value (R_a) [39]). A Veeco Dimension 3100⁶⁶ with a Nanoscope 4 controller was used. The microscope was operated in tapping mode using silicon tips of 350 Hz resonance frequency. Table 4.9 shows the roughness of deposited layers.

Table 4.9: Roughness (R_a) of deposited layers

| Element | Au | Pt | Ag | Cu | Ni | Ru | Rh |
|------------|-----|-----|-----|-----|-----|---------------|---------------|
| R_a [nm] | < 1 | < 1 | < 1 | < 1 | < 1 | See table 4.1 | See table 4.1 |

4.2.5 Zeta potential measurement

A Zetasizer Nano-ZS, Malvern Instruments⁶⁷ with a DTS 1060C cell was employed to measure zeta potential of the beads based on electrophoretic light scattering [40-42] in 1% H_2O_2 solution.

Regarding gold and platinum surface, different methods were employed. An experimental setup was designed to measure zeta potential of the gold and platinum surface under the same conditions (figure 4.6). The water containing positively charged beads (P^+) was added to the confined space restricted between silicon wafer, spacer and cover glass. The particles moved over both gold and platinum surface after applying voltage. Sample fabrication and the data analysis are described in appendix 4.6.

⁶⁶ Veeco surface metrology group. Website: <http://www.veeco.com>

⁶⁷ Malvern Instruments Ltd website: <http://www.malvern.com>

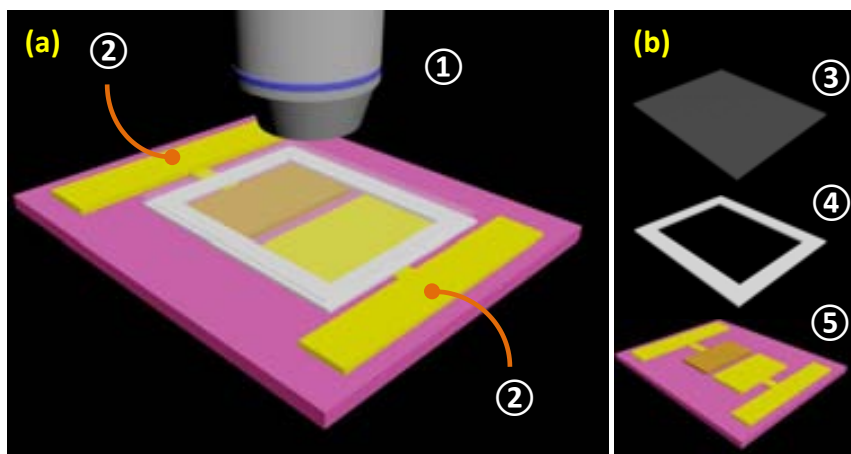


Figure 4.6: Experimental setup for tracking the particles under constant electric field a) assembled view b) exploded view ①Microscope objective ②Wires to connect gold contacts to the power supply ③Cover glass ④Spacer ⑤Sample . Two separate platinum (brown) and gold (yellow) area are connected to the gold contacts.

4.2.6 TAFEL plot measurement

A electrochemical workstation model: CH 660D⁶⁸ controlled by CHI software Ver.10.21 was used to record the electrochemical current as a function of the potential difference between a liquid and a metal electrode with scan rate equal to $1 \text{ mV} \cdot \text{s}^{-1}$. Figure 4.7 shows the experimental setup. Samples were silicon wafer coated with the metallic layer of interest. Metal deposition and cleaning process were done in the same way as what was applied for device fabrication. Electrolyte was 1 wt% hydrogen peroxide solution.

⁶⁸ CH Instruments, Inc. website : www.chinstruments.com

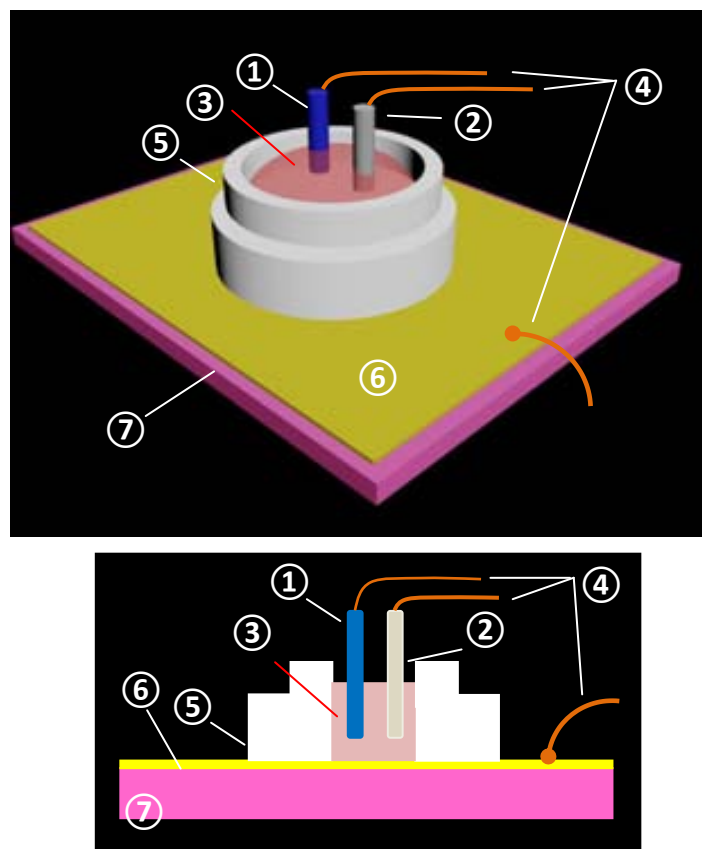


Figure 4.7 : Experimental setups for TAFEL plot measurement . ① Reference electrode ② Platinum counter electrode ③ Electrolyte ④ Contacts to the electrochemical workstation ⑤ Polytetrafluoroethylene (PTFE) liquid holder ⑥ The element deposited on silicon substrate and subjected to TAFEL test ⑦ Silicon substrate

4.2.7 pH measurement

The different pH solutions used for fluorescence calibrations as well as the ones for zeta potential measurements were measured with a pH-meter BASICS 20 (Crison Instrument⁶⁹).

⁶⁹ CRISON INSTRUMENTS, S.A. website: <http://www.crisoninstruments.com>

References:

- [1] S. Kakaç, B. Kosoy, D. Li, A. Pramuanjaroenij, *Microfluidics Based Microsystems: Fundamentals and Applications*, Springer, 2010.
- [2] C.S.S.R. Kumar, *Microfluidic Devices in Nanotechnology: Applications*, Wiley, 2010.
- [3] S.D. Minter, *Microfluidic Techniques: Reviews and Protocols*, Humana Press, 2006.
- [4] P. Tabeling, S. Chen, *Introduction to Microfluidics*, OUP Oxford, 2005.
- [5] A.G. Baca, J.B.D.N.B.P.N.C.O.D.A.E. A. G. Baca, J. Brown, D.N. Buckley, P. Nam, A. Etcheberry, *State-of-the-Art Program on Compound Semiconductors 50 (SOTAPOCS 50) -and- Processes at the Semiconductor Solution Interface 3*, Electrochemical Society, 2009.
- [6] A.P. Kanwal, R.T.S.U.o.N.J.-N.B.G.S.-N. Brunswick, *All Organic Memory Devices Utilizing Fullerene Molecules and Insulating Polymers*, Rutgers The State University of New Jersey - New Brunswick, 2008.
- [7] C.T. Laurencin, L.S. Nair, *Nanotechnology and Tissue Engineering: The Scaffold*, Taylor & Francis, 2008.
- [8] P. Schmuki, S. Virtanen, *Electrochemistry at the Nanoscale*, Springer, 2009.
- [9] P.M. Martin, *Handbook of Deposition Technologies for Films and Coatings: Science, Applications and Technology*, Elsevier Science, 2009.
- [10] D.M. Mattox, *Handbook of Physical Vapor Deposition (PVD) Processing*, Elsevier Science, 2010.
- [11] J. Singh, D.E. Wolfe, *J Mater Sci* 40 (2005) 1.
- [12] K. Wetzig, C.M. Schneider, *Metal Based Thin Films for Electronics*, Wiley, 2006.
- [13] N. Kanani, *Electroplating: Basic Principles, Processes and Practice*, Elsevier Science, 2004.
- [14] M. Schlesinger, M. Paunovic, *Modern Electroplating*, Wiley, 2011.
- [15] A. Watt, A. Philip, *The Electroplating and Electrorefining of Metals*, Wexford College Press, 2005.
- [16] W. Gissler, H.A. Jehn, *Advanced Techniques for Surface Engineering*, Springer, 1992.
- [17] K.L. Mittal, *Adhesion Measurement of Thin Films, Thick Films and Bulk Coatings*, Astm International, 1978.
- [18] L.J. Durney, *Graham's Electroplating Engineering Handbook*, Springer, 1984.
- [19] R.G. Compton, C.E. Banks, *Understanding Voltammetry*, Imperial College Press, 2011.
- [20] R. Holze, *Experimental Electrochemistry*, Wiley, 2009.
- [21] F. Scholz, A.A.M. Bond, *Electroanalytical Methods: Guide to Experiments and Applications*, Springer Berlin Heidelberg, 2010.
- [22] T. Kuwana, *Physical Methods in Modern Chemical Analysis*, Elsevier Science, 1983.
- [23] G.R. Brewer, J.P. Ballantyne, *Electron-beam technology in microelectronic fabrication*, Academic Press, 1980.
- [24] Z.L. Wang, Y. Liu, Z. Zhang, *Handbook of Nanophase and Nanostructured Materials: Synthesis*, Kluwer Academic/Plenum, 2003.
- [25] G. Wiederrecht, *Handbook of Nanofabrication*, Elsevier Science, 2010.
- [26] N.V. Cvetkovic, *Organic Electronics and Stencil Lithography Fabrication Methods: Organic Thin-Film Transistors and Circuits Fabricated by Stencil Lithography on Full-Wafer Flexible Substrates*, LAP Lambert Academic Publishing, 2012.
- [27] O.V. Mena, *Development of Stencil Lithography for Nanopatterning and for Electronic and Biosensing Applications*, EPFL, 2010.
- [28] K.A. Pataky, *Stencil Lithography and Inkjet Printing as New Tools for Life Sciences Research*, Hartung-Gorre, 2011.
- [29] M.A.F. Van den Boogaart, *Stencil Lithography: An Ancient Technique for Advanced Micro- and Nano-patterning*, Hartung-Gorre, 2006.

- [30] D.L. Taylor, P.J. Child, Y. Wang, METHODS IN CELL BIOLOGY,VOL 30 CTH: FLUORESCENCE MICROSCOPY OF LIVING CELLS IN CULTURE, PART B: QUANTITATIVE FLUORESCENCE MICROSCOPY-IMAGING AND SPECTROSCOPY: FLUORESCENCE MICROSCOPY OF LIVING CELLS IN CULTURE, PART B: QUANTITATIVE FLUORESCENCE MICROSCOPY-IMAGING AND SPECTROSCOPY, Elsevier Science, 1989.
- [31] B. Valeur, M.N. Berberan-Santos, Molecular Fluorescence: Principles and Applications, Wiley, 2013.
- [32] H.F. Wilkinson, F. Schut, Digital Image Analysis of Microbes: Imaging, Morphometry, Fluorometry and Motility Techniques and Applications, Wiley, 1998.
- [33] S. Hofmann, Auger- and X-Ray Photoelectron Spectroscopy in Materials Science: A User-Oriented Guide, Springer, 2012.
- [34] P. van der Heide, X-ray Photoelectron Spectroscopy: An introduction to Principles and Practices, Wiley, 2011.
- [35] J.M. Wagner, X-Ray Photoelectron Spectroscopy, Nova Science Publishers, Incorporated, 2011.
- [36] P.C. Braga, D. Ricci, Atomic Force Microscopy: Biomedical Methods and Applications, Humana Press, 2004.
- [37] P. Eaton, P. West, Atomic Force Microscopy, OUP Oxford, 2010.
- [38] G. Haugstad, Atomic Force Microscopy: Understanding Basic Modes and Advanced Applications, Wiley, 2012.
- [39] D.J. Whitehouse, Surfaces and their Measurement, Elsevier Science, 2004.
- [40] U. AUTHOR, Introduction to Dynamic Light Scattering by Macromolecules, Elsevier Science, 2012.
- [41] R. Beck, S. Guterres, A. Pohlmann, Nanocosmetics and Nanomedicines: New Approaches for Skin Care, Springer, 2011.
- [42] R. Xu, Particle Characterization: Light Scattering Methods, Springer, 2001.

Chapter 5

Introduction

This chapter covers the results of experimental activities and numerical simulations related with the Au-Pt system. Activation of Au-Pt catalytic micropumps, interaction between the micropump and charged tracers, evaluation of the spatial variations of the electric field, fluid flow and proton concentration around the devices are the important parts of experiments. The complexity of the chemomechanical process makes that a number of parameters involved in the process are ill-defined or are difficult to quantify. Under this context a powerful tool to measure independently the concentration of protons generated by the catalytic reaction has been implemented. That has helped to establish the role of such species in the catalytic actuation by contrasting the gradient of the concentration of protons against the spatial variation in the electric field. The experimental findings were complemented with numerical simulations which have reproduced the experimental data and have contributed to estimate additional parameters and improve the understanding of the chemomechanical actuation of catalytic pumps.

5.1 Activation of Au-Pt catalytic micropumps

Activation of Au-Pt devices was the first challenge in this research. Cleaning process C_5 (Chapter 4, table 4.3), which consisted in piranha and plasma treatment, could successfully overcome it. As mentioned before, without such treatment it could not be possible to see motion of the colloidal tracers. Figure 5.1.a shows an example of motion of P^+ tracers without neither directional motion nor pattern formation around an untreated Au-Pt device at 1 wt% hydrogen peroxide. After the activating process, P^+ tracers moved toward the platinum disk (figure 5.1.b). Reproducible interaction between differently charged tracers (P^0 , P^- and P^+) were observed. Motion patterns will be discussed later.

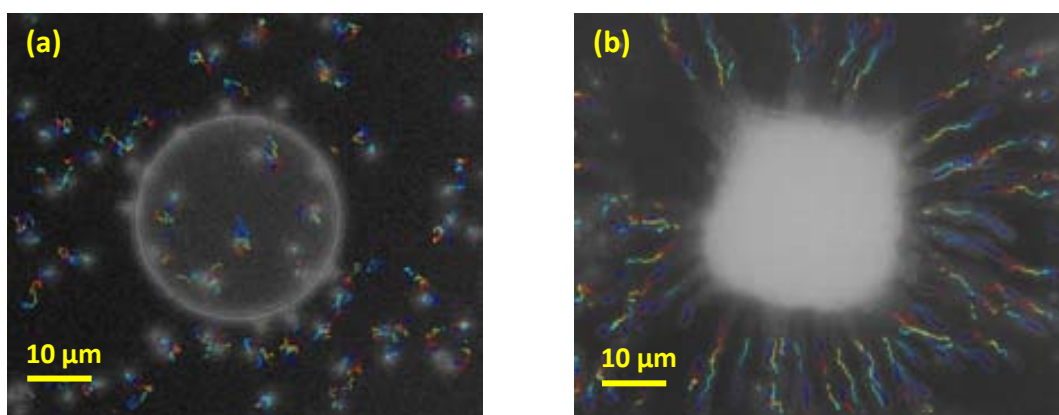


Figure 5.1: Tracking of P^+ tracers close to a Au-Pt device a) without C_5 treatment process. Tracers moved in random directions. b) Treated device with C_5 process. Tracers moved toward disk center. Gradient colorful lines show the motion path of tracers. Overlap technique was applied to produce tracks.

To find the origin of activation, X-ray photoelectron spectroscopy, electrochemical characterization based on TAFEL plot measurement and confocal fluorescence microscopy were done. Experimental data show that the cleaning process affected not only surface chemistry but also the electrochemical behavior of the surface. Below the different characterization results are described.

5.1.a X-ray photoelectron spectroscopy (XPS)

XPS results of Au and Pt samples, treated and non-treated with C_5 cleaning process, showed changes in surface chemistry of platinum and gold surface after cleaning. XPS curves represent the number of emitted photoelectrons which reach the detector versus their binding energy and they can be displayed in a wide scan spectrum up to 1100 eV or in a narrow spectrum focusing on the signal of the element of interest.

Besides main elements (Pt or Au), the wide range XPS curves depicted the presence of carbon, oxygen, and low amount of sulfur and nitrogen (not shown here). Physical adsorption from environment may explain the presence of carbon, nitrogen and sulfur.

Au 4f and *Pt 4f* peaks are usually used as characteristic peaks for gold and platinum respectively [1-5]. These characteristic peaks appear in a low photoelectron energy range up to 100 eV. XPS spectra of *Au 4f* and *Pt 4f* for treated and non-treated samples are shown in figure 5.2. In the spectra of non-treated gold and platinum samples (figure 5.2 a1 and b1), *4f* peaks appear as a typical doublet (two peaks related to $4f_{\frac{5}{2}}$ and $4f_{\frac{7}{2}}$ electron levels⁷⁰) due to spin-orbit splitting [6, 7].

Oxygen plasma treatment (cleaning process C_5) introduced high amount of oxygen on the surface of samples and produced certain degree of the oxidation on the platinum and gold surface [1-5]. Cleaning process C_5 increased oxygen functionality of gold surface from $3.2 \pm 1.5\%$ to $27 \pm 1.5\%$. In the case of platinum, oxygen amount changed from $9.4 \pm 1.5\%$ to $39.9 \pm 1.5\%$.

In the XPS spectra of cleaned samples shoulder-like peaks (indicated with arrows in figure 5.2 a2 and b2) emerge at higher binding energies. Distance from these peaks and the characteristics photoelectron peaks are 1.7 eV for gold and 2.8 eV for platinum. Such signals correspond to gold and platinum in oxidized states [1-5, 8, 9]. Oxidation states of an element are always shifted to higher binding energies. It is in agreement with the higher percentage of oxygen on treated samples. The simple physisorption of oxygen from the environment does not change the oxidation state of Au and Pt and does not introduce shoulders in the doublet peaks of Au and Pt. The appearance of shoulders at higher binding energies in both doublets evidences the formation of chemical bonds between the noble metal and oxygen.

It is concluded that surface chemistry of the metals was changed with the treatment.

Another interesting point to highlight is that the C_5 treatment is not maintained over time. XPS results showed that after two days of being subjected to C_5 treatment, the samples recover their XPS profile corresponding to the non-treated samples. That is, the shoulder peak appearance disappears with time. The same trend was observed with the TAFEL plots.

⁷⁰ Regarding peak quantum notation, $4f_{\frac{5}{2}}$ electron level represents electrons from orbital 4f with following quantum numbers: $l=3$, $s = -\frac{1}{2}$ and $j = \frac{5}{2}$

Similarly for $4f_{\frac{7}{2}}$ electron level, the quantum numbers are $l = 3$, $s = +\frac{1}{2}$ and $j = \frac{7}{2}$

Where the l , s and j are orbital momentum, spin momentum and total momentum respectively.

Therefore the catalytic actuation measurements should be performed during the day to see the electrohydrodynamic effects.

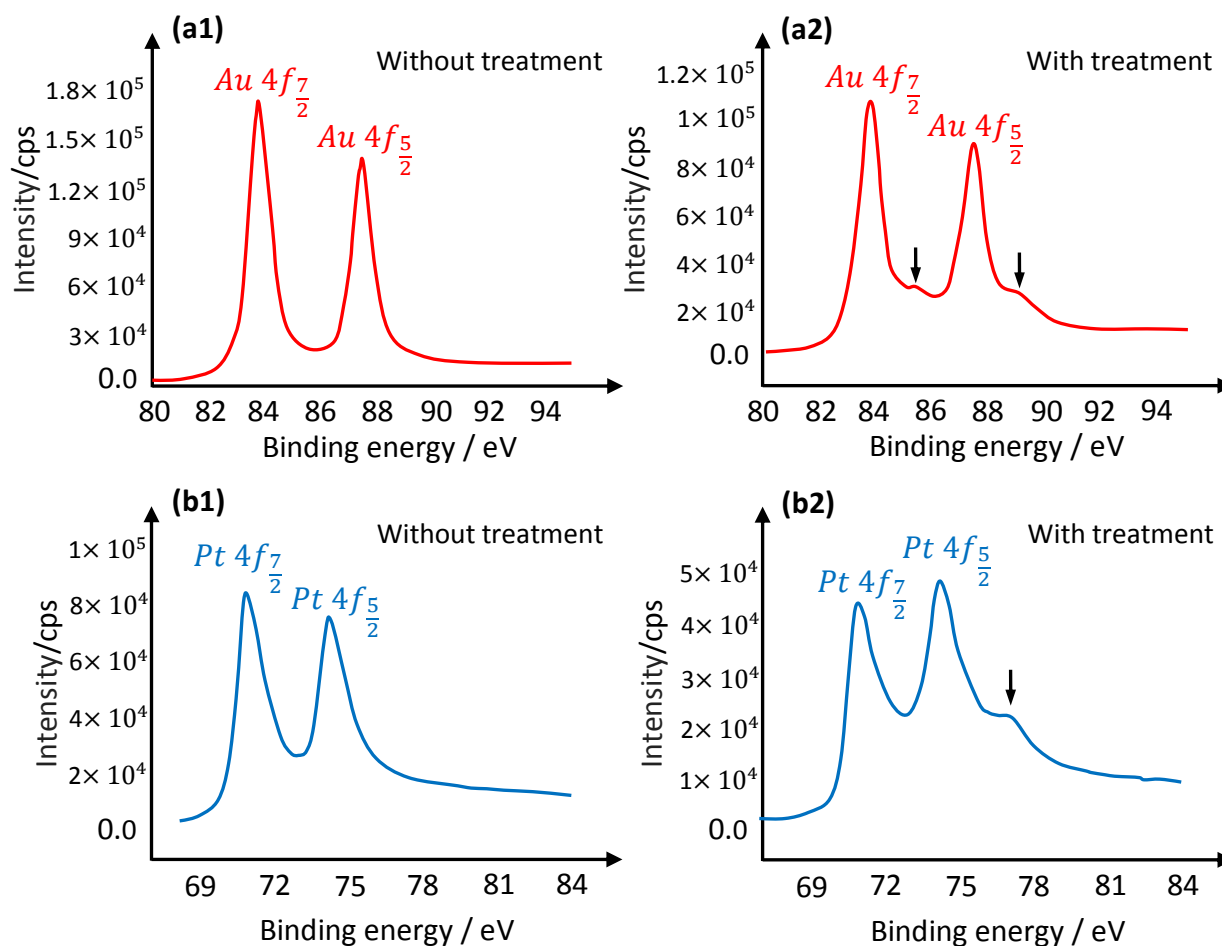


Figure 5.2: X-ray photoelectron spectroscopy spectra of a1) Au sample without plasma treatment, a2) Au sample with plasma treatment b1) Pt sample without plasma treatment b2) Pt sample with plasma treatment, The black arrows in a2 and b2 indicate peaks formed because of metals in oxidized state. *cps* is abbreviation of counts per second.

5.1.b TAFEL plot measurement

As shown with XPS studies, the plasma treatment (C_5 cleaning process) changes the surface chemistry of platinum and gold. Electrochemical characterization based on TAFEL measurements was the next step of the evaluation.

In this part the TAFEL measurements and the determination of the mixed potential for platinum and gold electrodes in presence of H_2O_2 (subjected or not to a pretreatment) are presented.

Extracting the mixed potentials for H_2O_2 for different metals helps to predict the role of the metal electrodes when they are electrically connected in presence of the redox species. The Appendix 5.1 provides the fundamentals of the TAFEL curves and also guidelines to extract useful information such as the mixed potentials. The metal which exhibits a more positive mixed potential would act as cathode whereas the metal with a more negative mixed potential would act as the anode. On the other side, the higher the difference between mixed potentials, the higher is the driving force for the catalytic actuation.

Figure 5.3 shows the TAFEL plots for Au and Pt in water only (a) and in presence of the electroactive species H_2O_2 with the electrodes subjected to the activation treatment. It can be observed that in presence of only water there is no redox behavior in that potential range. As soon as hydrogen peroxide is added, the anodic and cathodic branches, typical of the TAFEL plots, emerge. The mixed potential of Pt ($E_{Pt} = 0.39$ V) appears at more positive potential than the one of Au ($E_{Au} = 0.25$ V). As a result, platinum acts as the cathode and gold as the anode for hydrogen peroxide decomposition⁷¹. This finding is opposite to what has been reported for the catalytic motion of free suspending Au/Pt nanomotors in which anode role was ascribed to the platinum side. This difference may originate from the pretreatment performed to activate the catalytic pumps [10-13].

However if gold and platinum are not subjected to the treatment, their mixed potentials are similar. That points out the importance of the metal treatment for switching on the electrokinetic process. If the mixed potential difference of both electrodes is very small, the driving force for the catalytic actuation is very weak which explains the lack of colloidal motion when the pretreatment is not performed in the devices mentioned at the beginning of the chapter. It is quite probable that the oxygen functionalities at the gold and platinum surfaces modify the electrochemical response enhancing the thermodynamics of the redox process.

⁷¹ These results are independent of the way the metals are evaporated. Similar results were obtained using Joule and electron-beam evaporation.

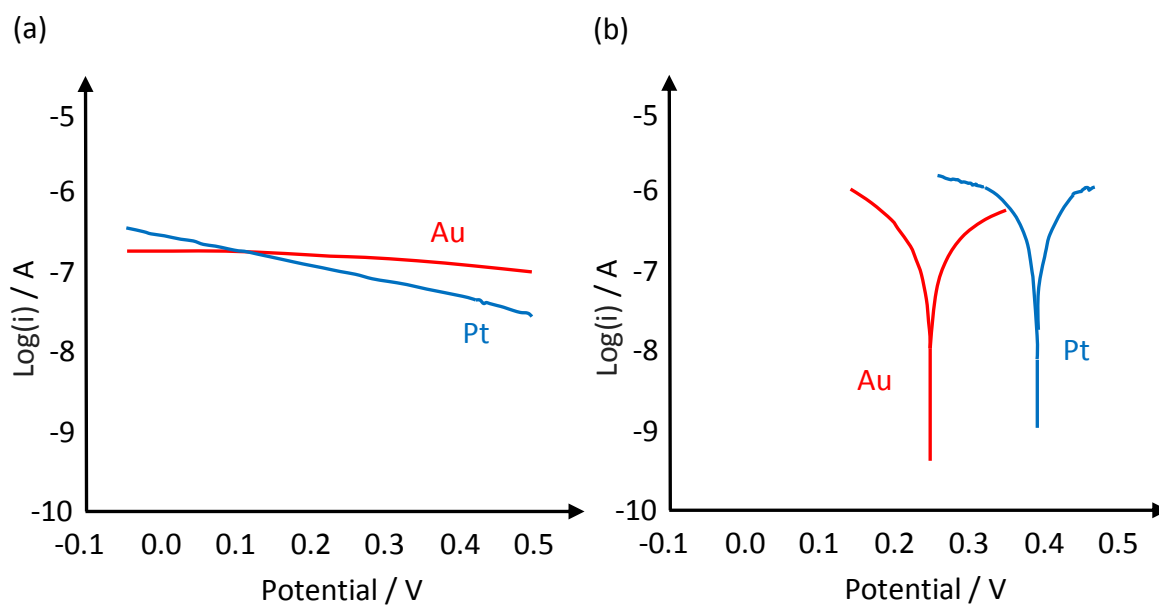


Figure 5.3 : Tafel plots for gold and platinum electrodes in contact with a) water b) 1 wt % hydrogen peroxide solution. The plots were taken at low scan rates $1 \text{ mV} \cdot \text{s}^{-1}$ to mimic steady state conditions.

5.1.c Proton concentration imaging on activated devices

Proton concentration and distribution at the bimetallic pump plays a crucial role to switch on the electrohydrodynamic process. That explains the need to search appropriate and powerful tools that can map and quantify this important parameter. Confocal fluorescence microscopy with pH sensitive dyes has been implemented to image and quantify the proton concentration on such catalytic pumps. These results represent the first report on proton concentration imaging at autonomous catalytic devices so far known. The results also provide an additional approach to verify the redox role of each metal at the catalytic device given the contradictory results obtained as compared with other research groups [10-13]

As described in 4.2.2 and appendix 4.5, pyranine molecule was selected to image proton concentration. It exhibits dual excitation. Dual excitation allows ratiometric measurements which is an ideal method to eliminate possible artifacts such as lack of dye concentration homogeneity, photobleaching, etc.

Before focusing on the proton imaging measurements with pyranine, some control experiments were previously addressed.

Since H_2O_2 is an oxidant it was analyzed the effect of hydrogen peroxide solution on the fluorescence stability of the pyranine. It was found that the fluorescent intensity of the dye is not altered in presence of 1% H_2O_2 .

It was also checked the response of the micropump in absence of hydrogen peroxide but in presence of the dye to evaluate background fluorescence from the metallic structure. Figure 5.4 shows the reflectance image of the device (figure 5.4a) together with the fluorescence response at the two excitation wavelengths in absence of H_2O_2 and at a pH solution of 7. It can be observed that the fluorescence is nearly uniform over the surface.

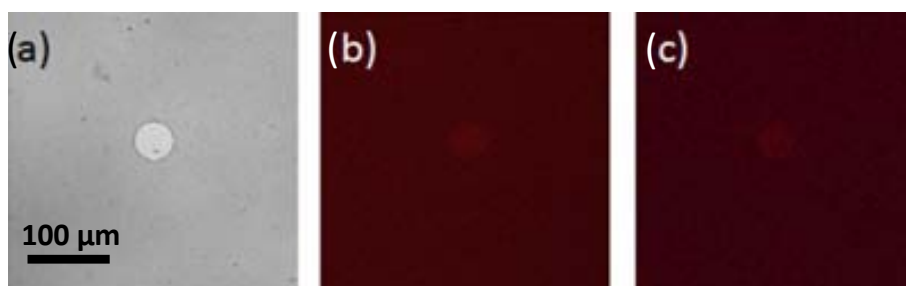


Figure 5.4: a) Reflectance image of a Au-Pt device exposed to water (no hydrogen peroxide) b) related confocal fluorescence at excitation wavelength $\lambda = 405 \text{ nm}$ c) related confocal fluorescence at excitation wavelength $\lambda = 458 \text{ nm}$. The fluorescence intensity remains quite homogenous over the surface. The disk radius is $15 \mu\text{m}$. Solution pH was 7.

After that, calibration fluorescence images were acquired to evaluate the change in the fluorescence signal with the pH at the two different excitation wavelengths and in absence of hydrogen peroxide. This methodology also helps to corroborate if the dye behaves in the way that is expected in presence of the device. For accomplishing that, different pH solutions in a

range between 4 and 9 were prepared in presence of the dye.⁷² Fluorescence images were collected for both excitation wavelengths at the different pH solutions and processed for extracting their fluorescence intensity. Figure 5.5 shows the calibration curves at both wavelengths of excitation as a function of the pH solution in absence of H_2O_2 . It can be observed two different behaviors.

At the excitation wavelength $\lambda_1 = 405$ nm, the fluorescence intensity decreases as the pH increases (figure 5.5 a), whereas the fluorescence signal increases as the pH increases when the dye is excited at $\lambda_2 = 458$ nm (figure 5.5 a).

The figure 5.5 b presents the ratio of fluorescence intensity at the two exciting wavelengths on the measured pH range. It can be observed high fluorescence sensitivity between pH 7 and 4, just in the range which is expected to have the pH gradients under catalytic actuation.

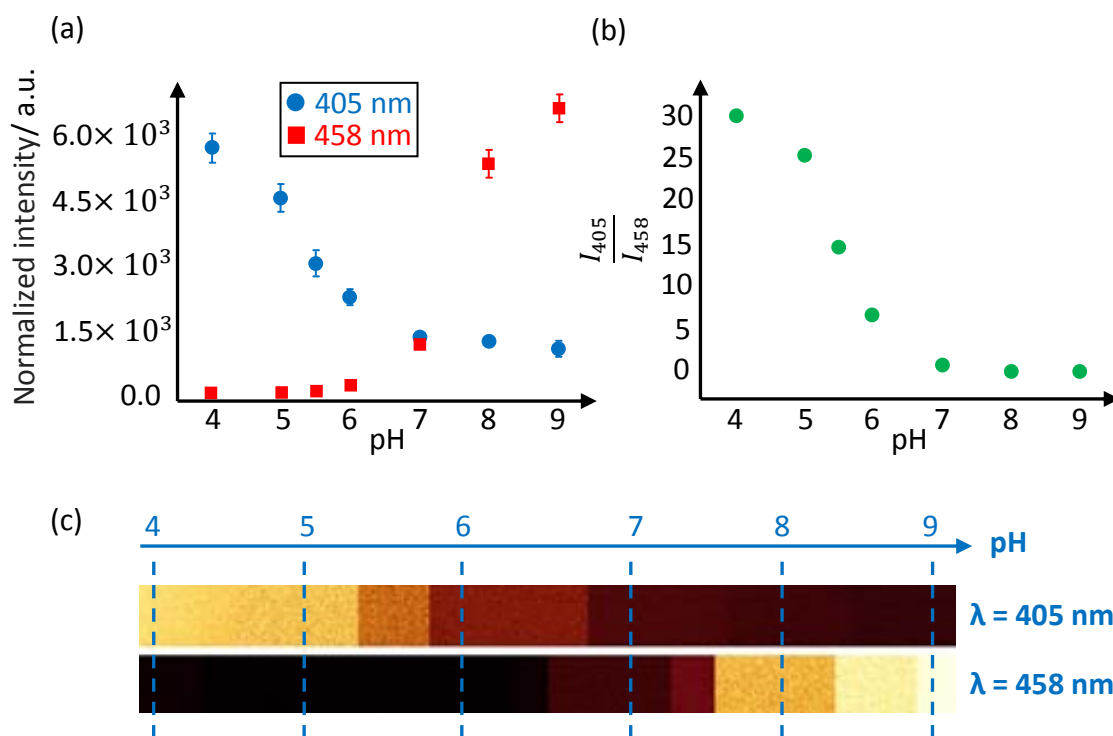


Figure 5.5: a) Fluorescence intensity as a function of pH for both excitation wavelengths, b) fluorescence signal ratio ($\frac{I_{405}}{I_{458}}$) as a function of pH, c) fluorescence intensity palette as a function of pH for both wavelengths. The solution was free of hydrogen peroxide. Dye concentration was $5 \mu M$.

⁷² The solutions at different pHs were prepared using acetate buffer and phosphate buffers for the lower and higher pH solutions respectively. Solutions were prepared with buffers to make sure that the pH was fixed at the desired value and it was not altered by any contamination from the air or from the contact with glass materials, etc. For pH solutions between 4 and 6, a buffer comprised of acetic acid/sodium acetate was used. For pH solutions between 6 and 9, a buffer of phosphate monobasic/phosphate dibasic was used. In the case of the buffer acetic acid/sodium acetate, the starting pH of the buffer is around 4.70. *HCL* or *NaOH* were used to vary pH to 4, 5 and 6. In the case of the phosphate buffer, the starting pH was 7. The pH was adjusted 6 to 9 adding *HCL* or *NaOH*.

The figure 5.5 c shows the color scale in order to get an idea of the general trends at both wavelengths. In the ratiometric measurements the important parameter for extracting the pH is the ratio between the fluorescence signals at both wavelengths. Therefore, the color palettes of figure 5.5 c are not representative of the actual pH and even more when non-uniformity in the dye concentration may exist.

After evaluating the behavior of the dye in calibration curves, it was proceeded to measure the pH gradient in the devices in presence of hydrogen peroxide at the two excitation wavelengths. The fluorescence images at 405 and 458 nm are depicted in figure 5.6.

To evaluate the pH, the standard calibration equation in terms of the ratio of fluorescence signals (appendix 4.5), was applied :

$$pH = pK_a + \log \left(\frac{R - R_A}{R_B - R} \times \frac{I_{A(\lambda_2)}}{I_{B(\lambda_2)}} \right) \quad \text{Equation 5.1}$$

The definition of parameters was mentioned in appendix 4.5. The proton concentration image shown in figure 5.7 b was obtained from the fluorescence images of Fig. 5.6 a and b and by applying this equation pixel by pixel.

The figure 5.6 shows the spatial variation of $[H^+]$ around a platinum disk (diameter: 50 μm) deposited on gold substrate. Proton concentration decreases as the distance from disk center decreases (figure 5.7 c).

Proton concentration gradient remained stable over experiment duration. Consequently, it implies that the system reached steady state conditions.

The experimental results clearly indicate that the electrochemical reactions undergo proton production on the gold surface and proton consumption on the platinum disk. Figure 5.7 c shows the proton profile along one radial path for better quantification. It can be observed that the proton concentration changes in almost one unit of pH.

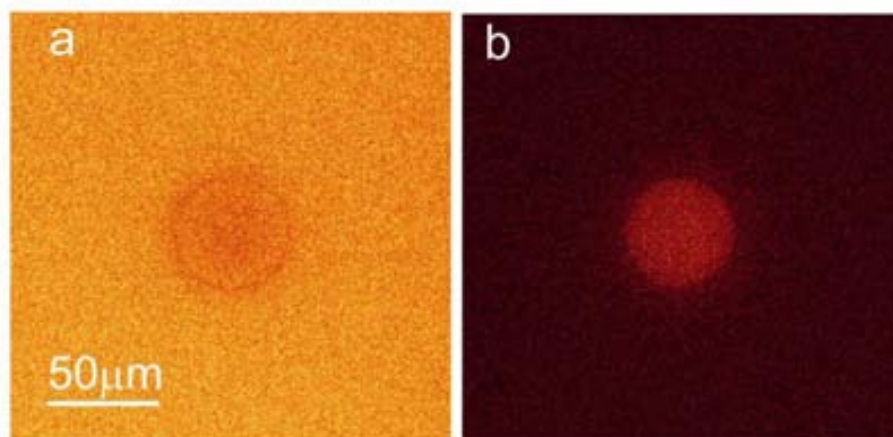
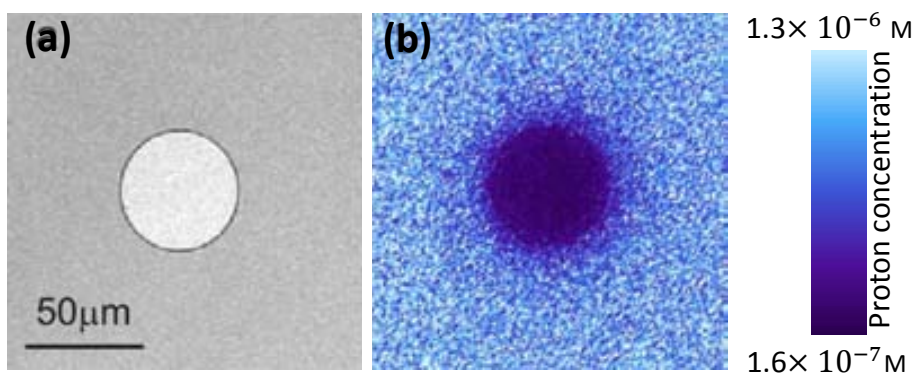


Figure 5.6: Fluorescence images of a Au-Pt device in presence of 1% H_2O_2 at excitation wavelength a) $\lambda = 405 \text{ nm}$ b) $\lambda = 458 \text{ nm}$. Dye concentration in solution was $5\mu\text{M}$. The disk radius is $25\mu\text{m}$.



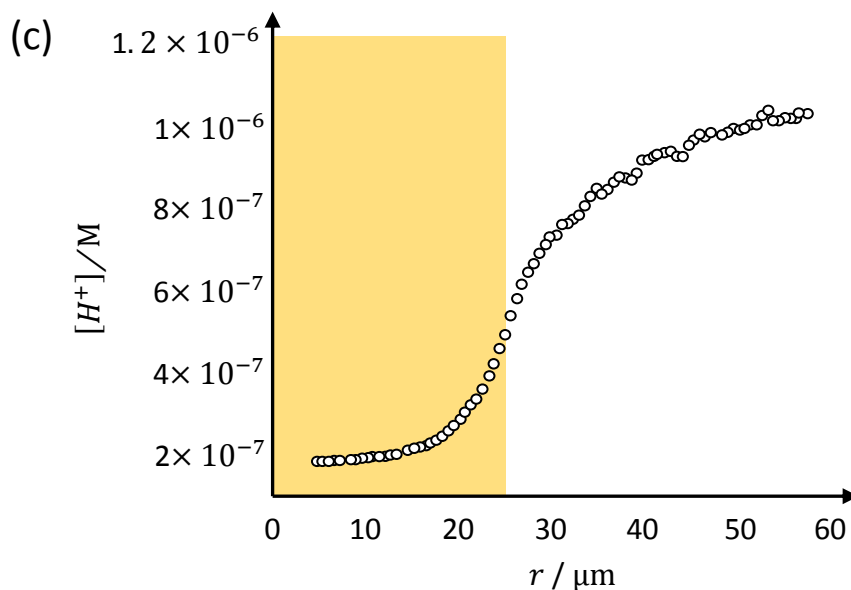


Figure 5.7: a) Reflectance image of the Au-Pt device b) the related proton concentration image c) The proton concentration as a function of radial distance from disk center (r). Yellow area represents the area on top of the disk. All images were obtained with a confocal fluorescence microscope. The disk radius was 25 μm .

These results are in agreement with TAFEL measurements. They predicted that gold surface was acting as anode producing protons and the platinum one as cathode consuming the protons. Again, the redox role of electrodes is opposite to the previous reports on catalytic nanomotors. Confocal fluorescence microscopy also confirms that no proton gradient forms around the Au-Pt device exposed to hydrogen peroxide-free electrolyte (water). Proton concentration gradient originates from chemical reaction involving hydrogen peroxide. It was observed that protons homogeneously distributed in the absence of H_2O_2 at both exciting wavelengths (figure 5.4).

It has also been observed that such pH gradient is not formed if the Au/Pt sample is not pretreated with C5 process, corroborating again the importance of the activation process to switch on the catalytic actuation.

5.2 Zeta potential of the surfaces

As previously mentioned the zeta potential of surfaces is a key parameter in electrokinetic processes. In order to characterize the actuation of the Au-Pt catalytic pump in combination with charged colloidal tracers or to complement the electrohydrodynamic process with numerical simulations is important to have an estimation of the zeta potentials of the colloids and of the Au and Pt surface. The zeta potential of the colloids can be easily obtained by using an electrophoretic light scattering methodology and the table below shows the zeta potential values of the charged tracers used in this thesis.

The values are reported in table 5.1.

Table 5.1 : Size and Zeta potentials (ζ) values of the colloidal tracers

| Tracer | Type | Size [μm] | ζ [mV] |
|--|--|------------------------|--------------|
| Positively charged particles (P^+) | polystyrene spheres functionalized with amidine groups ⁷³ | 2 | 46 \pm 1 |
| Negatively charged particles (P^-) | silica spheres ⁷⁴ | 2 | -83 \pm 1 |
| Quasi-neutral particles (P^0) | polystyrene spheres ⁷⁵ | 2 | -12 \pm 1 |

However the estimation of the wall zeta potential of the pumps is not so trivial. The zeta potential of the pump surface is a very relevant parameter for controlling the fluid flow. In many cases the fluid velocity can be approached to the electro-osmosis velocity (V_{eo}), in which a proportional relation of this parameter with the fluid velocity is established.

$$V_f(r) = V_{eo} \quad \text{Equation 5.2}$$

$$V_f(r) = -\frac{\varepsilon \zeta_{Au}(r)}{\eta} E_r(r) \quad \text{Equation 5.3}$$

$\zeta_{Au}(r)$: zeta potential of the gold substrate

As mentioned, the zeta potential of the pump becomes a very relevant input when performing electrohydrodynamic simulations to support the experimental data as it is the case of this thesis work.

One way to estimate the zeta potential of the surface (Au and Pt) has been addressed in Appendix 4.6. The method is based on tracking the motion on top of gold and platinum surface (Figure 5.8). Average velocity of tracers on top of the gold ($V_{P^+/Au}$) and platinum ($V_{P^+/Pt}$) were 17 $\mu\text{m} \cdot \text{s}^{-1}$ and 21 $\mu\text{m} \cdot \text{s}^{-1}$ respectively.

According to appendix 4.6 - equation 7, the difference between P^+ velocities over 2 different surfaces is proportional to the difference between relevant zeta potentials.

$$\zeta_{Au} - \zeta_{Pt} = -\frac{\eta}{\varepsilon_r \varepsilon_0 E} \left(V_{P^+/Au} - V_{P^+/Pt} \right) \quad \text{Equation 5.4}$$

⁷³ Life Technologies Corporation Website: <http://www.invitrogen.com>

⁷⁴ Kisker Biotech GmbH & Co. KG Website: <http://www.kisker-biotech.com>

⁷⁵ Kisker Biotech GmbH & Co. KG Website: <http://www.kisker-biotech.com>

Parameters were described in the appendix 4.6 .When the difference between velocities is not equal to zero (equation 5. 5), the existence of non-equal zeta potential values imply (equation 5.6).

$$\frac{V_{p^+}}{Au} - \frac{V_{p^+}}{Pt} \neq 0 \quad \text{Equation 5.5}$$

$$\zeta_{Au} - \zeta_{Pt} \neq 0 \quad \text{Equation 5.6}$$

Where ζ_{Au} and ζ_{Pt} are zeta potential of gold and platinum surface respectively.

As per Appendix 4.6 – equation 9, relation between zeta potential of platinum and gold surface regardless of the applied electric field can be written as follow:

$$\zeta_{Au} = \left(1 - \frac{V_{p^+}}{V_{p^+}} \frac{Au}{Pt}\right) \zeta_{Pt} + \frac{V_{p^+}}{V_{p^+}} \frac{Au}{Pt} \cdot \zeta_{Pt} \quad \text{Equation 5.7}$$

Incorporating the $\frac{V_{p^+}}{Au}$ and $\frac{V_{p^+}}{Pt}$ values, the equation 5.7 becomes:

$$\zeta_{Au} \cong 8.761 + 0.8\zeta_{Pt} \quad [mV] \quad \text{Equation 5.8}$$

The estimation of the surface zeta potential is independent from the applied electric field. Considering appendix 4.6, the ζ_{Pt} and ζ_{Au} values were about -37 mV and -21 mV respectively.

There is an alternative way to estimate zeta potential of the gold substrate , $\zeta_{Au}(r)$, based on fluid velocity and radial electric field data according to the data of figure 5.22 a and b. If the fluid velocity is as approached to electrosmotic velocity described in chapter 3, the zeta potential of the gold surface can be calculated as:

$$\zeta_{Au}(r) = \frac{\eta}{\varepsilon} \frac{V_f(r)}{E_r(r)} \quad \text{Equation 5.9}$$

$E_r(r)$: Radial electric field strength at distance r from disk center [$V.m^{-1}$]

$V_f(r)$: Radial velocity of liquid toward platinum disk center at distance r from the disk center [$m.s^{-1}$]

It was obtained that $\zeta_{Au}(r)$ remains nearly constant as a function of the radial distance, with an average value of -33 ± 1.5 mV. This is close to the values considered for the zeta potential of Au in previous studies [14, 15].

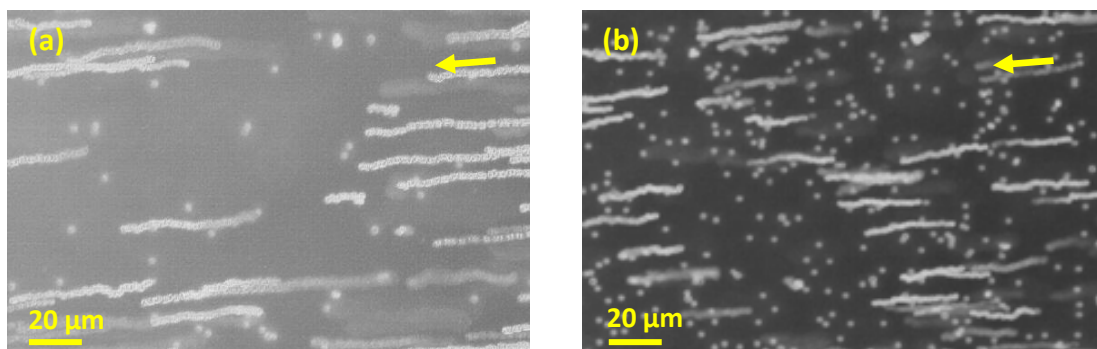


Figure 5.8: Tracking of P^+ tracers on top of a) cleaned Pt surface b) cleaned Au surface under applied electric field. Arrows show direction of electric field and particle velocity. Electric field strength is approximately $320 \text{ V} \cdot \text{m}^{-1}$. Average particle velocity on top of the gold and platinum are 3.14 ± 0.25 and $5.61 \pm 0.25 \mu\text{m} \cdot \text{s}^{-1}$ respectively. Overlap technique was used to show the particle movement.

5.3 Studying the activated Au-Pt devices

Optical microscopy and tracking of quasi-neutral particles (P°), positively charged (P^+) and negatively charged particles (P^-) showed interesting interactions between tracers and treated devices as described below.

5.3.a Quasi-neutral particles (P°)

Quasi-neutral⁷⁶ particles shows three motion patterns (figure 5.9a). Generally, the particles move toward the platinum disk center. Calculation of the directionality coefficient (Π_r), defined in appendix 4.4, shows the particles tendency to move toward platinum disk center which increases as they become closer to the disk (figure 5.10a). Some of the tracers settle on the gold surface either close or far from platinum disk (figure 5.9 a, pattern A and B). The rest of them change their movement direction and go far from the surface (figure 5.9a, pattern C).

As an example of motion according to pattern A, Figure 5.11 shows a series of images in which a particle moves toward the disk center. Once it arrives to the platinum disk border or its vicinity, the particle sticks to the surface. Similar to pattern A, particles can also move toward the disk center but settle on the gold surface before arriving to platinum disk (pattern B, figure 5.12).

Regarding the pattern C, particles move toward the disk center but the direction of motion changes after crossing the platinum - gold border (figure 5.13). They show tendency to move in the direction which is perpendicular to the surface. They go away far from the surface more and more until leaving the volume which is under optical inspection.

Although tracking provides information about coordinates of particle at x-y plane, it is not possible to determine how far particles are from the surface. The motion pattern C provides valuable information about direction of fluid flow around the platinum disk.

As a general behavior of the quasi-neutral particles (P°), the average radial velocity versus normalized distance to disk center is reported on figure 5.9b. The particles reach a maximum radial velocity of $3.5 \pm 0.25 \mu\text{m} \cdot \text{s}^{-1}$ close to the boarder. Their velocity becomes zero $\mu\text{m} \cdot \text{s}^{-1}$ if they settle on the gold surface.

⁷⁶ The particles are named quasi-neutral due to their small zeta potential.

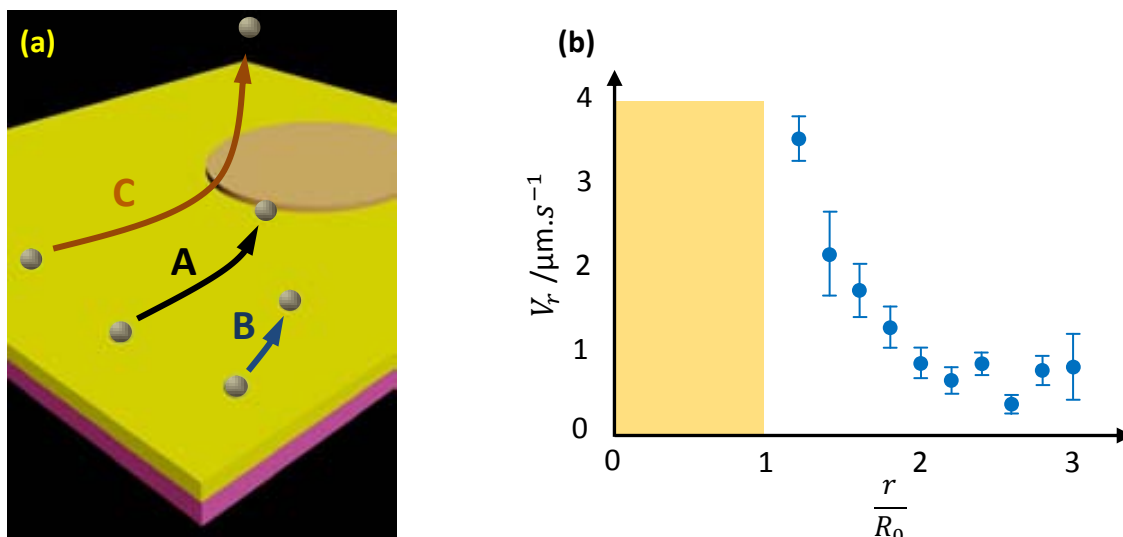


Figure 5.9: a) schematic presentation of quasi-neutral particles (P°) movement for pattern A, B and C toward platinum disk on an Au-Pt device b) average radial velocity (V_r) of P° tracers versus normalized distance to disk center at 1 wt% hydrogen peroxide solution. r and R_0 are the distances of the particle from the disk center and disk radius respectively. Disk radius (R_0) is $15 \mu\text{m}$. The $\frac{r}{R_0}$ values are equal to 0 and 1 at the platinum disk center and platinum disk border respectively. Yellow area represents the area above the platinum disk. The graph represents the averaged behavior of 25 particles.

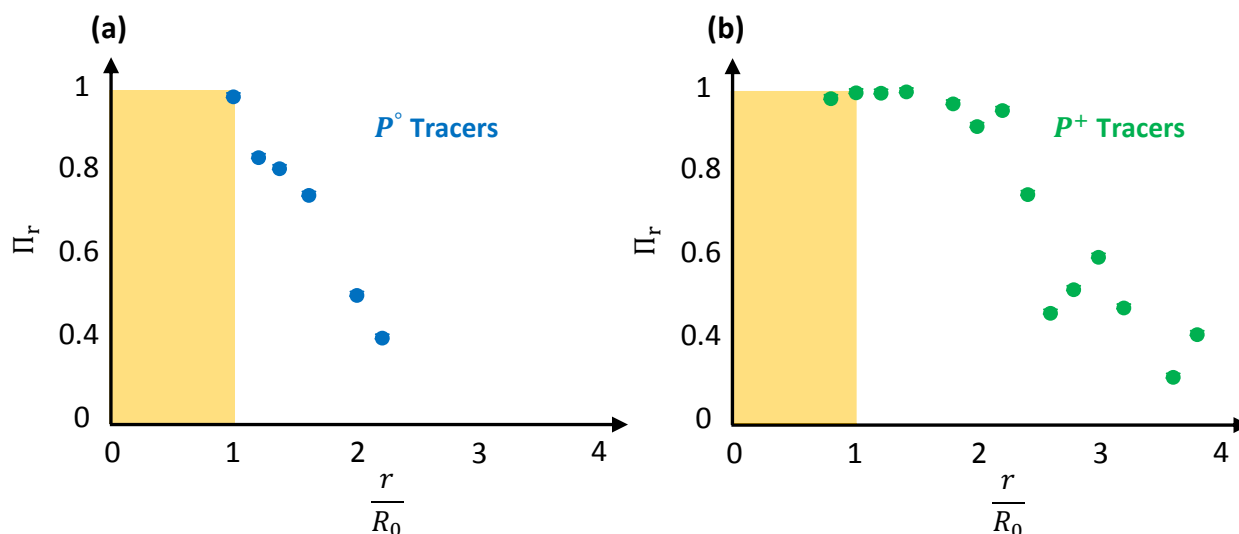
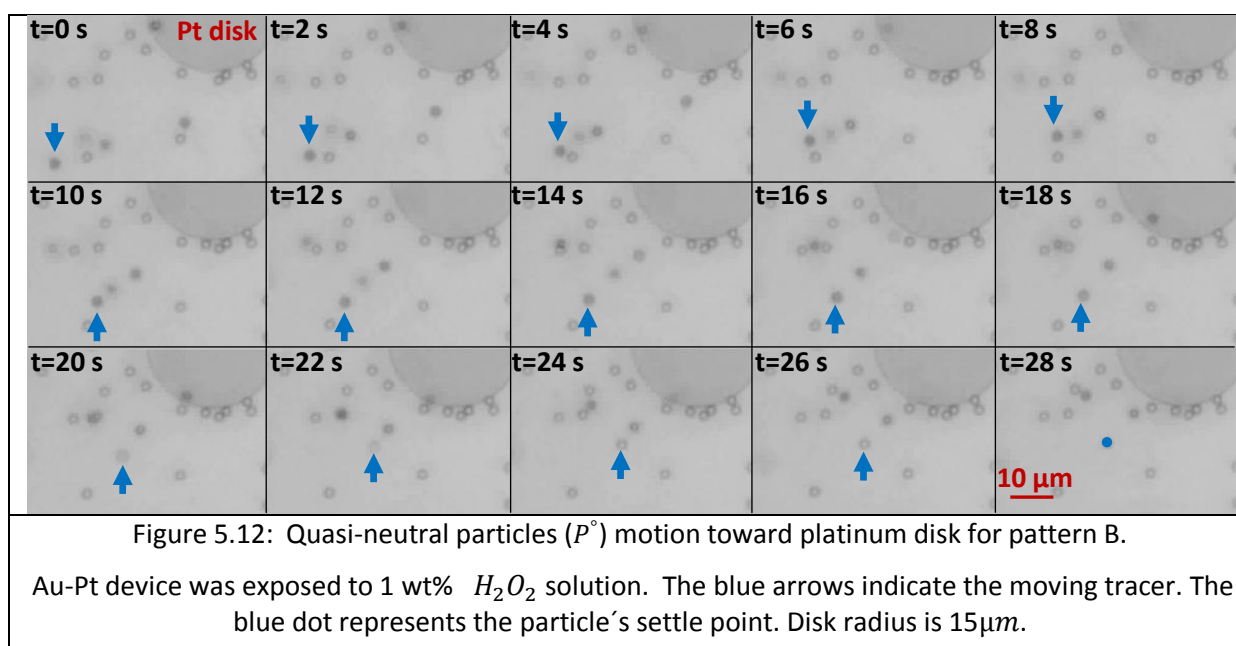
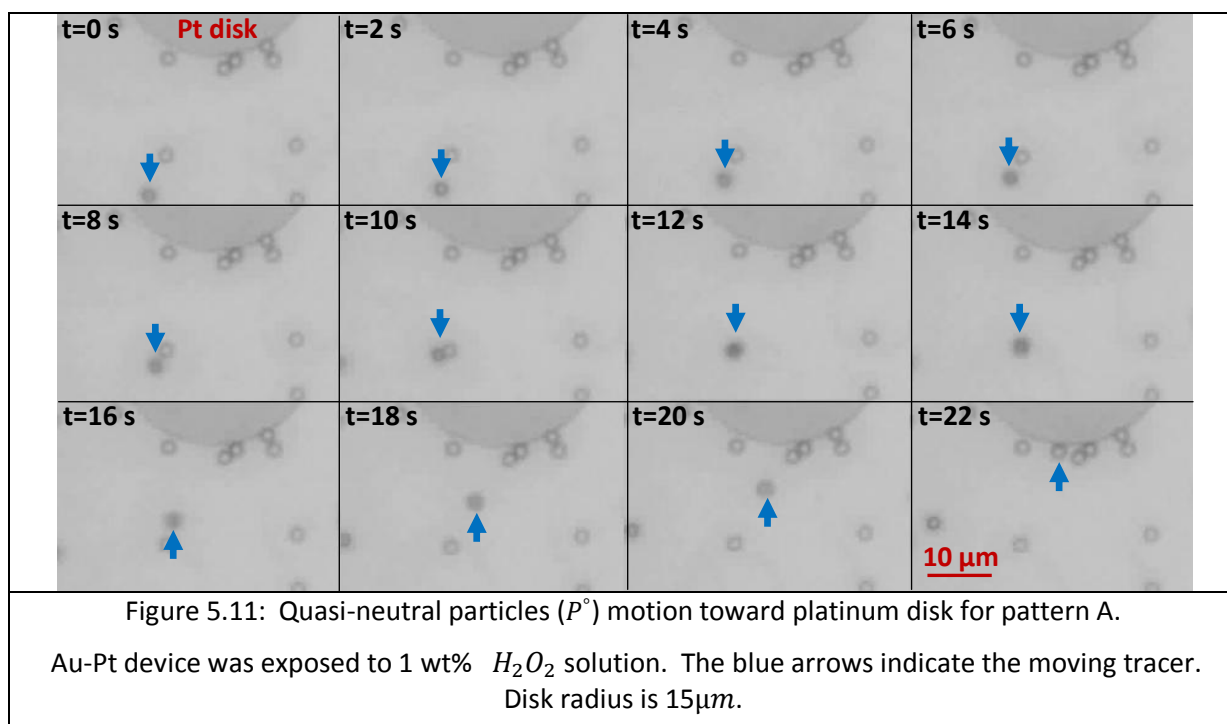
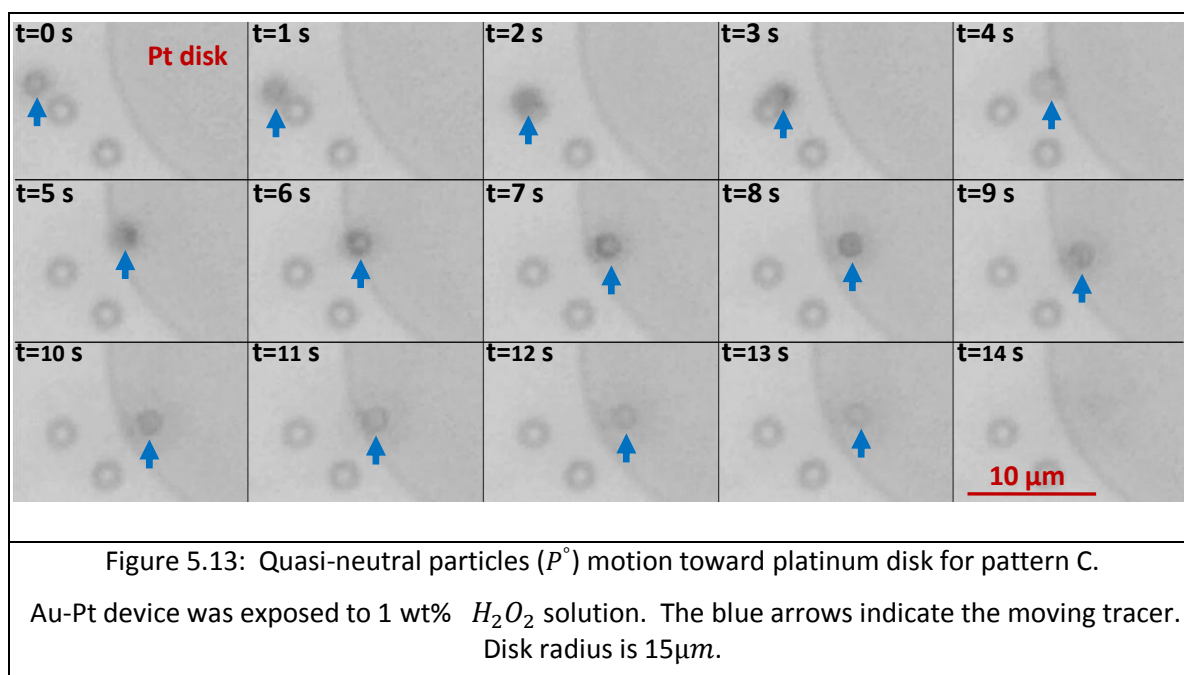


Figure 5.10: directionality coefficient (Π_r) versus normalized distance to platinum disk center at 1 wt% hydrogen peroxide solution for a) quasi-neutral particles (P°) and b) positively charged particles (P^+). r and R_0 are the distances of the particle from the disk center and disk radius respectively. Disk radius (R_0) is $15 \mu\text{m}$. The $\frac{r}{R_0}$ values are equal to 0 and 1 at the platinum disk center and platinum disk border respectively. Yellow area represents the area above the platinum disk.





5.3.b Positively charged particles (P^+)

When the Au-Pt device is exposed to 1 % hydrogen peroxide solution containing positively charged particles (P^+), the particles are attracted to the platinum disk center. Figure 5.14.a illustrates schematically the observed motion patterns at the devices. Pattern A represents tracers which are very close to the substrate. They move toward platinum disk and settle on the platinum disk (figure 5.15). As an interesting point, the device attracts not only particles which are very close to the surface but also those which are far from the surface (figure 5.14 a, pattern B).

Figure 5.16 shows the attraction of a positively charged particle from a level which is higher than gold surface. The particle comes closer to the surface and at same time moves toward the platinum disk.

Further observations showed that the device can attract particles distributed above the disk even from planes with relatively high z values (figure 5.14 a, pattern C). Figure 5.17 illustrates the motion for pattern C.

The device is a $40\mu m \times 40\mu m$ platinum square which attracts tracers from different heights up to $30\mu m$ from the substrate surface. Tracking of particles at different heights results in similar velocity pattern but with different values. As the height from the surface increases, the velocity decreases (figure 5.17.d).

Regarding velocity profile, figure 5.14 b shows the radial velocity of positively charged tracers which were close to the surface versus normalized distance to disk center. As they come closer to the disk, their radial velocity increases. In the vicinity of gold-platinum border, the average velocity reaches its maximum of $19.4 \pm 6.8\ \mu m \cdot s^{-1}$. When moving particle passes over the

platinum disk toward disk center, the particle velocity dramatically decreases because the particles settled on the platinum surface.

Regarding particle directionality toward platinum disk center, Π_r increases as they become closer to the disk (figure 5.10b). The directionality follows similar trend as in the case of P^0 but it reaches maximum values at relatively larger $\frac{r}{R_0}$ as compared to the P^0 tracers

Finally the positively charged tracers form a non-ordered colloidal layer on the platinum disk (Figure 5.18). Incoming tracers move on the platinum surface to find a vacant area to settle between the attached particles or on top of them.

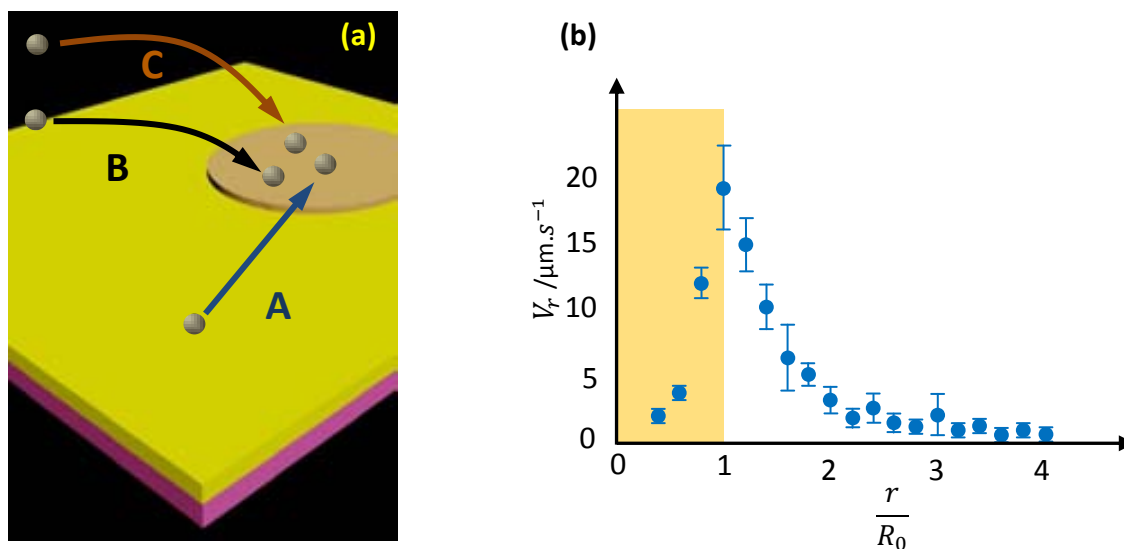
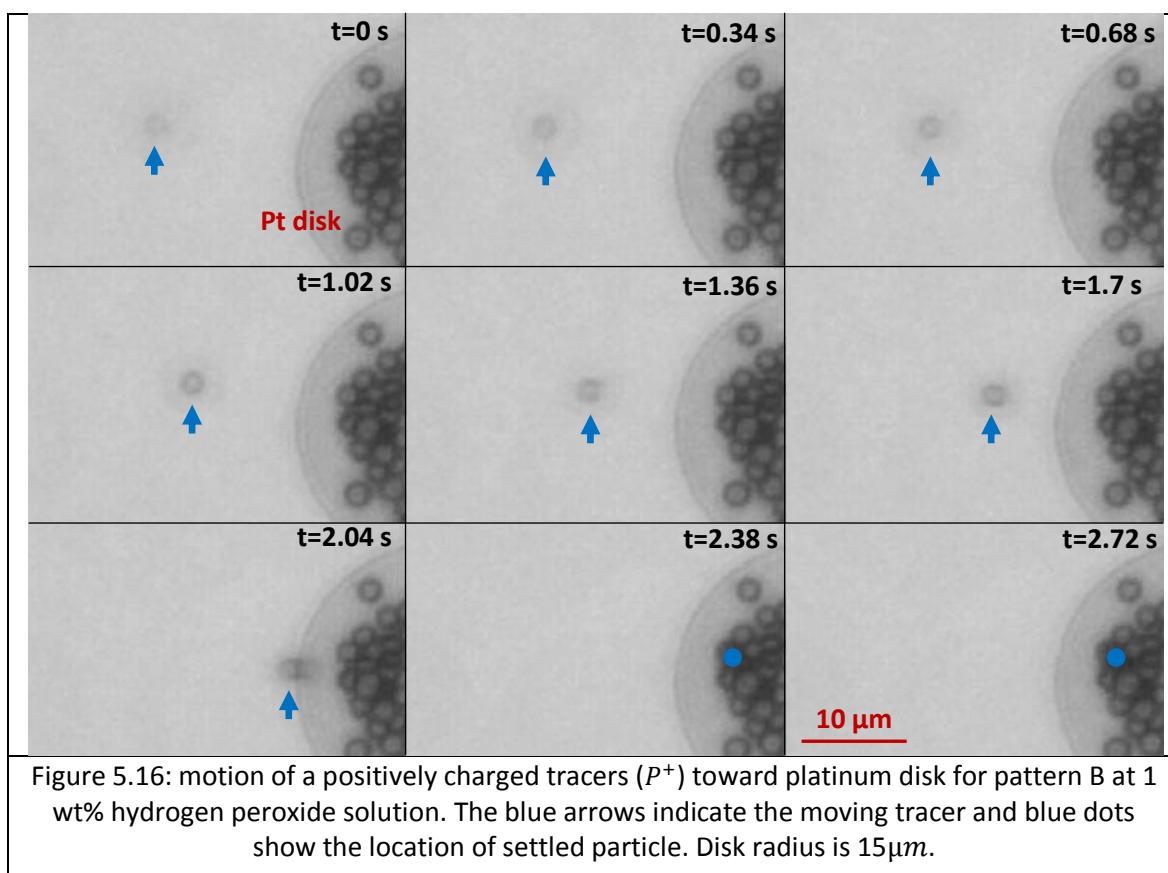
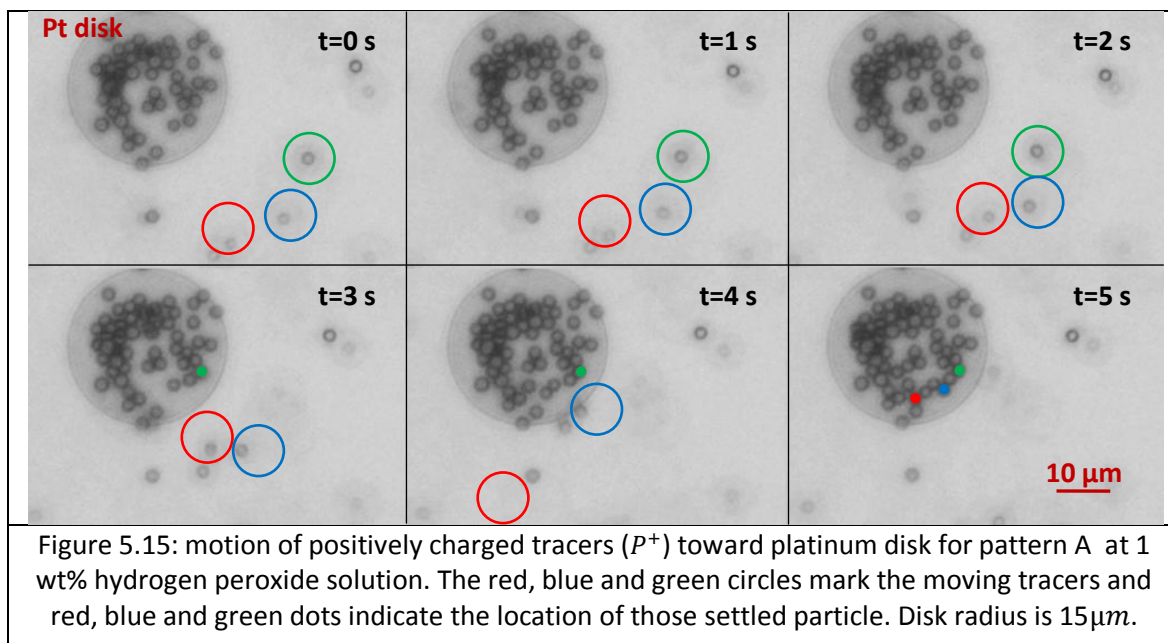


Figure 5.14: a) schematic representation of positively charged particles (P^+) movement for pattern A, B and C toward the platinum disk on the Au-Pt device b) average radial velocity (V_r) of P^+ tracers versus normalized distance to disk center at 1 wt% hydrogen peroxide solution. r and R_0 are the distances of the particle from the disk center and disk radius respectively. Disk radius (R_0) is 15 μm . The $\frac{r}{R_0}$ values are equal to 0 and 1 at the platinum disk center and platinum disk border respectively. Yellow area represents the area above the platinum disk. The graph represents the averaged data of 10 devices and 78 particles.



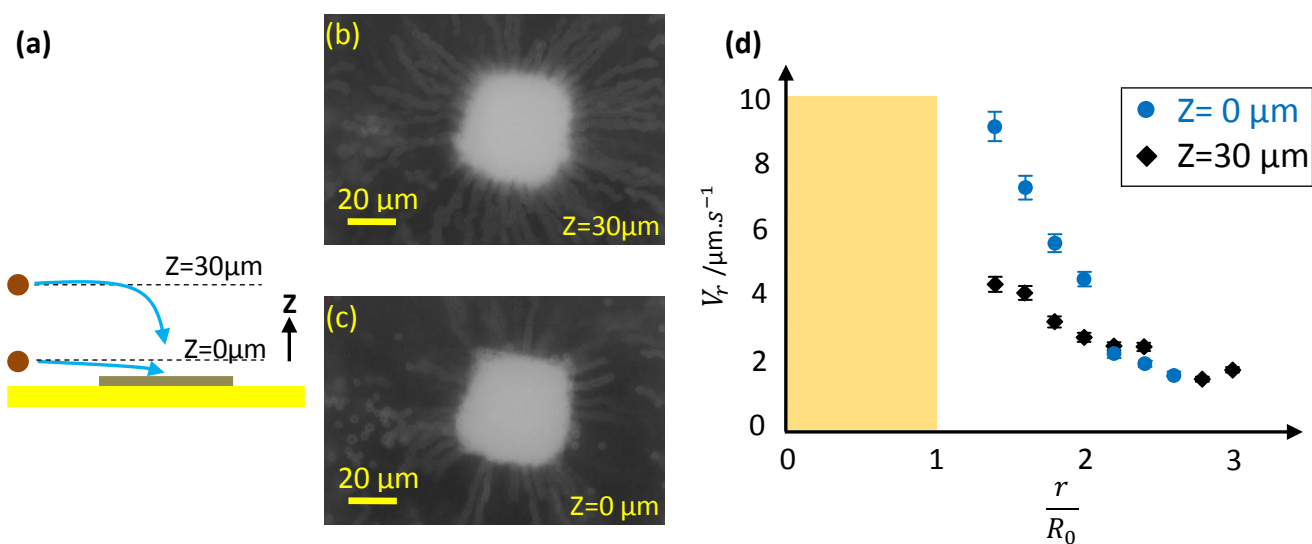
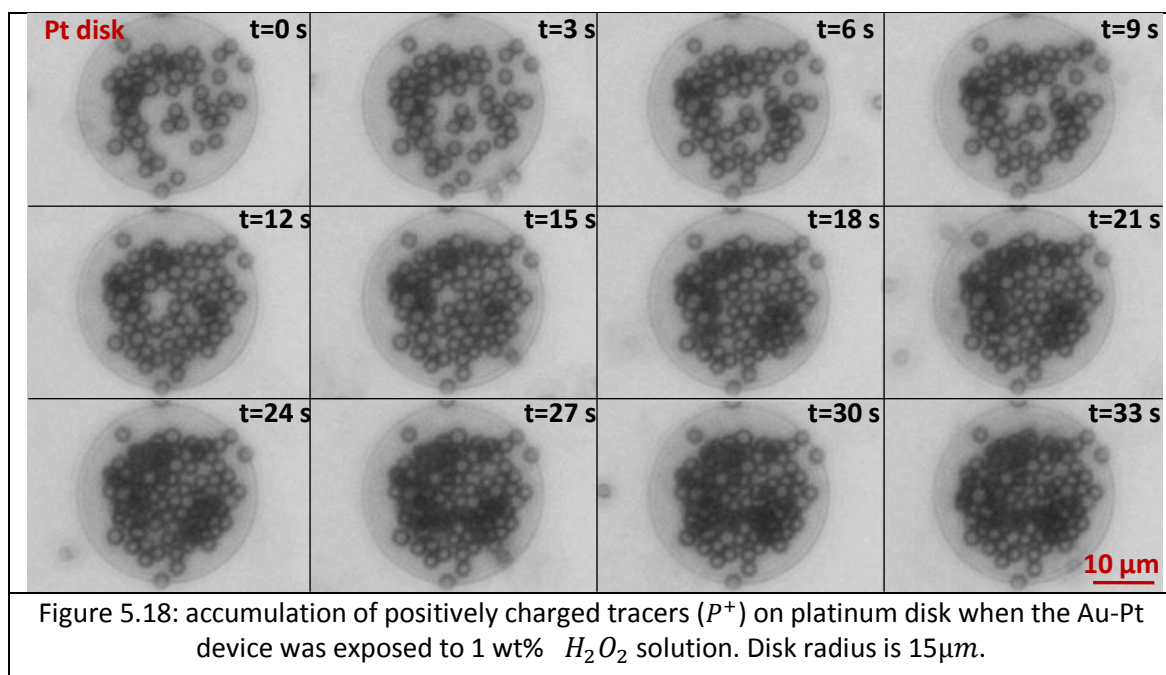
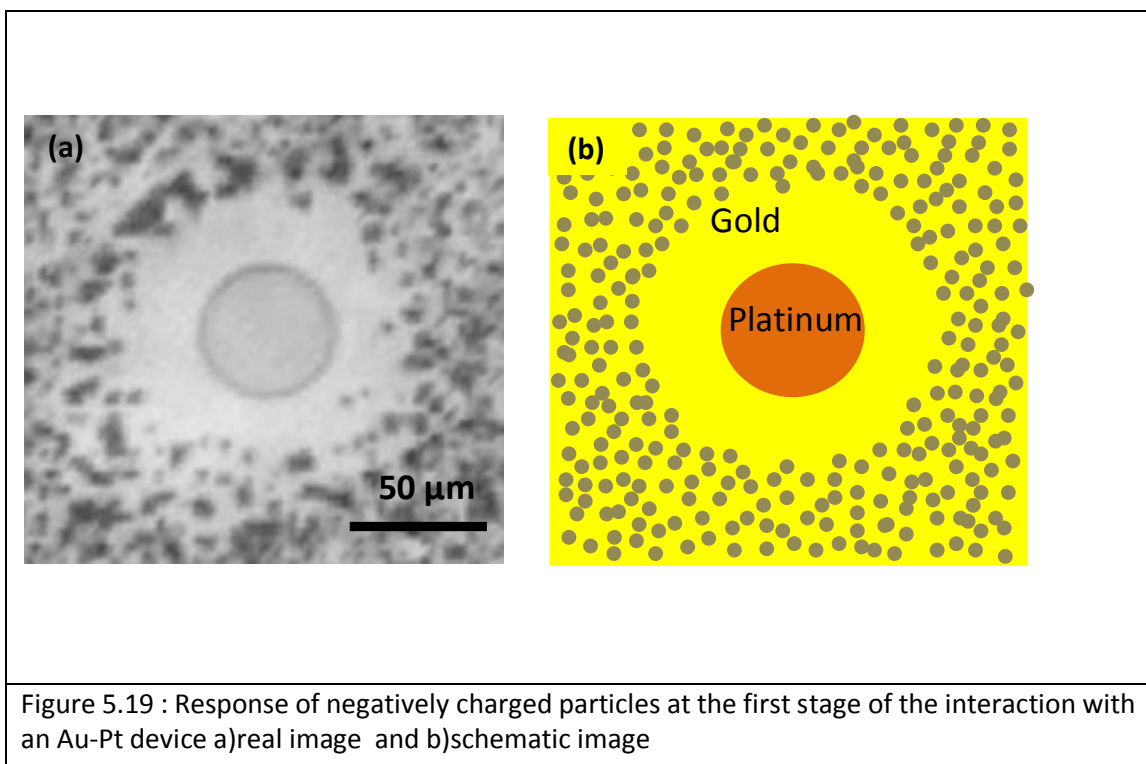


Figure 5.17: motion of positively charged tracers (P^+) toward a $40\ \mu\text{m} \times 40\ \mu\text{m}$ platinum square for pattern C at 1 wt% hydrogen peroxide solution. a) Schematic representation of tracers moving toward the square from elevations close to the surface ($Z=0\ \mu\text{m}$) and from $30\ \mu\text{m}$ higher level b). Tracking of P^+ tracers at level $Z=30\ \mu\text{m}$. c) Tracking of P^+ tracers at level $Z=0\ \mu\text{m}$. d) Average radial velocity (V_r) of P^+ tracers versus normalized distance to the square center in a 1 wt% hydrogen peroxide solution at heights of 0 and $30\ \mu\text{m}$. r and R_0 are the distances of particle from the disk center and half of side length of the square respectively. R_0 is $20\ \mu\text{m}$. The $\frac{r}{R_0}$ values are equal to 0 and 1 at the platinum disk center and platinum disk border respectively. Yellow area represents the area above the platinum disk. Overlap technique was applied to produce tracks.



5.3.c Negatively charged particles (P^-)

The interaction between negatively charged particles and Au-Pt exhibits a richness of different steps which will be deeply described in chapter 6. However in this section the first stage of interaction of the negative colloids with the Au-Pt system will be briefly described. It has been found at the first stage of the experiment that negatively charged particles do not move towards the Pt disk. They remained more than 20 μm away from its edge. A band without particles is formed around the disk due to the repulsion induced by the electric field. Figure 5.19 illustrates such behavior.



5.4 Electric field and fluid flow around Au-Pt devices

Extracting information about the direction and strength of the spontaneous electric field, velocity and direction of fluid flow from the motion of tracers was the next level of research.

Fluorescence microscopy showed the existence of a proton concentration gradient along the Au/Pt(figure 5.18 c). As mentioned, a higher concentration of protons was found at the gold surface and a depletion of protons at the platinum side. That suggests that gold surface acts as anode decomposing hydrogen peroxide to generate protons whereas platinum acts as the cathode consuming the protons. That is in line with the results of TAFEL measurements. The gradient of proton generation during the electrochemical reaction self-generates an electric field around the device. The electric field which points from the anode (gold) to the cathode

(platinum) induces the motion of fluid in the same direction by electro-osmosis. Figure 5.20 illustrates the electric field and fluid flow direction together with proton gradient generation. The motion of the colloidal tracers can probe the direction and strength of the electric field and fluid flow. The velocity of the particles has two contributions, one coming from the electrophoretic force of the particle (V_{eof}) and the other arisen from the fluid flow (V_f)

$$V_r(r) = V_{eof}(r) + V_f(r) \quad \text{Equation 5.10}$$

$V_r(r)$: Radial velocity of tracer toward platinum disk center at distance r from the disk center [m.s⁻¹]

$V_{eof}(r)$: Radial electrophoresis velocity of tracer toward platinum disk center at distance r from the disk center [m.s⁻¹]

$V_f(r)$: Radial velocity of liquid toward platinum disk center at distance r from the disk center [m.s⁻¹]

Considering equation 3.58 for the electrophoresis, equation 5.10 can be re-written as :

$$V_r(r) = \frac{\varepsilon \zeta_p}{\eta} E_r(r) + V_f(r) \quad \text{Equation 5.11}$$

$E_r(r)$: radial electric field strength at distance r from disk center [V.m⁻¹]

ζ_p : Zeta potential of a kind of tracer [V]

Quasi-neutral particle has low zeta potential. The electric field affects this kind of particles in a lesser extent than when using positively or negatively charged ones. Although electric field and fluid flow influence P° tracer motion toward platinum disk, the fluid flow term is more dominant⁷⁷. In this case, the P° tracers follow more the direction of fluid flow. Therefore the particle motion according to pattern C (figure 5.9a, pattern C) is a good approximation of solution flow around the platinum disk (figure 5.20 a).

⁷⁷ Just recall that the fluid velocity can be approached to the electro-osmosis equation

$V_f(r) = - \frac{\varepsilon \zeta_{surface}(r)}{\eta} E_r(r)$ and the zeta potential of the surface has a relevant influence. In this case the surface zeta potential is more negative than the one corresponding to the particle, which makes this term dominate over the electrophoretic term.

Unlike P° tracers, the electric field greatly affects the motion of P^+ tracers. The P^+ particles tend to follow electric field lines. In other words, motion pattern of P^+ could be an estimation of electric field lines (figure 5.20 a). Considering directionality coefficient (figure 5.10 b) and high tendency of positively charged tracers to go to the disk center, it can be claimed that the electric lines cross the disk center (figure 5.20 b). Moreover the negatively charged particles are also greatly affected by the electric field which makes them form a repulsion band around the Pt disk during their first stage of interaction with the device. These results suggest a built-up electric field pointing towards the Pt disk which is in line with TAFEL plot results and the fluorescence microscopy.

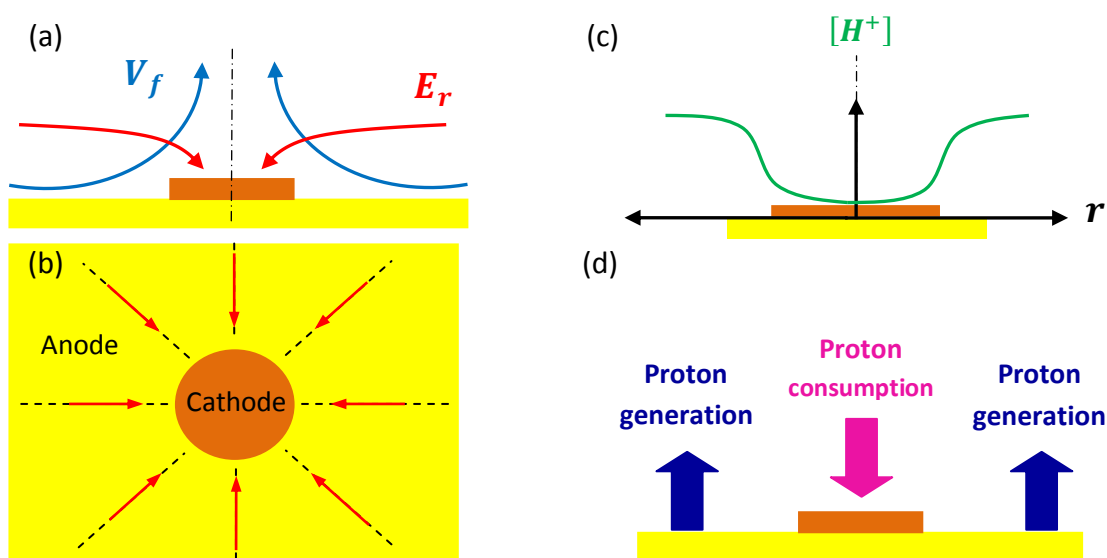


Figure 5.20: schematic illustration of a) electric field (E_r) and fluid flow (V_f) around the Au-Pt device b) electric field lines cross the disk center. Gold acts like anode and platinum as cathode. c) Proton concentration ($[H^+]$) distribution around Au-Pt device d) Proton generation and consumption on gold and platinum. r is the particle distance from the disk center.

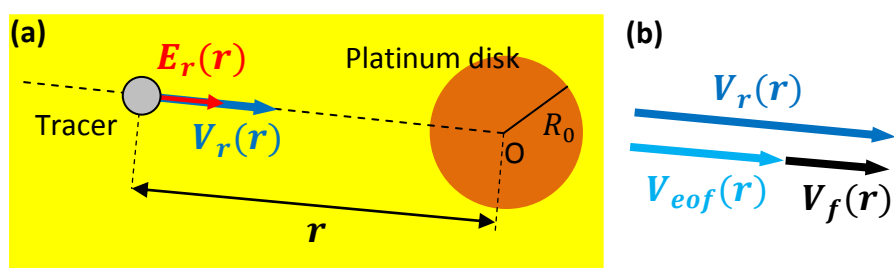


Figure 5.21: a) model for describing tracer motion toward platinum disk center due to presence of electric field and fluid flow. r and R_0 are the distances of the particle from the disk center and radius of platinum disk respectively. $E_r(r)$ is the radial electric field strength and $V_r(r)$ is the radial velocity of tracer toward platinum disk center at distance r from the disk center. b) Schematically illustration of the relation between total radial velocity ($V_r(r)$), radial electrophoresis velocity ($V_{eof}(r)$) and radial velocity of liquid ($V_f(r)$) of tracer toward

platinum disk center at distance r from the disk center.

For extracting the electric field strength and fluid flow, it is considered the velocity of P° and P^+ tracers according to equation 5.11 and the model of Figure 5.21.

Equation 5.11 can be written for P^+ (equation 5.12) and P° (equation 5.13) tracers:

$$V_r^{P^+}(r) = \frac{\varepsilon \zeta_{P^+}}{\eta} E_r(r) + V_f(r) \quad \text{Equation 5.12}$$

$$V_r^{P^\circ}(r) = \frac{\varepsilon \zeta_{P^\circ}}{\eta} E_r(r) + V_f(r) \quad \text{Equation 5.13}$$

$V_r^{P^+}(r)$: Radial velocity of P^+ tracer toward platinum disk center at distance r from the disk center [m.s^{-1}]

$V_r^{P^\circ}(r)$: Radial velocity of P° tracer toward platinum disk center at distance r from the disk center [m.s^{-1}]

ζ_{P^+} : Zeta potential of P^+ tracer [V]

ζ_{P° : Zeta potential of P° tracer [V]

$E_r(r)$ and $V_f(r)$ are extracted from equation 5.12 and 5.13, when $V_r^{P^+}(r)$ and $V_r^{P^\circ}(r)$ are available for certain distance r :

$$E_r(r) = \frac{\eta(V_r^{P^+}(r) - V_r^{P^\circ}(r))}{\varepsilon(\zeta_{P^+} - \zeta_{P^\circ})} \quad \text{Equation 5.14}$$

$$V_f(r) = \frac{\zeta_{P^+} \cdot V_r^{P^\circ}(r) - \zeta_{P^\circ} \cdot V_r^{P^+}(r)}{\zeta_{P^+} - \zeta_{P^\circ}} \quad \text{Equation 5.15}$$

Figure 5.22 presents the results of the calculation for $V_f(r)$ and $E_r(r)$ as a function of r . Both of them decrease as the distance from the disk center increases. The electric field and the fluid velocity at the edge of the Pt disk are about 280 V.m^{-1} and $6 \mu\text{m.s}^{-1}$, respectively. The electrostatic potential over the device can be calculated as per equation 3.1 (figure 5.23)

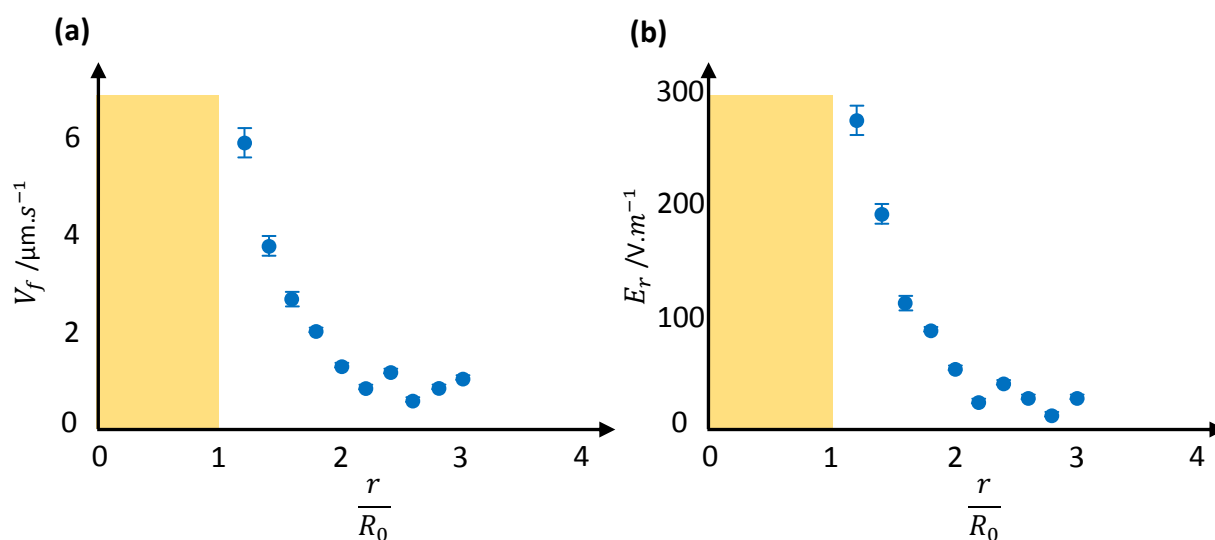


Figure 5.22: a) Radial velocity of liquid, b) radial electric field strength at distance r from disk center versus normalized distance to disk center at 1 wt% hydrogen peroxide solution. r and R_0 are the distances of the particle from the disk center and disk radius respectively. Disk radius (R_0) is 15 μm . The r/R_0 values are equal to 0 and 1 at the platinum disk center and platinum disk border respectively. Yellow area represents the area above the platinum disk.

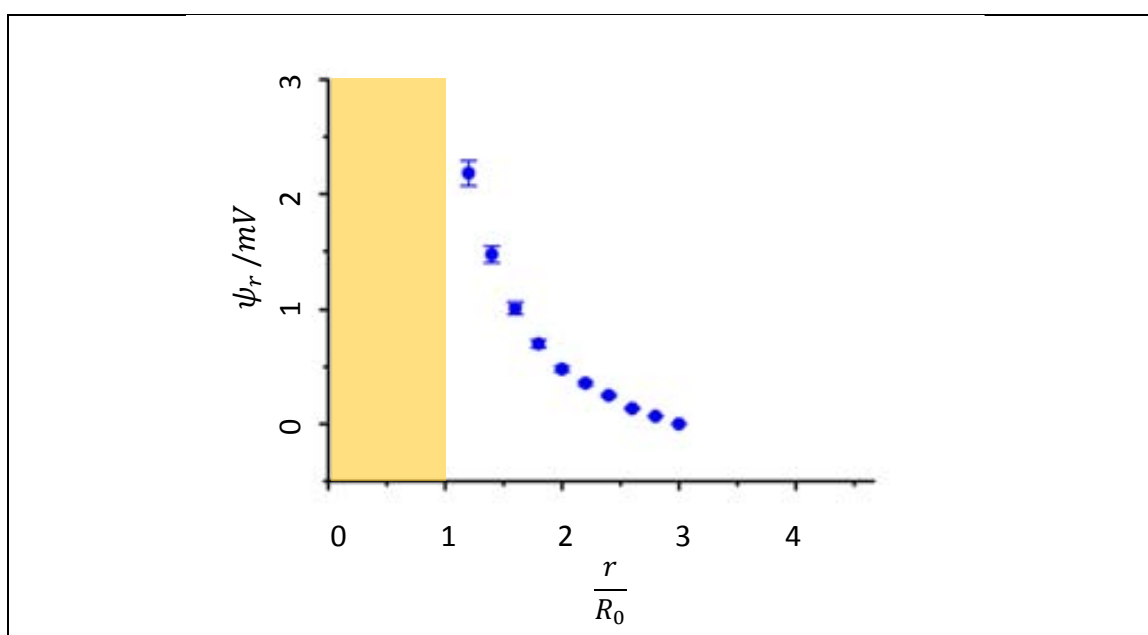


Figure 5.23: Radial electric potential at distance r from disk center versus normalized distance to disk center at 1 wt% hydrogen peroxide solution. r and R_0 are the distances of particle from the disk center and disk radius respectively. Disk radius (R_0) is 15 μm . The r/R_0 values are equal to 0 and 1 at the platinum disk center and platinum disk border respectively. Yellow area represents the area above the platinum disk

5.6 simulations

In order to complement and improve the understanding of the experimental data with the Au-Pt system finite element simulations were implemented using the Comsol Multiphysics software⁷⁸ version 4.4.

The studies were based on solving the coupled governing equations already introduced in Chapter 3, though they will be briefly revisited below:

A) Poisson equation for electrostatics:
$$\nabla^2 \psi = -\frac{\rho_f}{\varepsilon_r \varepsilon_0}$$

Where ε_r is the relative permittivity of the medium, ε_0 is the free space permittivity, ψ is the electrostatic potential, and ρ_f is the free volumetric charge density.

B) Navier–Stokes equation for fluid motion:
$$-\nabla P + \eta \nabla^2 \mathbf{u} - \rho_f \nabla \psi = 0$$

C) Fluid continuity equation:
$$\nabla \mathbf{u} = 0$$

Where \mathbf{u} is the fluid velocity, P is the pressure, η is the fluid viscosity, and the fluid is considered as incompressible.

D) Nernst-Planck equation for mass transport:
$$\nabla \left[n_i \mathbf{u} - D_i \nabla n_i - \frac{en_i z_i}{k_B T} D_i \nabla \psi \right] = 0$$

Where n_i is the number concentration of i^{th} specie, D_i is the diffusion coefficient of i^{th} specie, z_i is the valence of the i^{th} ionic specie including appropriate sign. The relation between diffusion coefficient of i^{th} specie and its mobility (μ_i) is defined through the Nernst–Einstein equation as $D_i = \mu_i RT$.

E) Electrochemical current at the anode (Gold):
$$j_{Au} = k_{Au} \cdot [H_2O_2]$$

F) Electrochemical current at the cathode (Platinum):
$$j_{Pt} = -k_{Pt} \cdot [H_2O_2] \cdot [H^+]^2$$

Where $[H_2O_2]$ and $[H^+]$ represent the concentration of hydrogen peroxide and protons respectively. k_{Au} and k_{Pt} are the rate constants for the anode and cathode respectively.

Figure 5.24 shows a scheme of the model used for the simulations which corresponds to a bimetallic micropump with axial symmetry and variable radius for both metallic structures. Only stationary studies (solutions) were performed corresponding to steady state conditions. In the simulations, four different charged species were considered: protons, hydroxide ions and the two ionic species of 1:1 salt. The presence of salt or extra ions was considered to have a more realistic approach. Very small concentration of ion impurities is unavoidably present in the system. Such extra ion impurities could come, for instance, from contamination during the fabrication and measurement of the pumps or from the CO_2 dissolved in the liquid. The following boundary conditions were defined for the electrostatic potential:

$$\psi_{z_{max}} = 0 \quad \text{Equation 5.16}$$

⁷⁸ COMSOL Inc. website: <http://www.comsol.com/>

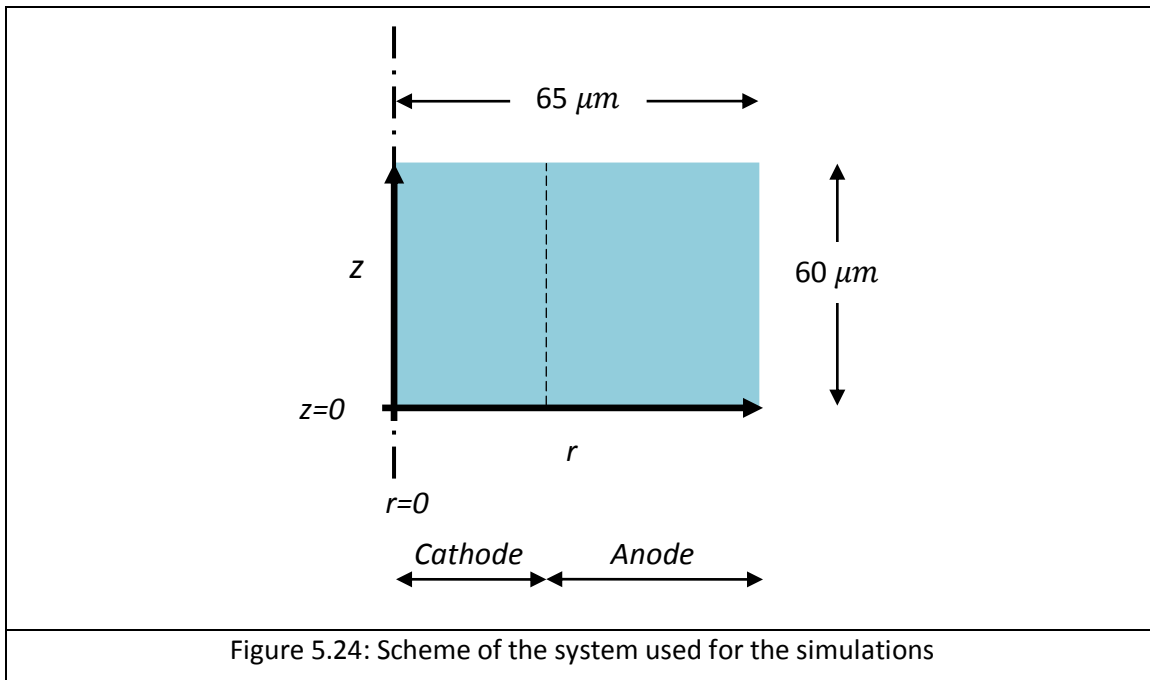
$$\psi_{z=0} = \psi_{substrate} \quad \text{Equation 5.17}$$

z_{max} : Upper boundary of the simulation system, typically placed at $60 \mu m$ above the surface

For the fluid velocity, stick boundary conditions were imposed on the substrate (fluid velocity is considered as zero.) and slip boundary conditions for elsewhere (the fluid can have non zero velocity.). For the concentrations of the different species, the bulk values were imposed at the upper boundary z_{max} . Table 5.2 contains the parameters applied in the numerical analysis.

| Parameter | Description | Value |
|----------------------------|---|---|
| | Proton diffusion coefficient | $9.3 \times 10^{-9} m^2 s^{-1}$ |
| D_{H^+} | Hydroxide ions diffusion coefficient | $5.3 \times 10^{-9} m^2 \cdot s^{-1}$ |
| pH | pH at the bulk | 6.25 |
| ψ_{Pt} | Surface potential of the platinum | -0.033 V |
| ψ_{Au} | Surface potential of the gold | -0.033 V |
| k_{Pt} | Constant rate of the platinum | 0.01 $m^7 \cdot s^{-1} \cdot mol^{-2}$ |
| k_{Au} | Constant rate of the gold | $4.11 \cdot 10^{-10} m \cdot s^{-1}$ |
| $[H_2O_2]$ | H_2O_2 concentration | 0.3M (1% wt) |
| R_0 | Radius of the platinum disk | $15 \mu m$ |
| R_{Au} | Radius of gold ring | $50 \mu m$ |
| $[A^+] \text{ and } [B^-]$ | Monovalent ions concentration | $1.6 \mu M$ |
| $D_1 \text{ and } D_2$ | Diffusion coefficient of the additional ionic species | $1.0 \times 10^{-9} m^2 \cdot s^{-1}$ |

The rate constants for gold and platinum and the concentration of the salt (monovalent ions) were taken as fitting parameters and the values reported are the ones which achieved the best agreement between data and simulations. The pH at the bulk was measured and the surface potential of the metal substrate (considered to be uniform between Au and Pt) was estimated in 5.4. . The rest of the values were known.



5.5.1 Results and Discussion

As per model explained in 5.3, the electric field is self-generated from the electrochemical decomposition of hydrogen peroxide at the two metallic surfaces. One of metal acts as anode and the other one performs the role of cathode.

In such process an electric field is self-generated and a proton flow is produced from the anode to the cathode. That induces the fluid motion. Therefore, the electric field, fluid flow, charge density, proton flow, proton concentration and pH are the most important electrokinetic variables in this system. These variables were subjected to the simulation process. The results are as follow:

5.5.1 a Electric field

Figure 5.25a shows the map of the electric field distribution. The simulation confirms the experimental findings. The electric field points from the anode (gold surface) towards the cathode (platinum disk). The electric field becomes intense near the disk edge. Far from the disk center ($55\mu\text{m} < r < 65\mu\text{m}$), the electric field has a relatively low magnitude and its direction is approximately perpendicular to the surface. Figures 5.26 and 5.27 show the experimental and simulation data for the radial electric field and electric potential plotted as a function of the radial distance from the disk center. The simulations can reproduce the electric potential and both the magnitude and the spatial dependency of the electric field.

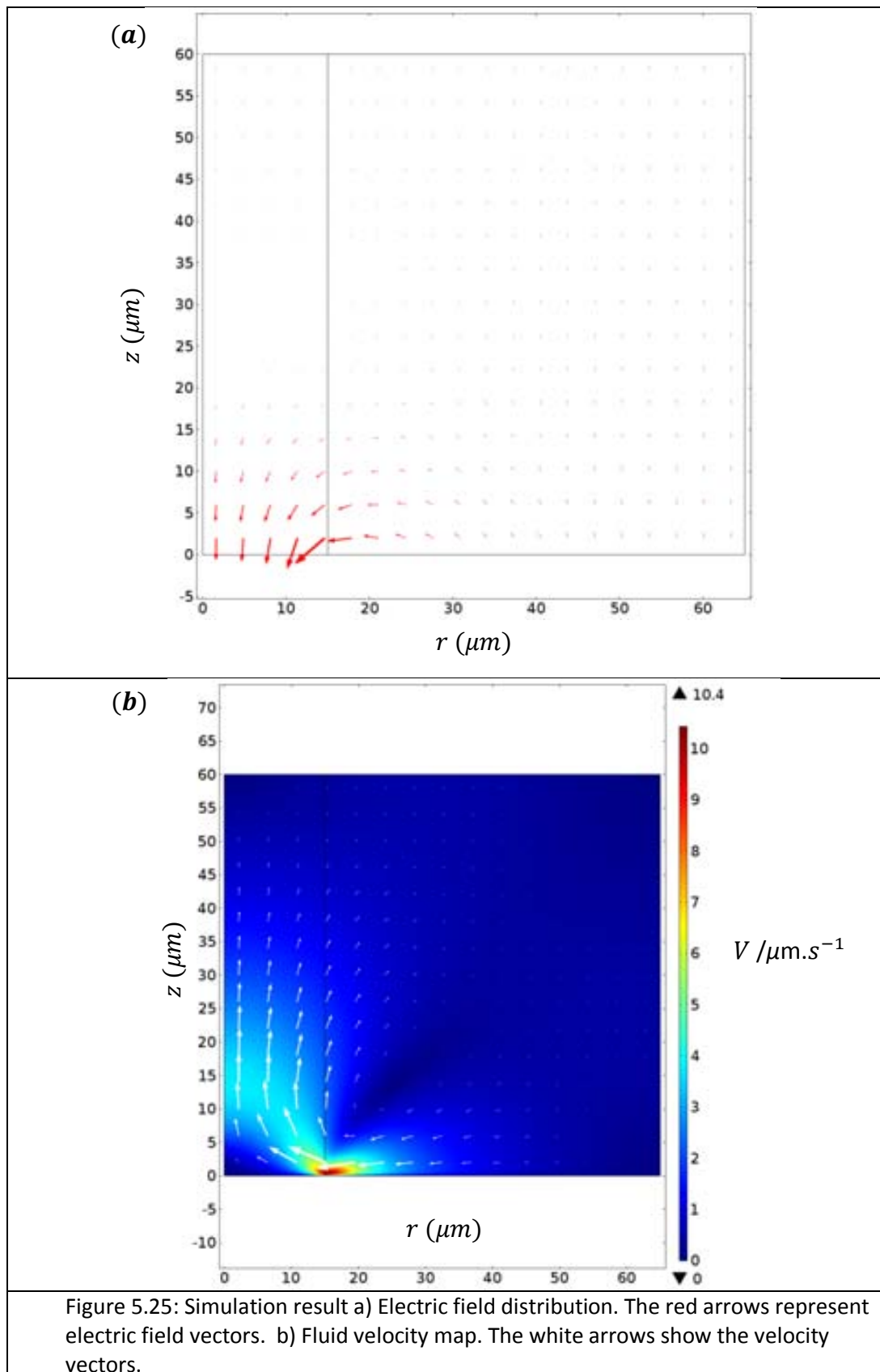


Figure 5.25: Simulation result a) Electric field distribution. The red arrows represent electric field vectors. b) Fluid velocity map. The white arrows show the velocity vectors.

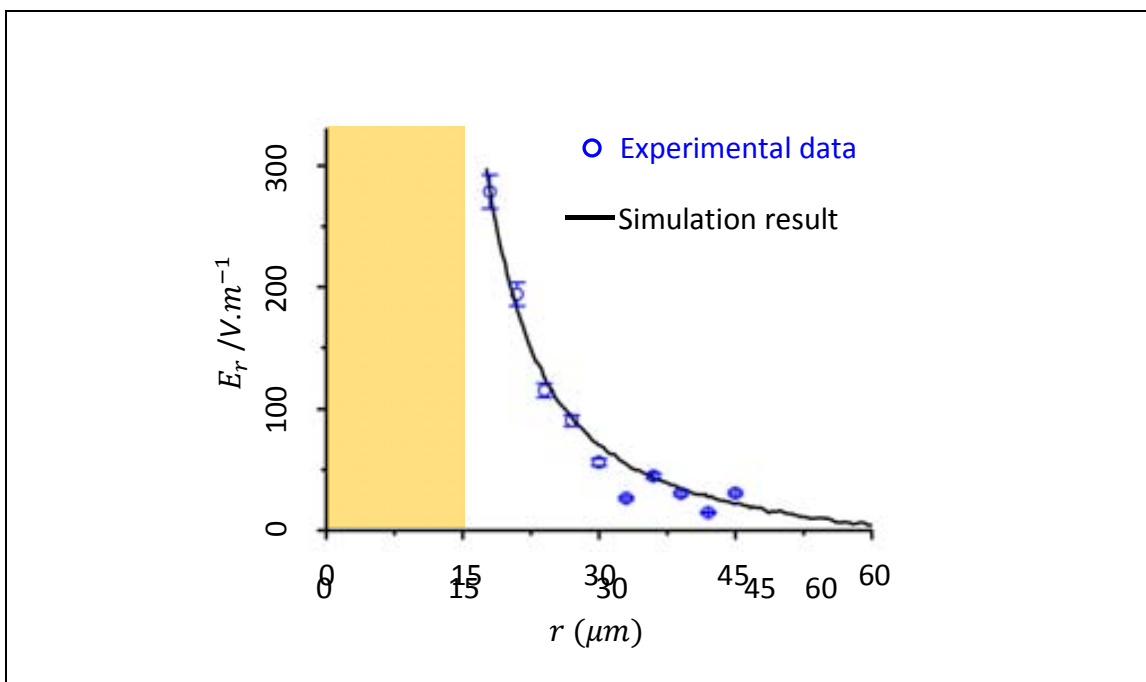


Figure 5.26: Experimental and simulation results of the radial electric field versus radial distance from the disk center over the Au-Pt device. The black line represents the simulation result and the blue circles are experimental data. Yellow area represents the area above the platinum disk.

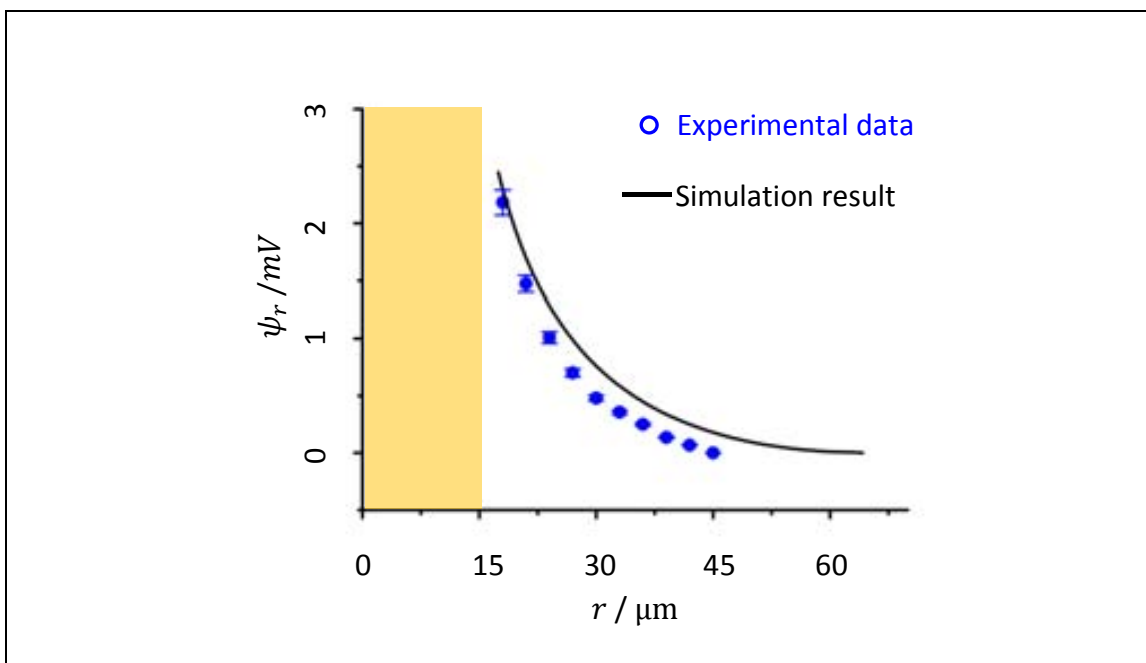
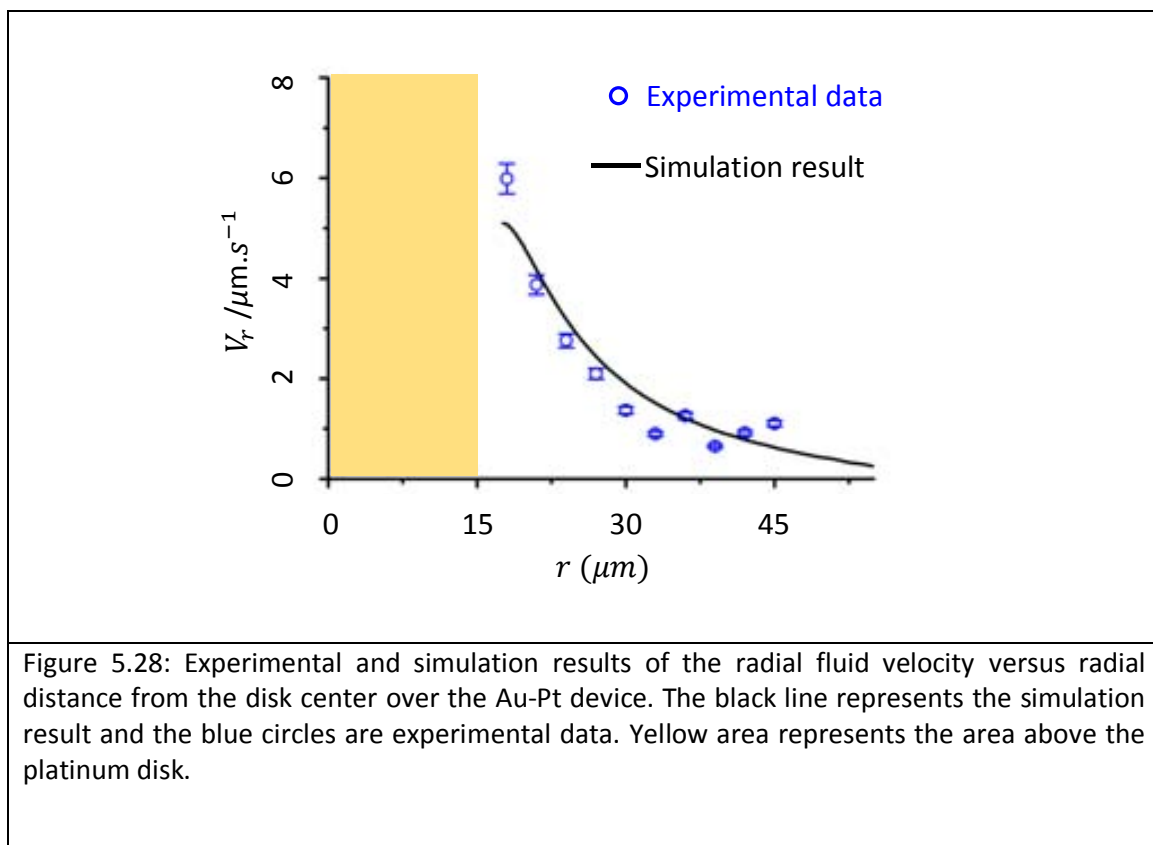


Figure 5.27: Experimental and simulation results of the radial electric potential versus radial distance from the disk center over the Au-Pt device. The black line represents the simulation result and the blue circles are experimental data. Yellow area represents the area above the platinum disk.

5.5.1 b Fluid flow

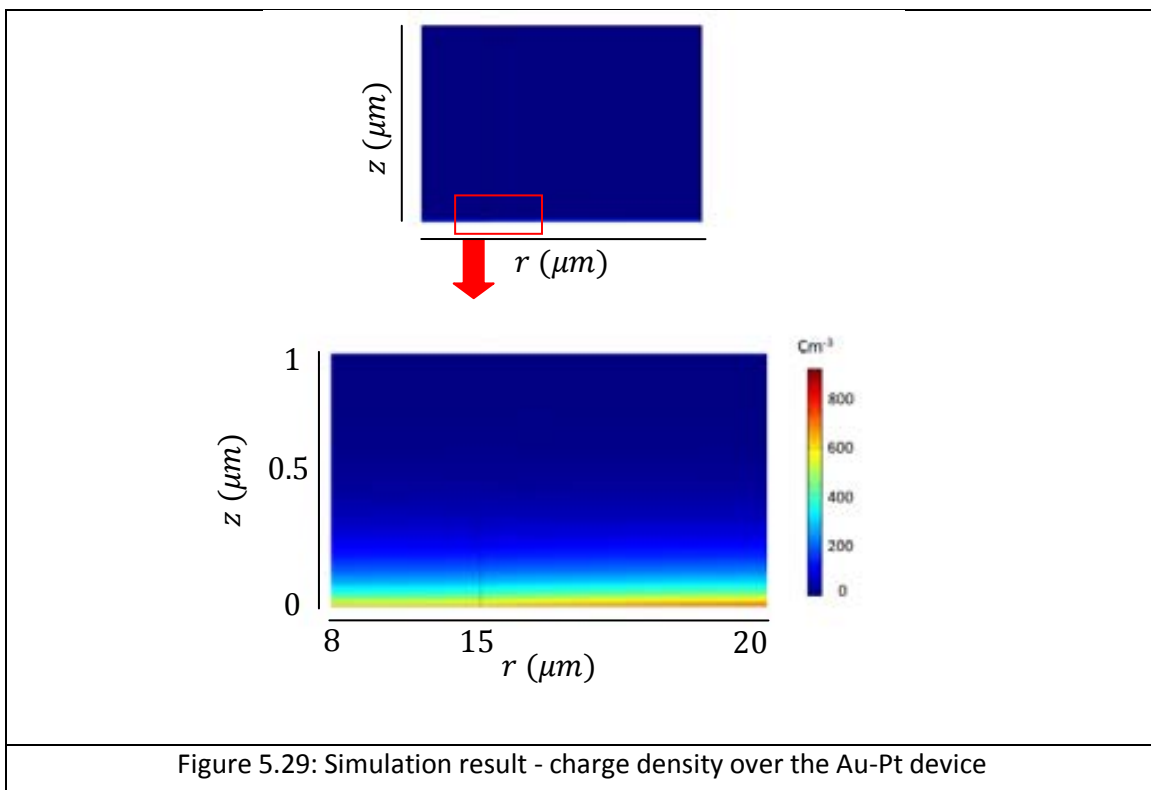
Regarding the fluid flow, the fluid moves towards the platinum disk (figure 5.25 b). The radial pumping velocity is maximal near the platinum disk edge. After crossing the platinum-gold border, the fluid changes its direction of motion to the direction perpendicular to the disk surface due to fluid continuity. The fluid is pumped upwards near the disk center.

Figure 5.28 shows the good agreement between the experimental and simulation data for the fluid velocity plotted as a function of the radial distance from the disk center.



5.5.1 c Charge density

The 2D Map of the charge density is demonstrated in figure 5.29 . A net positive charge is confined inside the double layer which has a thickness of about 200 nm. It can also be observed that the charge distribution inside the double layer is asymmetric along the radial distance. More positive charge is accumulated on the anode as compared to the cathode. This simulation result is in line with the experimental results which show generation of protons at the anode and proton consumption at the cathode. Figure 5.29 shows clearly that charge density of fluid above the double layer is equal to zero. It means the fluid is electroneutral. It is necessary to emphasize that the electric field on the parts with charge density equal to zero, is not equal to zero.



5.5.1 d Proton concentration, pH and proton flow

Investigating about proton concentration and proton flow is one of the interesting parts of the simulations. Figure 30.a shows the top view map of proton concentration over the Au-Pt device at a distance from the surface equal to $2 \mu\text{m}$. It shows the existence of higher concentration of protons on the anode (gold surface) as compared with the cathode (platinum surface). The simulation result is in agreement with the experimental data obtained from fluorescence microscopy (figure 5.31).

Figure 5.30b shows a 2D map of pH of the system as a function of the height between the surface and 60 . Just close to the metallic surfaces, the pH on the anode (gold surface) is less than on the cathode (platinum). However, at larger heights from the metallic surface, the pH tends to the bulk values (pH=6.25). The simulated radial profile of the pH together with the experimental data shows the nice agreement between them (figure 5.32).

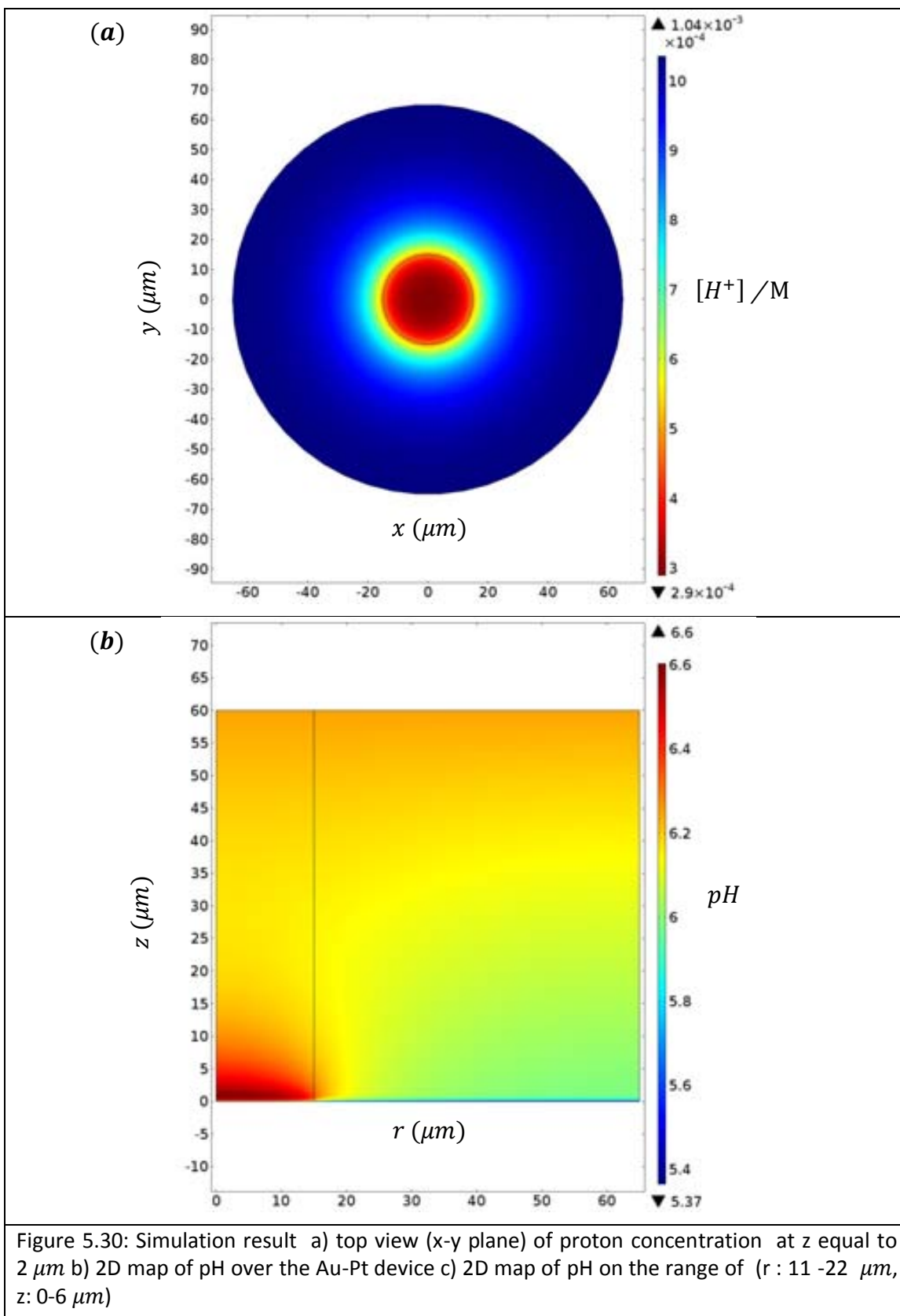


Figure 5.30: Simulation result a) top view (x-y plane) of proton concentration at z equal to $2 \mu m$ b) 2D map of pH over the Au-Pt device c) 2D map of pH on the range of $(r : 11 - 22 \mu m, z : 0 - 6 \mu m)$

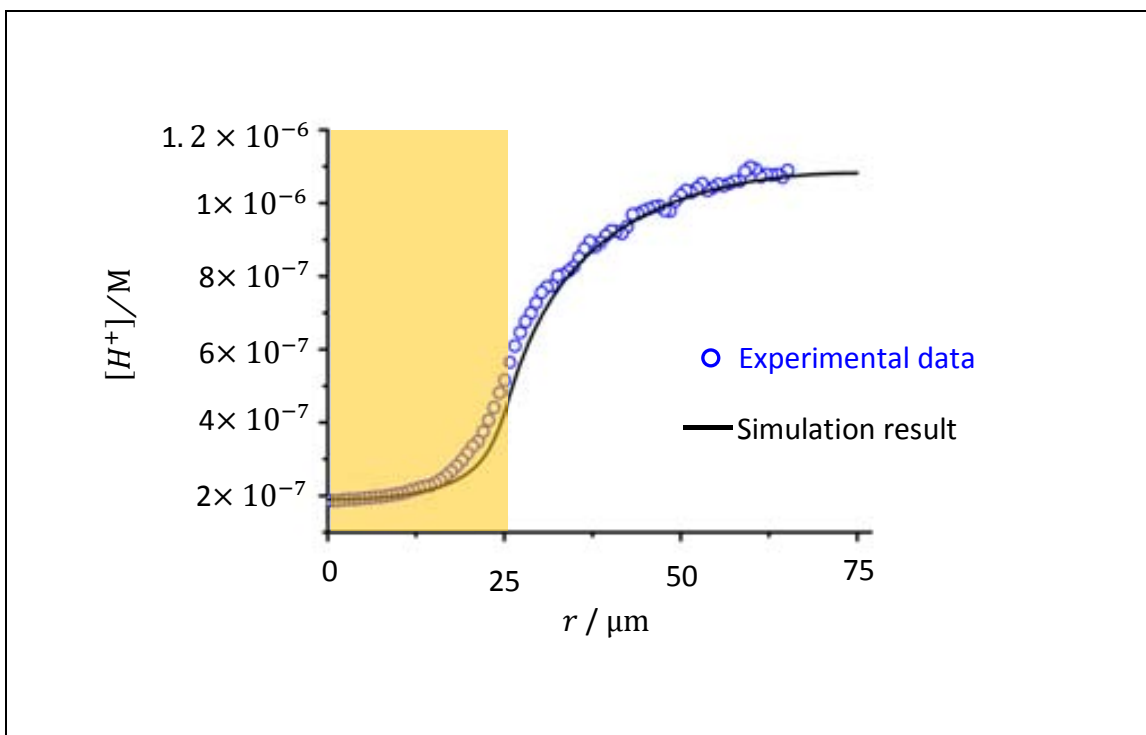


Figure 5.31: Experimental and simulation results of the proton concentration versus radial distance from the disk center over the Au-Pt device. The black line represents the simulation result and the blue circles are experimental data. Yellow area represents the area above the platinum disk.

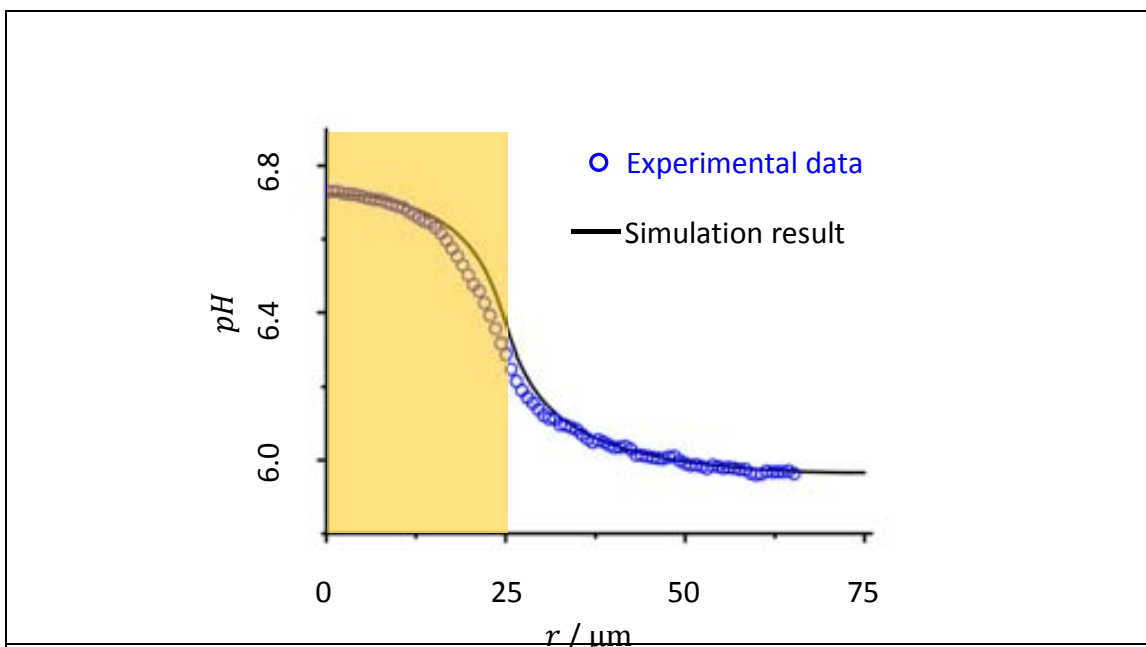


Figure 5.32: Experimental and simulation result of pH versus radial distance from the disk center over the Au-Pt device. The black line represents the simulation result and the blue circles are experimental data. Yellow area represents the area above the platinum disk.

The overlap of the electric field and proton flow is presented on figure 5.33. The protons move in the same direction as the electric field (from the anode to the cathode). The motion of protons beyond the electric double layer self-generates an electric field in which the electric field vectors coincide with the flow of protons. The generation of the electric field of moving charged species can be related to Ohm 's law [16]:

$$E = \frac{j}{k_f} \quad \text{Equation 5.18}$$

j : The current of the species [$A \cdot m^{-2}$]

k_f : The conductivity of the fluid [$kg^{-1} \cdot m^{-3} \cdot s^3 A^2$]

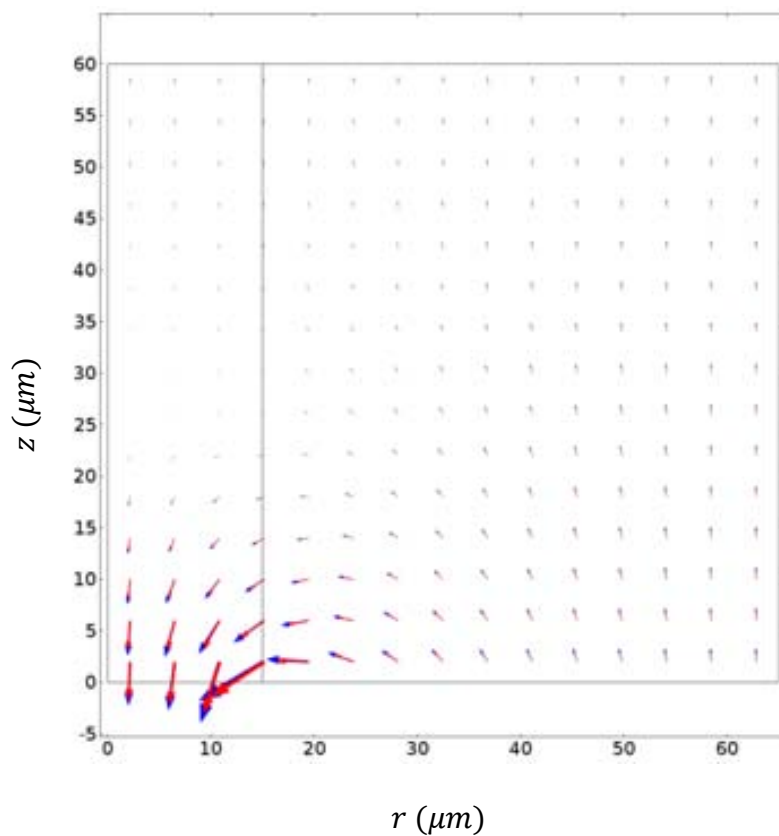


Figure 5.33: Simulation result - the electric field distribution (red arrows) and the local flow of protons (blue arrows)

5.6 Conclusions

In this chapter the Au-Pt micropump has been characterized to extract quantitative information of the spatial dependence of the electrokinetic parameters involved in the catalytic actuation. First of all the importance of the surface treatment to enhance the catalytic reactions and trigger the electrokinetic process was addressed. Then two complementary approaches have been used to evaluate the electrokinetic parameters: one based on confocal fluorescence microscopy with fluorescent pH indicators and the other one based on the motion of differently charged colloidal tracers.

The first experimental tool allows the 2D imaging and quantification of the proton gradient generation around the Au-Pt device as a consequence of the electrochemical reactions. This technique provided information of the redox role of the gold and platinum. It was found a higher concentration of protons on the gold side and proton concentration depletion at the platinum surface. That suggests that gold surface acts as the anode producing protons and the platinum as the cathode consuming the protons which was in line with the predictions of TAFEL measurements. Thus, the electrochemical reaction can self-generate an electric field pointing from the gold to the platinum. Quantification of such gradient showed that during the catalytic process the pH is changed about one unit along the Au/Pt device. The spatial imaging and quantification of this relevant parameter constitutes the first reported study in the field of catalytic motors and can be a source of inspiration to address similar experimental challenges in a wide range of electrochemical systems.

On the other side, differently charged colloidal tracers allowed mapping and quantifying the spatial distribution of the electric field and fluid flow due to the interaction of their charge with the self-generated electric field. It has been found that the electric field strength and the fluid velocity are maximal just at the Au/Pt border. The findings also confirm an electric field pointing toward the Pt.

The experimental data have been supported with numerical simulations that can reproduce the experimental results. By comparing the experimental findings to numerical simulations it was possible to estimate the concentration of extra ions that are unavoidably present in the catalytic pumps and the constant rates of the electrochemical reactions at the anode and cathode. The simulations have shown that due to the chemical reaction a net positive charge was confined inside the double layer with a charge distribution asymmetry along the radial distance. Such asymmetry can induce an electric field. However the existence of the electric field can be extended above the electric double layer at distances in which the fluid is electroneutral. That could be explained as a consequence of the motion of protons from the anode to cathode beyond the double layer. All these results contribute to build a better understanding of the chemomechanical actuation of the catalytic pumps

References:

- [1] J. J. Blackstock, D. R. Stewart, and Z. Li, "Plasma-produced ultra-thin platinum-oxide films for nanoelectronics: physical characterization," *Applied Physics A*, vol. 80, pp. 1343-1353, 2005/03/01 2005.
- [2] P. Fuchs, K. Marti, and S. Russi, "Materials for mass standards: long-term stability of PtIr and Au after hydrogen and oxygen low-pressure plasma cleaning," *Metrologia*, vol. 49, p. 615, 2012.
- [3] F. Parmigiani, E. Kay, and P. S. Bagus, "Anomalous oxidation of platinum clusters studied by X-ray photoelectron spectroscopy," *Journal of Electron Spectroscopy and Related Phenomena*, vol. 50, pp. 39-46, // 1990.
- [4] C. Peter and S. Naoko, "Stability of reference masses V: UV/ozone treatment of gold and platinum surfaces," *Metrologia*, vol. 50, p. 27, 2013.
- [5] H. Tsai, E. Hu, K. Perng, M. Chen, J.-C. Wu, and Y.-S. Chang, "Instability of gold oxide Au₂O₃," *Surface Science*, vol. 537, pp. L447-L450, 7/1/ 2003.
- [6] C. R. Brundle, C. A. Evans, and S. Wilson, *Encyclopedia of Materials Characterization: Surfaces, Interfaces, Thin Films*: Butterworth-Heinemann, 1992.
- [7] P. van der Heide, *X-ray Photoelectron Spectroscopy: An introduction to Principles and Practices*: Wiley, 2011.
- [8] A. I. Stadnichenko, S. V. Koshcheev, and A. I. Boronin, "Oxidation of the polycrystalline gold foil surface and XPS study of oxygen states in oxide layers," *Moscow University Chemistry Bulletin*, vol. 62, pp. 343-349, 2007/12/01 2007.
- [9] J. Xu, X. Liu, Y. Chen, Y. Zhou, T. Lu, and Y. Tang, "Platinum-Cobalt alloy networks for methanol oxidation electrocatalysis," *Journal of Materials Chemistry*, vol. 22, pp. 23659-23667, 2012.
- [10] Y. Wang, R. M. Hernandez, D. J. Bartlett, J. M. Bingham, T. R. Kline, A. Sen, *et al.*, "Bipolar Electrochemical Mechanism for the Propulsion of Catalytic Nanomotors in Hydrogen Peroxide Solutions[†]," *Langmuir*, vol. 22, pp. 10451-10456, 2006/12/01 2006.
- [11] W. F. Paxton, S. Sundararajan, T. E. Mallouk, and A. Sen, "Chemical Locomotion," *Angewandte Chemie International Edition*, vol. 45, pp. 5420-5429, 2006.
- [12] W. F. Paxton, A. Sen, and T. E. Mallouk, "Motility of Catalytic Nanoparticles through Self-Generated Forces," *Chemistry – A European Journal*, vol. 11, pp. 6462-6470, 2005.
- [13] W. F. Paxton, P. T. Baker, T. R. Kline, Y. Wang, T. E. Mallouk, and A. Sen, "Catalytically Induced Electrokinetics for Motors and Micropumps," *Journal of the American Chemical Society*, vol. 128, pp. 14881-14888, 2006/11/01 2006.
- [14] T. R. Kline, W. F. Paxton, Y. Wang, D. Velegol, T. E. Mallouk, and A. Sen, "Catalytic Micropumps: Microscopic Convective Fluid Flow and Pattern Formation," *Journal of the American Chemical Society*, vol. 127, pp. 17150-17151, 2005/12/01 2005.
- [15] T. R. Kline, J. Iwata, P. E. Lammert, T. E. Mallouk, A. Sen, and D. Velegol, "Catalytically Driven Colloidal Patterning and Transport," *The Journal of Physical Chemistry B*, vol. 110, pp. 24513-24521, 2006/12/01 2006.
- [16] S. Friedlander and D. Serre, *Handbook of Mathematical Fluid Dynamics*: Elsevier, 2003.

Chapter 6

Introduction

One of the potential applications of the self-generated electrohydrodynamic process at catalytic pumps can be the local patterning formation of hierarchical assemblies without the need of a lithographic mask [1,2]. Nowadays, autonomous dynamic self-assembly represents a topic of huge research interest. Impressive examples of dynamic self-assembly have been also shown with catalytic self-propelled nanomotors which represent a rich framework for understanding microscopic interactions and emergent collective dynamics [3-9].

These out-of equilibrium processes fed by an internal energy have a great potential to create novel multifunctional or dynamic architectures not possible in other conditions. They could bring promising applications in many technological fields [6, 9, 10-15] (e.g. nanophotonics, smart (bio) chemical sensing, catalysis, matter transport and separation, etc.).

Catalytic pumps become ideal systems to trigger guided self-assembly of matter to determined locations and represent an important alternative to other more traditional methods which use external energy injection [16-27]. Recently there have been some attempts to guide colloidal crystallization using similar concepts with galvanic microreactors made of a gold electrode together with a sacrificial copper electrode [28-30]. The dissolution of copper and the reduction of oxygen at the gold electrode induce electronic and ionic current at the metal and electrolyte interface respectively which turn on electrohydrodynamic processes.

In this chapter Au-Pt catalytic pumps immersed in hydrogen peroxide will be used to study colloidal transport and self-organization far from equilibrium powered by the internal chemical decomposition of the fuel. The colloids will be guided by the local chemical-driven electrohydrodynamic forces and by the interaction of the zeta potential of the colloids with such electrohydrodynamic forces. The patterning process will be followed in real time and will be evaluated using either negatively or positively charged particles. It will be shown that negatively charged particles can selectively pattern the gold regions forming a 2D ordered colloidal crystal starting from the Pt edges. The in-situ colloidal self-assembly bears an impressive resemblance to Tetris video game [31]. The self-assembly process with negative particles also comprises unexpected features provided by the local change of the colloidal zeta potential due to the catalytic reaction.

On the other hand, positively charged particles could build a colloidal pattern on the Pt regions characterized by a more 3D and not as ordered growth.

6.1 Pattern formation with negatively charged particles

When a Au-Pt device is exposed to 1 % hydrogen peroxide solution containing negatively charged particles (P^-), the tracers are primarily repelled from the platinum disk (figure 6.1) as discussed in chapter 5. Figure 6.1 shows the electrostatic repulsion areas, repulsive bands,

around different size platinum disks in presence of high concentration of P^- tracer. There is no tracer in the repulsive bands. However, the repulsion band is not permanent. Figure 6.2 shows the different stages of the process evolution. After the initial repulsion, silica spheres (P^- tracers) form two-dimensional close-packed clusters outside of the repulsion band. Then these clusters together with singlet silica immediately start moving towards the platinum disk and stop at the edge of the disk. As more clusters arrive at the platinum edge, the dynamics of 2D silica crystallization can be monitored in real time. Real-time monitoring of colloidal self-assembly at the disk edge is one of most important achievements provided with the applied experiment set-up

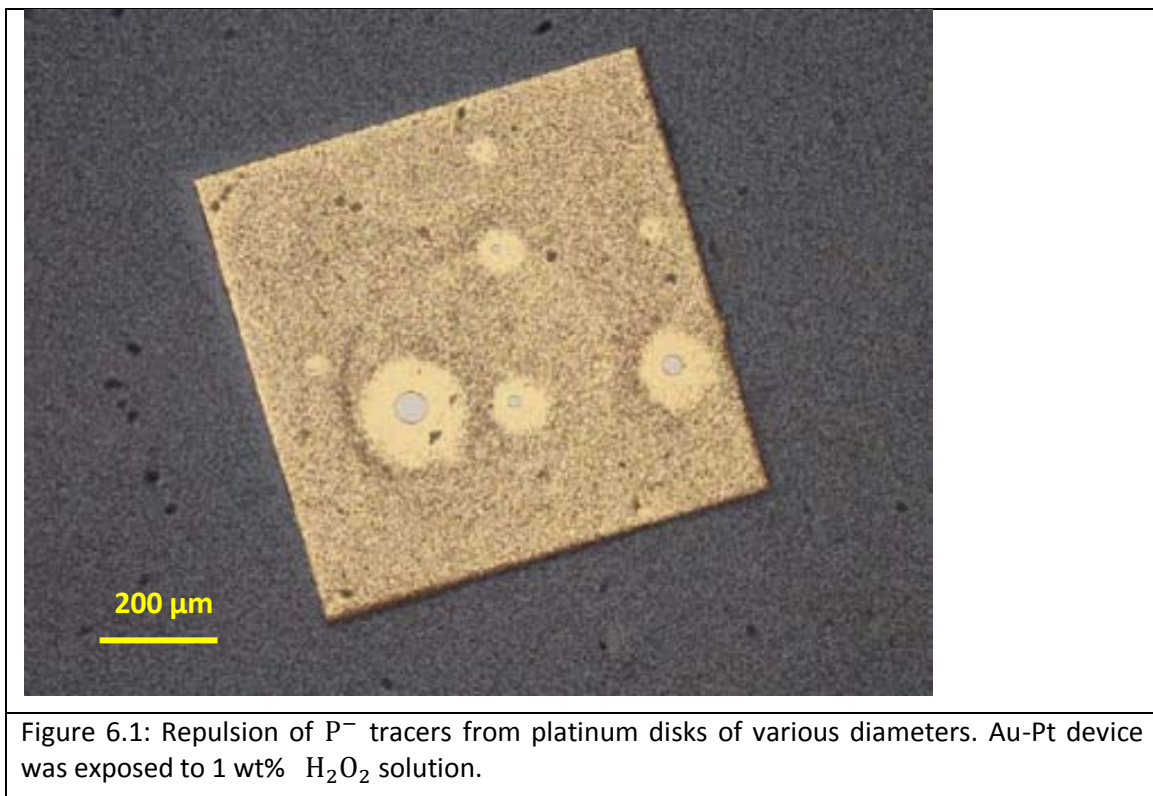
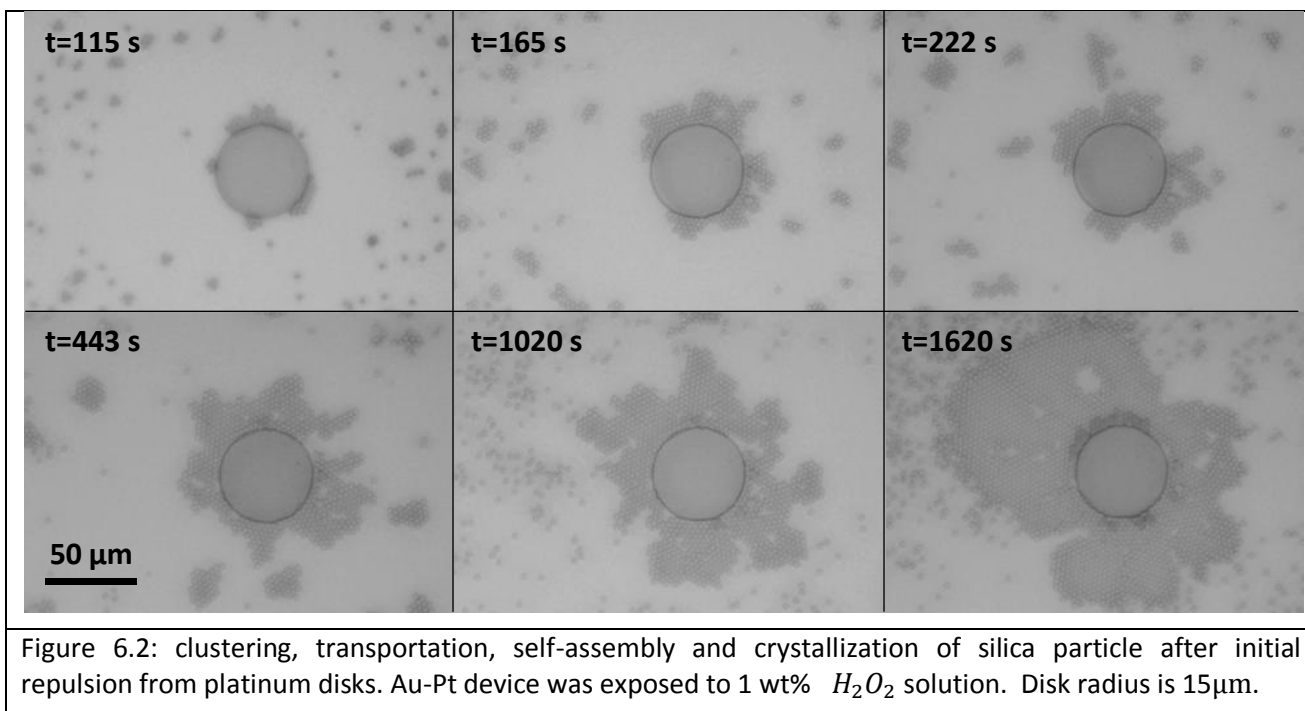


Figure 6.1: Repulsion of P^- tracers from platinum disks of various diameters. Au-Pt device was exposed to 1 wt% H_2O_2 solution.



6.2 Sequential stages in the patterning process

The colloidal self-assembly of negatively charged particles can be summarized in the following steps: electrostatic repulsion, clustering formation beyond the repulsive band, cluster transportation to the Pt disk edge, silica patterning formation at the Pt disk edge (figure 6.3)

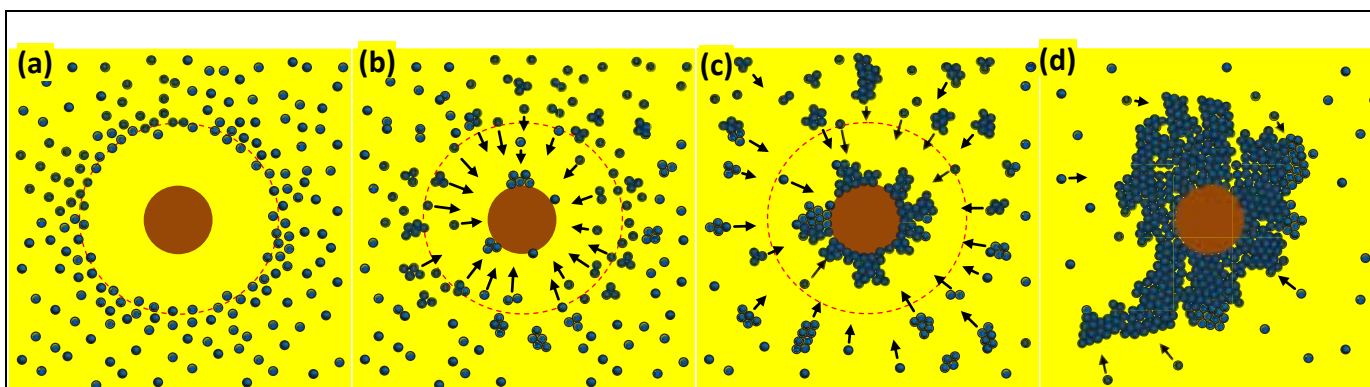


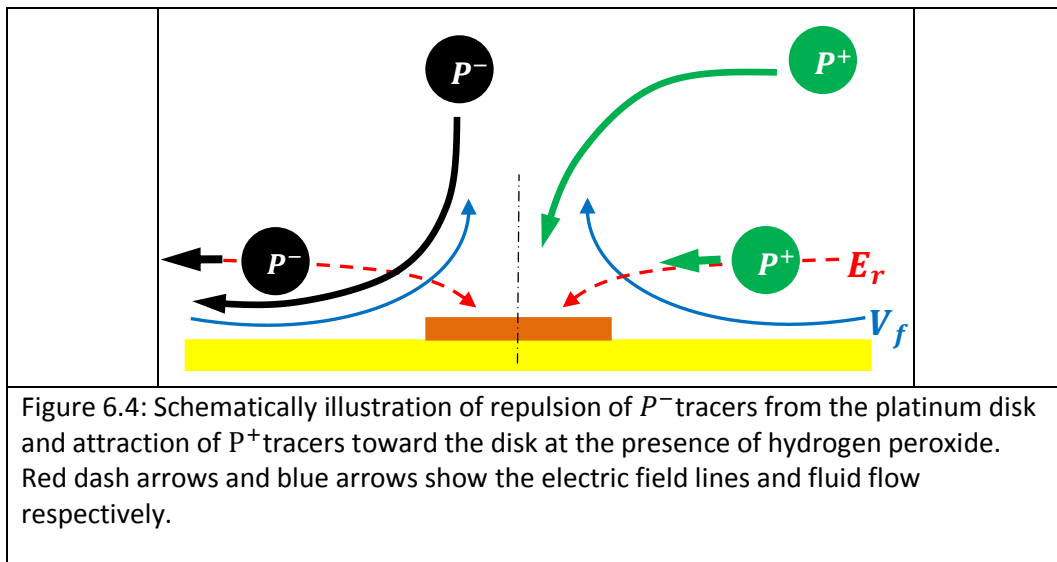
Figure 6.3 schematically illustration of time line of the interaction between Au-Pt device and negatively charged particles a) electrostatic repulsion and formation of repulsive band, b) clustering formation beyond the repulsive band, c) cluster and singlet transportation toward the disk, pattern formation on the Pt disk edge, d) growth of silica crystal at the Pt disk edge. Red dash line represents the area from which the tracers were repulsed primarily. Black arrows show the direction of motion of particle(s) or clusters.

6.2.a Electrostatic repulsion

Primary interaction of negatively charged tracers and electric field and fluid flow around Au-Pt device is electrostatic repulsion of tracers from the platinum disk (figure 6.3.a). Repulsion generates a free particle region on the Pt disk and on a band around the platinum disk at the gold side. The electrostatic repulsion also affects particles coming from high z distances above the platinum disk. When these particles move down closer to the Pt structure, they experience the electrostatic force that expelled them outside the region where the repulsion band is formed.

The d_c is defined as the width of repulsive band. The initial electrostatic repulsion of the negatively charged tracers is the expected behavior in presence of hydrogen peroxide.

The model described in 5.3 can explain the behavior of P^- tracers. In contrast to P^+ tracers, the P^- tracers with relatively large negative charge moves in opposite direction of electric field and fluid flow (figure 6.4). Figure 6.4 illustrates the interaction of differently charged tracers with Au-Pt device in presence of hydrogen peroxide.



In order to estimate the width of the repulsive band it will be used the velocity equation already introduced in section 5.3 (chapter 5) applied to the negative tracers (equation 6.1).

$$V_r^{P^-}(r) = \frac{\varepsilon \zeta_{P^-}}{\eta} E_r(r) + V_f(r) \quad \text{Equation 6.1}$$

$V_r^{P^-}(r)$ represents the repulsion velocity of the negative tracer and can be estimated by using the electric field and fluid velocity of the Au-Pt system as a function of the radial distance which were extracted in chapter 5 and the zeta potential of P^- (also listed in such chapter).

For estimating the width of the repulsive band (d_c) with equation 6.1, it will be considered another parameter, r_c . This parameter represents the distance from the disk center at

which the velocity of a repelled P^- tracer becomes zero. The relation between d_c and r_c is as follows:

$$r_c = R_0 + d_c \quad \text{Equation 6.2}$$

R_0 : Radius of platinum disk [m]

Considering the definition of r_c , the particle velocity is zero:

$$V_r^{P^-}(r_c) = 0 \quad \text{Equation 6.3}$$

Considering equation 6.1, equation 6.3 can be written as:

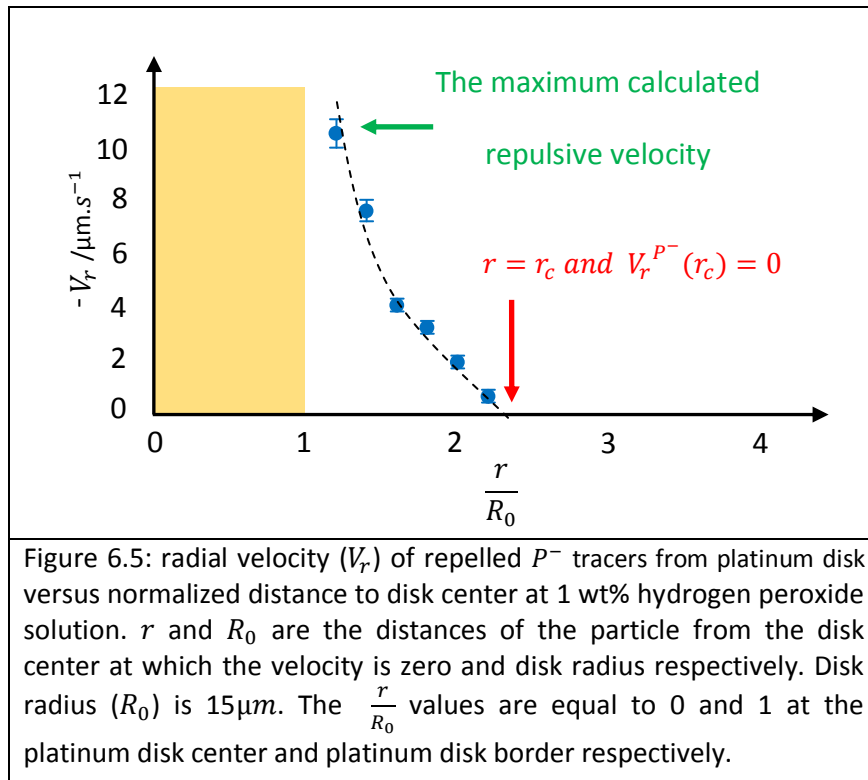
$$\frac{\varepsilon \zeta_{P^-}}{\eta} E_r(r_c) + V_f(r_c) = 0 \quad \text{Equation 6.4}$$

Solving equation 6.4 provides the approximated value of r_c . Figure 6.5 shows the radial velocity of repelled P^- tracers from the platinum disk versus normalized distance to disk center at 1 wt% hydrogen peroxide solution. The maximum calculated repulsive velocity is $10.56 \pm 0.25 \mu\text{m}\cdot\text{s}^{-1}$ at $\frac{r}{R_0} = 1.20$ (indicated on figure 6.5). The velocity decreases as the traces get away from the disk. It is estimated that the velocity becomes zero at $\frac{r_c}{R_0} = 2.40 \pm 0.3$ for the disk with $15 \mu\text{m}$ radius. Therefore, the d_c is:

$$d_c \cong 1.4R_0 \pm 0.3R_0 \quad \text{Equation 6.5}$$

Or:

$$d_c \cong 21 \pm 4.5 \mu\text{m} \quad \text{Equation 6.6}$$



The measurements showed the width of the repulsive band for a platinum disk with $15\mu m$ radius in terms of r_c and d_c were $34 \pm 1\mu m$, $19 \pm 1\mu m$ respectively. The experimental results are close to what the model predicts.

It has also been observed that during the initial repulsion the particle tracers are more concentrated just in the region close to the repulsive band as compared to other areas far away from the disk which are not under the influence of the electric field and fluid flow.

6.2.b Clustering formation outside the repulsive band

After initial repulsion, the cluster formation occurs. The clustering formation just outside of the repulsion band could be explained by considering the simultaneous action of different factors.

These factors are:

- 1- Generation of protons on the gold surface as described in chapter 5
- 2- The co-action of two opposite forces: the electrostatic repulsion and the fluid flow

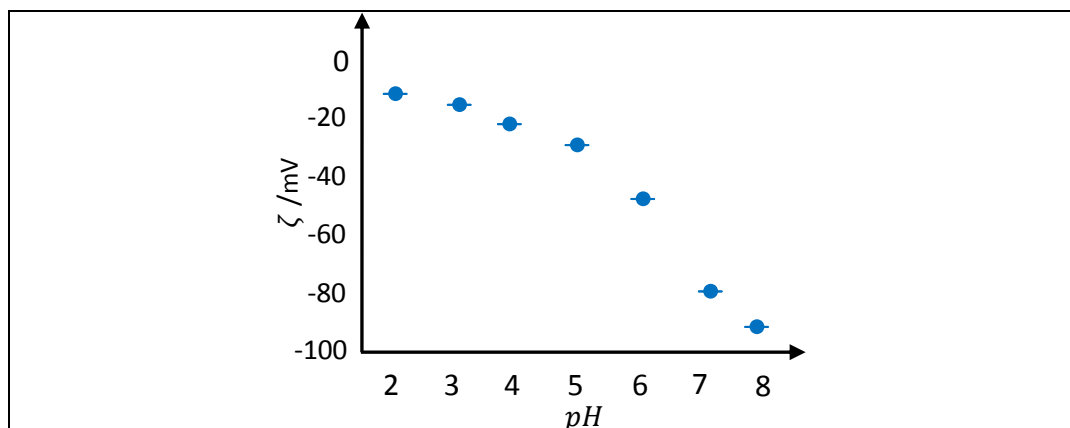


Figure 6.6: Zeta potential change of silica as a function of the pH. The measurements were done by preparing different pH solutions in a 1 mM buffer phosphate

The most important and dominant factor seems to be the continuous production of protons on the gold surface. It was shown in chapter 5 that the proton concentration is higher on the gold surface than on the Pt side. Therefore negatively charged silica particles on gold side will be exposed to a higher concentration of protons.

The protons can protonate the negative oxygen moieties of surface groups of the silica particle. The protonation can decrease the particle surface charge changing its zeta potential. To understand the zeta potential variation with pH, the zeta potential of the silica particles in water solution at different pHs were measured. Figure 6.6 shows the variation of the silica zeta potential as function of pH. When the concentration of hydronium ion increases (in other words, the pH decreases.), the zeta potential changes to less negative values.

Further experiments were done to observe the behavior of silica particles on the gold surface at different pHs in absence of H_2O_2 . It showed that silica particles start clustering at a pH around 5.5⁷⁹. If the pH decreases more the tendency to cluster formation increases (figure 6.7).

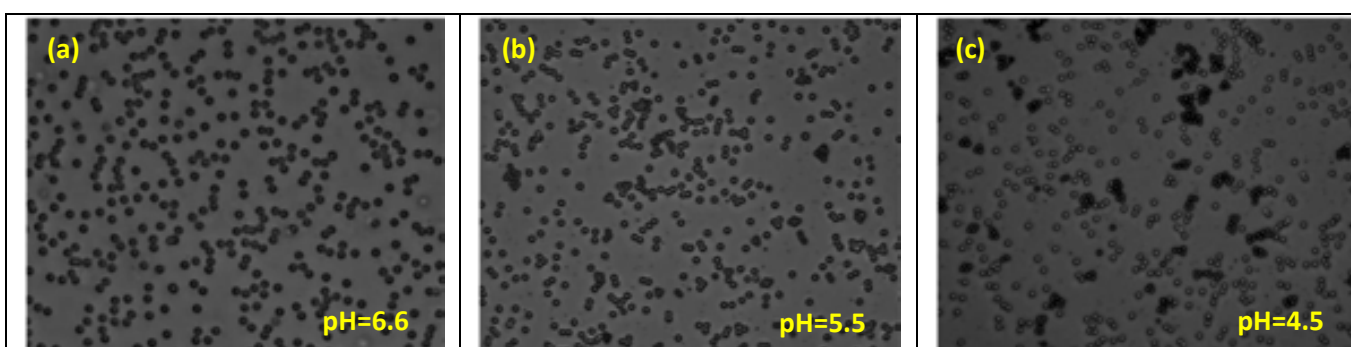


Figure 6.7: Optical snapshots of the colloidal silica on gold substrate at a) pH=6.6 b) pH=5.5 c) pH=4.5 in absence of hydrogen peroxide. The silica clustering starts at a pH around 5.5.

⁷⁹ Indeed the pH at which the clusters start to aggregate is close to the pH values calculated on the gold surface during the catalytic actuation.

Screening the surface charge of silica particles promotes interaction among them. The importance of the proton production in the clustering and motion of the silica particles and the role of the gold surface for proton production is reflected in figure 6.8. Figure 6.8 shows how the clustering process is only limited to the gold surface whereas the particles are only governed by Brownian motion at the silicon side without any cluster formation.

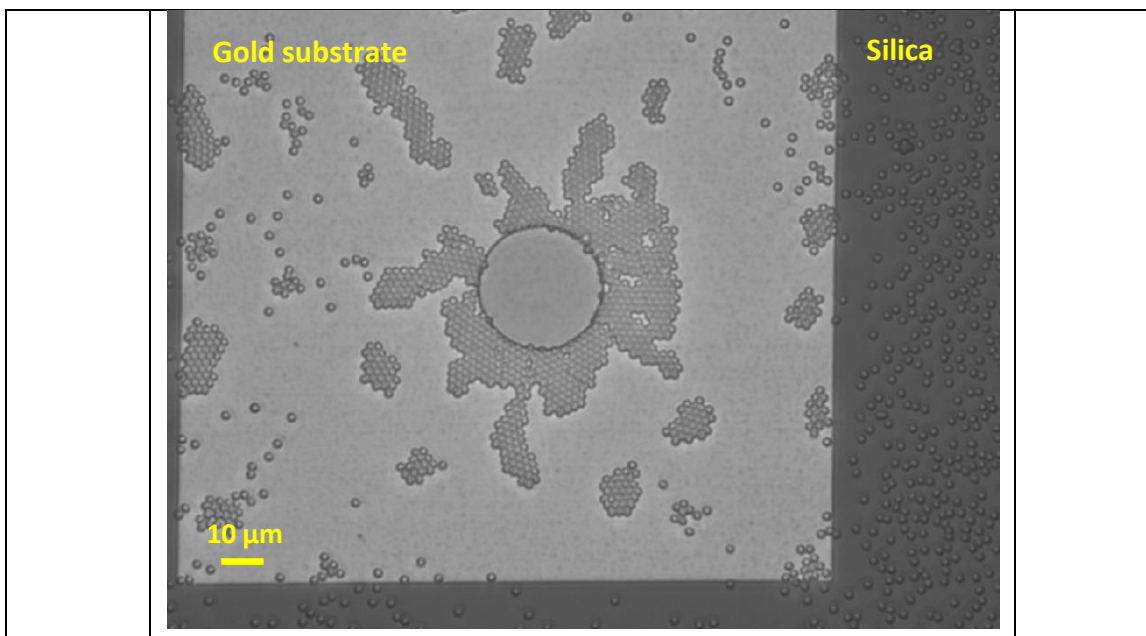


Figure 6.8: The silica clustering only takes place on the gold surface whereas on silicon oxide only a random particle motion is observed.

The initial electrostatic repulsion of negatively charged silica particles from the platinum disk is another important factor that can aid in the cluster formation. As mentioned before, initial electrostatic repulsion of negatively charged particles from the platinum disk forms the repulsive band with particle density equal to zero. The repelled particles increase the particle density on a limited area over the repulsive band.

This band is referred as overpressure band in this dissertation. The particle density at the overpressure band is higher than in the areas far enough from the disk which are not affected by either the generated electric field or the fluid flow. Regarding the impact of fluid flow over the repulsive band, the fluid flow can help to bring closer the colloidal tracer since operates in opposite direction to the electric field and also enhance the protonation of the silica moieties.

Therefore the contribution of the essential factors described above (pH, fluid flow and initial electrostatic repulsion) causes clustering on such overpressure band.

6.2.c Cluster transportation to the Pt disk edge

The change of the zeta potential of the silica singlets and clusters can explain the motion of the particles towards the platinum disk. It decreases the repulsive electrophoretic force and consequently fluid flow towards the platinum disk can become more dominant. The zeta

potential of the silica particles at the overpressure band changes from its primary value of around -80 mV (ζ_{p^-}) to less negative values ($\zeta_{p^-}^*$) (equation 6.7).

$$\zeta_{p^-} < \zeta_{p^-}^* \quad \text{Equation 6.7}$$

Considering equation 6.1, the radial velocity toward platinum disk for the particles with zeta potential values ζ_{p^-} and $\zeta_{p^-}^*$ are $V_r^{P^-}(r)$ (equation 6.8) and $V_r^{P^-*}(r)$ (equation 6.9) respectively.

$$V_r^{P^-}(r) = \frac{\varepsilon \zeta_{p^-}}{\eta} E_r(r) + V_f(r) \quad \text{Equation 6.8}$$

$$V_r^{P^-*}(r) = \frac{\varepsilon \zeta_{p^-}^*}{\eta} E_r(r) + V_f(r) \quad \text{Equation 6.9}$$

According to equation 6.7, 6.8 and 6.9, the relation between $V_r^{P^-}(r)$ and $V_r^{P^-*}(r)$ is:

$$V_r^{P^-}(r) < V_r^{P^-*}(r) \quad \text{Equation 6.10}$$

If the $V_r^{P^-}(r)$ is zero at the overpressure band, $V_r^{P^-*}(r)$ has positive value. It means that the particles with $\zeta_{p^-}^*$ value may move toward the platinum disk. Average radial velocity (V_r) of silica particles versus normalized distance to disk center at 1 wt% H_2O_2 during the early stages of silica transport to the Pt edge is shown in figure 6.9. The velocity of the particles increases remarkably just close to the edge of platinum disk. Silica particles or clusters stop at the platinum-gold boarder starting the first stage of silica crystallization. They particles build a lattice in which the particles tend to form a close-packing structure of equal spheres [1] which starts expanding towards the gold surface.

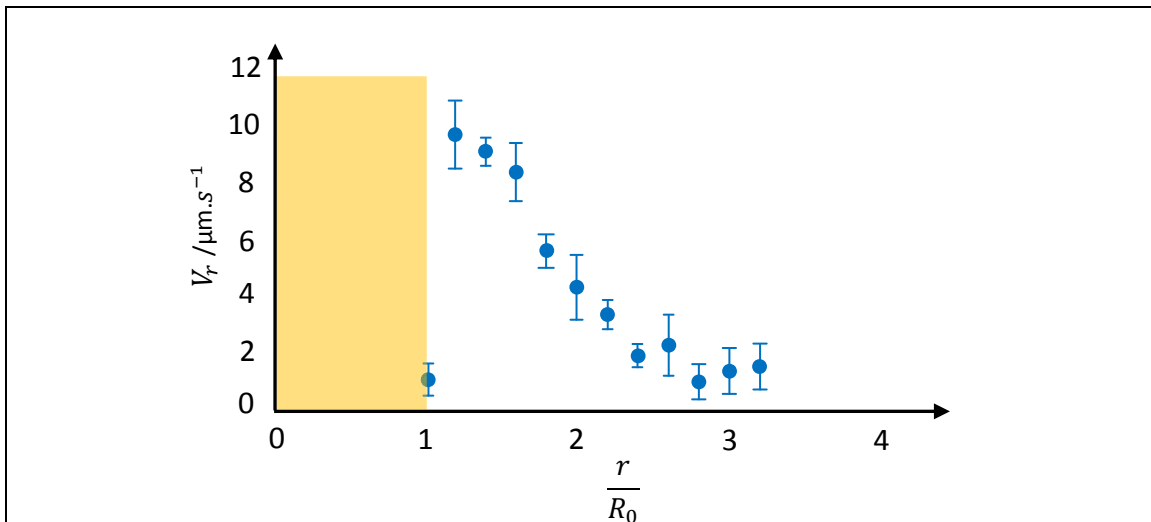


Figure 6.9: Average radial velocity (V_r) of P^- tracers (silica particles) versus normalized distance to disk center at 1 wt% hydrogen peroxide solution at the initial step of crystallization for the device shown in the figure 6.2. r and R_0 are the distances of the particle from the disk center and the disk radius respectively. Disk radius (R_0) is $15\mu\text{m}$. The $\frac{r}{R_0}$ values are equal to 0 and 1 at the platinum disk center and platinum disk border respectively. Yellow area represents the area above the platinum disk.

The size of the clusters arriving at the platinum disk edge increases with time either by the incorporation of single particles or by the addition of other clusters during their way toward the disk.

Figure 6.10 shows the increase of the average size of incoming clusters to the growing silica crystal with time. However at larger times, the clustering process becomes weaker.

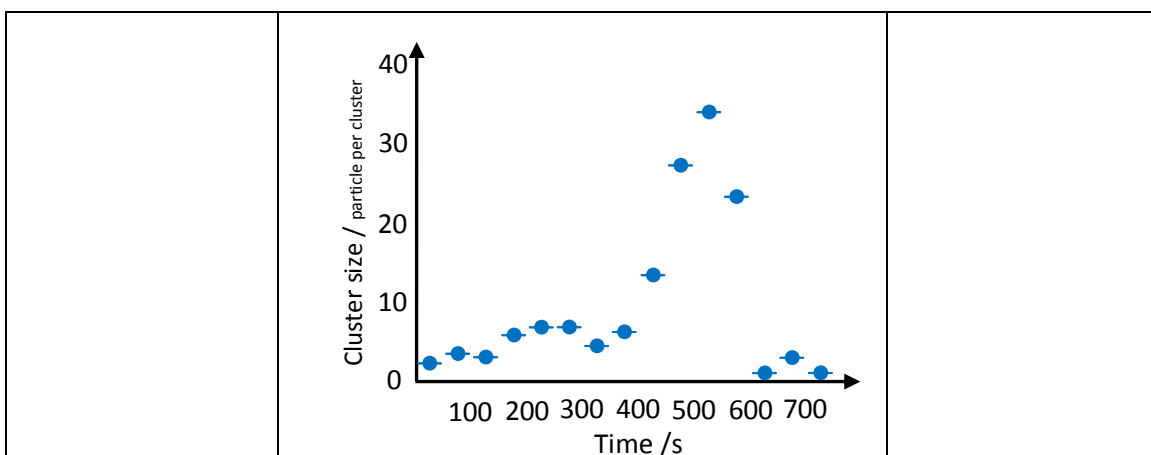


Figure 6.10: Average cluster size (average number of particles per cluster) arriving at the platinum edge as a function of time for the device shown in the figure 6.2

Figure 6.11 shows the percentage of incoming clusters which adjoin the silica crystal at the platinum edge, as a function of cluster size for the device shown in figure 6.2. In this context, the cluster size is defined as the number of silica particles forming the cluster prior to the moment of adjoining to the growing silica ensemble at the disk edge.

The shape of the clusters was characterized. Clusters arranged in a more linear or elongated fashion than in a rounded one. This feature becomes more obvious in case of strong catalytic actuation or for concentrated colloidal dispersions. That is because of the operating but opposite forces (electrostatic force and fluid flow) which make the clustering process take place in non-equilibrium conditions. Under this situation, aggregation of particles is dictated by the kinetics leading to such more linear rearrangements, rather than by energetic considerations that would favour rounded clusters where particles arrange in a more coordinated fashion. Clustering process in absence of forces is expected to be dominated by the Brownian motion which helps the particles to find the more stable locations (high coordinated sites) yielding in this case to more rounded cluster shapes.

Appendix 6.1 contains the configuration of the adjoining clusters related to the figure 6.11. The concentration of silica particles in the aqueous dispersion is a very important parameter which affects the cluster size. Larger cluster sizes were observed with higher silica concentrations. Figure 6.12 demonstrates the effect of particle concentration on the size of the clusters. In dispersions with high concentration of silica particles (figure 6.12 a), the particles are closer together. Therefore, larger clusters are formed much faster. In this case, the silica crystal growth rate is very high (figure 6.13).

At lower concentration of silica particles (figure 6.12 b), the probability of forming clusters with high number of particles is lower because the particles are more far from each other.

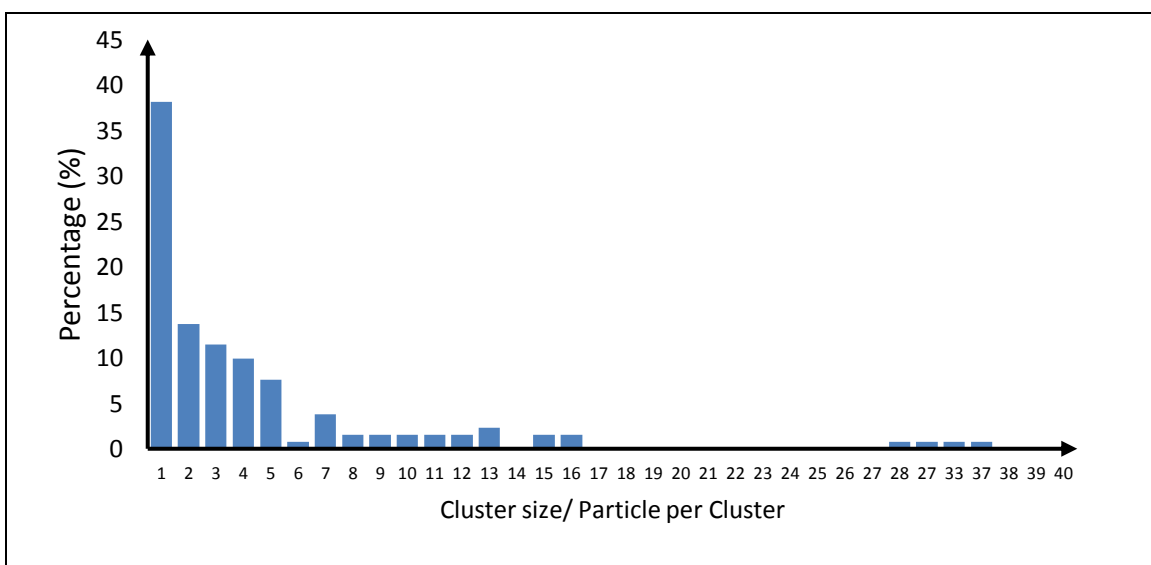


Figure 6.11: Percentage distribution of clusters arriving at the edge of platinum disk for the device shown in the figure 6.2. The smaller clusters are more frequent during the very early stages of the silica crystallization whereas the bigger clusters become important at longer times.

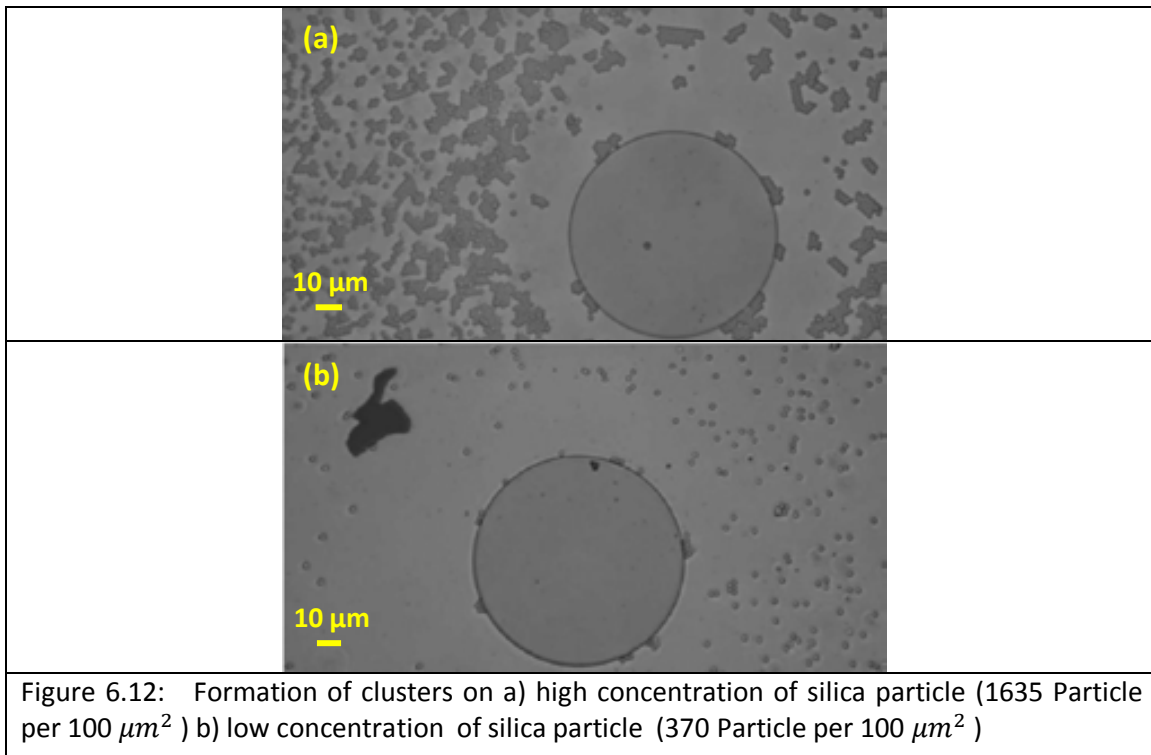


Figure 6.12: Formation of clusters on a) high concentration of silica particle (1635 Particle per $100 \mu\text{m}^2$) b) low concentration of silica particle (370 Particle per $100 \mu\text{m}^2$)

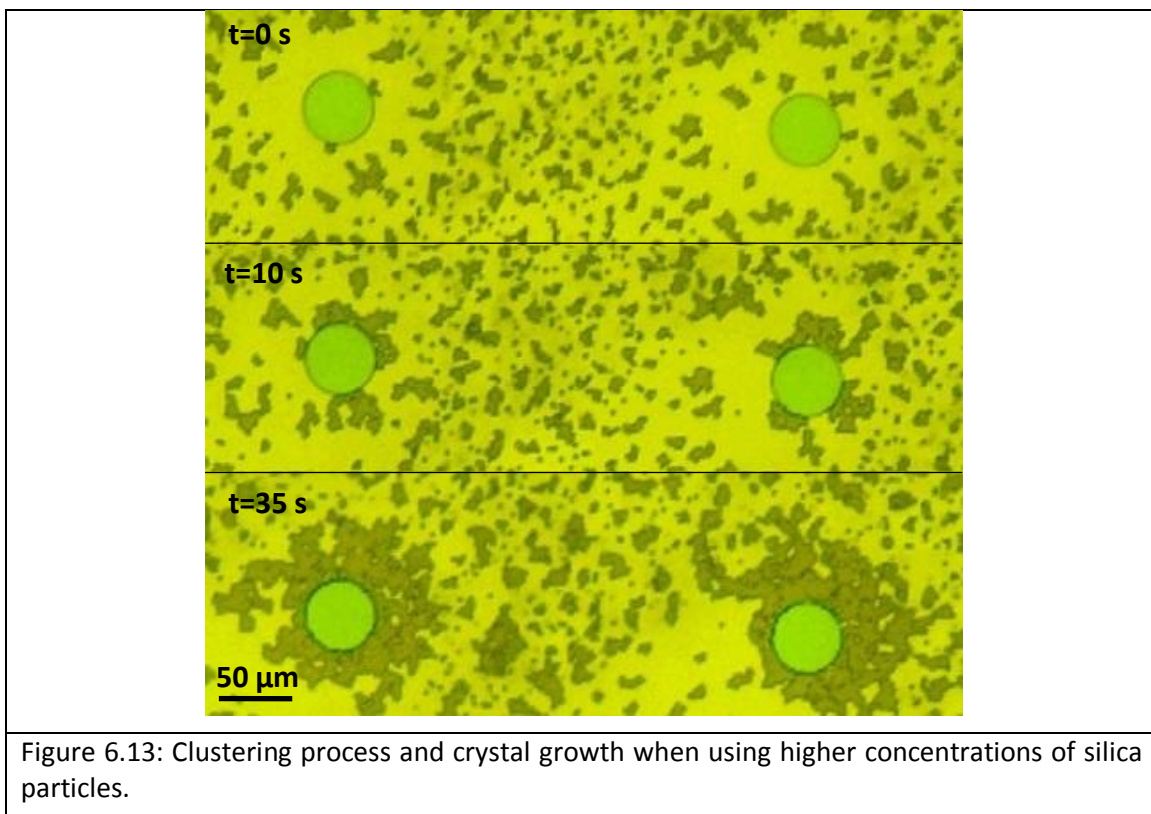


Figure 6.13: Clustering process and crystal growth when using higher concentrations of silica particles.

Although the clusters move to the edge of the platinum disk, the electrostatic repulsion of the negative particles still exists. It is powerful enough to prevent the particles or clusters from overcoming the Pt edge and moving more toward the platinum center. Figure 6.14 shows the repulsion of a silica particle which comes from higher heights when the crystallization is going on.

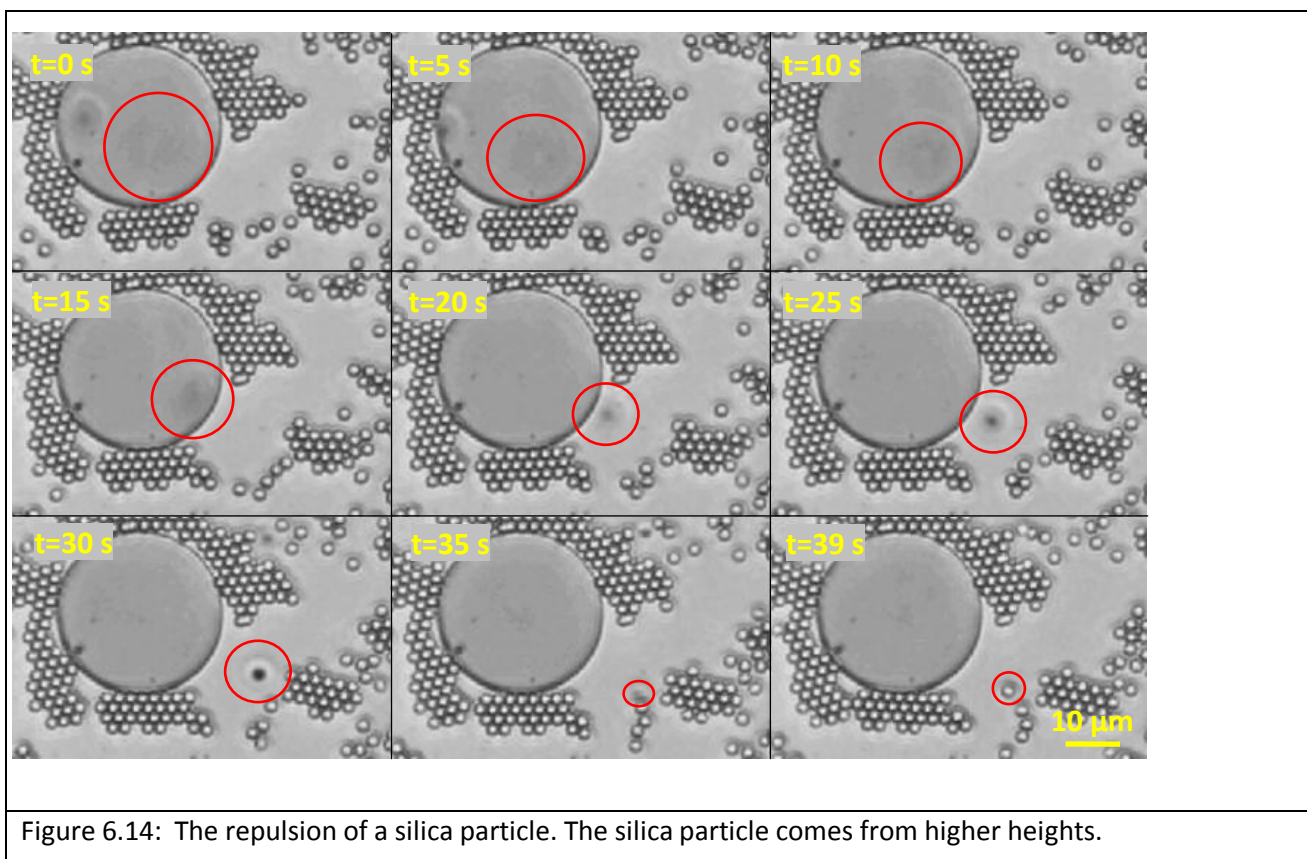


Figure 6.14: The repulsion of a silica particle. The silica particle comes from higher heights.

Additional interesting phenomena have been captured during the first stages of the self-assembly such as the fast motion of particles or clusters around the rims of the disk up to find a neighbor particle or cluster to enhance their stabilization. Figure 6.15 shows an example of this kind of behavior. The average rotational velocity of the cluster was $1.5 \pm 0.25 \mu\text{m} \cdot \text{s}^{-1}$.

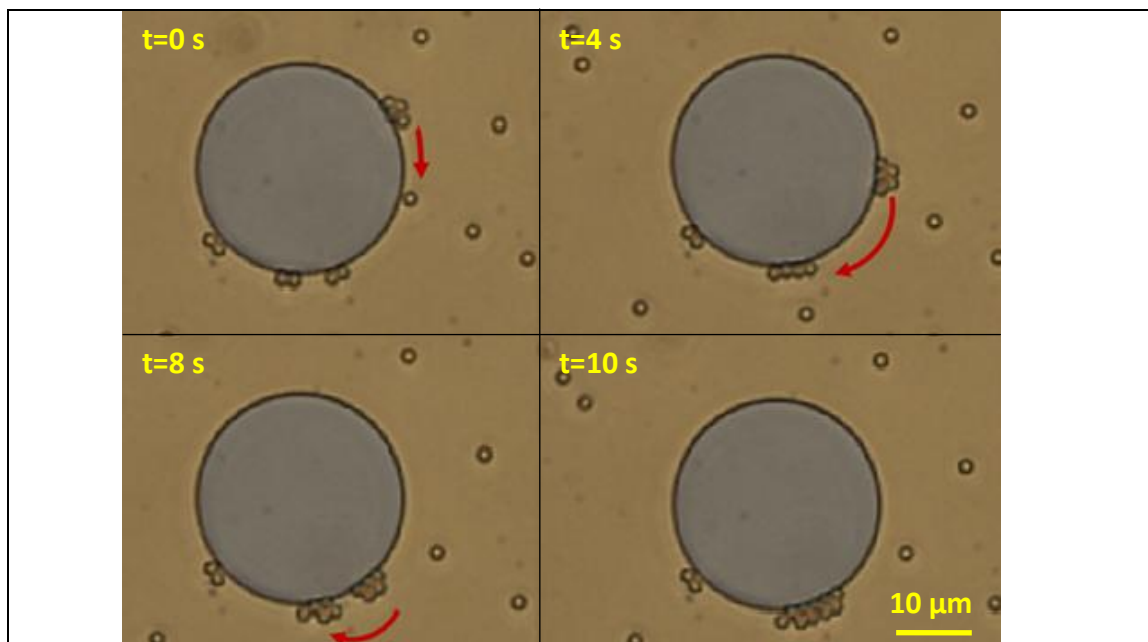


Figure 6.15: Rotational motion of a silica cluster around the platinum disk.

The average rotational velocity of cluster : $1.5 \pm 0.25 \mu\text{m} \cdot \text{s}^{-1}$

The rotational motion can appear as a consequence of the presence of physical barriers at the disk edge. The physical obstacles are the Pt step and also the already anchored clusters. The fluid lines can be distorted at those barriers making part of the fluid move at the sides of the cathode disk. That can push the incoming clusters to move around the disk. Rotational patterns have been also predicted in non-equilibrium models of self-propelled particles when interacting with rounded reflective boundaries [32].

6.2.d Silica crystallization

The incoming clusters re-orient themselves upon approaching the disk to fit in a stable location at the lattice of the growing silica crystal. That is aided by the fluid motion which promotes torques rotations, bendings or even cluster deformations and also by the Brownian contributions that helps to find the more coordinated places especially when individual particles approach the crystal.

Figure 6.16 illustrates the approach of some clusters and how they join and re-orientate to build a 2D close-packing arrangement around the disk edge. The continuous liquid pumping can also push up the first rows of silica around the edge of the Pt disk producing a second layer on top as also seen in figure 6.17.

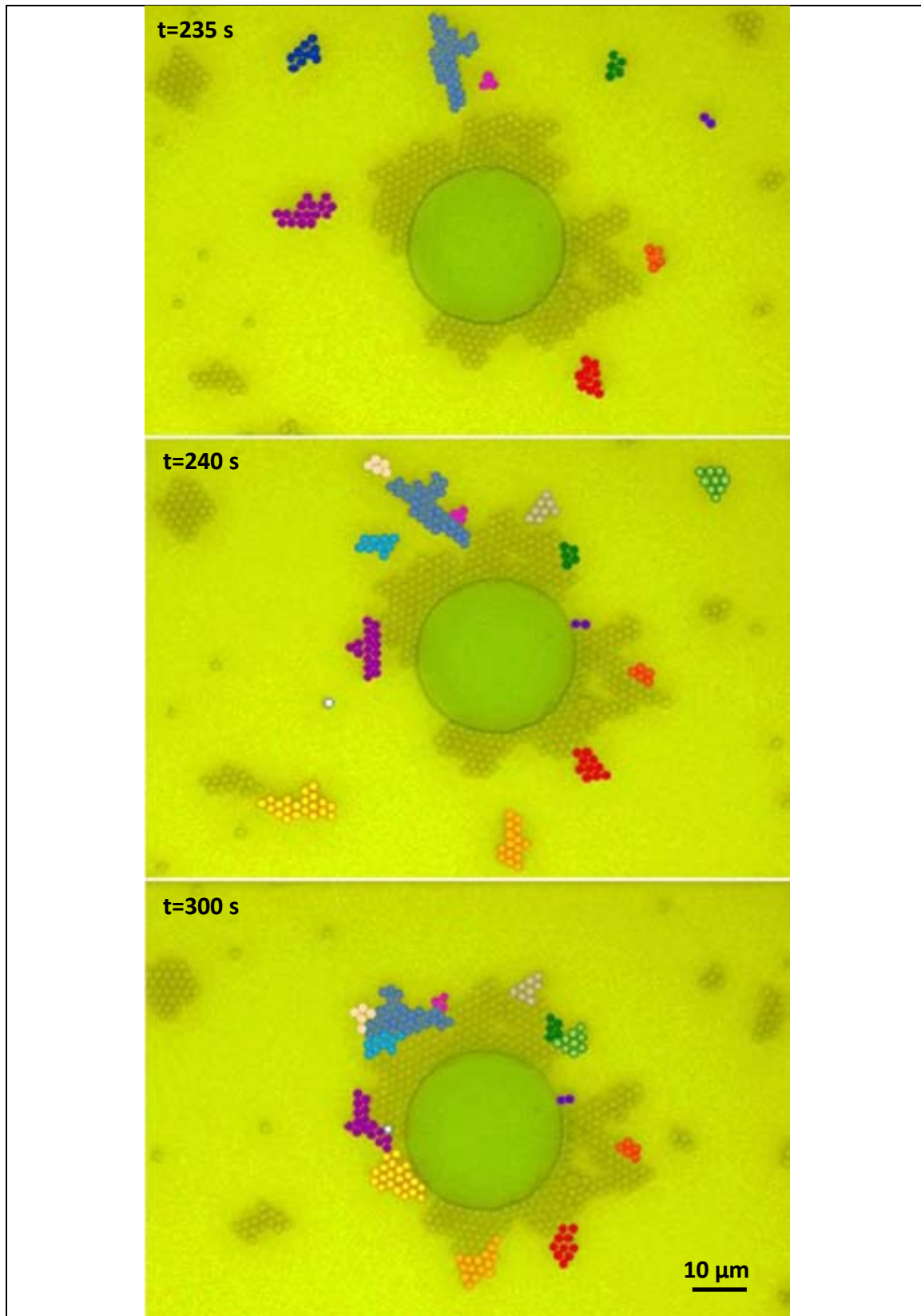
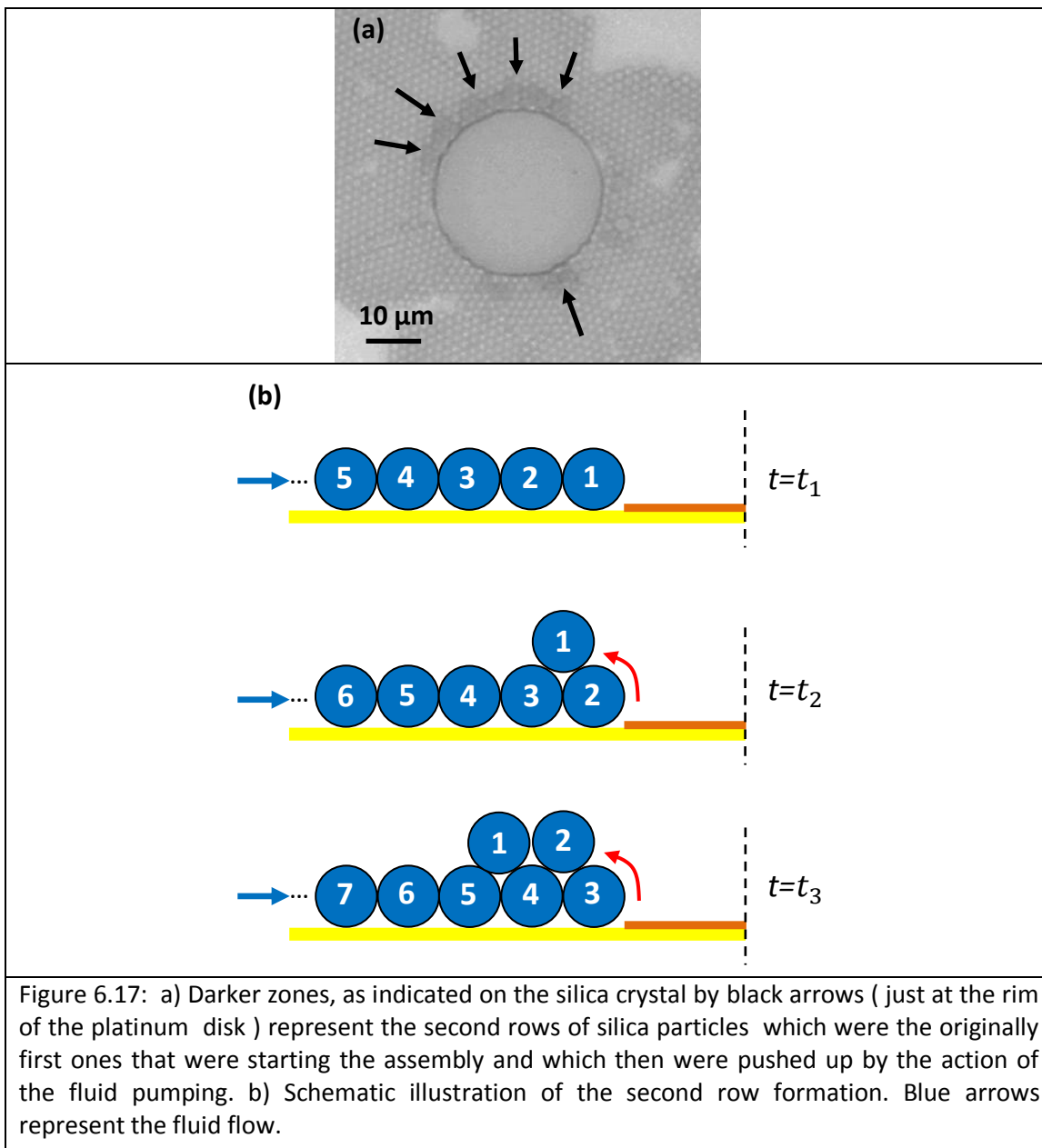


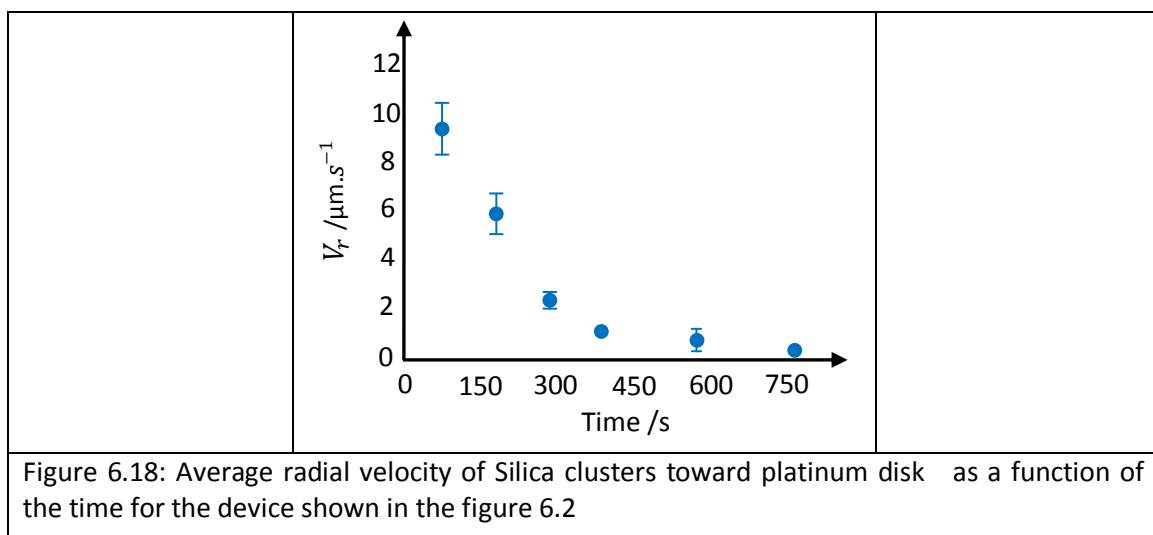
Figure 6.16: Growth of silica crystal. The incoming clusters have been colored to easily observe how they approach the disk region and how they re-orientate to fit in the growing crystal with close-packing arrangement.



The cluster transportation and patterning of the silica, which are very obvious at the beginning, are not steady in time. At long time, the declination of cluster transportation occurs and the progress of silica crystallization becomes dramatically low. As shown before, production of protons at the gold surface plays the main role in triggering the electrohydrodynamic process. The absence of sufficient proton production may be the reason to start the step shown in figure 6.3d. Passivation of the active gold surface around the platinum disk with particles and the decrease of hydrogen peroxide concentration in the aqueous dispersion may be two reasons to explain the end of the proton production and self-limiting crystal growth.

The frame at $t=1620$ s on figure 6.2 shows how the active part of the gold around the disk edge is covered by the self-assembly of silica. At this stage, the clustering and transport of silica beyond such patterned region are turned off and only the Brownian motion of singlet particles around the colloidal pattern is observed. That self-limits the dimensions of the crystal growth. Figure 6.18 illustrates the decay of the cluster motion toward the platinum disk with time.

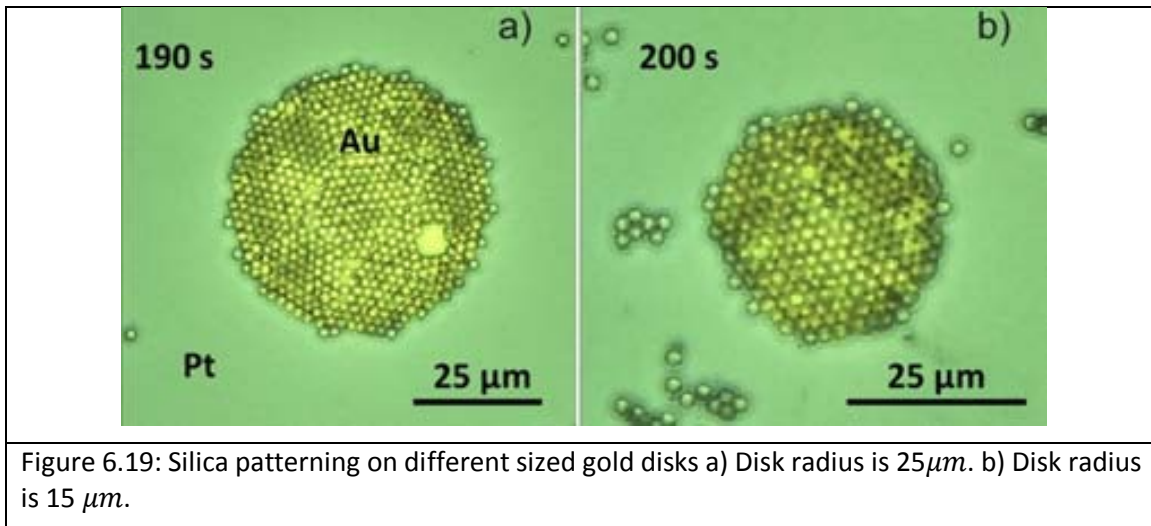
Another characteristic indicative of the importance of the gold surface has been captured when repeating the experiment in a second round. Fresh plasma pretreated devices exposed to the chemical fuel gather, in a very reproducible way, the different processes outlined above. However if previously used devices are immediately exposed again to fresh fuel, the initial clustering, cluster transportation and silica self-assembly are suppressed. Only the repulsive band free of silica particles is created around the platinum disk. That is a very reproducible phenomenon and we believe that is connected with a depression in the proton production at the gold surface due to contamination. Although the gold surface still generates protons to trigger the electrokinetic process, its production is not high enough for silica clustering and transportation to the edge.



6.3 Pattern formation on Pt-Au system

Since negative particles can pattern 2D silica layers on gold regions, it turns out also interesting to prove if the inversion of the configuration of the device can induce disks of colloidal patterning. In the case of Pt-Au devices, different diameter gold disks were patterned on a

platinum surface. A very nice 2D closed packed silica pattern can be observed on the gold micro-structures as depicted in figure 6.19.



6.4 Pattern formation with positively charged particles

Positively charged particles move towards the platinum disk governed by the co-action of the electrophoretic and electro-osmotic forces as also predicted by model described in 5.3. A pattern of such particles is built at the platinum surface as can be observed in figure 6.20 a-b in which squared platinum structures were used. Important to stand out is the difference in the assembly process when using positively or negatively charged particles. As with the first ones a not so ordered 3D pattern is generated with the second ones an ordered 2D assembly is achieved.

It was observed that positive particles can come not only from the plane parallel to the Pt surface but also from vertical distances of more than $10\mu\text{m}$ away from the surface. In the latter case, the particles have a downward velocity component in the z-axis which opposes the direction of the upwards flow of the liquid above the platinum surface. This fact shows the importance of the electrophoretic term in the process. The in plane radial velocity of the positive particles was previously reported and its maximum value found at the Pt edge was about $19.4\pm 6.8\mu\text{m}\cdot\text{s}^{-1}$. The action of these forces makes the particles stick in a more irreversible way and randomly at the platinum surface. The strength of the process limits the Brownian motion at the surface which could help to promote the surface diffusion of the particles to find the best coordinated site and thus providing more ordered patterns. Rather, the process favors the formation of unordered 3D particle aggregates. The colloidal patterning is quite stable on the platinum surface which can be mediated by the Pt surface chemistry.

Plasma treatment induces oxidized moieties on the platinum surface as demonstrated by XPS which could promote the sticking properties between the surface and the colloids.

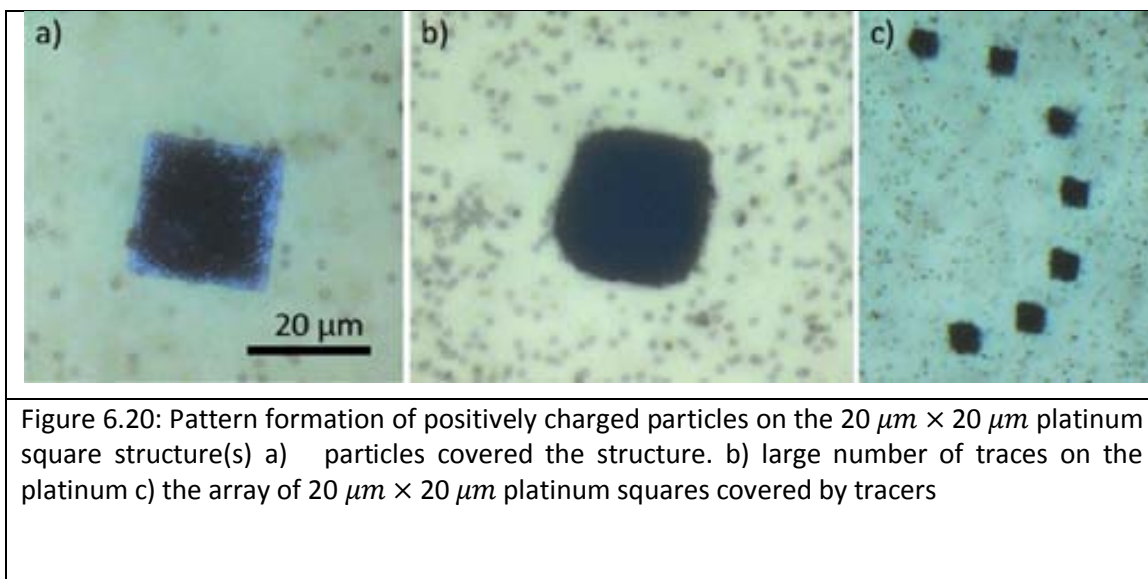


Figure 6.20: Pattern formation of positively charged particles on the $20\ \mu\text{m} \times 20\ \mu\text{m}$ platinum square structure(s) a) particles covered the structure. b) large number of traces on the platinum c) the array of $20\ \mu\text{m} \times 20\ \mu\text{m}$ platinum squares covered by tracers

Conclusions

Bimetallic catalytic pumps made of Au-Pt are capable to guide colloidal self-assembly at precise locations without any external energy source. The local self-generated electrohydrodynamic forces triggered by electrochemical reactions at both metals together with the nature of the colloidal charge and the surface treatment are the basic ingredients for tailoring the patterning process. It was possible to achieve guided colloidal patterning using negatively and positively charged particles. The use of negative particles allowed patterning the gold surface starting from the Pt edge and forming more 2D ordered colloidal crystal. Instead, the use of positive particles allowed patterning unordered but stable 3D colloidal aggregates on the platinum disks. In the case of negatively charged particles it was possible to monitor in real time many unexpected features during the patterning process: electrostatic repulsion, silica clustering, silica transport to the Pt edges and the fascinating dynamics of silica crystallization at the gold surface from the platinum edge. These self-guiding processes may become a very versatile tool to approach technological important challenges in nanofabrication. The autonomous accumulation of material to precise locations can have impact in the design of photonic crystals, smart nanostructured surfaces for sensing or catalysis, photovoltaics, corrosion protection, self-healing systems among others.

[1] Kline, T.R.; Paxton, W.F.; Wang, Y.; Velegol, D.; Mallouk, T.E.; Sen, A.; Catalytic Micropumps: Microscopic Convective Fluid Flow and Pattern Formation, *J. Am. Chem. Soc.* 2005, 127, 17150-17151.

[2] Kline, T.R.; Iwata, J.; Lammert, P.E.; Mallouk, T.E., Catalytically driven colloidal patterning and transport, *J. Phys. Chem. B* 2006, 110, 24513-24521.

[3] Schaller, V.; Weber, C.; Semmrich, C.; Frey, E.; Bausch, A.R.; Polar patterns of driven filaments *Nature* 2010, 467, 73-77.

- [4] Theurkauff, I.; Cottin-Bizonne, C.; Palacci, J.; Ybert, C.; Bocquet, L.; Dynamic clustering in active colloidal suspensions with chemical signaling, *Phys. Rev. Lett.* 2012, 108, 268303.
- [5] Farrell, F.D.C.; Marchetti, M.C.; Marenduzzo, D.; Tailleur, J.; Pattern formation in self-propelled particles with density-dependent motility, *Phys. Rev. Lett.* 2012, 108, 248101.
- [6] Palacci, J.; Sacanna, S.; Steinberg, A.P.; Pine, D.J.; Chaikin, P.M.; Living crystals of light – activated colloidal surfers, *Science* 2013, 339, 936-940.
- [7] Mognetti, B.M.; Saric, A.; Angioletti-Uberti, S.; Cacciuto, A.; Valeriani, C; Frenkel, D.; Living clusters and crystals from low-density suspensions of active colloids , *Phys. Rev. Lett.* 2013, 111, 245702.
- [8] Yan, J.; Bloom, M.; Bae, S.C.; Luitjen, E.; Granick, S.; Linking synchronization to self-assembly using magnetic Janus colloids, *Nature* 2012, 491, 578-581.
- [9] Wang, W.; Duan, W.; Sen, A.; Mallouk, T.E., Catalytically powered dynamic assembly of rod-shaped nanomotors and passive tracer particles, *Proc. Natl. Acad. Sci. USA* 2013, 110, 17744-17749.
- [10] Ibele, M.; Mallouk, T.E.; Sen, A.; Schooling behavior of light-powered autonomous micromotors in water, *Angew. Chem. Int. Ed.* 2009, 48, 3308-3312.
- [11] Duan, W.; Liu, R.; Sen A.; Transition between collective behaviors of micromotors in response to different stimuli, *J. Am. Chem. Soc.* 2013, 135, 1280-1273.
- [12] Dobnikar, J.; Snezhko, A.; Yethiraj, A.; Emergent colloidal dynamics in electromagnetic fields, *Soft Matter* 2013, 9, 3693-3704.
- [13] Sapozhnikov, M.V.; Tolmachev, Y.V.; Aranson, I.S.; Kwok, W.K.; Dynamic self-assembly an patterns in electrostatically driven granular media, *Phys. Rev. Lett.* 2003, 90, 114301.
- [14] Aranson, I.S.; Sapozhnikov, M.V.; Theory pattern formation of metallic microparticles in poorly conducting liquids, *Phys. Rev. Lett.* 2004, 92, 234301.
- [15] Bartlett, A.P.; Agarwal, A.K.; Yethiraj, A.; Dynamic templating of colloidal patterns in three dimensions with nonuniform electric fields, *Langmuir* 2011, 27, 4313-4318.
- [16] Trau, M.; Saville, D.A.; Aksay, I.A., Field-induced layering of colloidal crystals, *Science* 1996, 272, 706-708.
- [17] Böhmer, M., In situ observation of 2-dimensional clustering during electrophoretic deposition, *Langmuir* 1996, 12, 5747-5750.
- [18] Giersig, M.; Mulvaney, P., Preparation of ordered colloid monolayers by electrophoretic deposition, *Langmuir* 1993, 9, 3408-3413.
- [19] Trau, M.; Saville, D.A.; Aksay, I.A., Assembly of colloidal crystals at electrode interfaces, *Langmuir* 1997, 13, 6375-6381.

- [20] Solomontsev, Y.; Böhmer, M.; Anderson, J.L., Particle clustering and pattern formation during electrophoretic deposition: a hydrodynamic model, *Langmuir* 1997, 13, 6058-6068.
- [21] Yeh, S.; Seul, M.; Shralman, B.I., Assembly of ordered colloidal aggregates by electric-field-induced fluid flow, *Nature* 1997, 386, 57-59.
- [22] Solomontsev, Y.; Guelcher, S.A.; Bevan, M.; Anderson, J.L., Aggregation dynamics for two particles during electrophoretic deposition under steady fields, *Langmuir* 2000, 16, 9208-9216.
- [23] Ristenpart, W.D.; Aksay, I.A.; Saville, D.A., Assembly of colloidal aggregates by electrohydrodynamic flow: kinetic experiments and scaling analysis, *Phys. Rev. E* 2004, 69, 021405.
- [24] Zhang, K.; Liu, X.Y., In situ observation of colloidal monolayer nucleation driven by an alternating electric field, *Nature* 2004, 429, 739-743.
- [25] Bigioni, T.P.; Lin, X.; Nguyen, T.T.; Corwin, E.I.; Witten, T.A.; Jaeger, H.M., Kinetically driven self-assembly of highly ordered nanoparticle monolayers. *Nature Materials* 2006, 5, 265-270.
- [26] Liu, Y.; Liu, X.; Narayanan, J., Kinetics and equilibrium distribution of colloidal assembly under an alternating electric field and correlation to degree of perfection of colloidal crystals, *J. Phys. Chem.* 2007, 111, 995-998.
- [27] Ristenpart, W.D.; Aksay, I.A.; Saville, D.A., Electrically driven flow near a colloidal particle close to an electrode with a faradaic current, *Langmuir* 2007, 23, 4071-4080.
- [28] Punckt, Ch.; Jan, L.; Jiang, P.; Frewen, T.A.; Saville, D.A.; Kevrekidis, I.G.; Aksay, I.A. Autonomous colloidal crystallization in a galvanic microreactor, *J. Appl. Phys.* 2012, 112, 074905.
- [29] Jan, L.; Punckt, Ch.; Khusid, B.; I.G.; Aksay, I.A. Directed motion of colloidal particles in a galvanic microreactor. *Langmuir* 2013, 29, 2498-2505.
- [30] Jan, L.; Punckt, Ch.; Aksay, I.A. Cementation of colloidal particles on electrodes in a galvanic microreactor. *ACS Appl. Mater. Interfaces* 2013, 5, 6346-6353.
- [31] J. Kappraff, *Connections: The Geometric Bridge Between Art and Science*: World Scientific, 2001.
- [32] A. Czirók and T. Vicsek, "Collective behavior of interacting self-propelled particles," *Physica A: Statistical Mechanics and its Applications*, vol. 281, pp. 17-29, 2000.

Chapter 7

Introduction

This chapter is devoted to explore alternative X-Y bi-metallic devices for microfluidic pumping. The motivation is the increasing interest in finding novel materials and strategies for device fabrication that can meet the requirement of low cost. For instance bimetallic micropump fabrication based on electroplating methods with materials such as ruthenium or rhodium, or the use of cheaper coinage materials such as nickel, copper, silver are attractive alternatives. In some of these cases the timelife of the devices can be a disadvantage as compared to bimetallic pumps made from more noble constituents. However these alternative materials can be suitable for applications in which the endurance is not the most crucial parameter. The chapter makes a general overview of the catalytic actuation of different bimetallic structures capturing interesting phenomena that need to be analyzed in more detail in further research which is not covered by this thesis. TAFEL plot measurements are the starting point of this chapter and have been used to characterize the different electrode materials and also as a tool to predict potential X-Y metallic couples that can switch electrokinetic processes in presence of hydrogen peroxide.

7.1. TAFEL plot measurements

Different metals such as Rh, Ru, Ni, Cu and Ag were characterized by the electrochemical TAFEL technique. Figure 7.1 shows the TAFEL response of the different materials together with the response of gold electrodes. The measurements were taken in presence of 1% H_2O_2 .

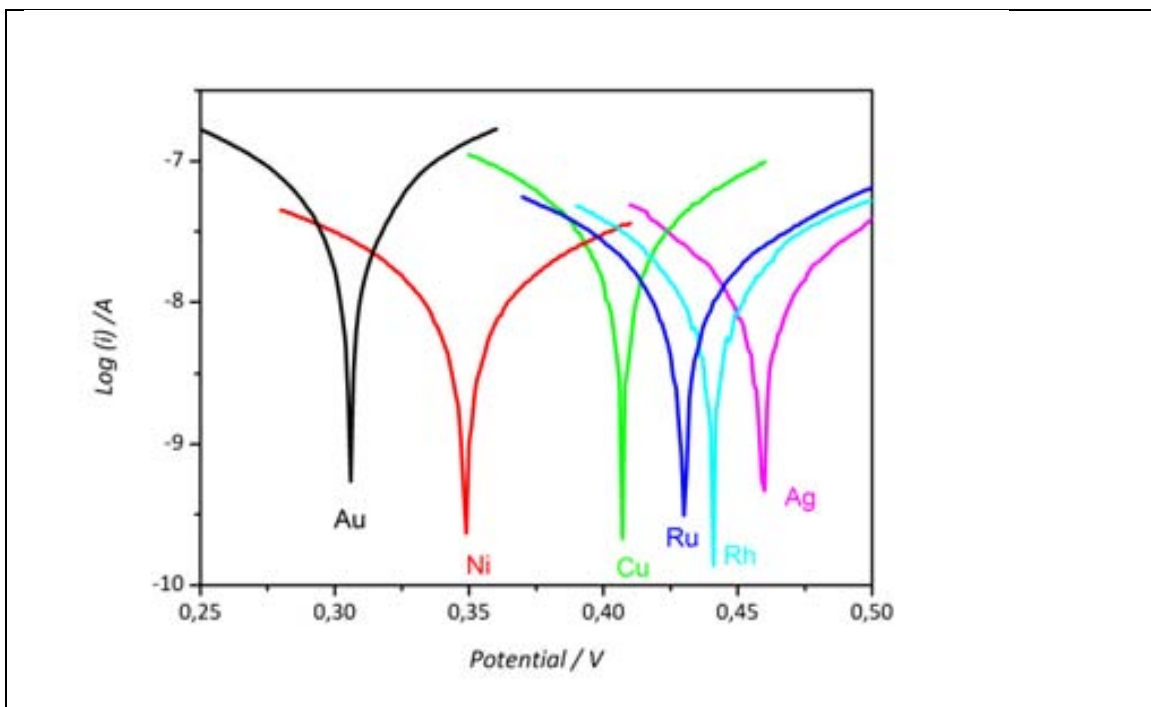


Figure 7.1: TAFEL plot for the different metals explored in this chapter together with the response of gold electrode. The plot was taken in presence of 1% H_2O_2 with a scan rate of $1 \text{ mV}\cdot\text{s}^{-1}$ and vs a Ag/AgCl/KCl reference electrode.

The important parameter to extract from these plots is the mixed potential of the metal for the oxidation and reduction of hydrogen peroxide. As mentioned before in this thesis (appendix 5.1, chapter 5), the mixed potential is a kind of equilibrium potential in which the net electrochemical reaction is zero. Such value can be extrapolated from the intersection of the cathodic and anodic branches of the metal. Extracting the mixed potentials for H_2O_2 for different metals helps to predict the role of the metal electrodes when they are electrically connected in presence of the redox species. The mixed potential for the different metals were the following:

| Element | Ni | Cu | Ru | Rh | Ag | Au ⁸⁰ |
|---------------------|-------|-------|-------|-------|-------|------------------|
| Mixed potential / V | 0.305 | 0.407 | 0.430 | 0.440 | 0.459 | 0.305 |

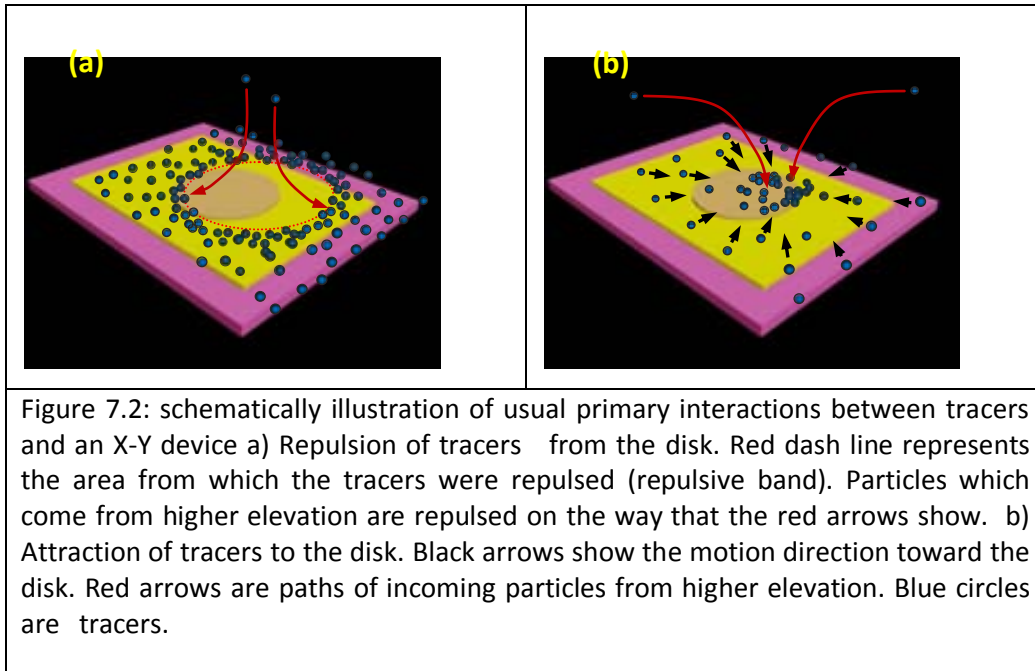
From these values it was proposed different metal couple combinations for designing new X-Y micropumps. It is predicted that the metal with higher mixed potential would act as cathode and the one with lower mixed potential as anode.

7.2 X-Y Bimetallic micropumps

According to the mixed potentials it was proposed the following combinations. Au-Rh, Au-Ru, Cu-Ag, , Ni-Cu, Ni-Ru, Ni-Ag and Au-Ag devices where the first metal would act as anode and the second as cathode. The pumps were fabricated according to the methodology explained in chapter 4.

Under catalytic actuation, the experiments show that there are general interactions between the tracers and the devices similar to the ones found with Au-Pt system. These interactions may be affected by other phenomena related with the less noble behavior of the materials. The first kind of primary interaction is repulsion of tracers from the disk (figure 7.2 a). This interaction is similar to the initial repulsion of silica particles from platinum disk on the Au-Pt system (chapter 6). The tracers are repulsed from the disk and a repulsive band is formed. The other interaction is the attraction of tracers to the disk (figure 7.2 b). It is similar to the interaction between positively charged tracers and the platinum disk on Au-Pt system (chapter 5). Interaction of each X-Y system and tracers will be described below.

⁸⁰ The mixed potential of Au is a little bit bigger than the obtained in chapter 5. That is because of the reference electrode.



7.2.1 Au-Ru Devices

Figure 7.3 shows an Au -Ru device fabricated as per procedure F3 (Chapter 4). The procedure F3 based in electroplating is an alternative fabrication strategy to the electron beam evaporation or sputtering of ruthenium. Price of ruthenium target for electron beam evaporation or sputtering is relatively much higher than the solution for ruthenium electroplating. The procedure F3 provides a reliable, reproducible, low cost and fast fabrication method which meets the design requirements.

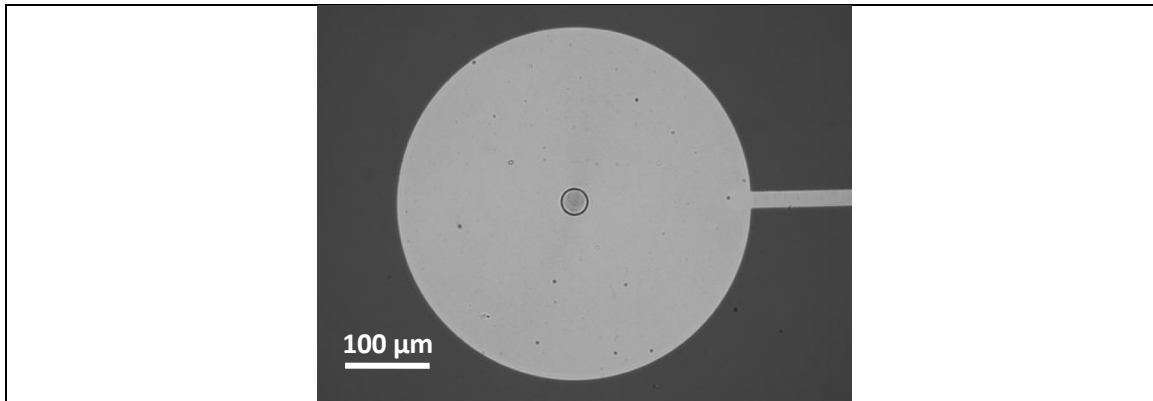
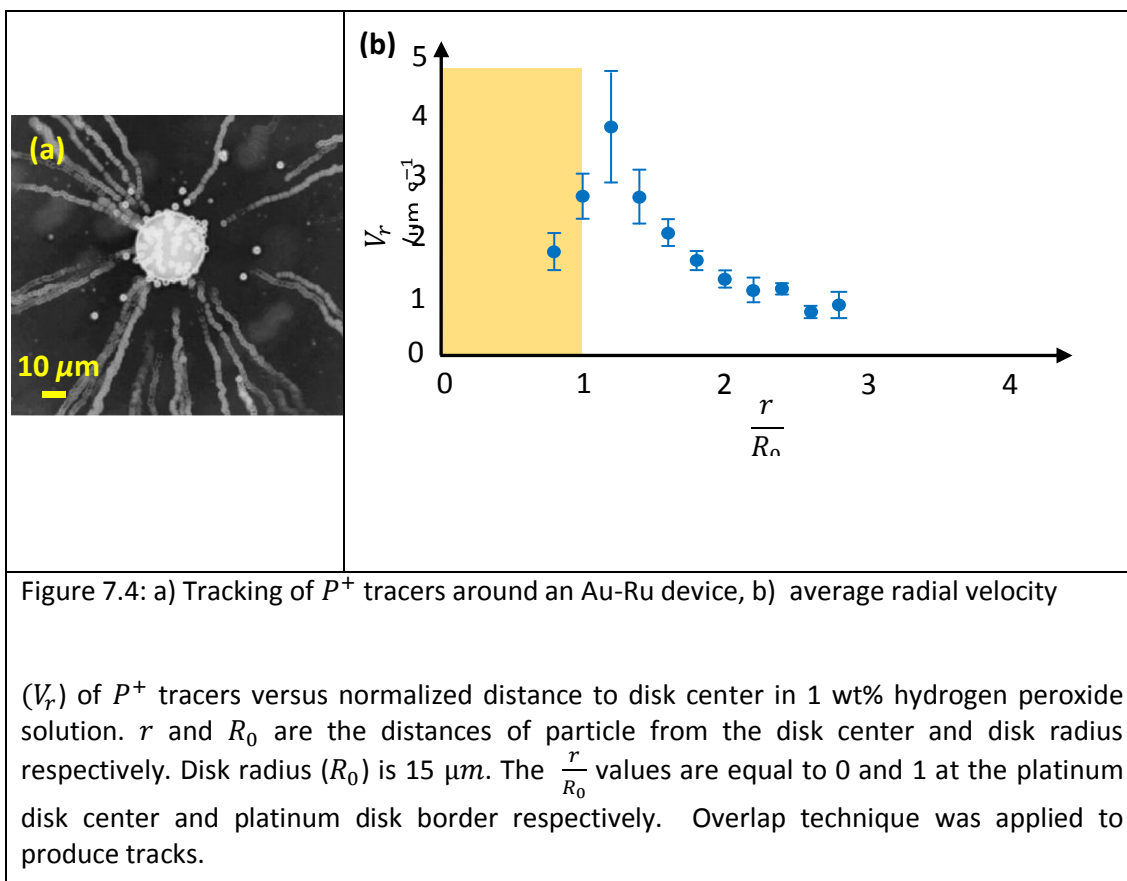


Figure 7.3: a Au-Ru device. A ruthenium disk (diameter: $30\ \mu\text{m}$) was deposited in the middle of a gold disk (diameter: $400\ \mu\text{m}$). The gold disk is connected to the main gold contact with a high length-to width ratio rectangle.

Positively charged tracers are attracted into the Ru disk in presence of 1 wt% H_2O_2 solution (figure 7.4 a). Tracers move toward the ruthenium disk and settle on it. The average radial velocity of the tracers increases as they become closer to the disk (figure 7.4 b). The radial velocity reaches to its maximum near the edge of ruthenium disk. After crossing the ruthenium-gold border, the velocity of tracers decrease and they find a proper location to settle (figure 7.4 b).



It was observed that these devices in presence of 1% H_2O_2 produced a high density of bubbles which made very difficult the inspection and evaluation of the catalytic actuation⁸¹. This concentration of H_2O_2 might also oxidize the ruthenium layer with time and deactivate the device⁸² [1-4]. In order to prevent bubbling, observe the interactions and increase the life time of the device, $\frac{1}{2}$ wt% H_2O_2 solution was applied in the case of negatively charged tracers. As clearly shown in figure 7.5, P^- tracers were repulsed from the Ru disk. Figure 7.6 shows another interesting example of P^- tracer repulsion from a Ru disk on a limited gold substrate ($130 \mu m \times 130 \mu m$ square). All the P^- tracers were pushed over the gold - silicon wafer border.

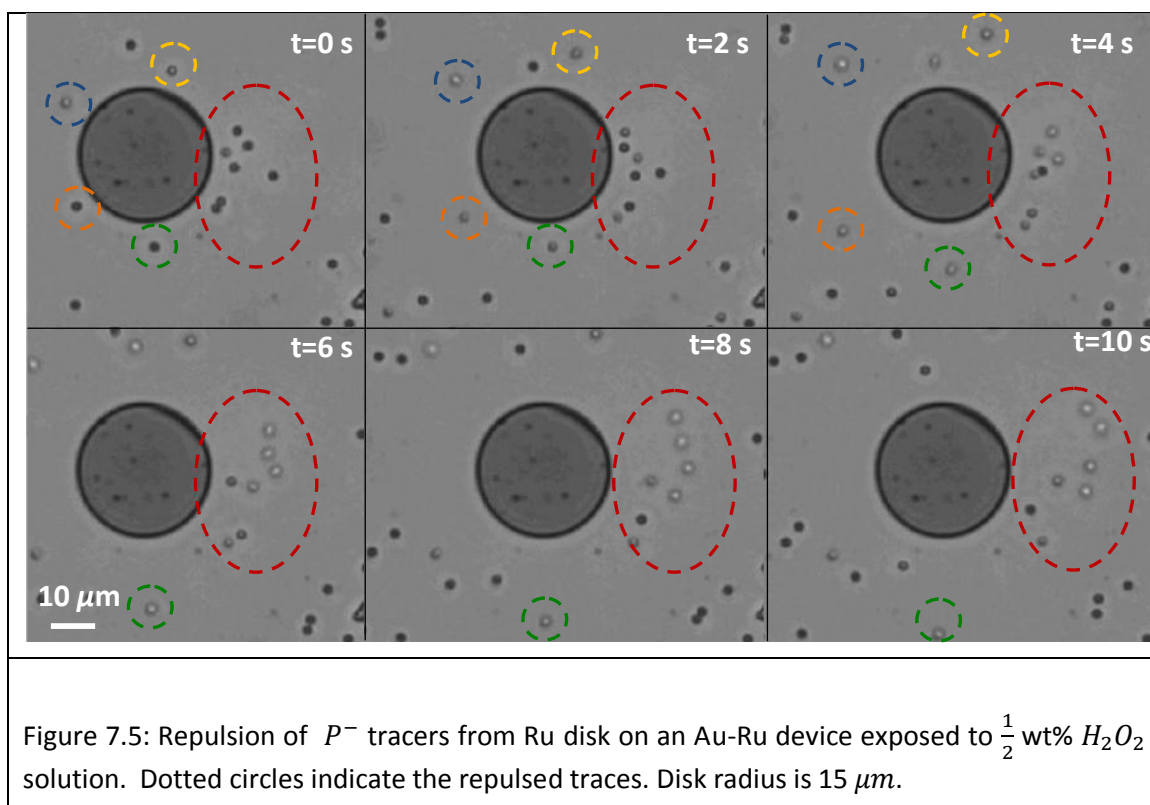
These results suggest an electric field pointing from the gold to the ruthenium in line with the role of the electrodes predicted by the TAFEL measurements.

However the electrokinetic process decays with time as illustrated with negative tracers in figure 7.7. The radius of repulsive band gradually reduces and finally the tracers can be on top of the Ru disk. The disappearance of the repulsion band with time could be associated with an

⁸¹ Ruthenium is an efficient catalyst for the non-electrochemical decomposition of H_2O_2 into O_2 and H_2O in absence of another electrode. The non-electrochemical decomposition of H_2O_2 can be observed in many elements of the platinum family (W. F. Paxton, P. T. Baker, T. R. Kline, Y. Wang, T. E. Mallouk, and A. Sen, "Catalytically Induced Electrokinetics for Motors and Micropumps," Journal of the American Chemical Society, vol. 128, pp. 14881-14888, 2006)

⁸² It is known that Ru is less noble than Pt or Rh

increase of the oxidation degree of the ruthenium surface in presence of the fuel or a decrease in the fuel concentration. More research in this aspect is needed.



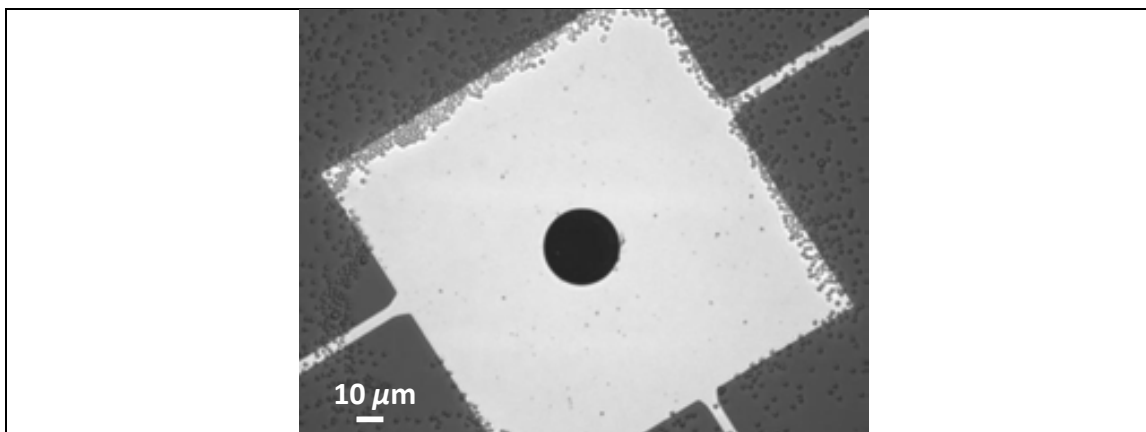


Figure 7.6: Repulsion of P^- tracers from Ru disk on an Au-Ru device exposed to $\frac{1}{2}$ wt% H_2O_2 solution. Disk radius is $15\mu m$. The Ru disk was deposited on a $130\mu m \times 130\mu m$ square gold area.

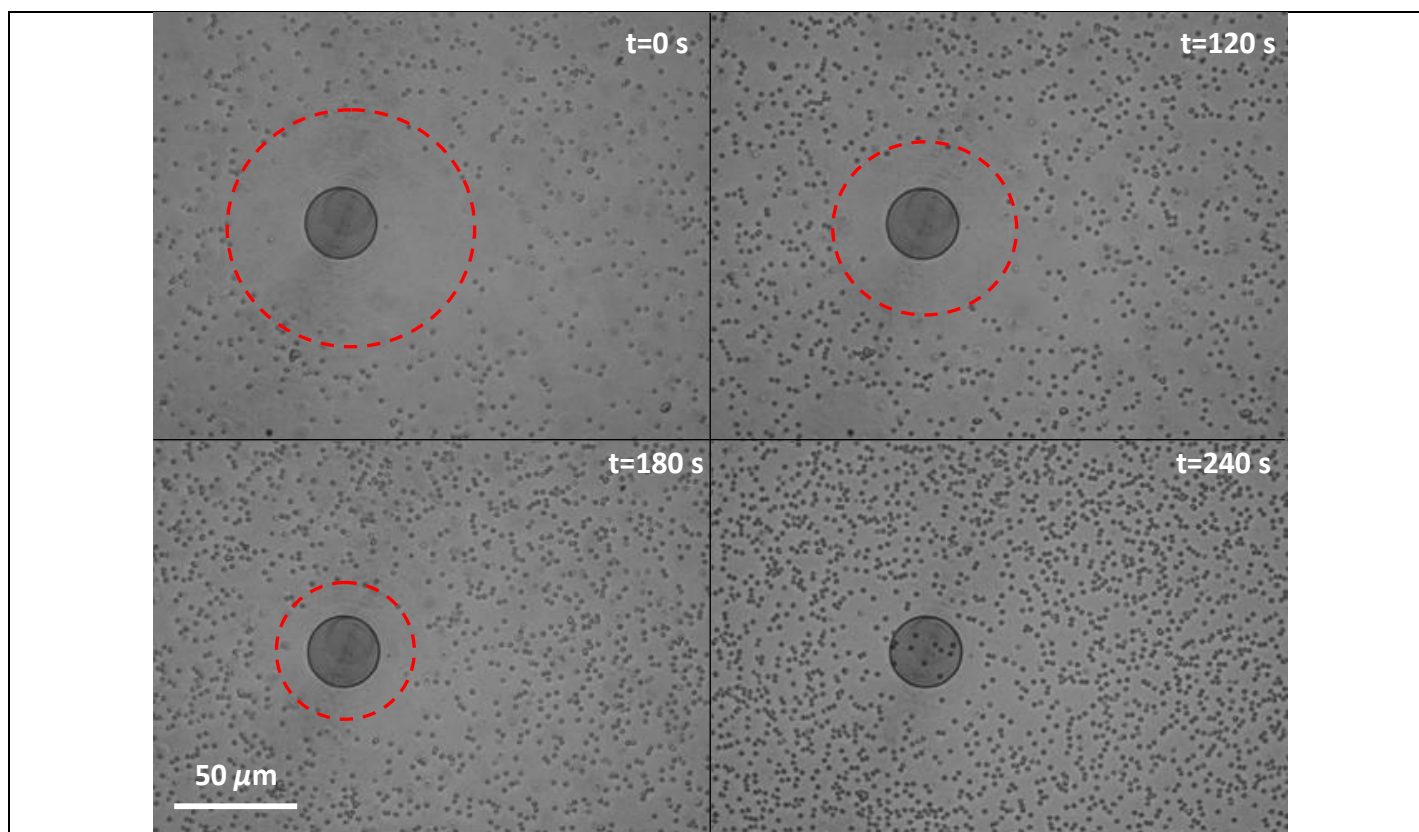


Figure 7.7: Repulsion of P^- tracers from Ru disk on an Au-Ru device exposed to $\frac{1}{2}$ wt% H_2O_2 solution. The red dash line represents the area from which the tracers were repulsed. The radius of the red dash line decreases and finally becomes zero with time. Disk radius is $15\mu m$.

7.2.2 Ni-Cu Devices

The P^- tracers are repulsed from the Cu disk (figure 7.8 a) and P^+ tracers attract to the disk (figure 7.8 b). Although the positively charged tracers move toward the disk, the maximum radial velocity is less than $2\mu\text{m}\cdot\text{s}^{-1}$ (figure 7.9). Again the response of the tracers to the electrokinetic parameters seems to be in line with the electrochemical reactions predicted by the TAFEL measurements.

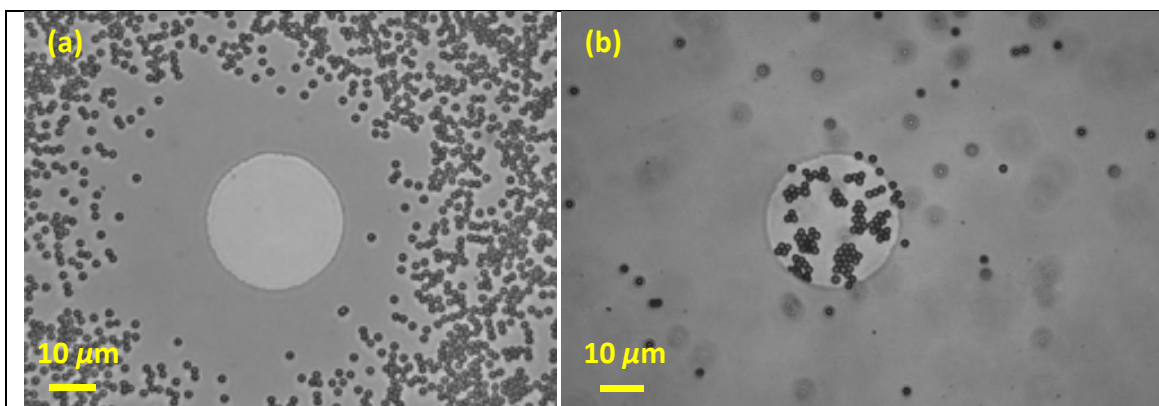


Figure 7.8: a) Repulsion of P^- tracers from Cu disk b) Attraction of P^+ tracers to the Cu disk on a Ni-Cu device. The device was exposed to 1 wt% H_2O_2 solution. Disk radius is $15\mu\text{m}$.

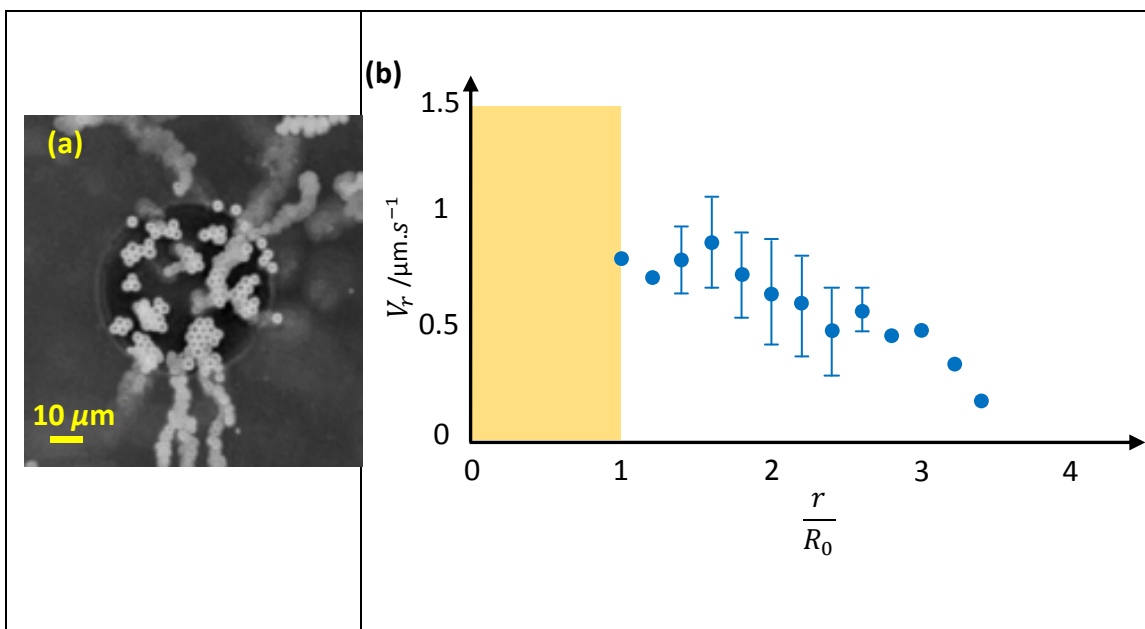


Figure 7.9: a) Tracking of P^+ tracers around a Ni-Cu device b) average radial velocity (V_r) of P^+ tracers versus normalized distance to disk center at 1 wt% hydrogen peroxide solution. r and R_0 are the distances of the particle from the disk center and disk radius respectively. Disk radius (R_0) is $25\mu\text{m}$. The $\frac{r}{R_0}$ values are equal to 0 and 1 at the platinum disk center and platinum disk border respectively. Overlap technique was applied to produce tracks.

7.2.3 Cu-Ni Devices

It is expected that inverting the configuration of the Ni-Cu system does not affect the redox role of the electrodes and only produces the inversion of the interactions with the tracers.

Indeed, the positively charged tracers were repelled from the Ni disk (figure 7.10 a) and negatively charged particles attracted into the disk (figure 7.10 b). The average radial velocities of the P^- tracers increased as the distance to the Ni disk was decreased (figure 7.11). The velocity was relatively low and not more than $2\mu\text{m}\cdot\text{s}^{-1}$.

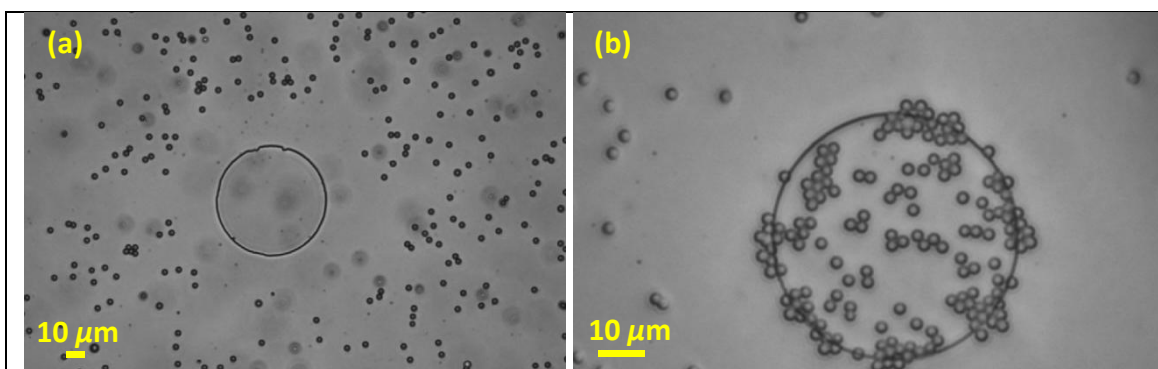


Figure 7.10: a) Repulsion of P^+ tracers from the Ni disk b) Attraction of P^- tracers to the Ni disk on a Cu-Ni device. The device was exposed to 1wt % H_2O_2 solution. Disk radius is $15\mu\text{m}$.

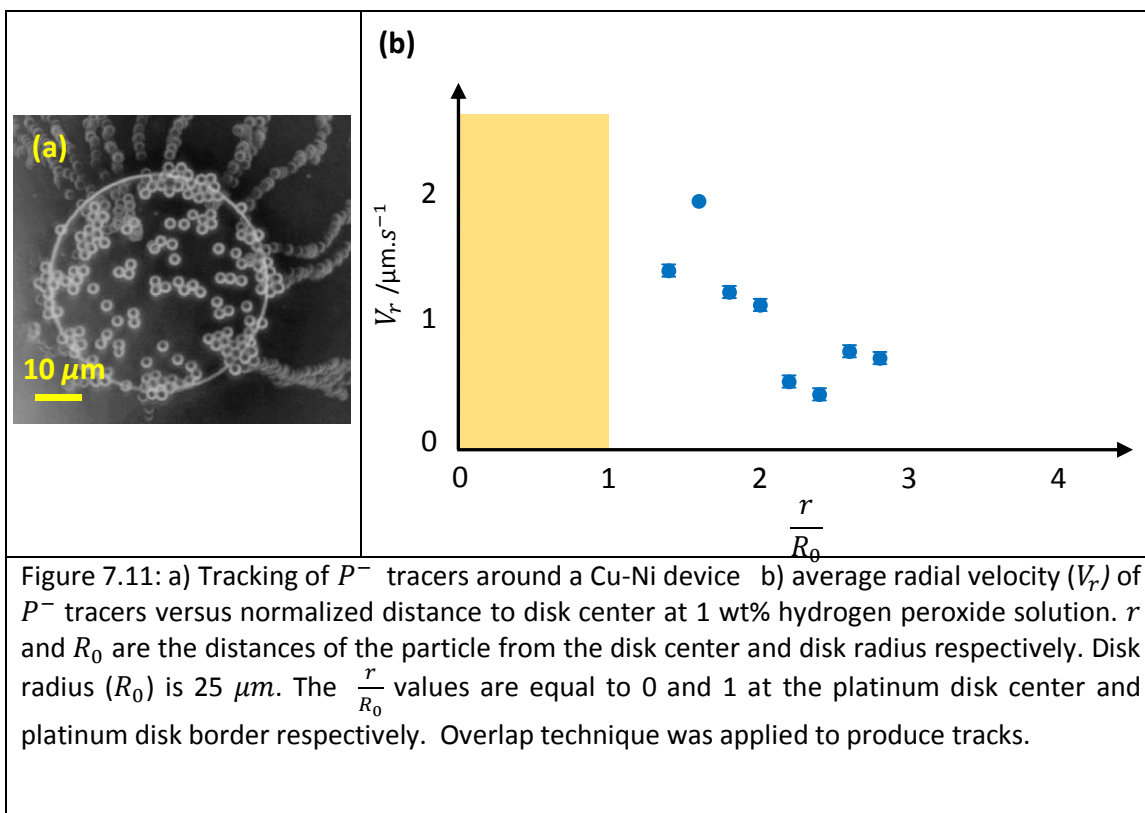


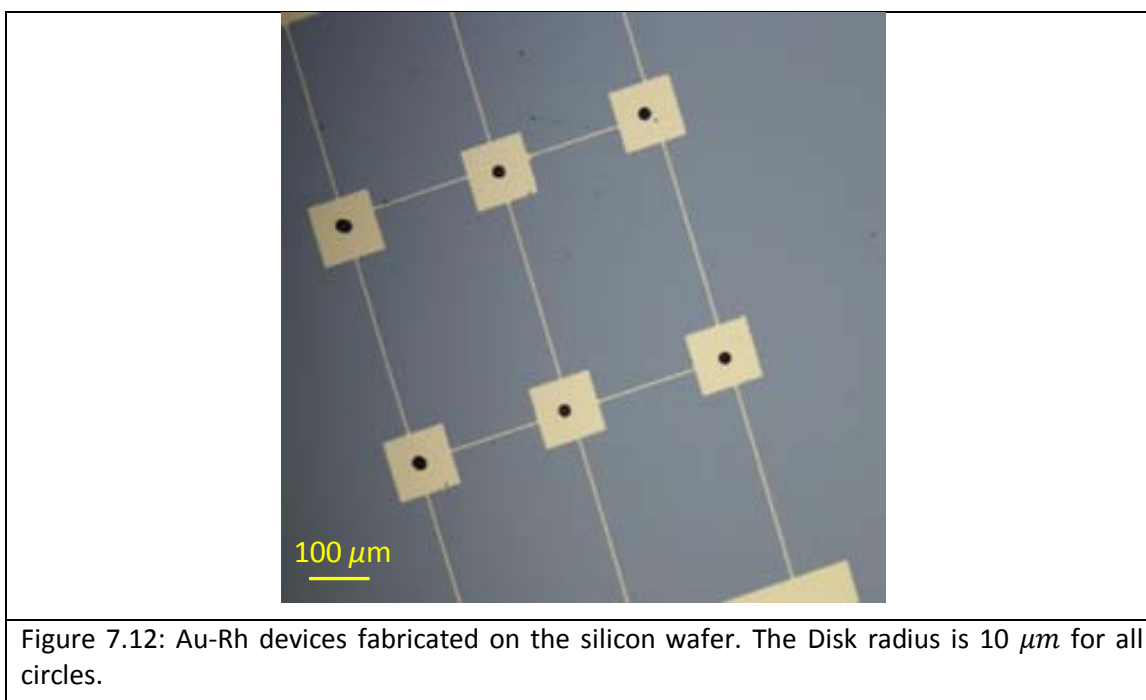
Figure 7.11: a) Tracking of P^- tracers around a Cu-Ni device b) average radial velocity (V_r) of P^- tracers versus normalized distance to disk center at 1 wt% hydrogen peroxide solution. r and R_0 are the distances of the particle from the disk center and disk radius respectively. Disk radius (R_0) is $25\mu\text{m}$. The $\frac{r}{R_0}$ values are equal to 0 and 1 at the platinum disk center and platinum disk border respectively. Overlap technique was applied to produce tracks.

7.2.4 Au-Rh Devices

Similar to the case of Au- Ru devices, the procedure F3 based in the Rh electroplating is a qualified fabrication procedure for Au- Rh devices. Figure 7.12 shows the rhodium disks with radius equal to $10\ \mu\text{m}$ on the gold surface. The gold wires connect the gold squares together in order to insure the conductivity required to deposit the rhodium layer. Similar to Ru layer, The Rh layer generates oxygen bubble from decomposition of hydrogen peroxide .Therefore, the experiments were done with the small disks (radius: $10\ \mu\text{m}$) at $\frac{1}{4}$ wt% H_2O_2 solution to avoid bubbling⁸³.

Regarding the interactions, P^+ tracers are attracted into the Rh disk, a fact that was expected according to the TAFEL predictions for this system (figure 7.13 a). The average radial velocities of the P^+ tracers increase as the distance between them and disk center decrease (figure 7.14).

However the interaction of the P^- tracers and Ru disk is different from the usual ones (figure 7.2). The P^- tracers (silica particles) move toward the Rh disk and they form a silica crystal around the Rh disk instead of settling on the disk (figure 7.13 b). Figure 7.15 shows the growth of silica crystal. As an interesting feature, the crystal grows in two layers of silica spheres (figure 7.16). In figure 7.16 a, the border of two silica layers were marked with blue and red dash lines on top view of the crystal around the disk. Blue and red dash lines are borders of the first and second silica layer respectively. Silica spheres join the crystal and build the first layer. Some of the tracers directly settle on top of the first layer and build the second one. Figure 7.16 b illustrates the growth of the layers schematically. Although this behavior resembles in certain aspects to the one found with Au-Pt systems, further investigations are required to understand this process.



⁸³ Rhodium is another efficient catalyst for the non-electrochemical decomposition of H_2O_2 into O_2 and H_2O in absence of another electrode.

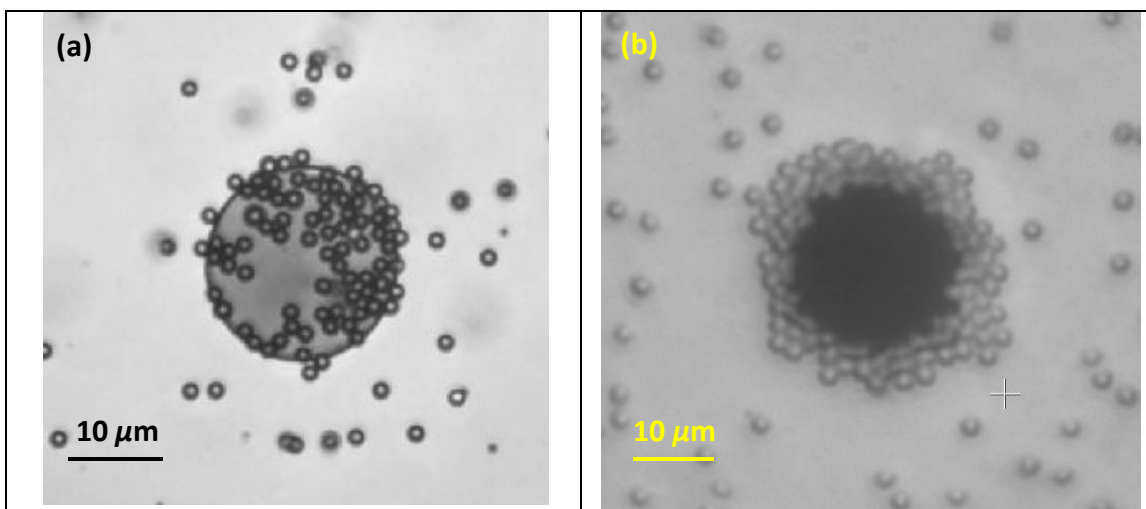


Figure 7.13: a) Attraction of P^+ tracers to the Rh disk b) Attraction of P^- tracers to the Rh disk on an Au- Rh device. The device was exposed to the $\frac{1}{4}$ wt% H_2O_2 solution. The disk radius was $10\mu m$.

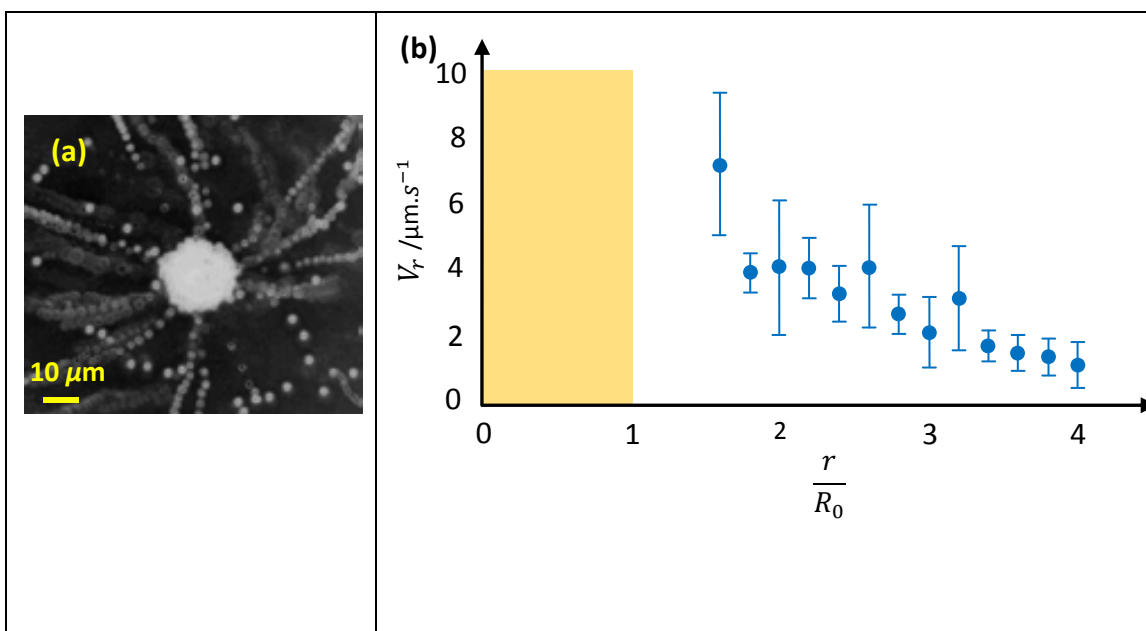


Figure 7.14: a) Tracking of P^+ tracers around an Au-Rh device b) average radial velocity (V_r) of P^+ tracers versus normalized distance to disk center at $\frac{1}{4}$ wt% hydrogen peroxide solution. r and R_0 are the distances of the particle from the disk center and disk radius respectively. Disk radius (R_0) is $10\mu m$. The $\frac{r}{R_0}$ values are equal to 0 and 1 at the platinum disk center and platinum disk border respectively. Overlap technique was applied to produce tracks.

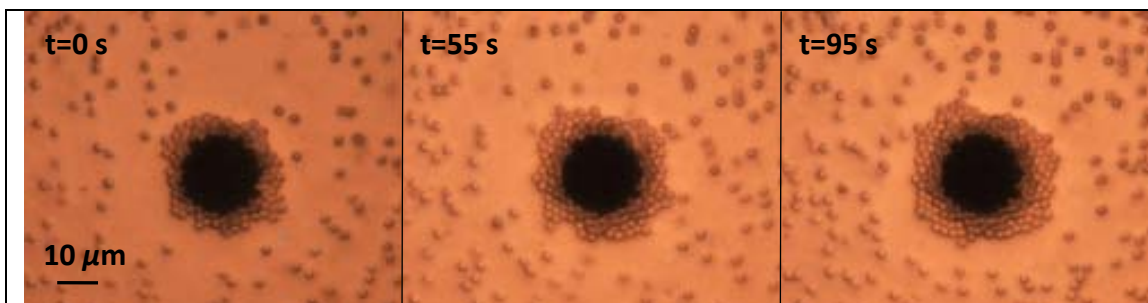


Figure 7.15: Attraction of P^- tracers to the Rh disk. The device was exposed to the $\frac{1}{4}$ wt% H_2O_2 solution. Disk radius was $10\mu\text{m}$.

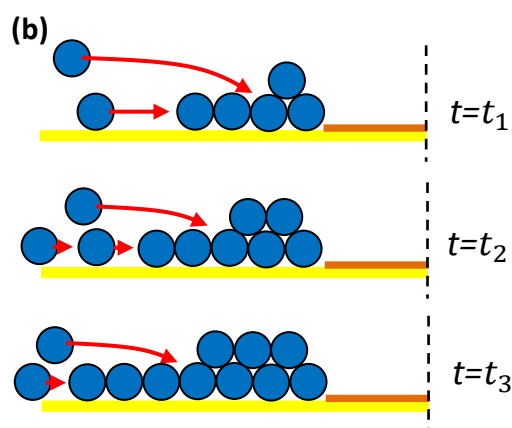
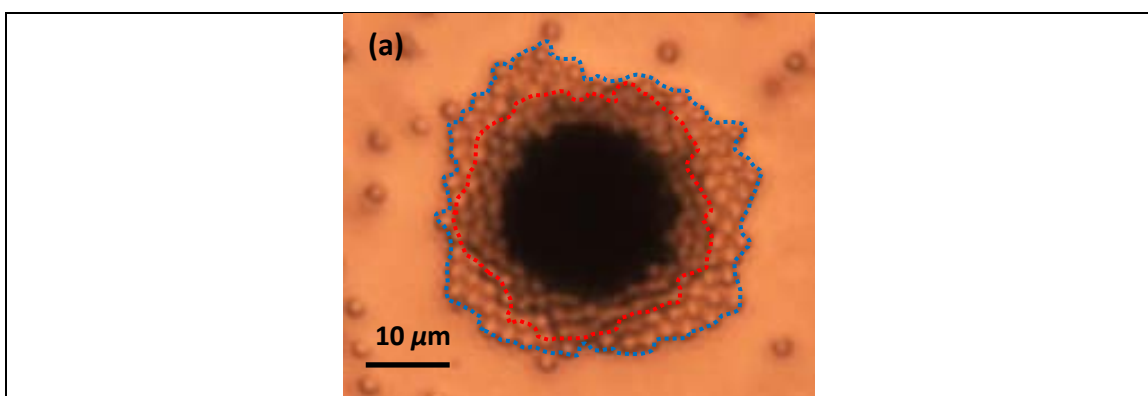
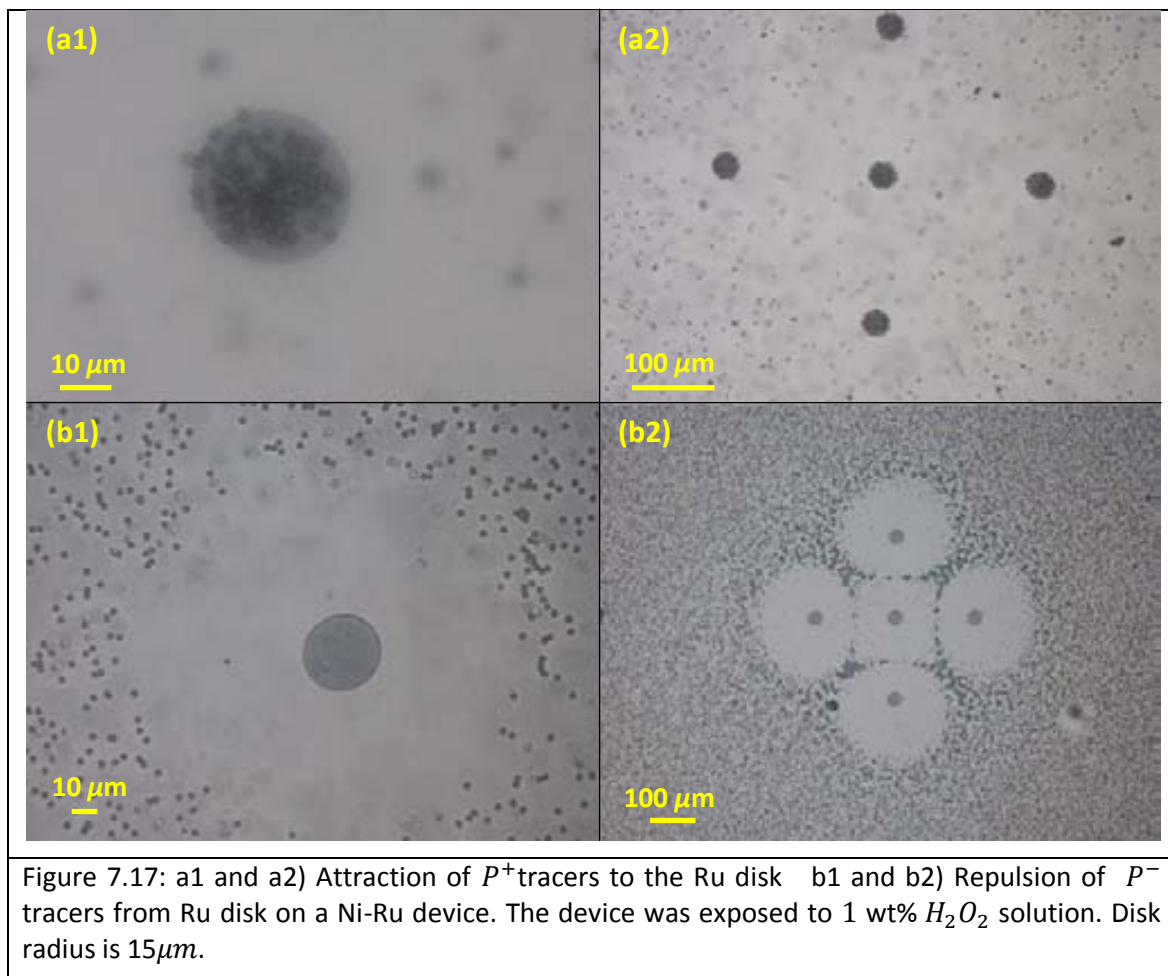


Figure 7.16 a) the border of two silica layers around the Rh disk. Blue and red dash lines are the borders of the first and second silica layer respectively. b) Schematic illustration of silica crystal growth around the Rh disk. Silica spheres join the crystal and build the first layer. Some of the tracers directly settle on top of the first layer and build the second one.

7.2.5 Ni-Ru Devices

Positively charged tracers are attracted into the Ru disk in presence of 1 wt% H_2O_2 solution (figure 7.17 a1 and a2) again in line with the TAFEL predictions. P^+ Tracers move toward the ruthenium disk and settle on it. The average radial velocity increases as the P^+ tracers become closer to the disk (figure 7.18).

Negatively charged tracers are repelled from the ruthenium disk (figure 7.17 b1 and b2). It was observed that an array of four Ru disks with radius of $15 \mu m$ can form a relatively large repulsive area in four-leaf clover shape (figure 7.19). Outside of repulsive bands, clusters form. Some of the particles located between two disks are trapped between two repulsive bands. The particle density on this restricted area is very high and the particles form clusters. Similar to what was discussed with the interaction of silica particles and Au- Pt devices (chapter 6), initial repulsions from two disks are very important in the local cluster formation. Gradually, most of the particles and clusters between the disks are pushed out and the repulsive area becomes larger. After long time, the clusters fall apart into individual particles.



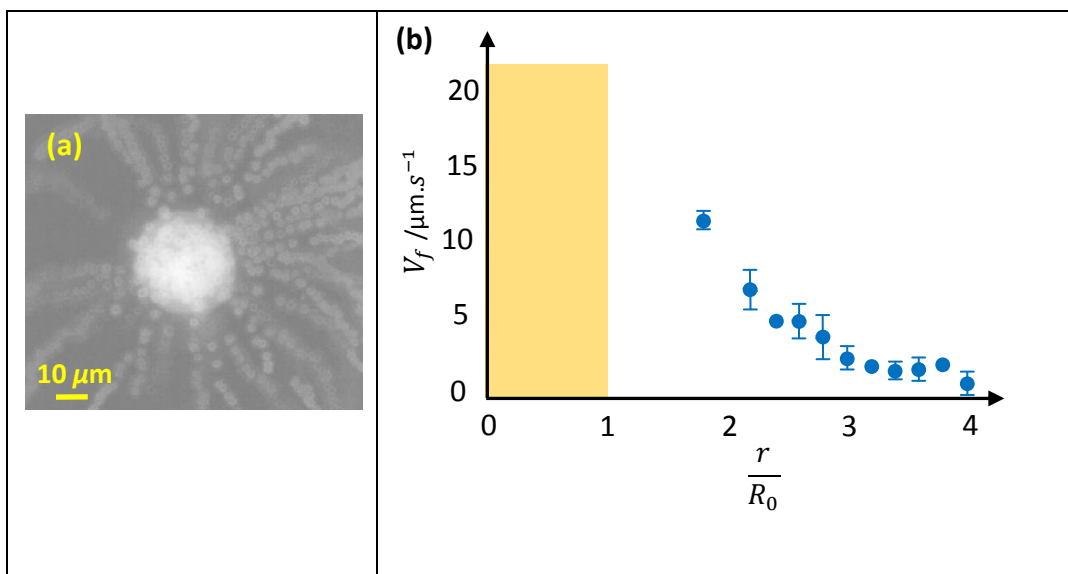


Figure 7.18: a) Tracking of P^+ tracers around a Ni-Ru device b) average radial velocity (V_r) of P^+ tracers versus normalized distance to disk center at 1 wt% hydrogen peroxide solution. r and R_0 are the distances of the particle from the disk center and disk radius respectively. Disk radius (R_0) is $15 \mu m$. The $\frac{r}{R_0}$ values are equal to 0 and 1 at the platinum disk center and platinum disk border respectively. Overlap technique was applied to produce tracks.

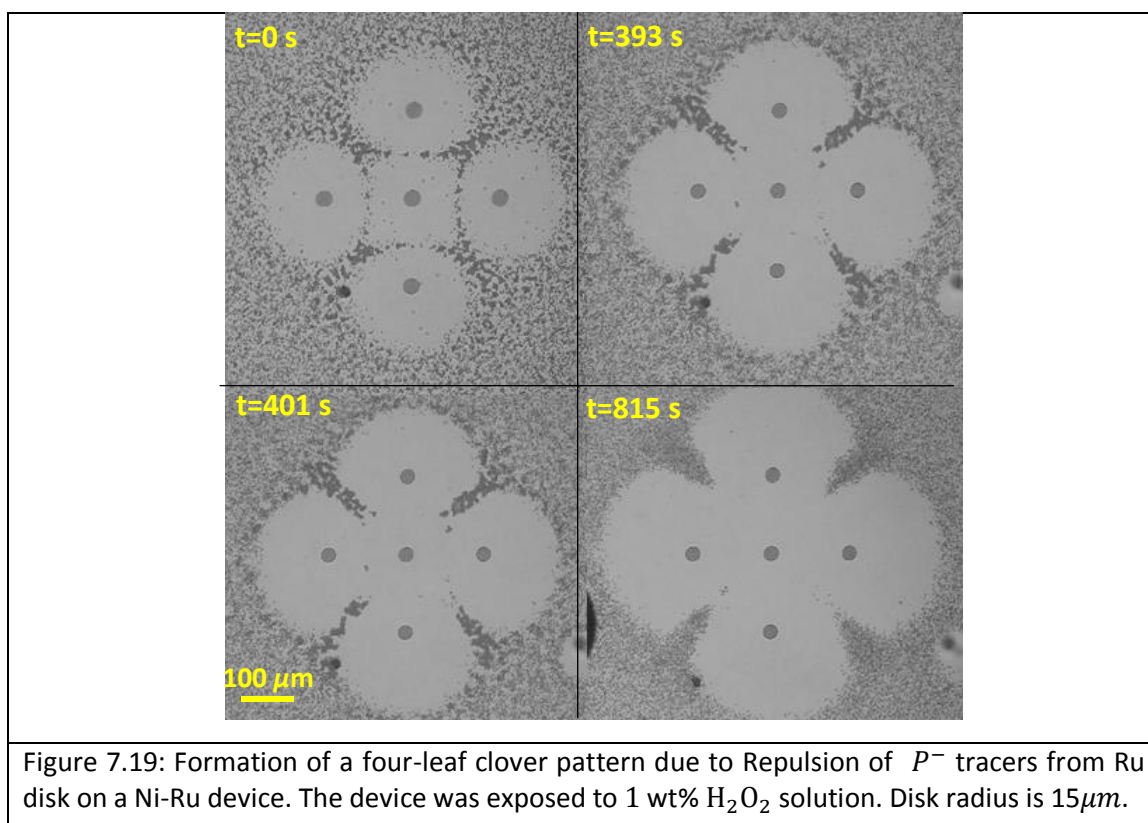


Figure 7.19: Formation of a four-leaf clover pattern due to Repulsion of P^- tracers from Ru disk on a Ni-Ru device. The device was exposed to 1 wt% H_2O_2 solution. Disk radius is $15 \mu m$.

7.2.6 Ni-Ag Devices

In the case of Ni-Ag devices, positively charged tracers are attracted into the Ag disk (figure 7.20 a) as expected. The average radial velocity of the P^+ tracers increases as the distance to the disk center decreases (figure 7.21). On the other side, negatively charged tracers are repelled from the silver disk (figure 7.20 b).

Some interesting behaviors of positively charged particles during interaction with Ni-Ag devices have been captured. Figure 7. 22a illustrates one of them. When the P^+ tracers arrive to the Ag disk, they tend to settle on the area of silver disk but far from the disk center. A ring of P^+ tracers is formed on the silver disk. The incoming tracers join into the inner border of the ring or settle on top of the tracers which form the ring. The tracers which come from higher elevations move toward the disk center, change their motion direction to join the inner border of the ring. Even tracers which come from the higher elevation to the disk center, show this behavior. Figure 7.22 b illustrates this kind of motion schematically.

Another kind of interaction between P^+ tracers and Ni-Ag device is presented in figure 7.23. In this case the tracers move toward the silver disk and settle more on the center of the disk. The other incoming tracers join the settled tracers to start forming an ordered hexagonal monolayer. Some of the incoming tracers settle on top of the others to start growing a second layer.

The reason of such behaviors is still not clear and needs more exploration. It could be related with the appearance of oxidized sites on the silver which could dictate the nucleation of the colloidal aggregates. In some cases (such as Au-Pt or Si-Pt, Si-Au which will be discussed later), it has been observed that oxygen functionalities on the metal induced by the plasma treatment help to immobilize the colloidal tracers on their surfaces. That shows that changes in the surface chemistry of the materials exert important influence in the nucleation and growth of adlayers on a surface.

A clear example of silver oxidation with time is shown in figure 7.24. The darker areas or dots on the silver surface correspond to oxidized sites. In the figure it can be observed that the oxidation seems to start from the edges of the Pt disk. The pump stops working when the extent of oxidation is very high (figure 7.24).

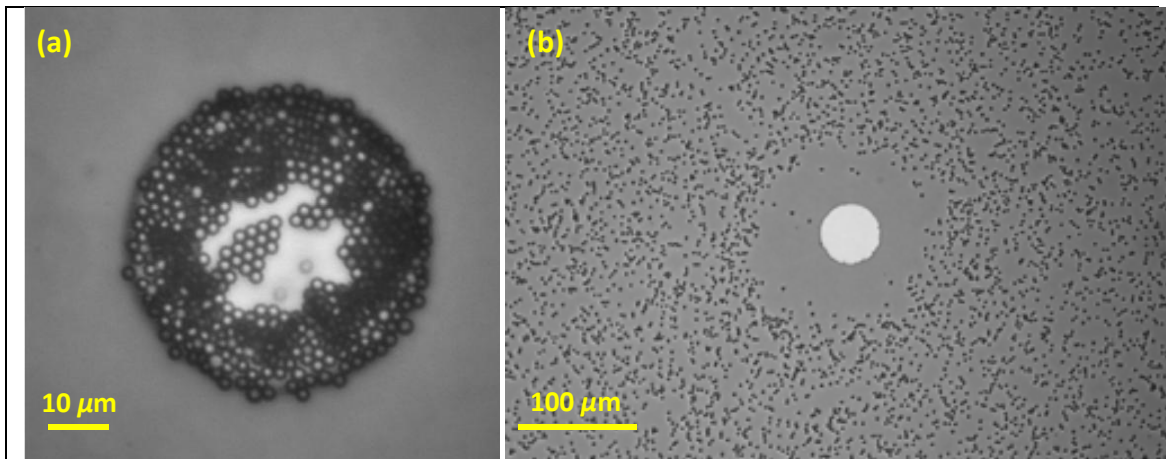


Figure 7.20: a) Attraction of P^+ tracers to the Ag disk b) Repulsion of P^- tracers from Ag disk on a Ni-Ag device. The device was exposed to 1 wt% H_2O_2 solution.

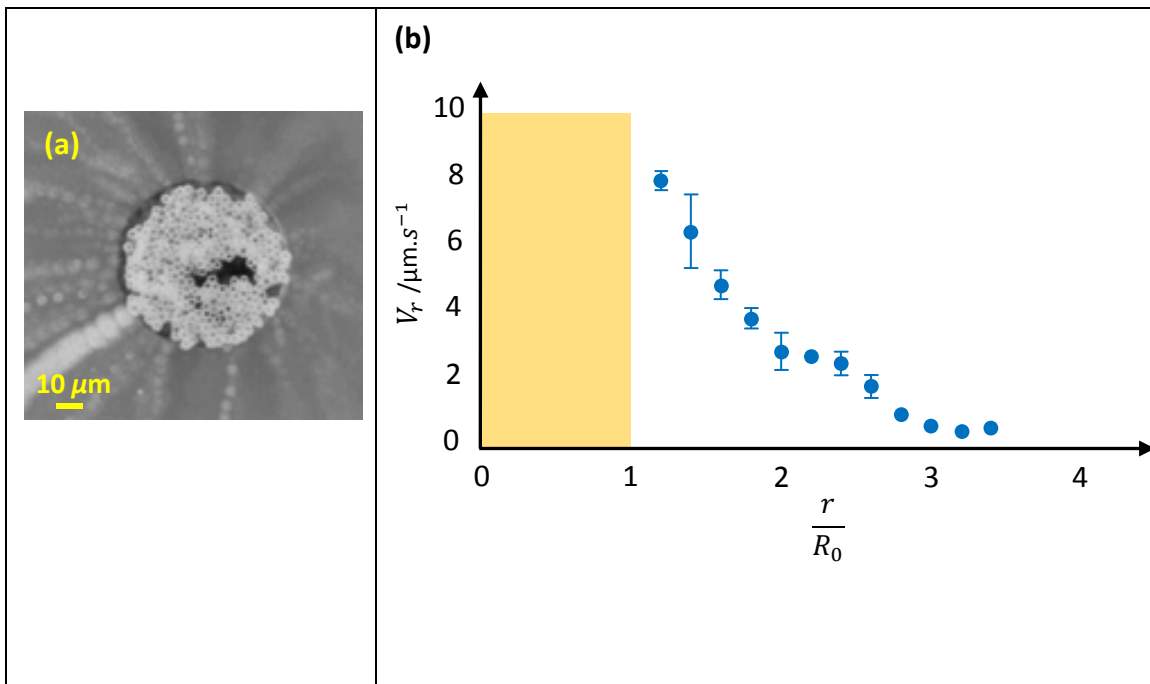
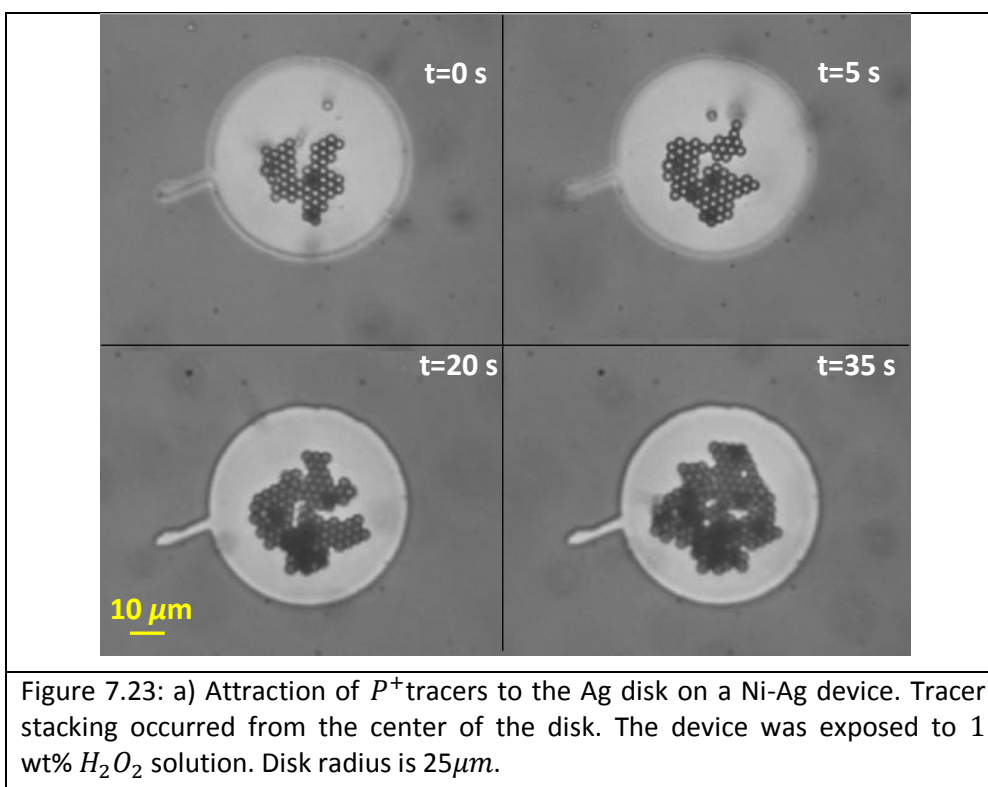
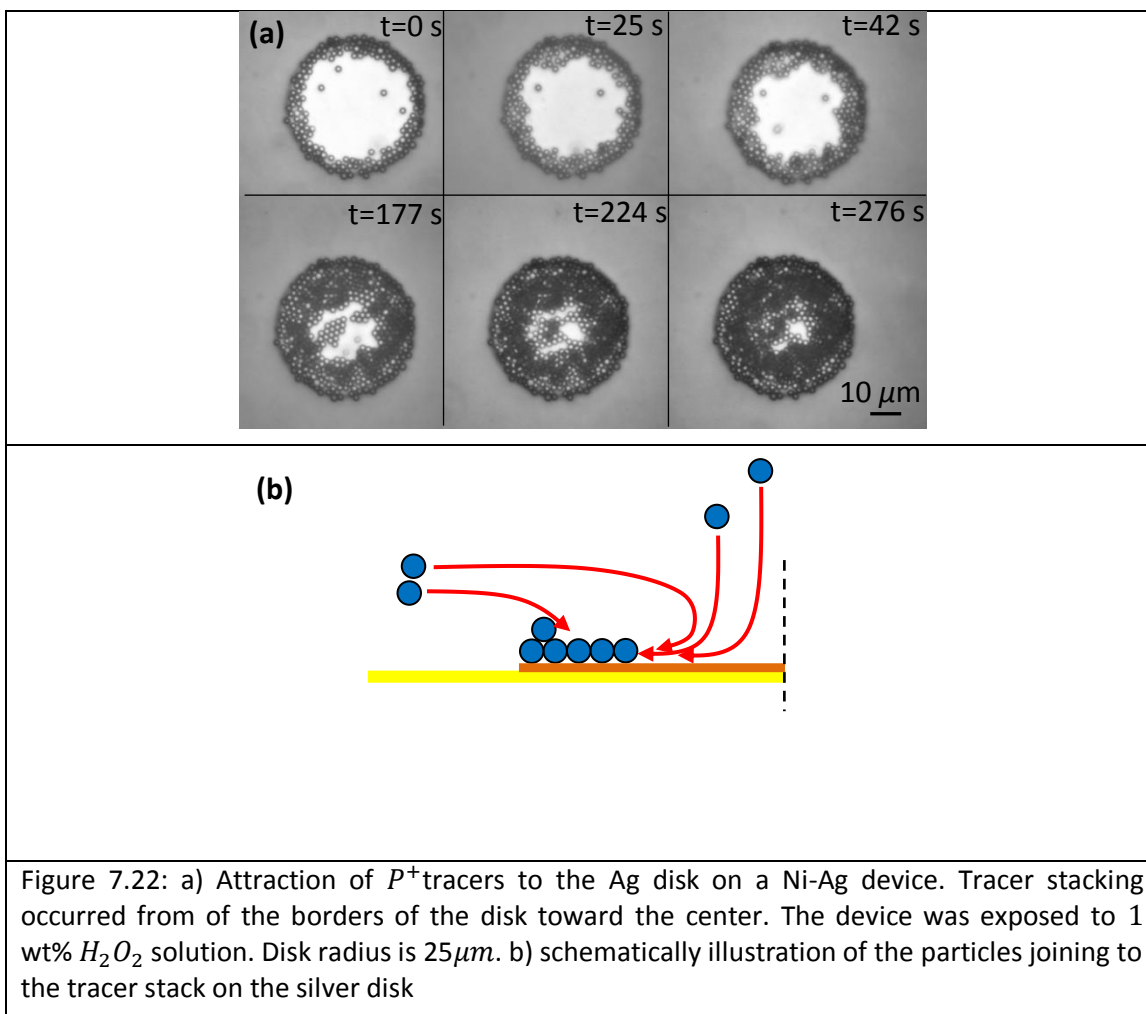
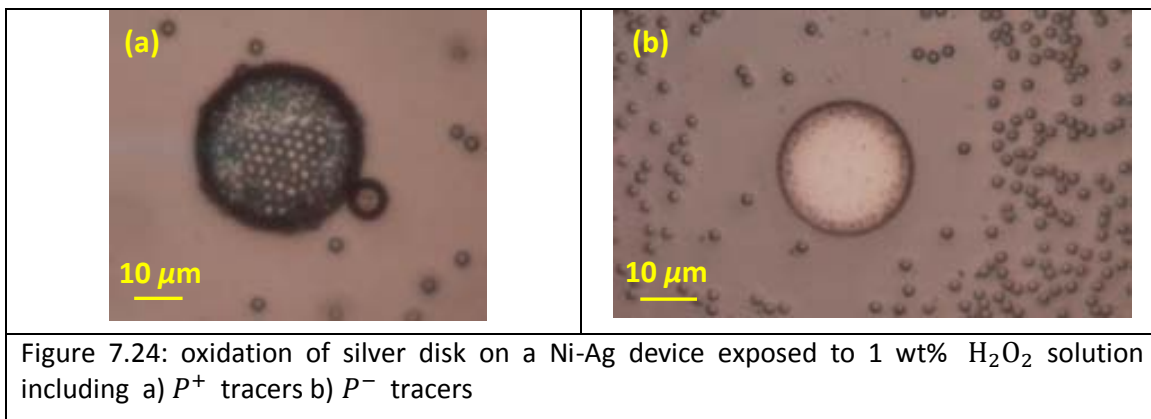


Figure 7.21: a) Tracking of P^+ tracers around a Ni-Ag device b) average radial velocity (V_r) of P^+ tracers versus normalized distance to disk center at 1 wt% hydrogen peroxide solution. r and R_0 are the distances of the particle from the disk center and disk radius respectively. Disk radius (R_0) is $25 \mu\text{m}$. The $\frac{r}{R_0}$ values are equal to 0 and 1 at the platinum disk center and platinum disk border respectively. Overlap technique was applied to produce tracks.





7.2.7 Cu-Ag

The fabrication of Cu-Ag devices was done by applying stencil lithography. So, there was no PMMA in the process. The silver disk attracts the P^+ tracers (figure 7.25 a) and repels the P^- ones (figure 7.25 b) in agreement with TAFEL predictions.

Appearance of darker dots on the silver disk and the copper substrate in the vicinity of the Ag disk was observed in the devices. Oxidation of silver and copper can explain the formation of these darker dots on their surfaces [5, 6].

Figure 7.26 shows that the density of black dots increases with passing time. The silver disk oxidized gradually until the whole disk becomes completely dark. Interesting to see on the copper side is an emerging band of darker oxidized area around the silver disk with time. This area delimits the more active corrosion area of copper which could be enhanced by the proton production in this part [5, 6]

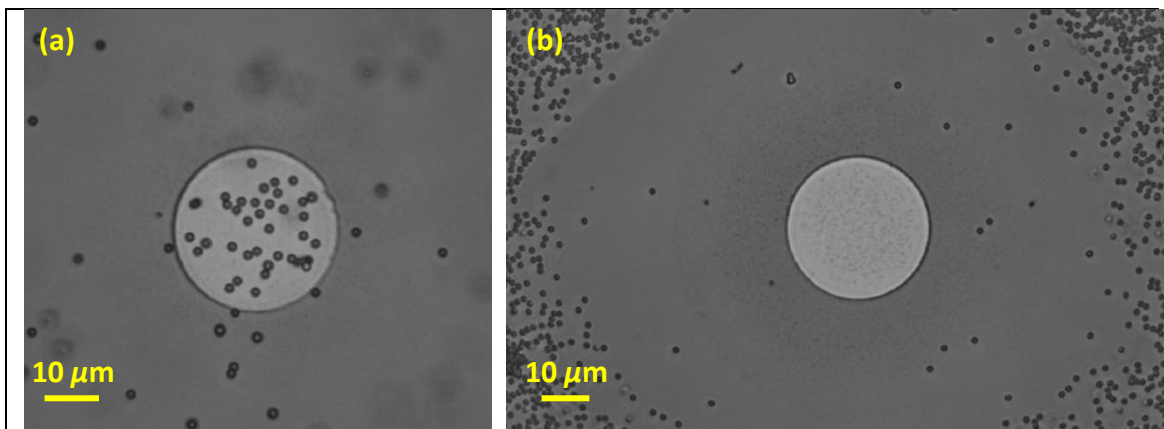


Figure 7.25: a) Attraction of P^+ tracers to the Ag disk b) Repulsion of P^- tracers from Ag disk on a Cu-Ag device. The device was exposed to 1 wt% H_2O_2 solution. Disk radius is $15\mu m$.

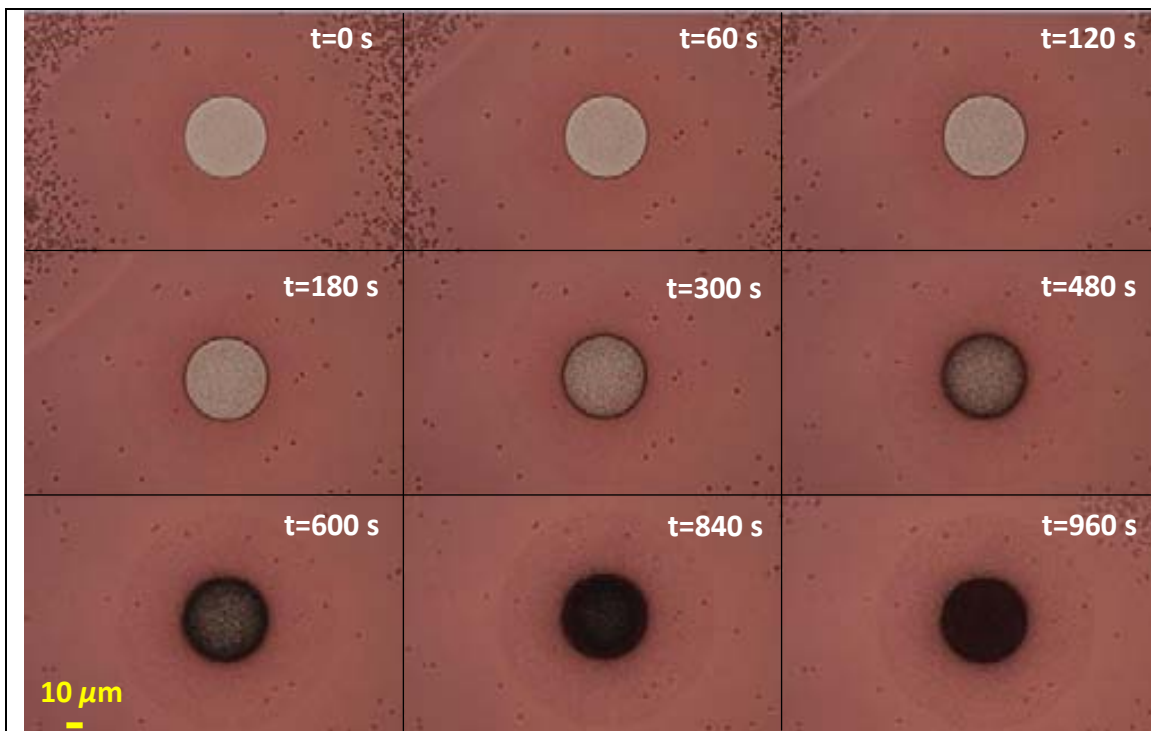


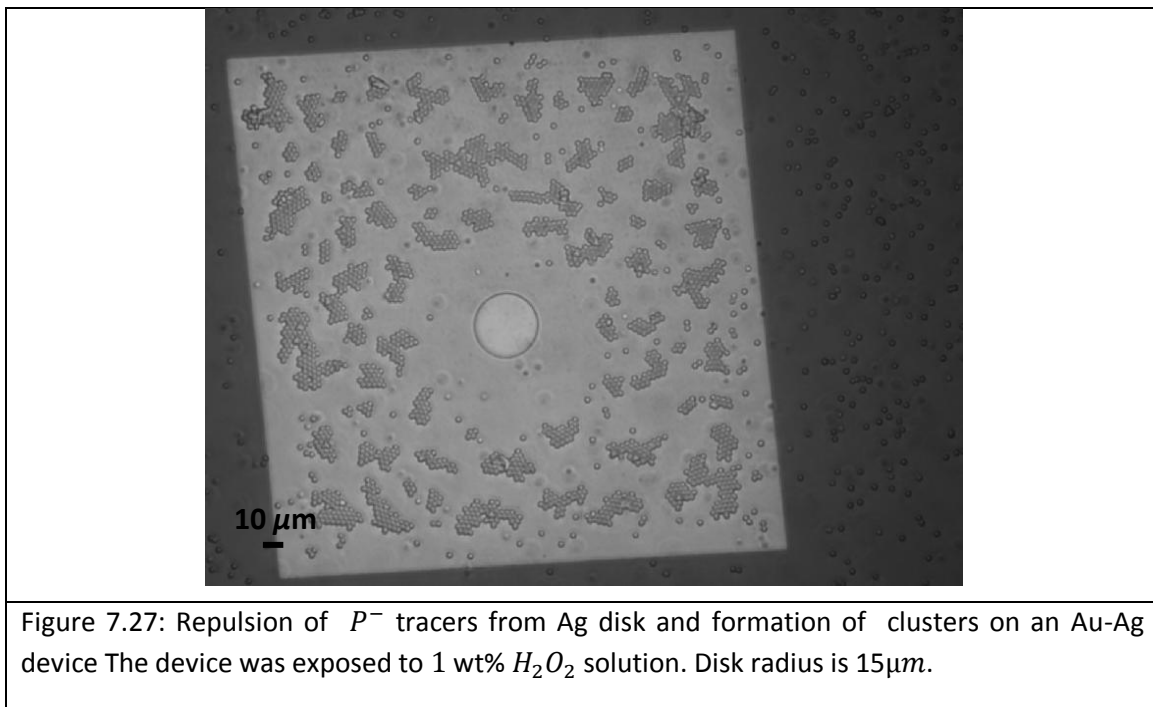
Figure 7.26: Repulsion of P^- tracers from Ag disk on a Cu-Ag device. The device was exposed to 1 wt% H_2O_2 solution. Disk radius is $25\mu m$. Oxidation of copper and silver occurs in the system.

7.2.8 Au-Ag

As mentioned, the Au-Ag system has been a model system to study catalytic micropumps by previous groups [7-10]. However nothing was mentioned about the stability of these devices. In order to approach this topic let's concentrate on the interaction of negatively charged tracers (silica beads) and the device. When the device is exposed to the 1 wt% H_2O_2 solution including P^- tracers, the repulsion of the tracers occurs (Figure 7.27). That is in agreement with previous results and with the TAFEL plots presented in this chapter in which was predicted that gold would act as anode and silver as cathode. Under this scenario the electric field is pointing from the gold to the silver repelling the negative tracer from the cathode disk.

Interesting to see is the silica clusters formation just on the gold surface out of the repulsive band, a feature also shared with the Au-Pt system. However and in contrast to the Au-Pt device, the clusters do not move toward the silver disk. Although it seems that the interacting forces and the pH are enough to start clustering, the decrease of the zeta potential of the silica is not so effective as in the case of the Au-Pt to trigger the transport towards the silver disk. Let's recall that in order to start moving the zeta potential of the silica should decrease enough so that the fluid velocity could dominate over the electrophoretic contribution.

Figure 7.28 shows the other levels of the interaction. The size of clusters increase with time by joining the silica particles repulsed from the disk, particles coming from higher elevations or by adjoining neighbor clusters. During that process the silver disk oxidizes and becomes darker and darker. When the silver disk is completely oxidized, the electrochemical reaction rates decay due to the change of the surface chemistry of the electrodes and consequently also the electrohydrodynamic effects. The repulsion of silica tracers stops. A few silica particles start moving and settling on the disk. Due to the declination of the electrohydrodynamic forces and proton production all the clusters formed on the gold surface fall apart to the single beads and start occupying the repulsive band. Accordingly to all these observations, the lifetime of these pumps could be much less than ten minutes.



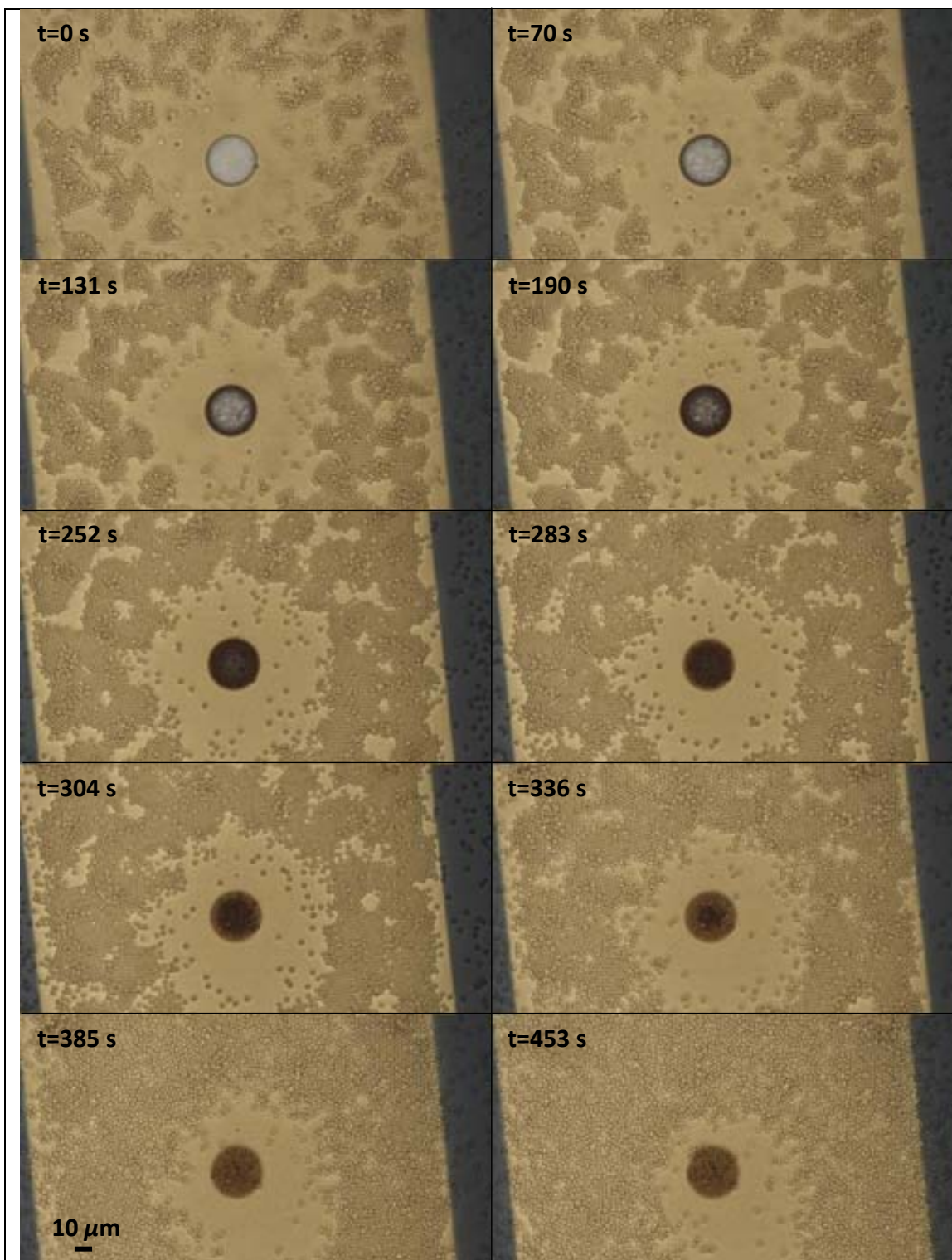


Figure 7.28: Levels of interaction between P^- tracers and Au-Ag device. The device was exposed to 1 wt% H_2O_2 solution. Disk radius is $15 \mu\text{m}$.

Conclusion

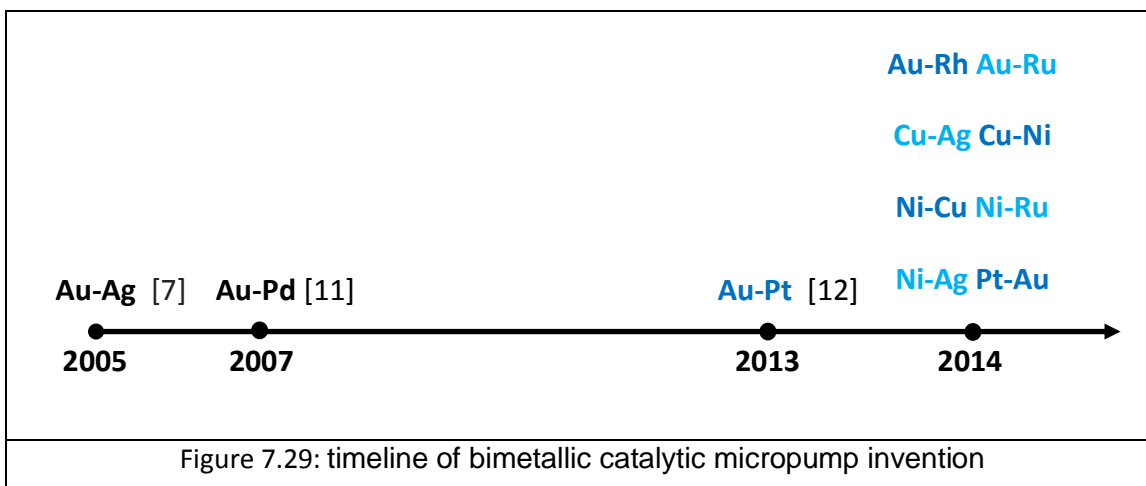
A general overview of alternative bimetallic X-Y micropumps was presented. Although some of the chosen materials are less noble than the Au-Pt system and could degrade with time, these systems could represent a more low cost alternative in applications which do not demand high lifetime devices.

TAFEL plots were used to predict potential X-Y systems based on their mixed potential which helps to assign the redox role of the metals when they are connected. The TAFEL plots could also provide information of the driving force of these pumps by evaluating the difference between their mixed potentials. However since the materials are not so noble and could undergo oxidative degradation, an accurate evaluation of such parameter is not so straightforward. A summary of the predictions and the results of the experiments are presented in the table 7.2. Except in the case of the interaction between Au-Rh device and negatively charged particles, the predictions were correct.

Many interesting phenomena have been captured with these X-Y bimetallic systems which require further investigation. However the idea was to settle a preliminary basis for future and detailed studies.

In summary, finding some X-Y systems which have potential to be applied in the micropumps is an important achievement. Figure 7.29 shows the timeline of bimetallic catalytic micropump invention. Besides Au-Ag [7] and Au-Pd [11], the rest of the systems (Au-Pt [12], Au-Rh, Au-Ru, Cu-Ag, Cu-Ni, Ni-Cu, Ni-Ru, Ni-Ag and Pt-Au) were introduced under scope of this dissertation.

| X-Y System | Prediction as per TAFEL plot | | | | Experimental result | |
|------------|------------------------------|---------|------------------|---------------|---------------------|-------------------|
| | Anode | Cathode | Interaction with | | Interaction with | |
| | | | P^+ tracers | P^- tracers | P^+ tracers | P^- tracers |
| Au-Rh | Au | Rh | Attraction | Repulsion | Attraction | Attraction |
| Au-Ru | Au | Ru | Attraction | Repulsion | Attraction | Repulsion |
| Cu-Ag | Cu | Ag | Attraction | Repulsion | Attraction | Repulsion |
| Cu-Ni | Ni | cu | Repulsion | Attraction | Repulsion | Attraction |
| Ni-Cu | Ni | Cu | Attraction | Repulsion | Attraction | Repulsion |
| Ni-Ru | Ni | Ru | Attraction | Repulsion | Attraction | Repulsion |
| Ni-Ag | Ni | Ag | Attraction | Repulsion | Attraction | Repulsion |



References:

- [1] J. Chaston, "The oxidation of the platinum metals," *Platinum Met Rev*, vol. 19, p. 135, 1975.
- [2] T. Aaltonen, M. Ritala, T. Sajavaara, J. Keinonen, and M. Leskelä, "Atomic layer deposition of platinum thin films," *Chemistry of materials*, vol. 15, pp. 1924-1928, 2003.
- [3] T. Aaltonen, M. Ritala, Y.-L. Tung, Y. Chi, K. Arstila, K. Meinander, *et al.*, "Atomic layer deposition of noble metals: Exploration of the low limit of the deposition temperature," *Journal of materials research*, vol. 19, pp. 3353-6658, 2004.
- [4] T. Aaltonen, "Atomic layer deposition of noble thin films " PhD, University of Helsinki, 2005.
- [5] D. Scott and G. T. Miller, "Oxidation of Copper Single Crystals in Aqueous Solutions of Inorganic Salts IV Effect of pH on Oxide Topography in and Solutions," *Journal of The Electrochemical Society*, vol. 113, pp. 883-886, 1966.
- [6] D.-T. Wasser, *Internal corrosion of water distribution systems*: The Foundation, 1996.
- [7] T. R. Kline, W. F. Paxton, Y. Wang, D. Velegol, T. E. Mallouk, and A. Sen, "Catalytic Micropumps: Microscopic Convective Fluid Flow and Pattern Formation," *Journal of the American Chemical Society*, vol. 127, pp. 17150-17151, 2005/12/01 2005.
- [8] T. R. Kline, J. Iwata, P. E. Lammert, T. E. Mallouk, A. Sen, and D. Velegol, "Catalytically driven colloidal patterning and transport," *The Journal of Physical Chemistry B*, vol. 110, pp. 24513-24521, 2006.
- [9] J. Zhang and J. Catchmark, "A catalytically powered electrokinetic lens: toward channelless microfluidics," *Microfluidics and Nanofluidics*, vol. 10, pp. 1147-1151, 2011/05/01 2011.
- [10] S. Subramanian and J. M. Catchmark, "Control of Catalytically Generated Electroosmotic Fluid Flow through Surface Zeta Potential Engineering," *The Journal of Physical Chemistry C*, vol. 111, pp. 11959-11964, 2007/08/01 2007.
- [11] M. E. Ibele, Y. Wang, T. R. Kline, T. E. Mallouk, and A. Sen, "Hydrazine Fuels for Bimetallic Catalytic Microfluidic Pumping," *Journal of the American Chemical Society*, vol. 129, pp. 7762-7763, 2007/06/01 2007.
- [12] A. A. Farniya, M. J. Esplandiu, D. Reguera, and A. Bachtold, "Imaging the Proton Concentration and Mapping the Spatial Distribution of the Electric Field of Catalytic Micropumps," *Physical Review Letters*, vol. 111, p. 168301, 10/14/ 2013.

Chapter 8

In this chapter the performance of a pump made from a metal in contact with a semiconductor will be evaluated. It is well known that the junction between a metal and a semiconductor generates an electric field [1, 2]. Therefore the first part of this chapter will be devoted to probe if this built-in electric field can trigger electrohydrodynamic processes in presence of pure water. This kind of semiconductor/metal system can also become a very promising device for inducing catalytic reactions activated by light which can, in turn, switch on or amplify the electrohydrodynamic process. Therefore in this part, the semiconductor/metal pump will be studied in combination with hydrogen peroxide fuel in presence of white light.

8.1 Primary experiments

The first experiments were done with the semiconductor/metal device immersed only in pure water in presence of either positively charged particles (P^+) or quasi-neutral particles (P^0). Before going into the details of the measurements, it is important to briefly recall the device layout. As mentioned in the experimental part, the semiconductor/metal device was made by patterning either platinum or gold disks on a doped silicon wafer (p or n). An adhesion layer of chromium was deposited between the platinum or gold disk and the silicon. That is important to mention since the electric field is built by the contact between the semiconductor and the chromium layer rather than with the Pt structure. In this particular case, in which there are no catalytic reactions taking place on the surface, the Pt structure would not be playing an important role in the electrodynamic processes.

Before the experiment, the devices were subjected to plasma treatment as per process C_4 (Table 4.3). As shown in figure 8.1a, the P^+ tracers move toward the platinum disk and stick to the surface. Regarding the velocity profile, figure 8.2 shows the radial velocity of positively charged tracers versus normalized distance to the disk center. As they come closer to the disk, their radial velocity increases. In the vicinity of platinum-silicon border, the average velocity reaches its maximum value of $12 \pm 2.5 \mu\text{m} \cdot \text{s}^{-1}$. Regarding the P^0 tracers, the particles move toward the disk center but the direction of motion changes after crossing the platinum-silicon border. They move in the direction which is perpendicular to the surface. They go far away from the surface more and more until leaving the volume inspected with the microscope. Figure 8.1b shows the tracking of P^0 tracers. The particles reach a maximum radial velocity of $8.5 \pm 1.25 \mu\text{m} \cdot \text{s}^{-1}$ close to the boarder.

Although no hydrogen peroxide was used in this experiment, interactions between the p-Si – Pt devices and the tracers were similar to experiments with Au-Pt devices in presence of hydrogen peroxide. Similar to Au-Pt devices, the model described in 5.3 can be applied to estimate the fluid velocity and electric field strength. The maximum values of V_f and E_r are $8.9 \mu\text{m} \cdot \text{s}^{-1}$ and $80 \text{V} \cdot \text{m}^{-1}$ respectively⁸⁴.

⁸⁴ Just for recalling chapter 5, the electric field and fluid velocity can be extracted by applying the following equation for each particle (P^+ and P^0): $V_r(r) = \frac{\epsilon \zeta P}{\eta} E_r(r) + V_f(r)$, in which the first term is the electrophoretic term of the particle and the second one is the fluid velocity.

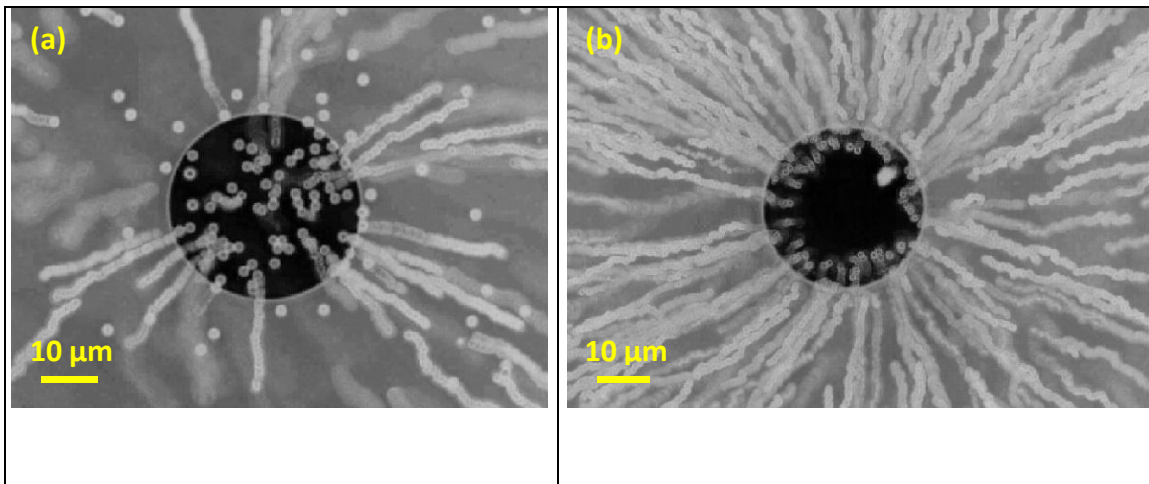


Figure 8.1: Tracking of the tracers on top of a p-Si – Pt device in water medium a) the P^+ tracers move toward the platinum disk center and settle on it. b) The P^- tracers move toward the platinum disk. After crossing the Si-Pt border, they are pushed upward. The overlap technique was used to show the movement of particles.

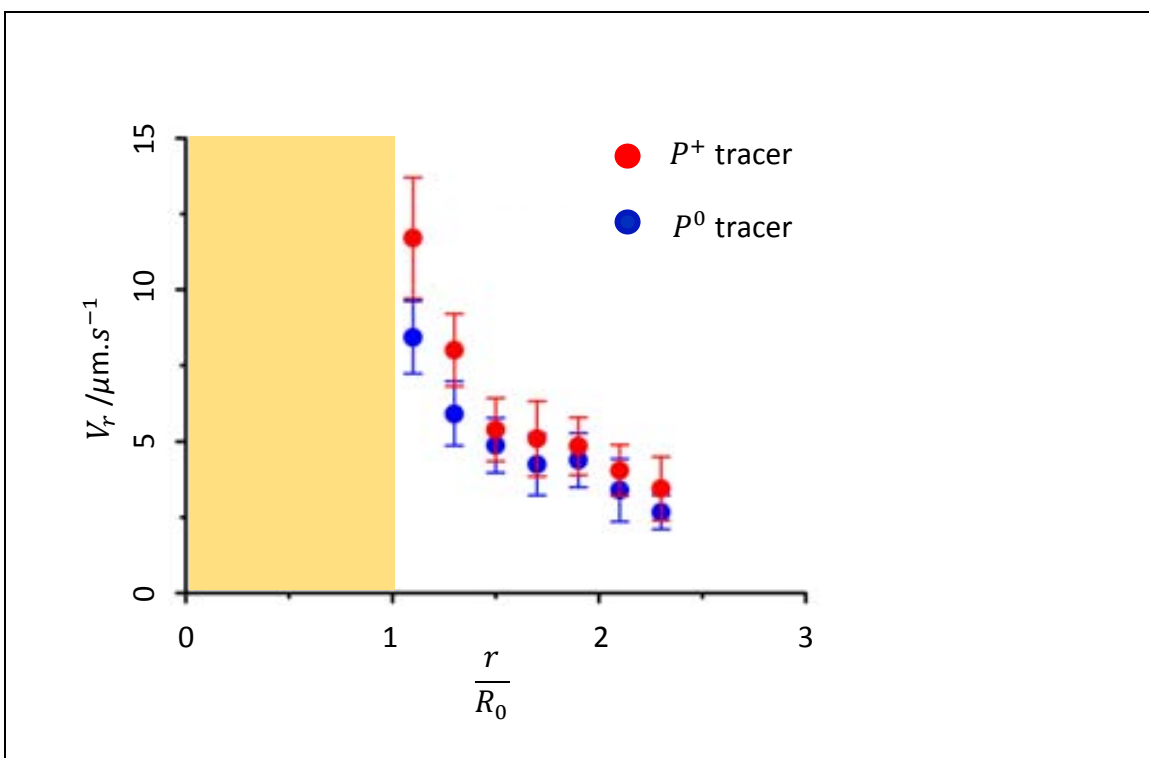


Figure 8.2: Average radial velocity (V_r) of P^+ and P^0 tracers versus normalized distance to the disk center on p-Si – Pt devices in water medium. r and R_0 are the distances of the particle from the disk center and disk radius respectively. Disk radius (R_0) is $25\mu\text{m}$. The $\frac{r}{R_0}$ values are equal to 0 and 1 at the platinum disk center and platinum disk border respectively. Yellow area represents the area above the platinum disk. Regarding the P^+ tracers, the graph represents the averaged data of 4 devices and 20 particles. For P^0 tracers, the graph obtains from data of 3 devices and 17 particles.

Figure 8.2 shows that the difference between velocity profiles of P^+ and P^0 tracers is not dramatic. Generally, the P^+ tracers move a little bit faster than P^0 tracers. Considering the model, the fluid velocity to total velocity ratio $\left(\frac{V_f(r)}{V_r(r)}\right)$ for any kind of particle demonstrates how many percent of the total velocity of those particles was created because of the electro-osmosis. The calculation shows that the average contribution of the fluid velocity in the velocity of P^+ tracers is about 75%. For P^0 tracers, this contribution is near to 100%. It is concluded that the electro-osmosis is dominant in the particle motion in water medium. The domain of the electro-osmosis is somewhat expected. As mentioned in previous chapter the fluid velocity can be approached to the electroosmosis equation $\left(V_f(r) = -\frac{\varepsilon \zeta_{surface}}{\eta} E_r(r)\right)$. Although the electric field is rather low, the zeta potential of the particle (considering in average the one of silicon) is very high ($\zeta_{Si} \cong -80$ mV), which makes this term dominate over the electrophoretic terms of the particles.

8.2 Effect of different parameters on the electrohydrodynamic process

After primary experiment, extra experiments were designed and performed to understand the effect of different parameters (hydrogen peroxide, light intensity, adding salt, silicon substrate type, replacing the platinum layer with gold layer and plasma treatment) on this electrohydrodynamic process. From now the variation of the different parameters will be made in presence of the chemical fuel. The results are as follow:

8.2a Effect of adding hydrogen peroxide

The primary experiments show that the electric field generated at the metal/semiconductor is rather low and the motion of the particles is mainly driven by electroosmosis provided by the high zeta potential of the pump walls. . Enhancement of this electrohydrodynamic effect can be done by inducing catalytic reactions at the metal/semiconductor surface in presence of hydrogen peroxide. At this point, Pt and Au surfaces become very relevant. Therefore, 1 wt% hydrogen peroxide dispersions with either positively charged (P^+), negatively charged (P^-) or Quasi-neutral particles (P^0) were applied to study the plasma treated (Table 4.3, C_4) p-Si – Pt devices. It was observed that the performance of the devices for moving tracers was highly improved in the presence of hydrogen peroxide. The results are as follow.

A) Positively charged tracers

Similar to previous experiments on 8.1, the P^+ tracers move toward the platinum disk and settle on it. Figure 8.3 a shows the tracking of the moving tracers. The radial velocity of P^+ tracers toward the disk center increases dramatically. Figure 8.4 shows the effect of adding 1 wt% H_2O_2 into the system. As compared to the experimental results on 8.1 and to the ones of Au-Pt devices (chapter 5), positively charged tracers acquire relatively high velocities even at far distances from the platinum disk. The maximum average velocity of $65.4 \pm 8.5 \mu m \cdot s^{-1}$ was possible to achieve near the platinum-silicon boundary. As one of the most interesting observations in this research, it was observed that positive particles move towards the platinum disk center at high velocity when illuminated with the white light of the microscope lamp. The positive particles stick on the platinum surface allowing the colloidal patterning of the disk. The light becomes an additional tool to selectively control the patterning of the disks. Figure 8.5 demonstrates the effect of the illumination on the patterning. The figure shows two close platinum disks patterned on the substrate. The platinum disk on the left side (indicated

on the figure 8.5) was exposed to the microscope light and was completely covered with P^+ tracers. Only a few particles settled on the other disk which had not been exposed to the microscope light (figure 8.5).

It is also very important to mention that no motion of tracers was observed if an insulating silicon oxide is used instead of p-Si substrate in contact with the metal. That suggests that transfer of electrons between the semiconductor and the metal is important to make this pump operative.

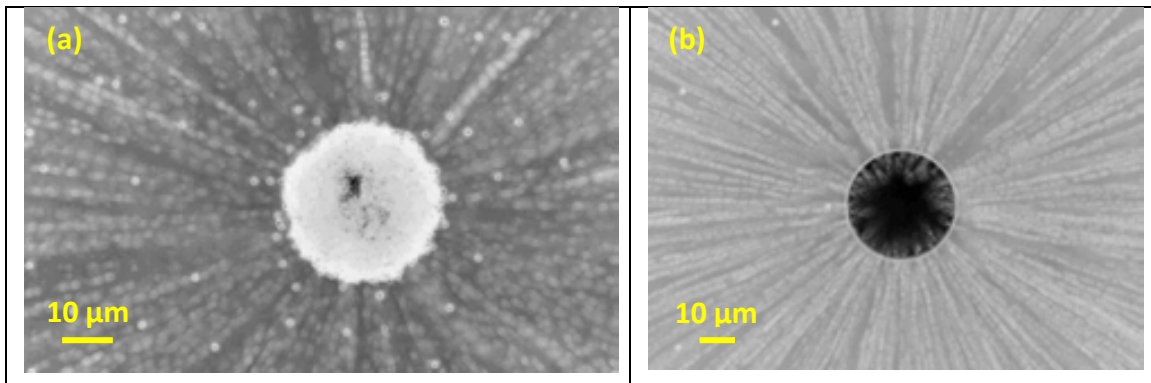


Figure 8.3: Tracking of the tracers on top of a p-Si – Pt device in 1 wt% hydrogen peroxide dispersions a) the P^+ tracers move toward the platinum disk center and settle on it. The disk look white due to the accumulation of particles on it b) The P^0 tracers move toward the platinum disk. After crossing the Si-Pt border, they are pushed upward. The overlap technique was used to show the movement of particles.

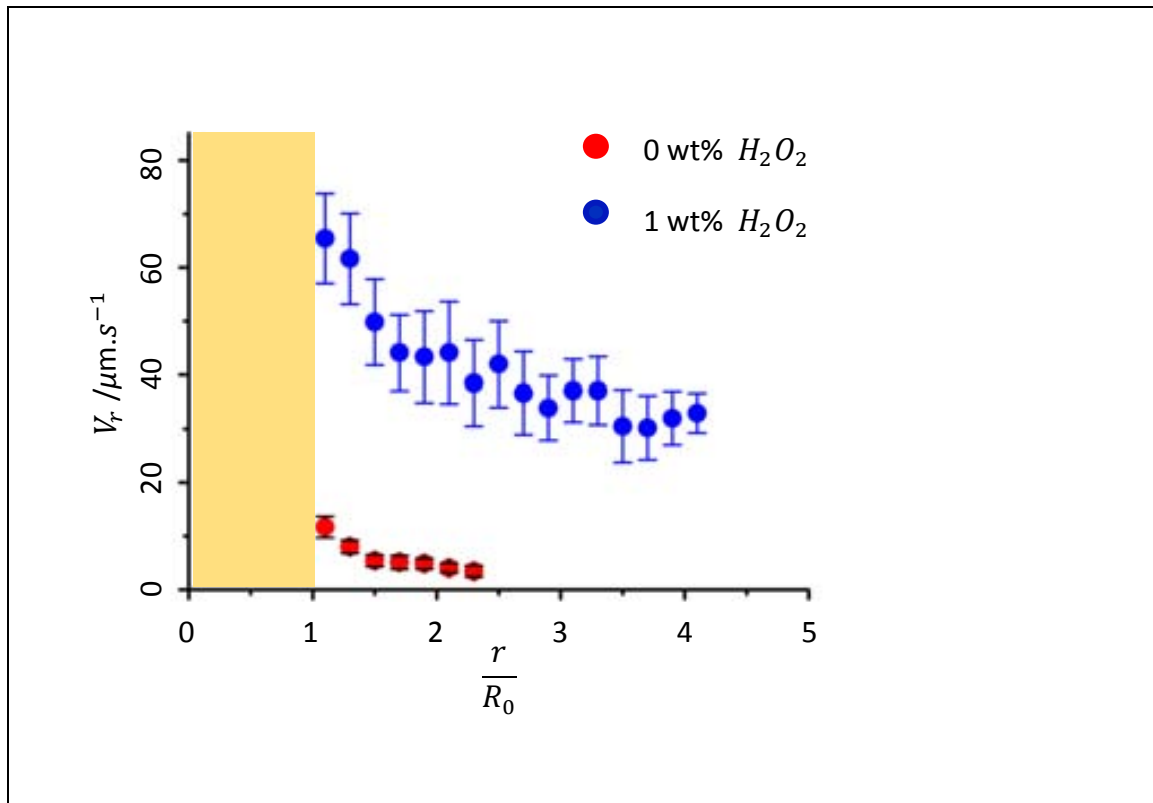


Figure 8.4: Effect of increasing 1 wt% hydrogen peroxide on the average radial velocity (V_r) of P^+ tracers versus normalized distance to disk center around p-Si – Pt devices. r and R_0 are the distances of the particle from the disk center and disk radius respectively. Disk radius (R_0) is $25\mu\text{m}$. The $\frac{r}{R_0}$ values are equal to 0 and 1 at the platinum disk center and platinum disk border respectively. Yellow area represents the area above the platinum disk. Regarding the water medium, the graph represents the averaged data of 4 devices and 20 particles. For 1 wt% hydrogen peroxide solution, the graph was obtained from data of 8 devices and 25 particles.

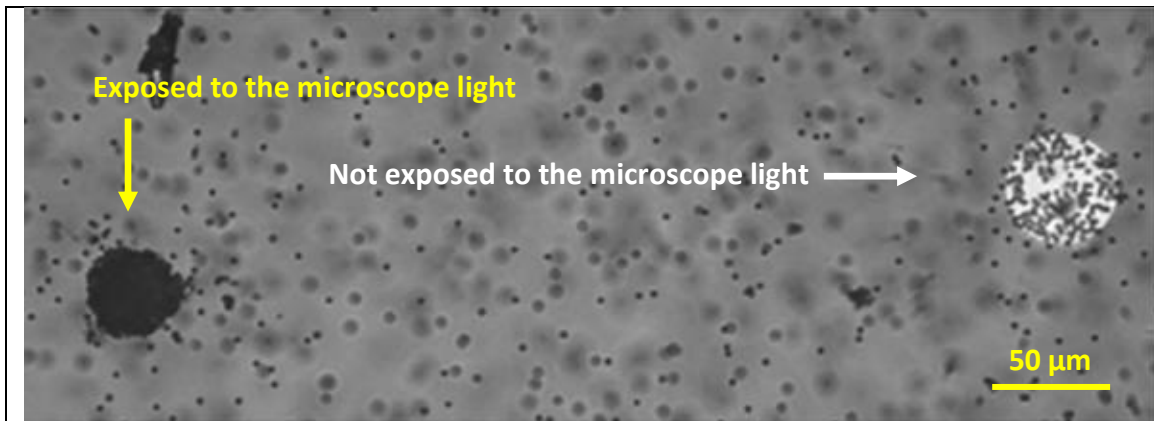
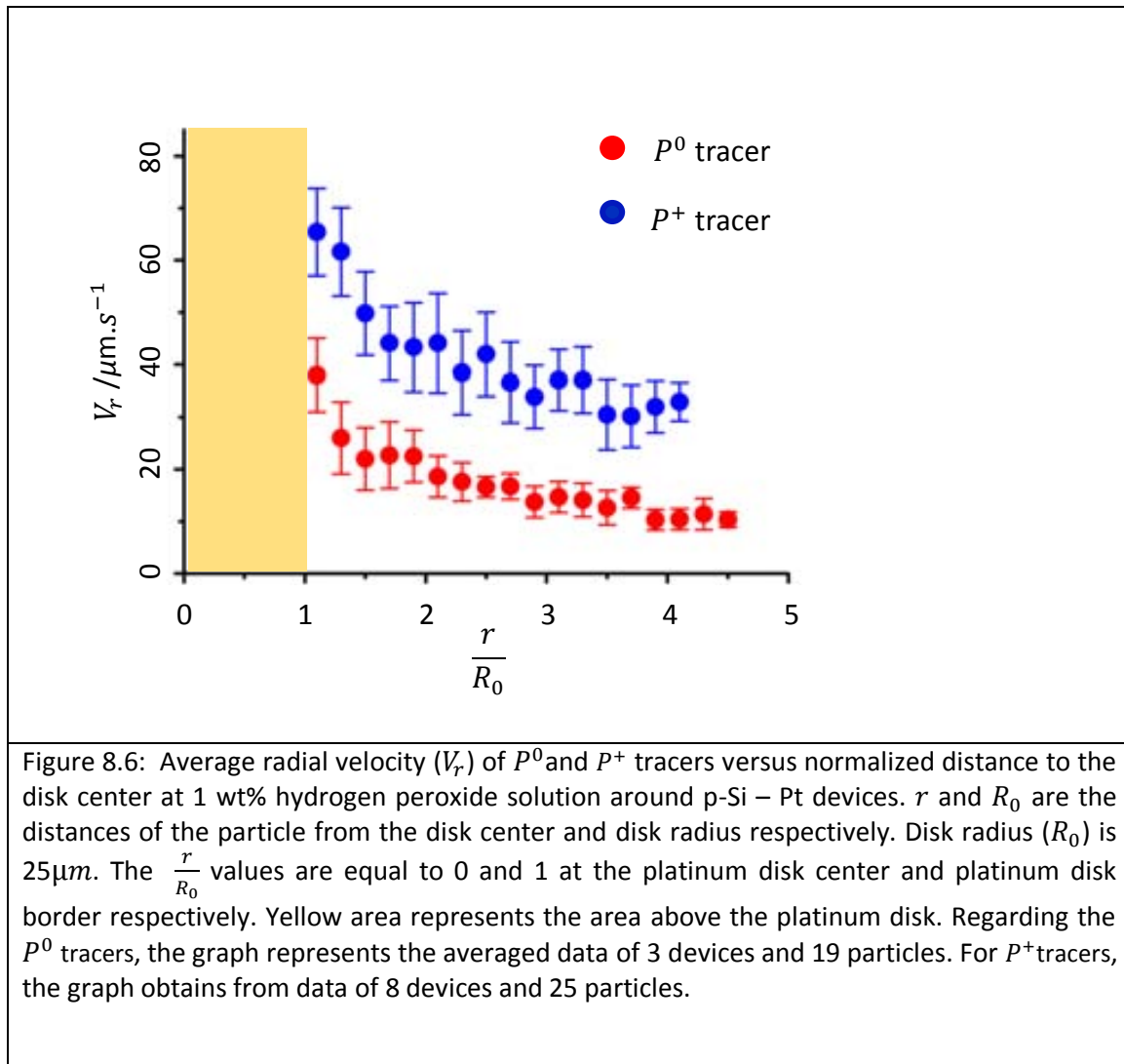


Figure 8.5: Effect of microscope light on patterning of platinum disk with P^+ tracers on p-Si – Pt device at 1 wt% hydrogen peroxide dispersions. The disk on the left side was exposed to the microscope light and completely covered with P^+ tracers. Only a few particles settled on the other disk which had not been exposed to the microscope light.

B) Quasi-neutral tracers

The motion of P^0 tracers is similar to figure 5.9 pattern C. The tracers move toward the disk and after crossing the platinum-silicon border the fluid flow push them up. Figure 8.3b shows the tacking of the tracers. The presence of hydrogen peroxide enhances the velocity of P^0 tracers (figure 8.6). The velocity of the P^0 tracer is significantly lower than the P^+ tracers.



Similar to calculations on 8.1, it is possible to extract the fluid velocity and electric field strength as a function of radial distance from the disk center as per the model mentioned in 5.3. The maximum values of V_f and E_r are $43\ \mu\text{m}\cdot\text{s}^{-1}$ and $680\ \text{V}\cdot\text{m}^{-1}$ respectively. Just as mentioned above, due to the effect of surface zeta potential of silicon ($-80\ \text{mV}$), the fluid velocity acquires higher values as compared to the Au-Pt devices.

C) Negatively charged tracers

When a p-Si – Pt device is exposed to 1 wt% hydrogen peroxide dispersion including P^- tracers, the repulsion of the tracers occurs. The P^- tracers move toward the platinum disk but they are prevented to move further (figure 8.7a). The repulsive band appears and remains stable for long time (figure 8.7b). The tracers aggregate over the repulsive band.

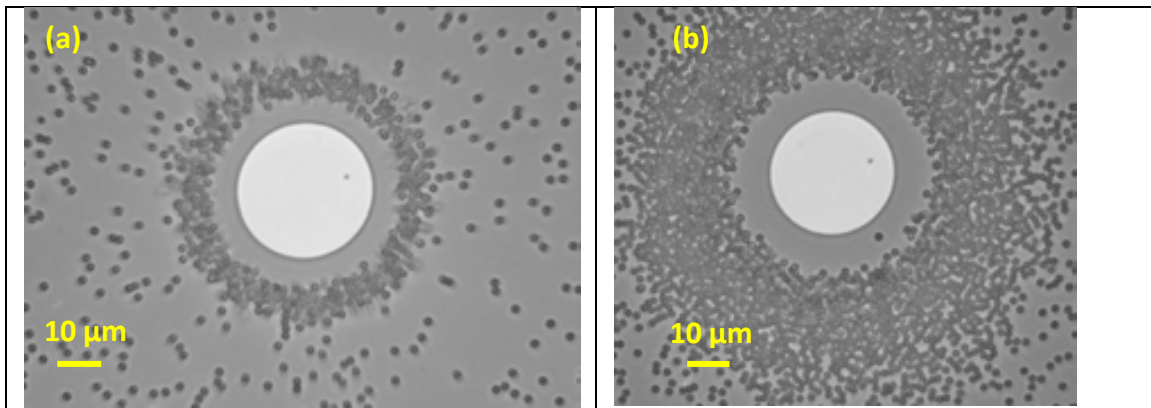


Figure 8.7: Interaction of P^- tracers and a p-Si – Pt device at 1 wt% hydrogen peroxide dispersion a) The P^- tracers move toward the platinum disk and are stopped over the repulsive band b) The repulsive band remains stable for long time.

The enhancement of the electrohydrodynamic process in presence of hydrogen peroxide suggests that a mechanism similar to the case of Au-Pt system is taking place.

Everything points out that under illumination the hydrogen peroxide decomposes on the metal/semiconductor structure. The decomposing reactions produce protons on one side (probably the silicon side) and cause proton consumption on the platinum side. To understand more about the mechanism, the effect of light and the presence of salt on the actuation of the system were studied.

8.2b Effect of light intensity

As mentioned in 8.2 a, the microscope light affects the performance of p-Si – Pt devices at 1 wt% H_2O_2 dispersion. In order to demonstrate the light intensity effect, experiments were done at two different illumination intensities. A neutral density (ND) filter with ability to reduce the intensity of all the white wavelengths into the 75 % of the primary intensity (25 % of transmittance is allowed.), was applied to control the light intensity.

Figure 8.8 shows the effect of the light intensity on the radial velocity of the P^+ tracers around the platinum disk on the plasma treated p-Si – Pt devices. The velocity of the tracers decreases as the light intensity drops.

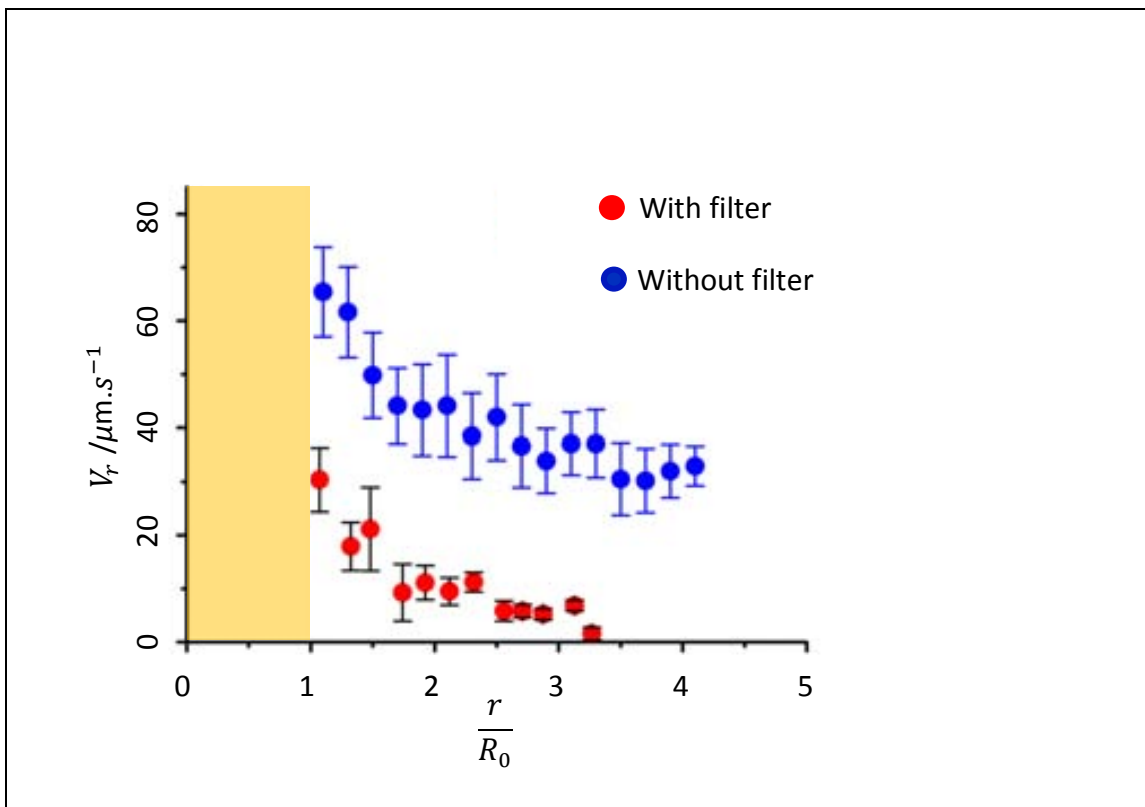
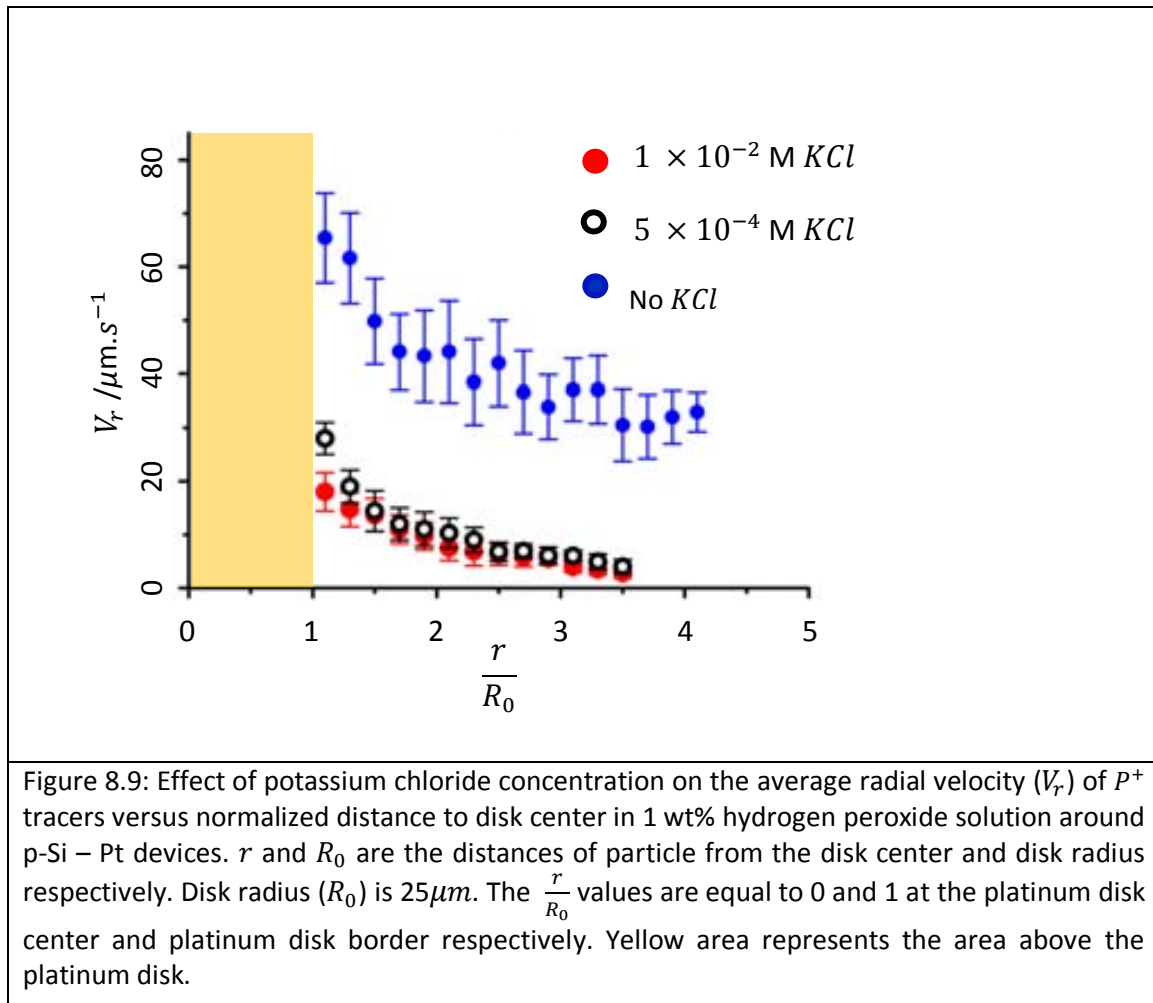


Figure 8.8: The effect of light intensity on the average radial velocity (V_r) of P^+ tracers versus normalized distance to the disk center at 1 wt% hydrogen peroxide solution around p-Si – Pt devices. r and R_0 are the distances of the particle from the disk center and disk radius respectively. Disk radius (R_0) is $25\mu\text{m}$. The $\frac{r}{R_0}$ values are equal to 0 and 1 at the platinum disk center and platinum disk border respectively. Yellow area represents the area above the platinum disk.

8.2c Effect of the salt concentration

In order to study effect of adding salt on the process, potassium chloride⁸⁵ (KCl) was selected as an additive salt to the 1 wt% hydrogen peroxide dispersion containing P^+ tracers. Figure 8.9 shows the effect of the salt on the velocity of the tracers. Adding salt to the metal/semiconductor system in presence of H_2O_2 , remarkably decreases the electrohydrodynamic effect. It suggests that the electrohydrodynamic process in presence of H_2O_2 is enhanced by the presence of an electric field generated by the chemical decomposition of the fuel at the metal/semiconductor interface. The electric field at the interface is screened with the addition of salts. The finding is compatible with the catalytic actuation in which the decomposition of H_2O_2 produces charged species which self-generate an electric field promoting the fluid motion.

⁸⁵ Potassium chloride, Purity: $\geq 99.0\%$, Supplier: Sigma-Aldrich Co. LLC. Website: <http://www.sigmaaldrich.com>



8.2d Effect of the silicon substrate type

Experiments were done to study the effect of changing the dopant type of the silicon substrate on the electrohydrodynamic process. So, n-doped silicon- platinum (n-Si – Pt) devices were subjected to similar experiments as in the case of p-Si – Pt devices.

The results show that the interaction between the n-Si – Pt device and tracers (P^+ , P^- or P^0) were similar to what was observed in 8.2a for p-Si – Pt devices. For instance, P^+ tracers move toward the platinum disk and settle on it. Figure 8.10 shows the tracking of P^+ tracers around an n-Si – Pt device. Figure 8.11 depicts the radial velocity of the P^+ tracers versus normalized radial distance for the n-Si – Pt and p-Si – Pt devices. The velocity of tracers on the p-Si – Pt devices are higher. It is very important to emphasize that the conductivity of the substrate is a key parameter in this system.

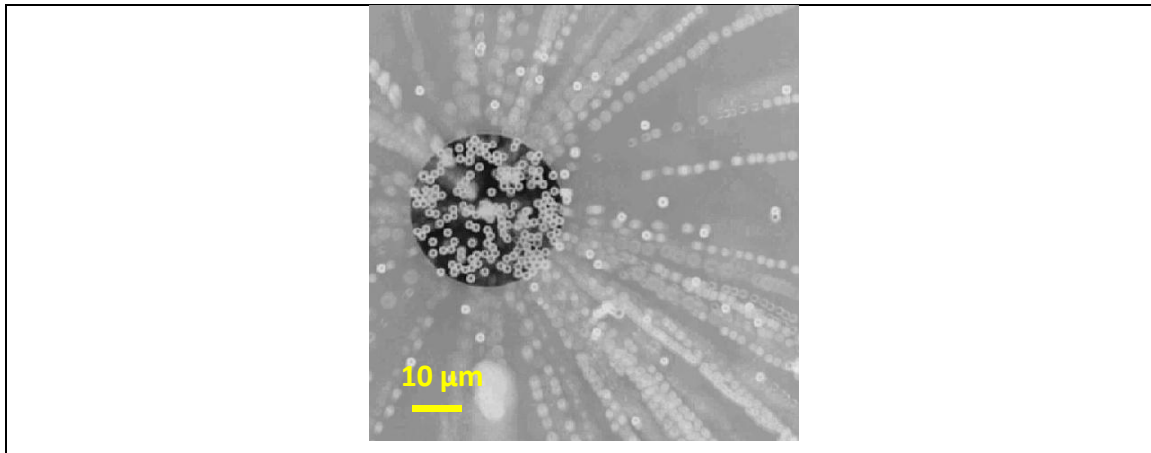


Figure 8.10: Tracking of the P^+ tracers on top of a n-Si – Pt device in 1 wt% hydrogen peroxide dispersions. The tracers move toward the platinum disk center and settle on it. The Overlap technique was used to show the movement of particles.

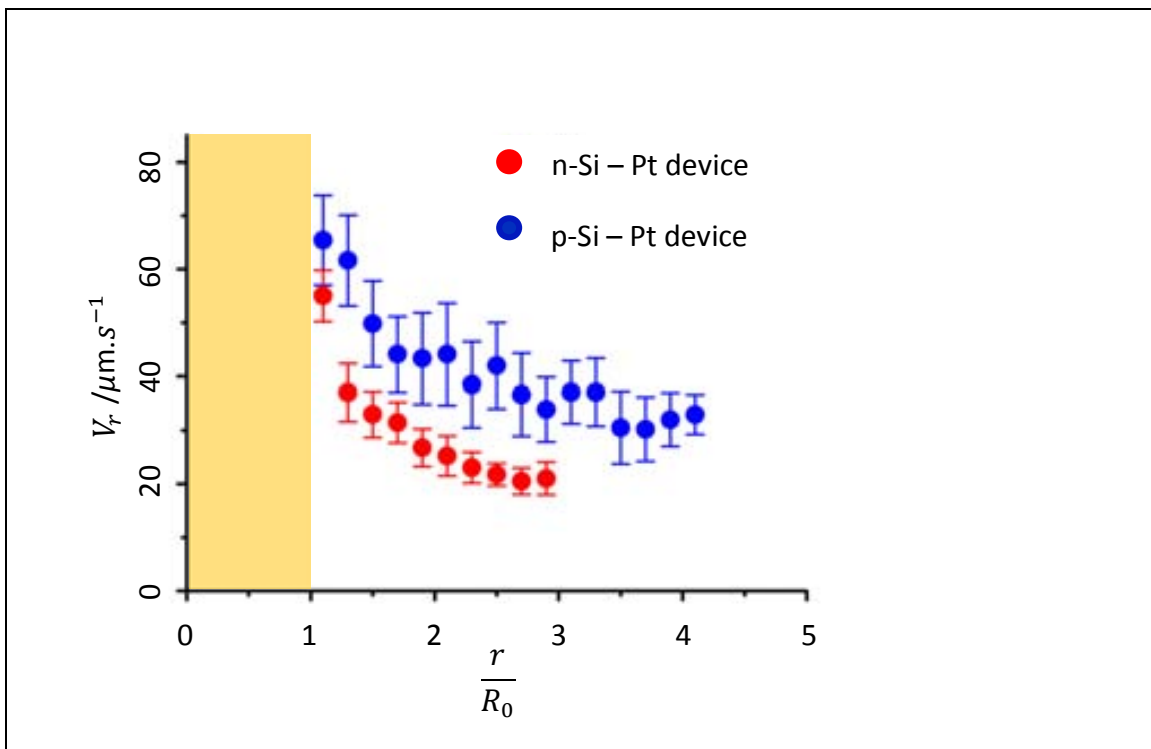


Figure 8.11: Effect of silicon substrate type on the average radial velocity (V_r) of P^+ tracers versus normalized distance to the disk center at 1 wt% hydrogen peroxide solution. r and R_0 are the distances of particle from the disk center and disk radius respectively. Disk radius (R_0) is $25\mu\text{m}$. The $\frac{r}{R_0}$ values are equal to 0 and 1 at the platinum disk center and platinum disk border respectively. Yellow area represents the area above the platinum disk.

8.2d Effect of replacing the platinum layer by gold

Using gold instead of platinum on the device provides opportunity to study the role different metallic layers on the electrohydrodynamic process.

The p-doped silicon- gold (p-Si – Au) devices were exposed to 1 wt% hydrogen peroxide dispersions containing either P^+ , P^- or P^0 tracers. The p-Si – Au devices show similar behavior as reported in 8.2a for p-Si – Pt devices.

Figure 8.12 shows the radial velocity of P^+ tracers versus normalized radial distance for p-Si – Au and p-Si – Pt devices. The velocities of the tracers follow the same trend on both types of devices.

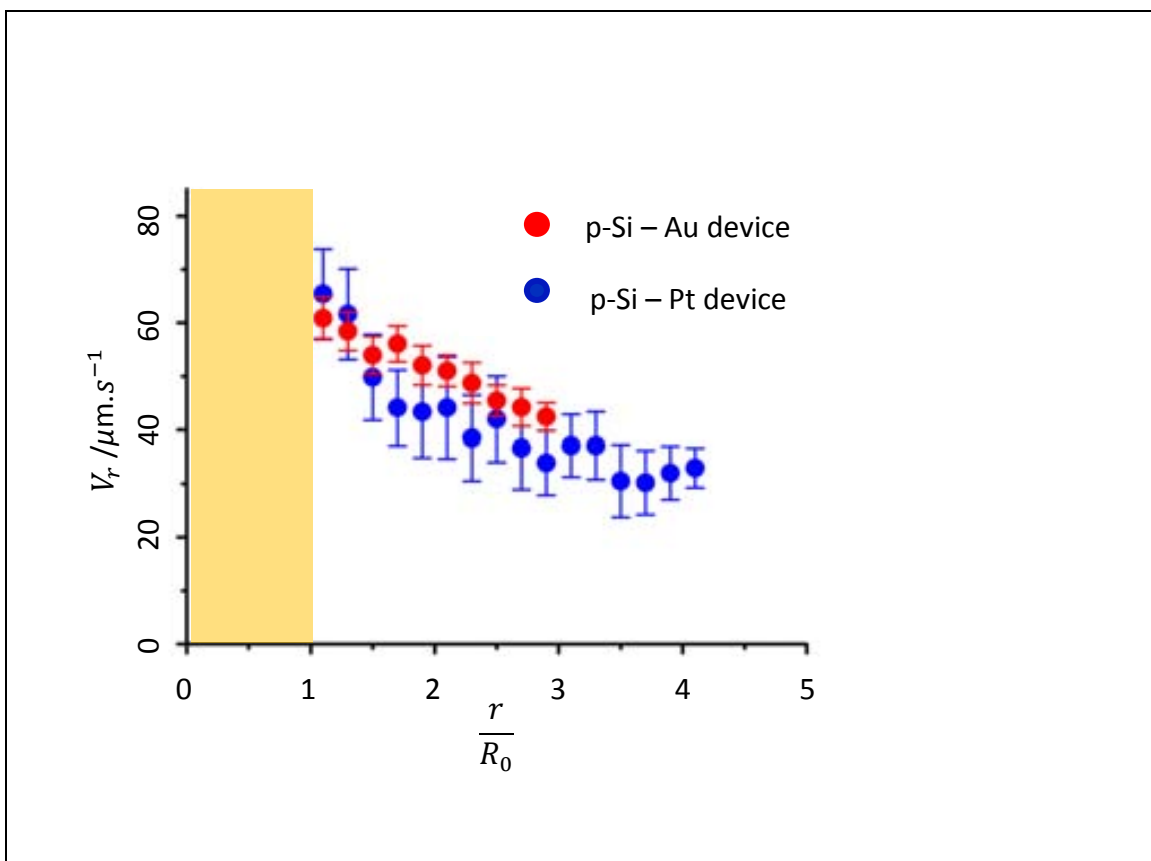


Figure 8.12: Effect of changing metallic material on the average radial velocity (V_r) of P^+ tracers versus the normalized distance to the disk center at 1 wt% hydrogen peroxide solution. r and R_0 are the distances of particle from the disk center and disk radius respectively. Disk radius (R_0) is $25\mu\text{m}$. The $\frac{r}{R_0}$ values are equal to 0 and 1 at the platinum disk center and platinum disk border respectively. Yellow area represents the area above the platinum disk.

8.2e Effect of the plasma treatment

Until now, the samples were subjected to a plasma treatment (Table 4.3, C_4) before the experiment. It is time to study the role of plasma treatment on the electrohydrodynamic effect.

The plasma treated and non-treated devices (from both types of n-Si – Pt and p-Si – Pt devices) were subjected to the experiment. Figure 8.13 and 8.14 show the effect of plasma treatment on radial velocity of P^+ tracers around p-Si – Pt and n-Si – Pt devices respectively. In both cases, the plasma treatment increases the velocity of the tracers. It was found that the plasma treatment is crucial for the Si – Au systems. No electrohydrodynamic effect was observed without plasma treatment in these systems.

The plasma treatment also aids to the adhesion and therefore the patterning of the positively charged particles on Au or Pt disks. Probably the oxygen functionalities generated at the metal surface favor the stickiness of the positive tracers.

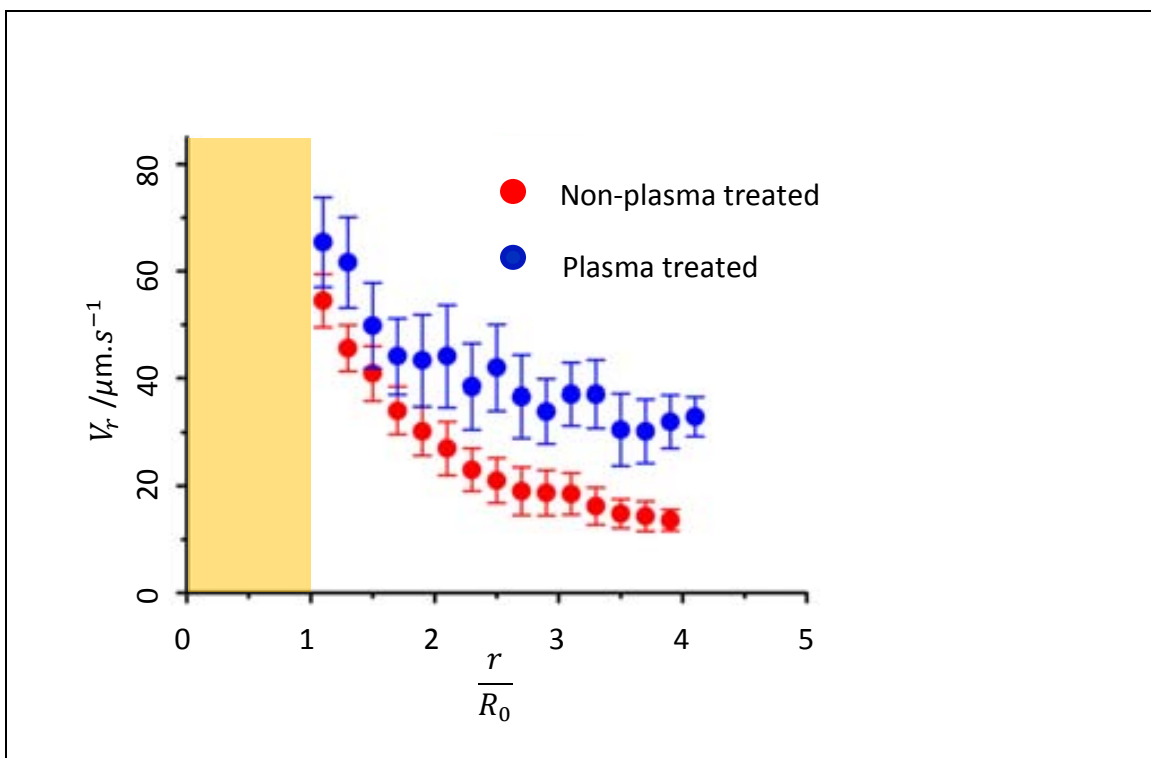
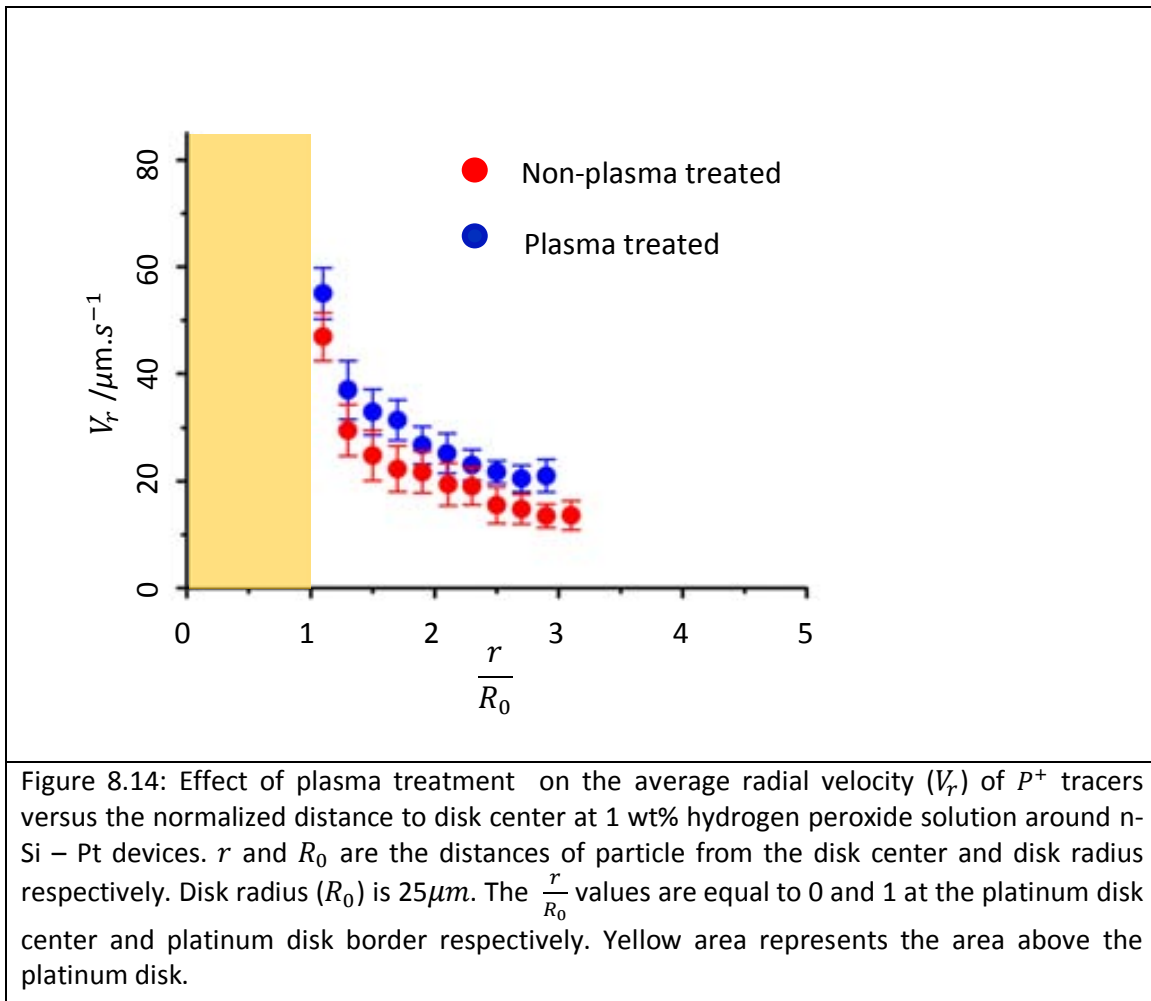


Figure 8.13: Effect of plasma treatment on the average radial velocity (V_r) of P^+ tracers versus the normalized distance to disk center at 1 wt% hydrogen peroxide solution around p-Si – Pt devices. r and R_0 are the distances of the particle from the disk center and disk radius respectively. Disk radius (R_0) is $25\mu\text{m}$. The $\frac{r}{R_0}$ values are equal to 0 and 1 at the platinum disk center and platinum disk border respectively. Yellow area represents the area above the platinum disk.

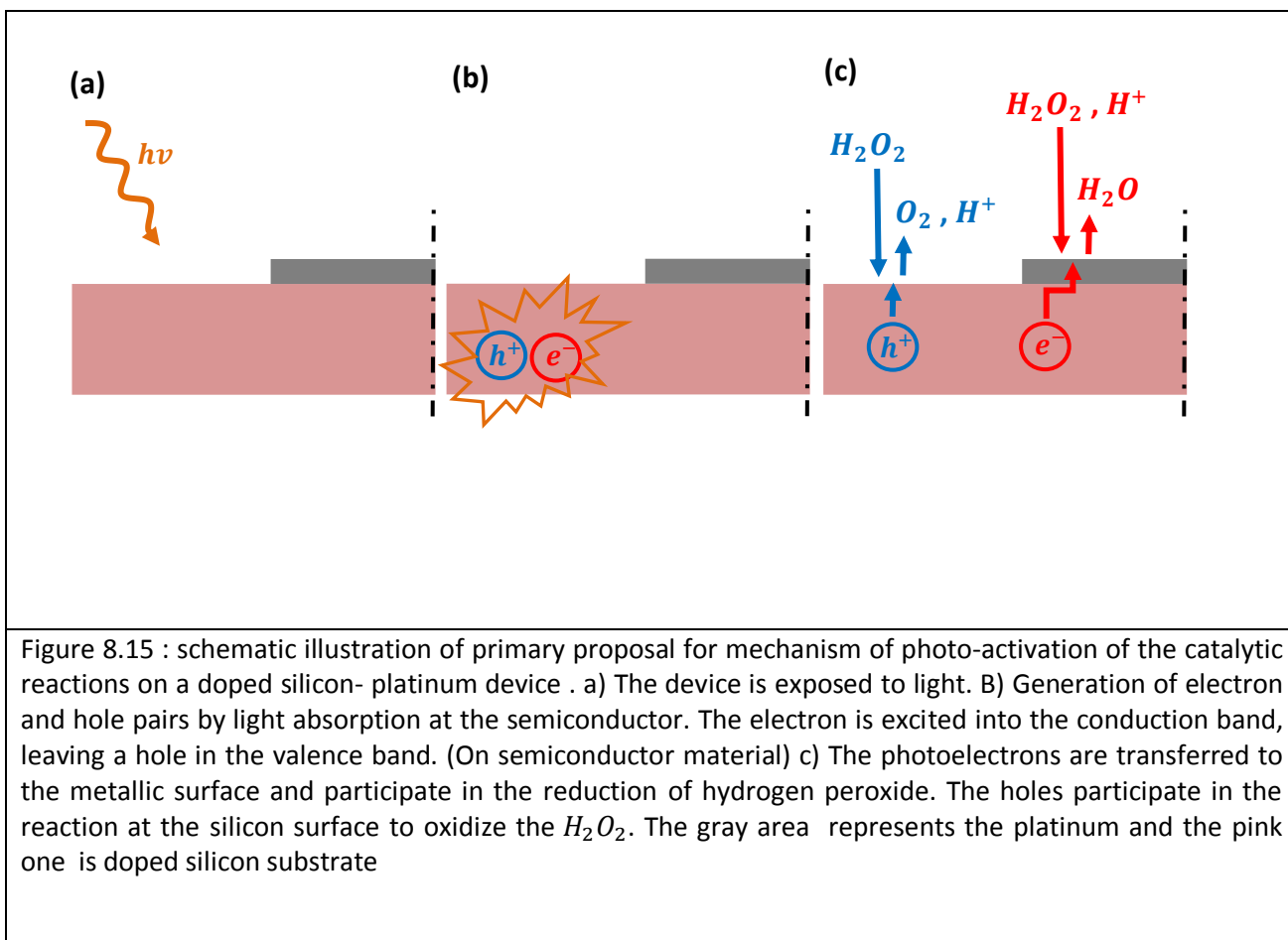


8.3 Conclusion

Firstly, it has been observed that the built-in electric field at the metal/semiconductor junction, although weak, is enough to trigger electrohydrodynamic effects in presence of only pure water. The fluid motion is favored by the high magnitude of the zeta potential of the pump surface. These findings could have an important impact in the development of nanomotors which can be operative in more biocompatible fluids.

More fascinating is the fact that electrohydrodynamic effects can be greatly amplified by adding a chemical fuel which can catalytically decompose on the metal/semiconductor surface in presence of light. The process can be framed as a photo-catalytic effect enhanced by the presence of the metal structure. Figure 8.15 schematically presents the primary proposal for mechanism of photo-activation of the catalytic reactions. During the light absorption by the doped silicon, electrons are excited from the valence band to the conduction band. Consequently, holes are created in the valence band. The excited electrons can be transferred into the metal. The holes generated at the semiconductor can oxidize the H_2O_2 producing protons whereas the metal counterpart can act as a cathode reducing the hydrogen peroxide. The transfer of the excited electrons from a semiconductor to a metal (Au or Pt) in contact with it, is a well known process [3, 4] and has been exploited to increase the efficiency of photo-catalysis in different applications.

Our results constitute the proof-of-concept of novel photochemical-electrohydrodynamic switches which can open new and promising research activities in the field of catalytic actuators and nanomotors.



Reference:

- [1] J. Bardeen, "Surface states and rectification at a metal semi-conductor contact," *Physical Review*, vol. 71, p. 717, 1947.
- [2] S. M. Sze and K. K. Ng, *Physics of semiconductor devices*: John Wiley & Sons, 2006.
- [3] V. Subramanian, E. Wolf, and P. V. Kamat, "Semiconductor–Metal Composite Nanostructures. To What Extent Do Metal Nanoparticles Improve the Photocatalytic Activity of TiO₂ Films?," *The Journal of Physical Chemistry B*, vol. 105, pp. 11439-11446, 2001/11/01 2001.
- [4] M. R. Hoffmann, S. T. Martin, W. Choi, and D. W. Bahnemann, "Environmental applications of semiconductor photocatalysis," *Chemical reviews*, vol. 95, pp. 69-96, 1995.

Chapter 9

In the previous chapter it was demonstrated that numerical simulations, based on solving the coupled governing equations involved in the catalytic reactions and the electrohydrodynamic process, can reproduce the experimental data. By comparing the experimental findings to the numerical simulations it was possible to estimate different parameters such as the concentration of ion impurities and the constant rates of the electrochemical reactions at the anode and cathode.

All that demonstrates that numerical simulations can become a powerful tool to shed light on the complex chemomechanical actuation of catalytic objects. Given the difficulties of an analytical approach [1], some research groups have already resorted to numerical methods trying to understand the involved phenomena [2-5]. Most of these studies have focused on bimetallic rods or bimetallic Janus particles using different assumptions and simplifications. However a thorough study of the effect on the catalytic motion of all the parameters taking part of the coupled processes is still lacking.

Therefore this chapter attempts to make a comprehensive and systematic numerical analysis of the influence of the different parameters involved in the actuation of catalytic micropumps. This study can not only provide a better understanding of the whole scenario behind this process but also important clues of how to design more efficient catalytic actuators.

9.1 Methodology

In order to understand the main parameters controlling and optimizing the performance of catalytic micropumps, it will be used the same methodology described in the previous chapter. It will be used the same finite element method to solve the coupled equations governing the motion of fluid, the electric field, and the transport of charged species taking into consideration the electrochemical currents represented (Chapter 5.6). The geometry of the system will be again a bimetallic micropump made of two concentric disks (anode/cathode) of radius R_{in} and R_{out} (Scheme 5.25, Chapter 5). It will be profited from the axial symmetry to simplify the calculations using a 2D geometry.

In the simulations, four different charged species will in general be considered: protons, hydroxide ions and the potential presence of different stoichiometric salts.

The boundary conditions for the electrostatic potential will be again:

$$\varphi(z_{max}) = 0$$

$$\varphi(z = 0) = \varphi_{subs}$$

Where φ_{subs} is the potential of the surface, and the upper boundary of the simulation, z_{max} , is placed at $60\mu m$ above the surface. For the fluid velocity, stick boundary conditions will be imposed on the substrate and slip elsewhere. For the concentrations of the different species, the bulk values will be imposed at the upper boundary z_{max} .

The typical reference parameters used in the simulations are listed in Table 1 and will be kept fixed unless otherwise mentioned.

Table 1. Typical values of the parameters used in the simulations.

| Description | Values |
|---|---|
| Proton's diffusion coefficient | $9.3 \cdot 10^{-9} [\text{m}^2 \text{s}^{-1}]$ |
| OH's diffusion coefficient | $5.3 \cdot 10^{-9} [\text{m}^2 \text{s}^{-1}]$ |
| Proton concentration in the bulk | $5.6 \cdot 10^{-4} [\text{mol}/\text{m}^3]$ (pH=6.25) |
| Zeta potential of cathode | -0.033 V |
| Zeta potential of anode | -0.033 V |
| Rate k_{cathode} | $0.1 [\text{m}^7 \text{s}^{-1} \text{mol}^{-2}]$ |
| Rate k_{anode} | $8 \cdot 10^{-10} [\text{m} \text{s}^{-1}]$ |
| H ₂ O ₂ concentration | 0.3M (300 mol m ⁻³ , 1%) |
| Radius of the cathode disk | 15 μm |
| Radius of anode ring | 50 μm |
| Concentration of additional monovalent ions in the solution | 5 μM |
| Diffusion coefficient of the additional ionic species | $1.0 \cdot 10^{-9} [\text{m}^2 \text{s}^{-1}]$ |

9.2 Results and Discussion

The typical results of the simulations were presented in the previous chapter and compared to the experimental findings. The electric field pointed from the anode towards the cathode disk and it was especially intense near the disk edge. The radial pumping velocity was also maximal near the disk edge and the fluid was pumped upwards near the disk center. It was also shown that the proton concentration was higher on the anode as compared to the cathode. The simulations also depicted that a net positive charge was confined inside the double layer with a charge distribution asymmetry along the radial distance. Such charge asymmetry can induce an electric field not only inside the double layer but also above the double layer at distances in which the fluid is electroneutral. That could be explained as a consequence of the motion of protons beyond the double layer which can self-generate an electric field as discussed in previous section.

In this section the impact of different physico-chemical variables on the most relevant characteristics of the bimetallic pump such as the electric field, fluid velocity, and local proton distribution will be evaluated. Special focus will be put on the effects of the surface potential, salt concentration and their diffusion coefficients, rate constants for anode and cathode, bulk H₂O₂ concentration, bulk proton concentration and radius of the anode/cathode structures.

9.2a Effect of the substrate surface potential

As mentioned in 3.5, the potential drop of the Stern layer ($\Delta \phi_i$) becomes very small at low concentration of salts (micromolar range or below). Under these conditions the surface potential of the device can be approximated to its zeta potential [13]. Generally, the zeta

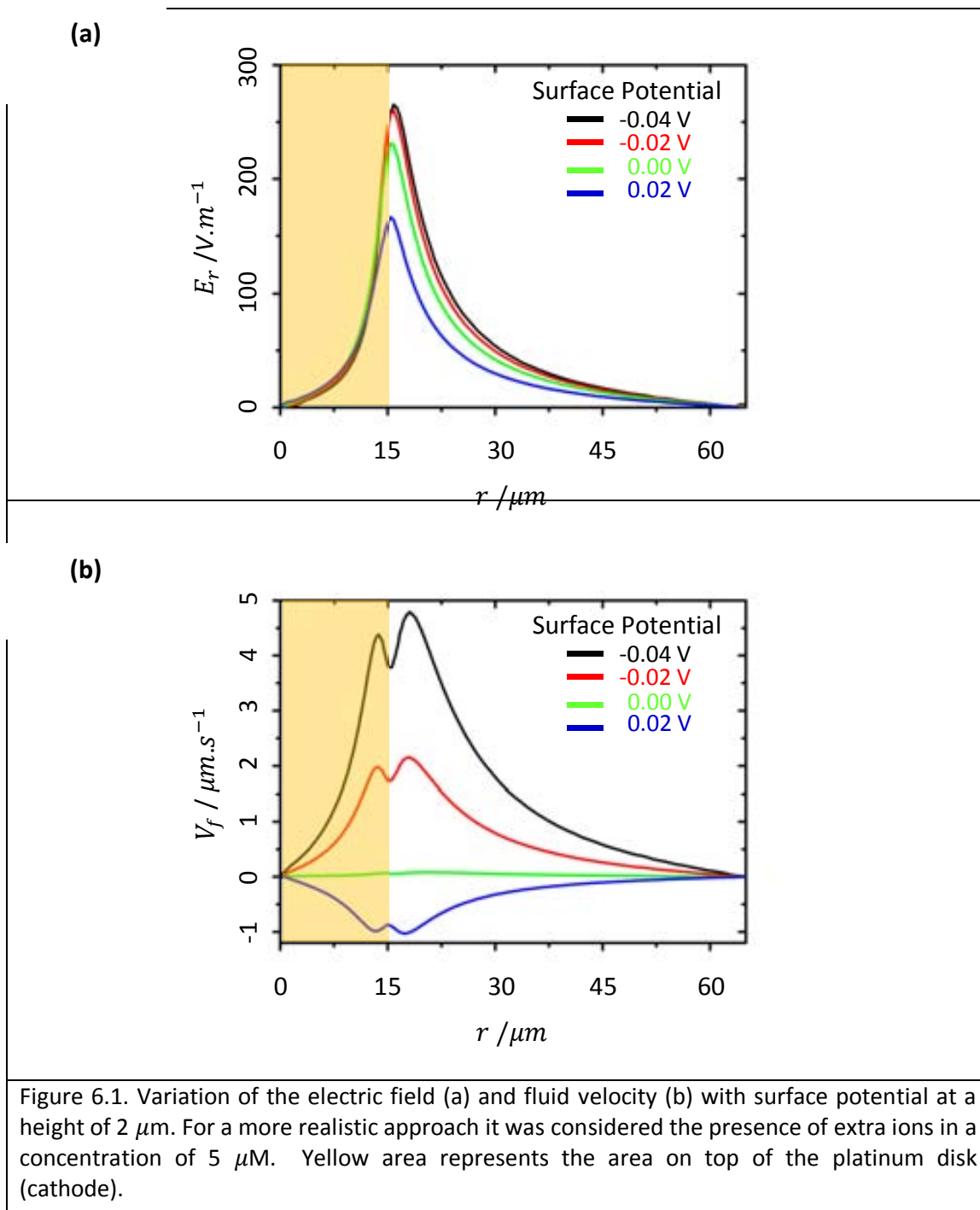
potentials of metals such as gold and platinum are negative⁸⁶. Since the motion of the fluid in catalytic pumps is ultimately related to a self-generated electro-osmotic flow, it becomes very interesting to evaluate the effect of the surface potential on the chemomechanical actuation. Experimentally, changes in the surface zeta potential could be reached either by using different electrode materials, by chemical functionalization of the surface or by polarization.

In numerical analysis, it was assumed that the bimetallic structure has a uniform surface potential. In other words, the surface potential of cathode (ψ_C) and anode (ψ_A) are equal:

$$\psi_C = \psi_A \quad \text{Equation 9.1}$$

Although the uniformity of the surface potential was considered as an approximation, the zeta potential can be changed during the evolution of the electrochemical reactions at the surface. Surface charge and potential are undoubtedly very important to control the fluid pumping as illustrated by figure 3. Figure a and b show the radial component of the electric field and fluid velocity at 2 micrometers above the surface for different values of the surface potential in the range from -0.04V up to 0.04 V. It can be observed that the absolute value of the electric field gets smaller as the surface potential increases. In fact, the fluid velocity direction can be even inverted if the substrate potential gets positive values.

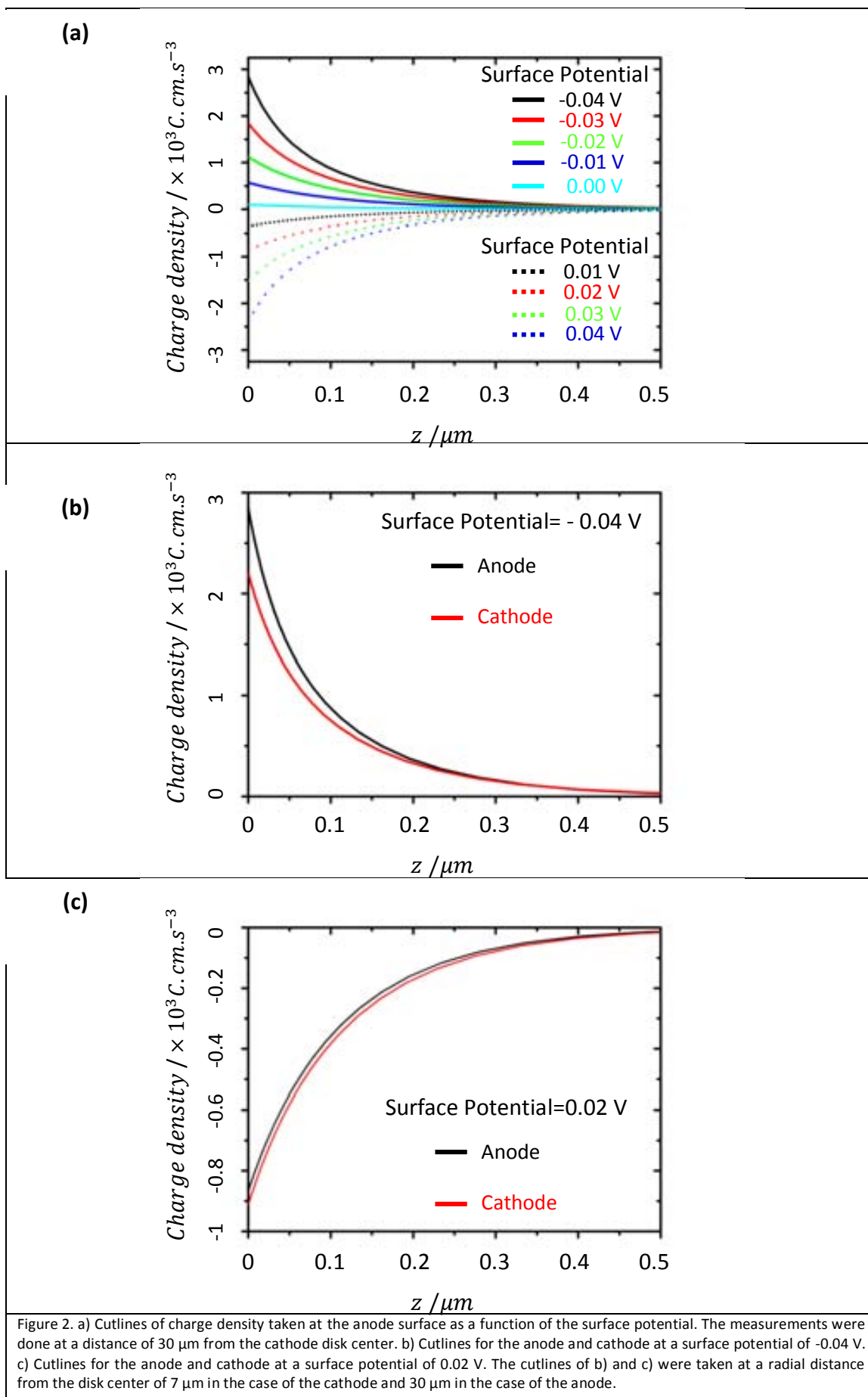
⁸⁶ For instance, zeta potential of typical gold layers is between -20 mV and -30mV.



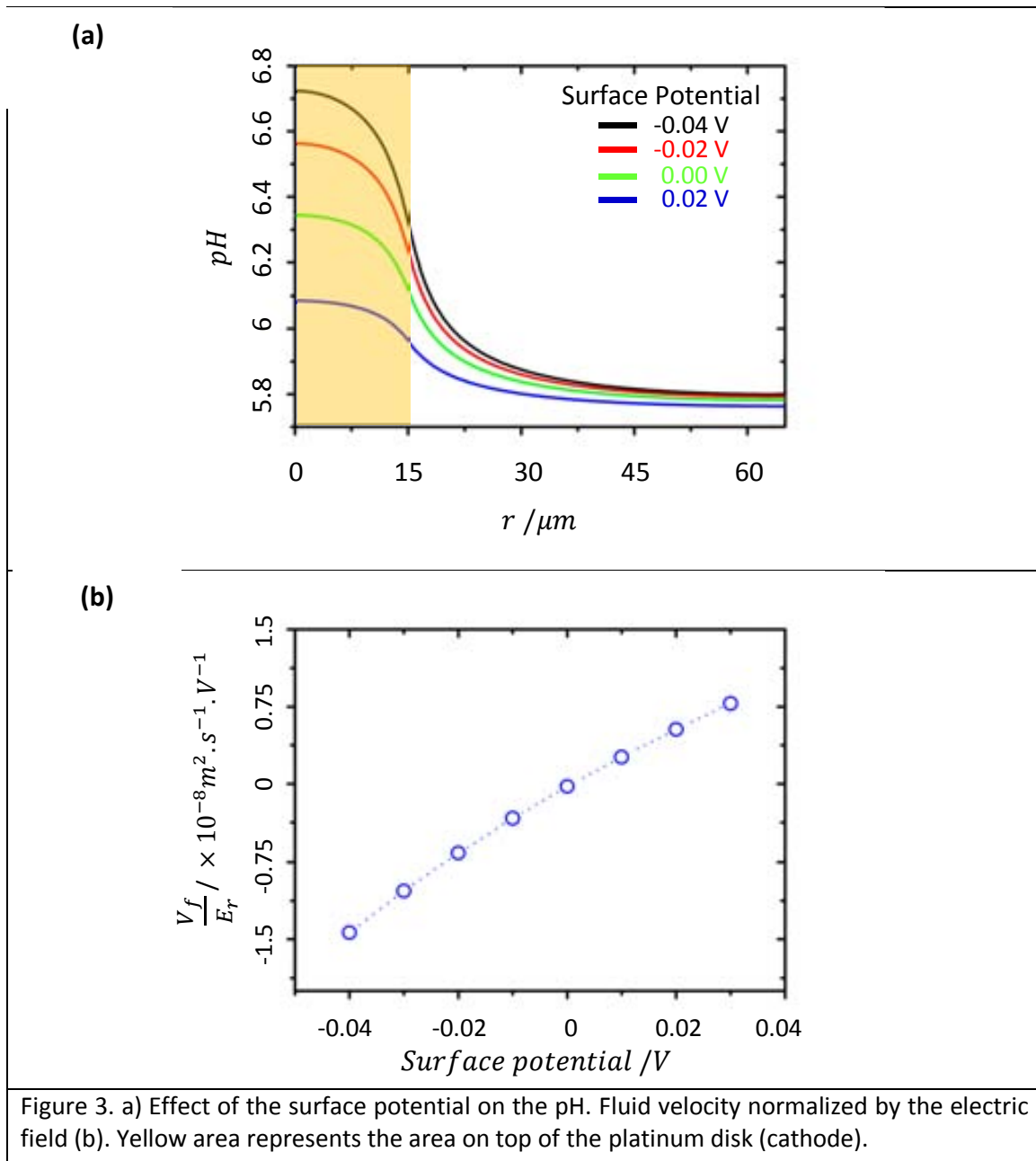
All these findings point out the importance of the surface potential in setting the double layer and the distribution of charged species in it. The charge distribution in the double layer ultimately governs the fluid pumping direction in presence of the chemically generated electric field in a similar way than in a conventional electro-osmosis process. However the charge

distribution of the double layer in catalytic pumps is not so much intuitive as compared to a static double layer in which a charged interface accumulates species of opposite charge (σD). In the present scenario there is also a reaction generating protons which are flowing through the double layer and contributing with additional charge (σr).

In order to gain more knowledge of the double layer charge distribution in presence of an electrochemical reaction, the charge density at the double layer was evaluated for different values of the substrate voltage or zeta potential. Figure 2 plots the charge density as a function of the height above the surface up to a distance of 500 nm from the bimetallic surface. It can be observed, for both electrodes, that in the case of negative surface potentials an accumulation of positive charge is produced in the double layer irrespective of the generation and consumption of protons at the anode and cathode respectively (solid lines Figure 2 a). Alternatively if the surface potential becomes positive an accumulation of negative charge is set at both electrodes (dashed curves of Figure 2 a). Figure 2b shows the charge density in the double layer at the anode and cathode surfaces when the surface potential is negative (-0.04 V). The figure depicts how the charge asymmetry along the anode and cathode increases as the height decreases (becoming closer to the surface of the electrodes). As mentioned before, this charge asymmetry inside the double layer can set up a radial electric field pointing out from the anode to the cathode and which can trigger the electrokinetic processes. However the magnitude of such electric field changes with surface potential. Negative surface potentials keep relatively higher radial charge asymmetry in the double layer from the proton excess and depletion on the anode and cathode respectively. But at positive surface potentials the charge asymmetric distribution decreases, weakening the electric field which still points out from anode to cathode. Moreover at such positive surface potentials more negative charges will be accumulated at the double layer and become the dominant carriers to respond to the already weakened electric field. Now these negative carriers would move towards the positive pole (anode) inverting the fluid pumping as compared to the case when negative voltages were accumulating more positive species at the double layer. The results also point out the importance of having a charged surface for inducing the fluid pumping [3].



The effect of surface potential on the local proton concentration was also analyzed. Figure 3 a shows the pH as a function of the radial distance for different values of surface potential. The change of surface potential has more impact on the proton concentration at the cathode side. The concentration of protons at the cathode increases as the surface potential becomes more positive. It suggests that a positive surface potential decreases the electron transfer rate of the protons at the double layer of the cathode. Consequently fewer protons are consumed increasing locally their concentration at that side.



In order to know if the electric field controls the fluid velocity (V_f) in a similar way as an electro-osmosis process, $V_f = \epsilon \epsilon_0 \zeta_w E / \eta$, the values of V_f were normalized with respect to the electric field E . Such normalization should give a linear dependence. Indeed, figure 3 b shows a linear behavior which suggests that the fluid velocity is mainly controlled by the electric field. Accordingly the analysis will be focused, from now, on the effect of the different physical variables on the electric field and pH.

Effect of the salt or other extra ions: concentration, diffusion coefficients and charge

As mentioned in previous chapter, it is impossible that catalytic devices can perform their actuation in a fluid completely free of ionic species. Thus considering the presence of extra ions in a form of a salt is quite a realistic approach. Fig. 4 a shows the values of the electric field as a function of the radial distance for different concentrations of a monovalent salt. The presence of extra ions or small amounts of salt affect dramatically the electric field. It has found that the electric field decreases by a factor of 14 as the salt concentration is increased by three orders of magnitude. A better inspection of the electric field decrease with the salt concentration is depicted in Fig. 4b. That is an expected behaviour due to the typical screening effects. The decay of the electric field can be correlated with the electric field expression which relates the current of ionic species (j) and the fluid conductivity (k),

$$E = \frac{j}{\frac{e}{k_B T} (\mu_{H^+} [H^+] + \mu_{OH^-} [OH^-] + (\mu_{A^+} + \mu_{B^-}) [AB])} \quad \text{Equation 9.2}$$

$[AB]$: Concentration of the AB salt [m^{-3}]

$[H^+]$: Concentration of the protons [m^{-3}]

μ_{H^+} : Mobility of the protons $ms^{-1}V^{-1}$ [$m^2V^{-1}s^{-1}$]

μ_{A^+} : Mobility of the A^+ ions [$m^2V^{-1}s^{-1}$]

μ_{B^-} : Mobility of the B^- ions [$m^2V^{-1}s^{-1}$]

k_B : Boltzmann constant [$1.3806 \times 10^{-23} J K^{-1}$]

T : Temperature [K]

e : Magnitude of the elementary charge on an electron [$1.602 \times 10^{-19} C$]

As the fluid conductivity of the fluid increases with the addition of salt, the electric field decreases. Eq. 9.2 can be rewritten in the expression below and used for fitting the data of the simulation

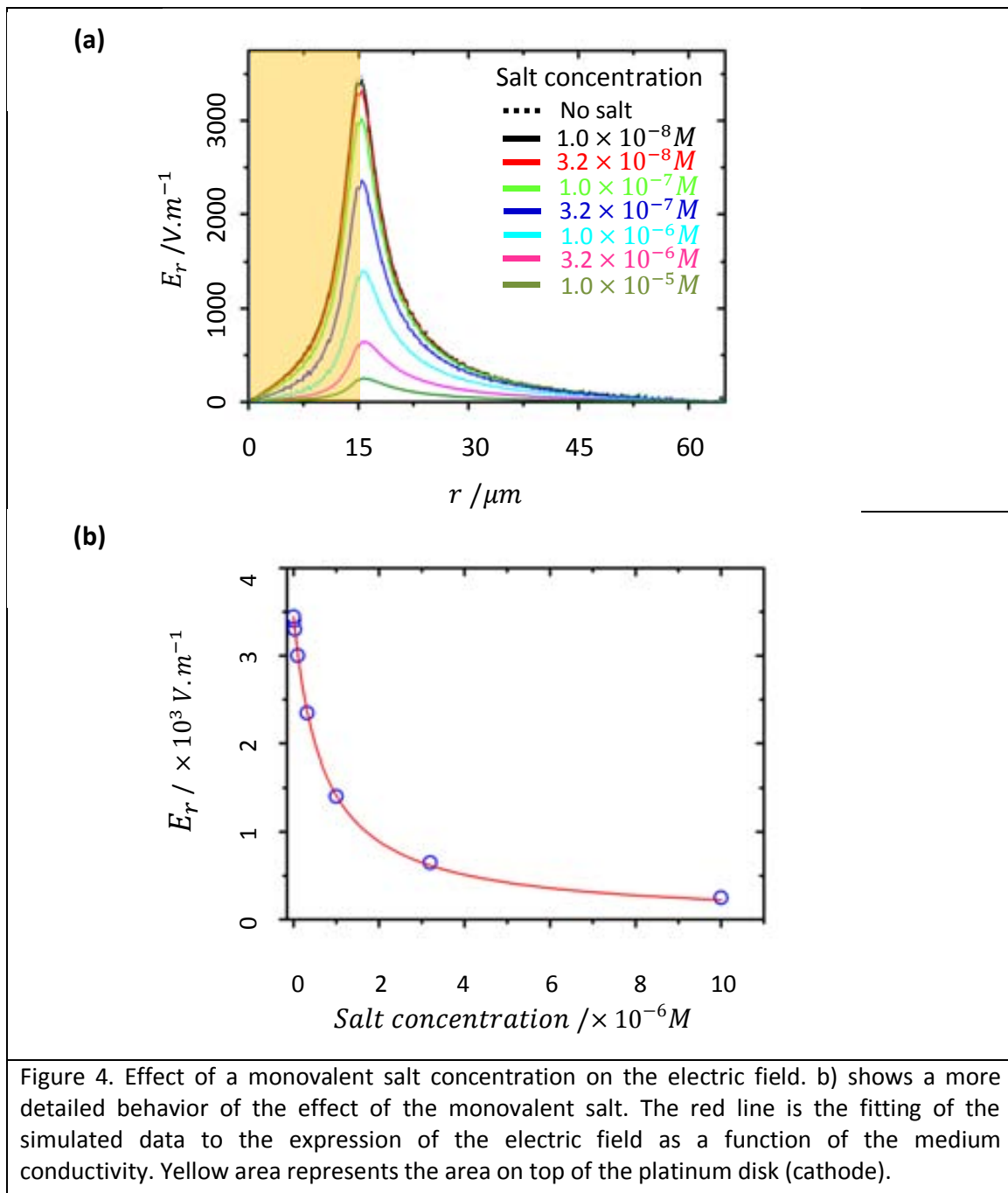
$$E = \frac{1}{a + b[AB]} \quad \text{Equation 9.3}$$

Where a and b are:

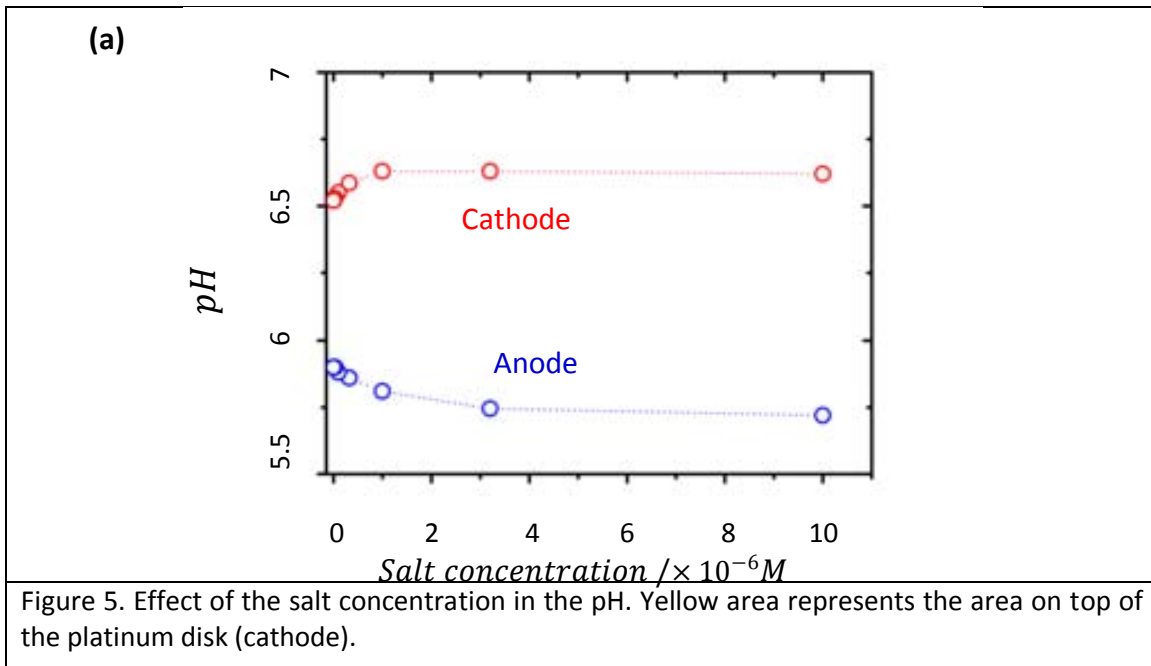
$$a = \frac{e}{j k_B T} (\mu_{H^+} [H^+]) \quad \text{Equation 9.4}$$

$$b = \frac{e}{jk_B T} (\mu_{A^+} + \mu_{B^-}) \quad \text{Equation 9.5}$$

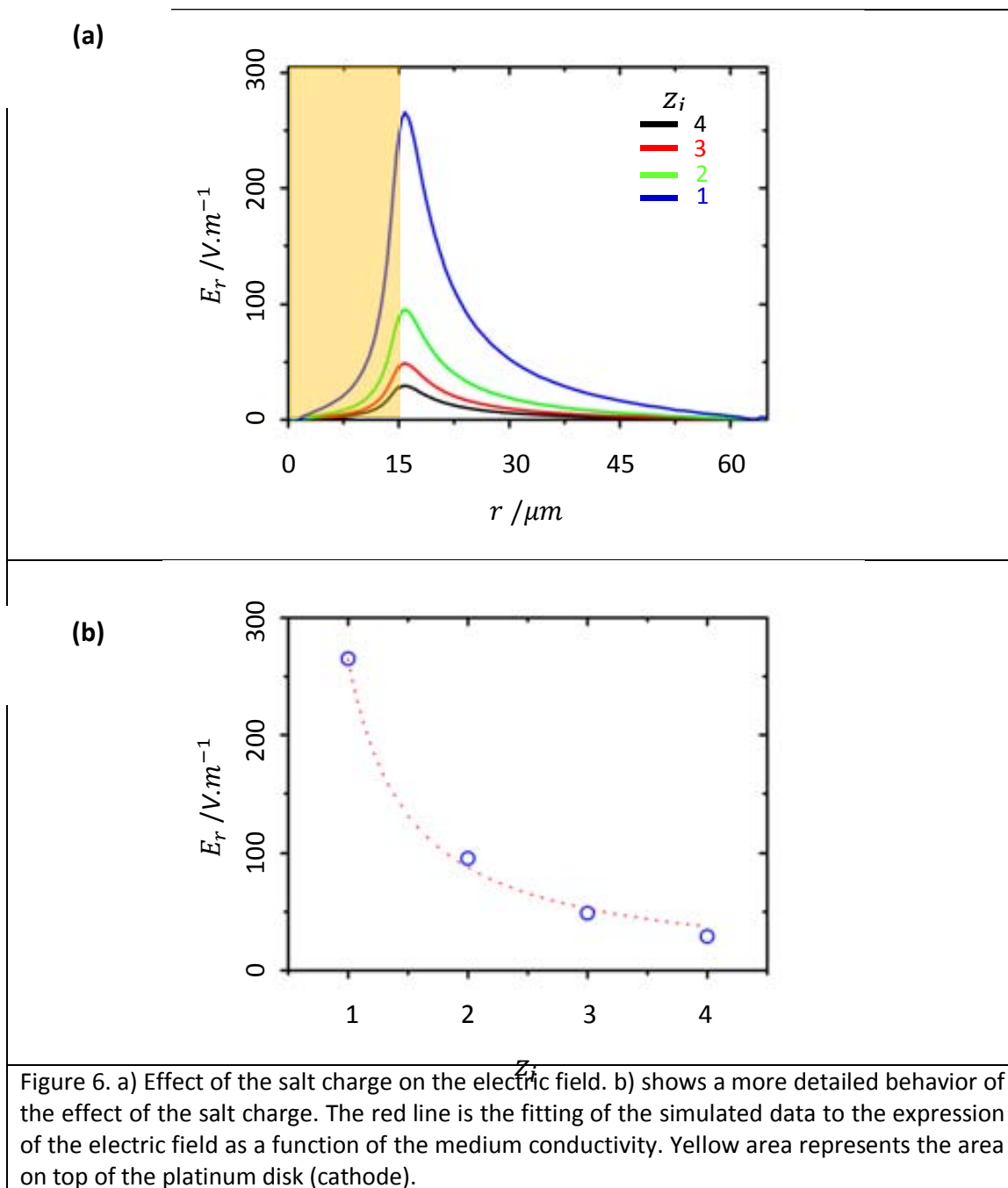
The dashed red line of Fig. 4b corresponds to the fitting of the electric field decay with eq. xx. It can be observed the good qualitative agreement between the numerical findings and the fitting according to eq. 9.3.



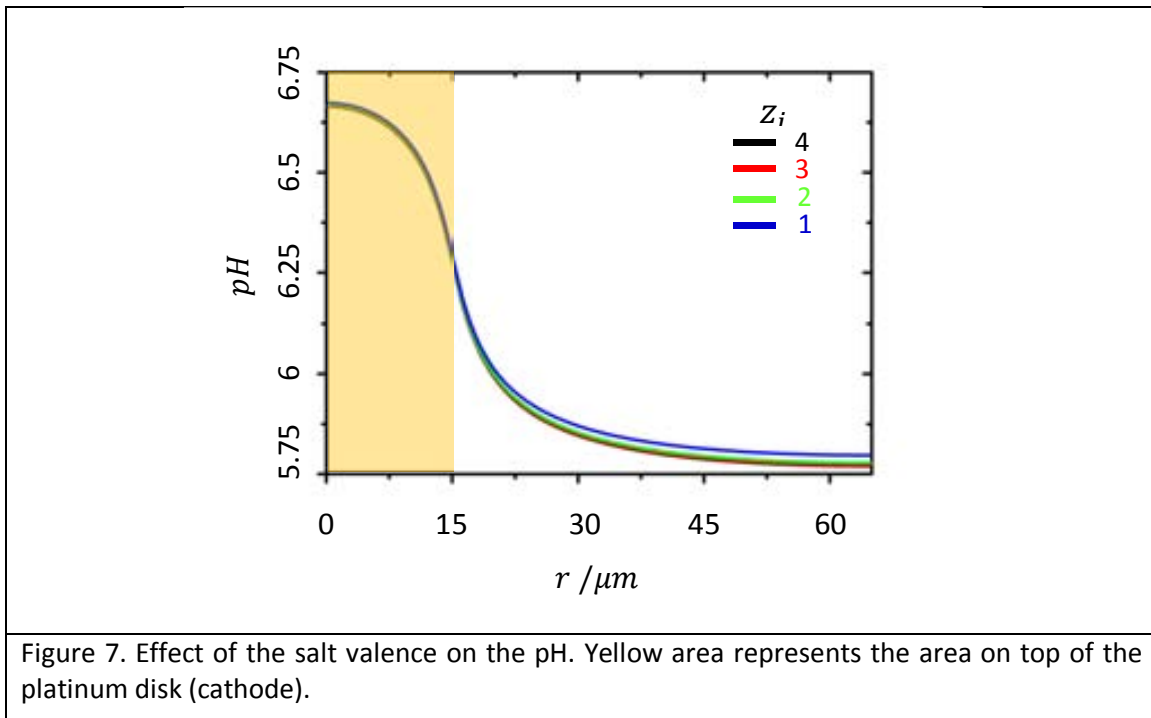
On the other side the addition of salt does not have a very important impact on the pH. Figure 5 shows that the local concentration of protons remains essentially unchanged, only decreases 0.14 units of pH at the anodic part and increases 0.11 units at the cathode one.



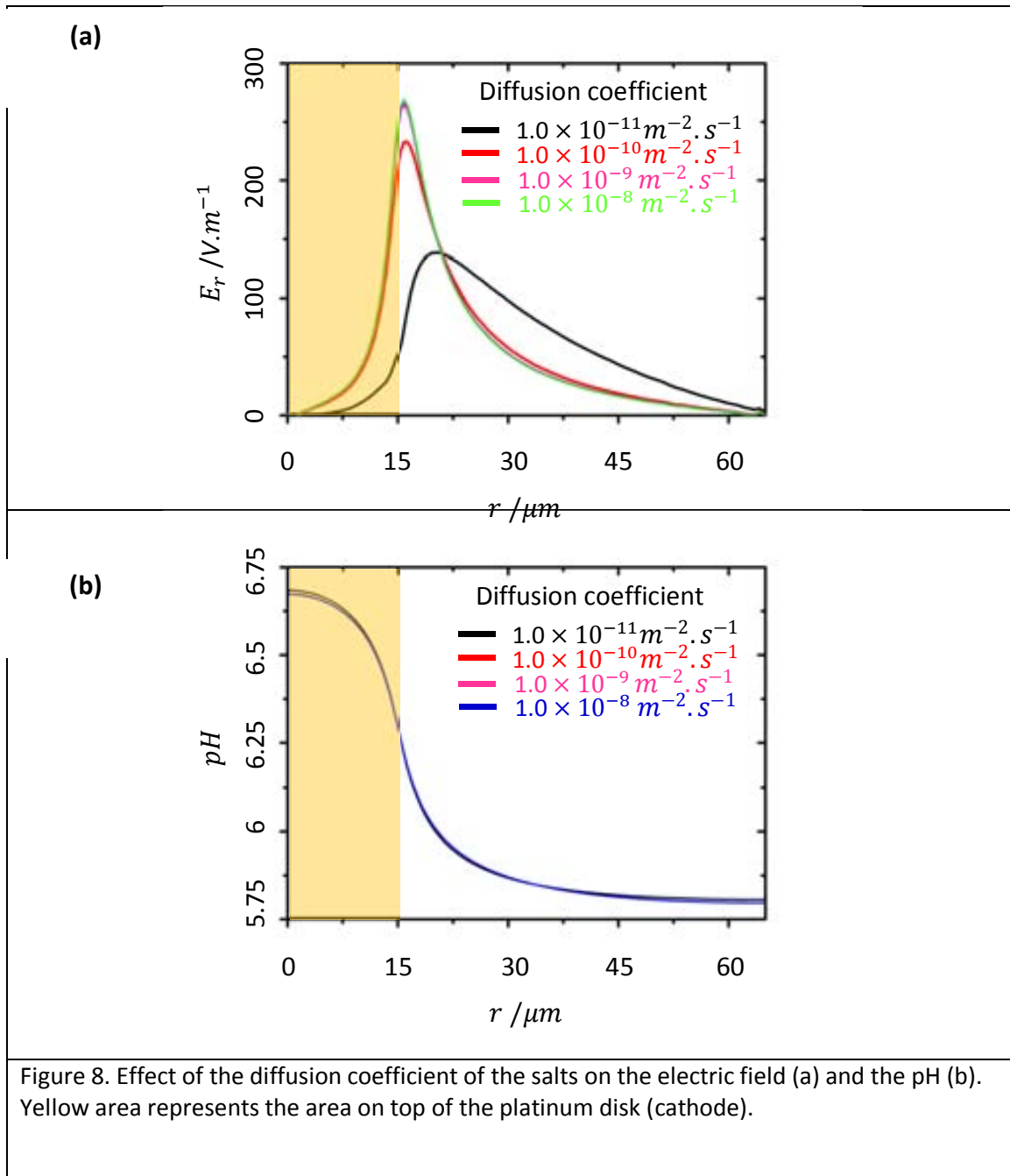
The valence of the extra ions or salts represents another parameter to take into consideration when analyzing the effect of salts. Figure 6 shows the variation of the electric field as a function of the radial coordinate for different multivalent salts. The charge of one of the ions (the positive one) is kept constant in a value of 1 and the other one is changed from 1 to 4 (1:1, 1:2; 1:3 and 1:4). As expected, the higher the charge in the salts, the lower is the electric field due to screening effects. Charges of 4 almost annihilate the electric field. The electric field decay with increasing charges can also be described by eq. 9.2. The red dashed line in Figure 6 b corresponds to the fitting of the data with an expression similar to eq. 9.3.



More interestingly the charge has no effect on the local proton concentration. Figure 7 shows that the pH distribution as a function of the radial distance remains essentially unaltered as the ion valence is varied.



Another parameter worthy to evaluate is the diffusion coefficient of the salt or extra ionic species in the fluid. Figure 8 shows the change of the electric field and pH as a function of the radial coordinate for different values of diffusion coefficients. The electric field is almost not affected for diffusion coefficients from around $5 \cdot 10^{-10} \text{ m}^2 \text{ s}^{-1}$ to $1 \cdot 10^{-8} \text{ m}^2 \text{ s}^{-1}$, which are in the range of the typical values for common salts. However lower, diffusion coefficients (typical for big size ionic species, such as proteins, DNA fragments, etc.) exert important changes in the electric field. In the figure it can be observed how the electric field not only decreases at such low values of the diffusion coefficient but also its spatial distribution profile is also altered. On the other side the diffusion coefficient have no effect on the proton distribution at the anode and cathode side.

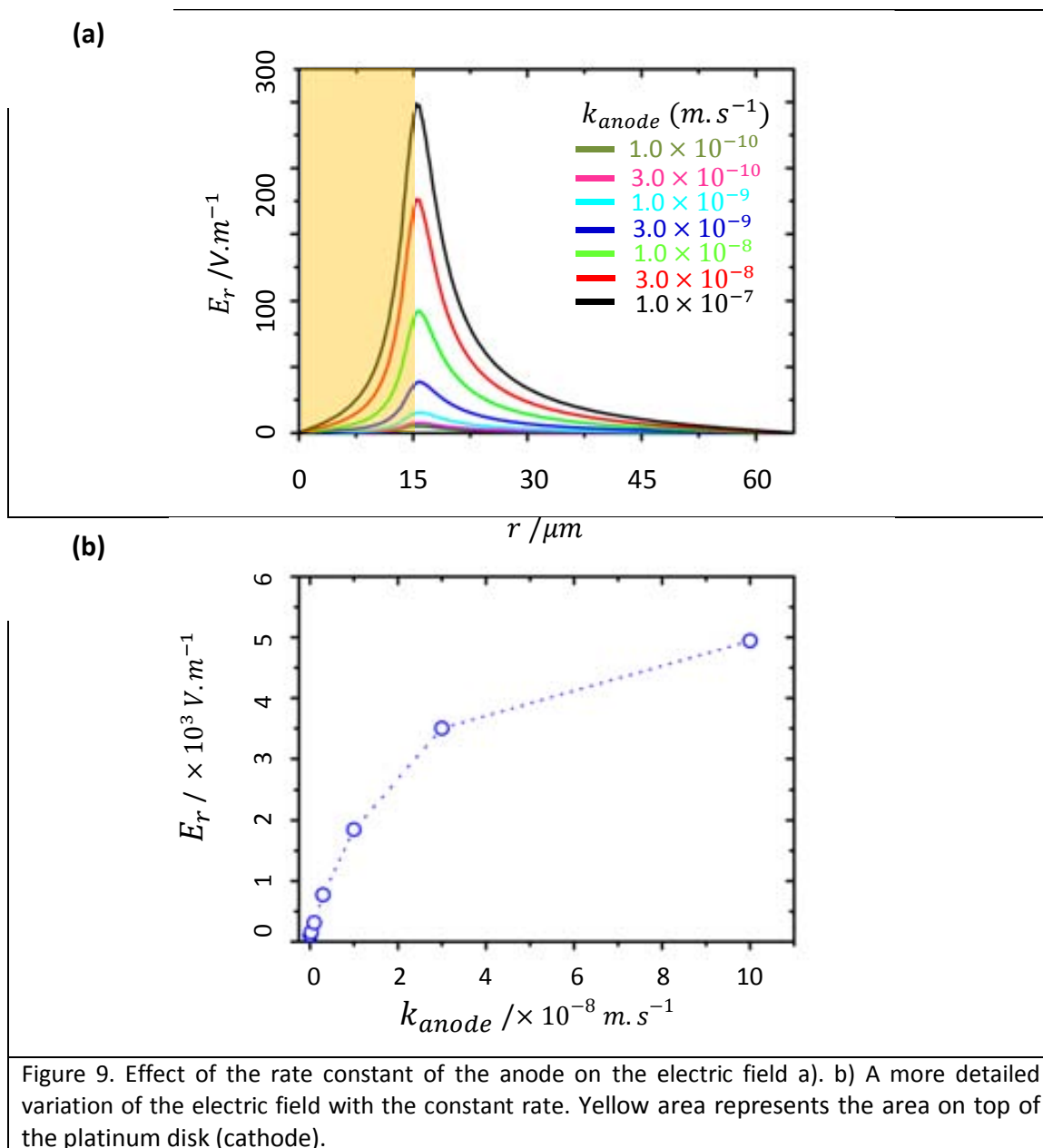


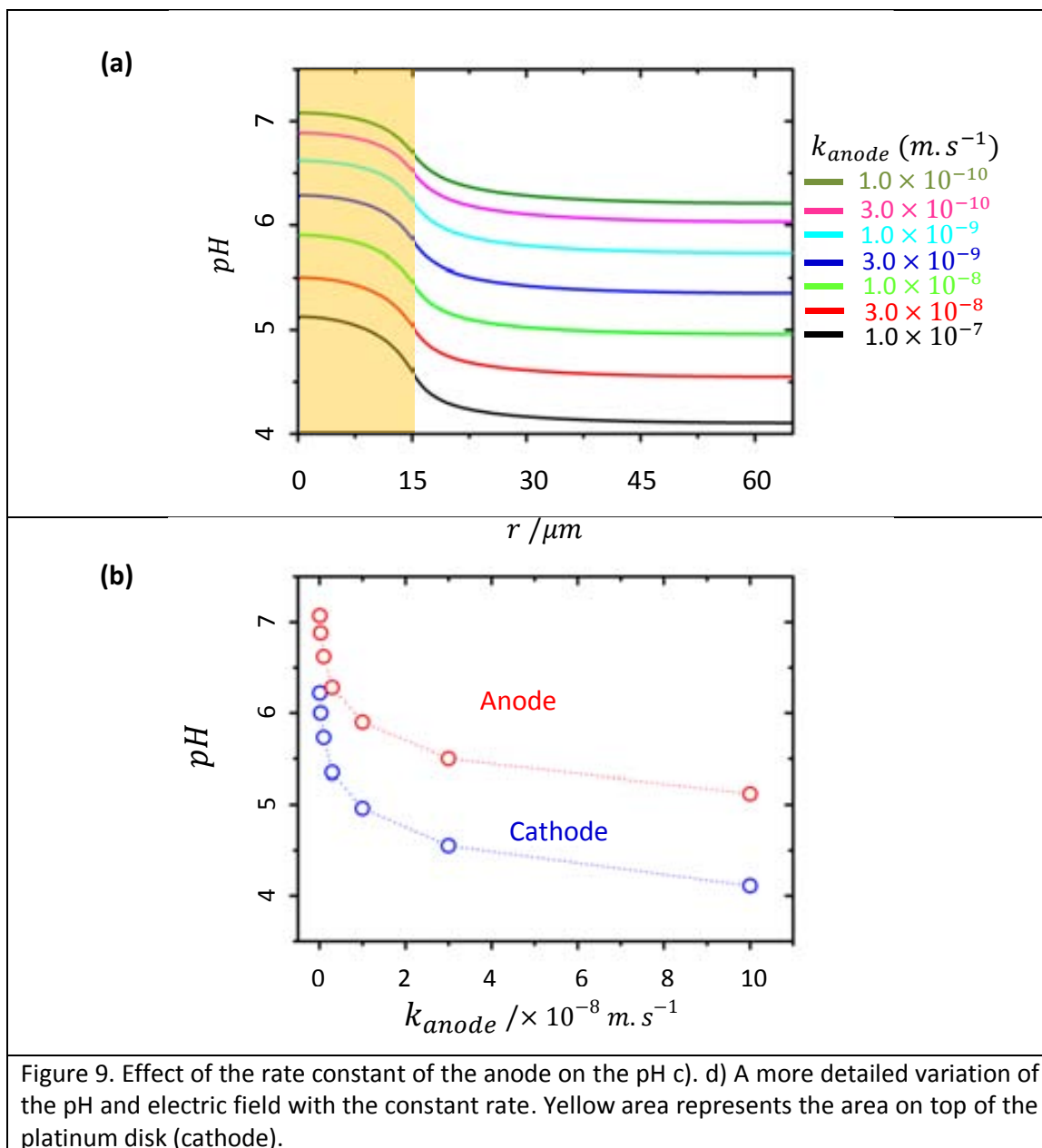
Effect of the rate constants of the anode and cathode

In this section it will be evaluated the effect of the rate constants of the anode and cathode on the electrokinetic parameters. The change of the rate constants can be thought as changes in the material constituting the micropump. Figure 9 a and c show the variation of the electric field and local proton concentration when the rate constant of the anode is varied by three orders of magnitude. The electric field increases as the anodic reaction rate becomes larger. For instance, the increase of three orders of magnitude in the anodic constant rate makes the electric field increase 50 times. It is also remarkable the wide variation on the pH either at the anodic or at the cathodic side when the anodic rate constant is varied. That is not surprising since the anode constant rate

plays a crucial role in the generation of proton species. Figure 9 b and c depict in more detail the variation of the electric field and pH. Both parameters tend to a plateau at very high anodic rate constants. This behavior can be understood by considering that the reaction rates on the anode and cathode are related by electroneutrality reasons and that changing k_{anode} is like varying the anode material while keeping the same cathode. One can have the best anode material but if the cathode is not able to consume all the products of the anode (limiting rate), the anode production will adjust to the limiting cathode. Under this case a saturation in the electrochemical reaction of the anode is achieved which can explain the saturation in the proton production and consumption and in the electric field.

In contrast to the dramatic effects that produce the change in the electrode kinetics of the anode on the electrokinetic parameters, the variation of the cathode rate constant only affects in a lesser extent. The increase of 3 orders of magnitude in the cathode rate constant only makes the electric field increase in a factor of 2 at very low rate constants and reaches a plateau at higher rate constant values (Figure 10 a and b). Such behavior can be explained following the same argument than before. At low rate constants of the cathode, the electrochemical reaction is controlled by the cathode but at higher rate constants the control is determined by the anode. With respect to the proton concentration, the concentration of protons keeps almost unchangeable on the anodic region (Figure 10 c). However a pH change of almost one unit is produced on the cathode side. The proton depletion on the cathode is increased with increasing cathode rate constants up to reach a plateau (at very high constant rates), in a similar way as in the case of the anode rate (Figure 10d).





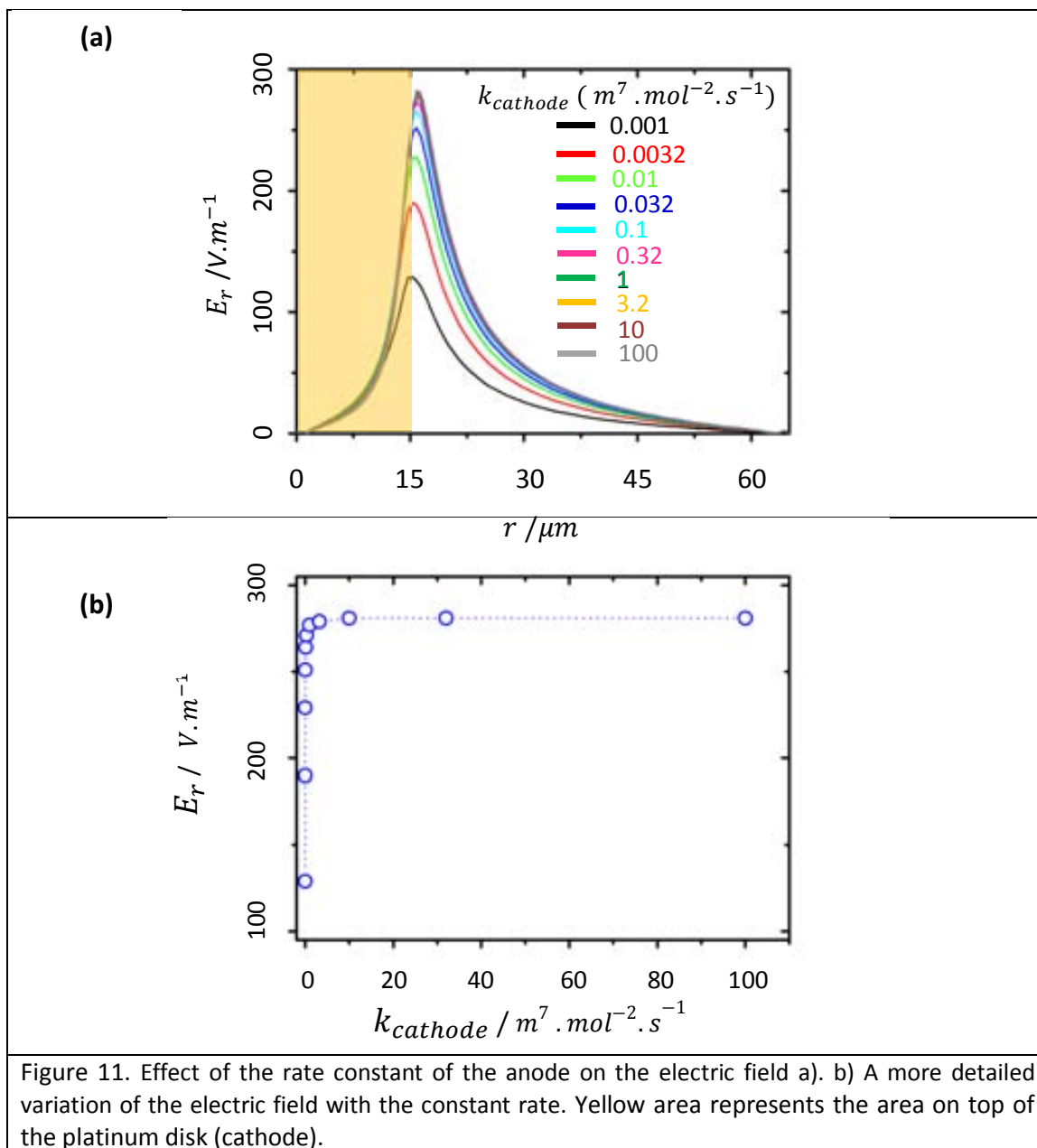
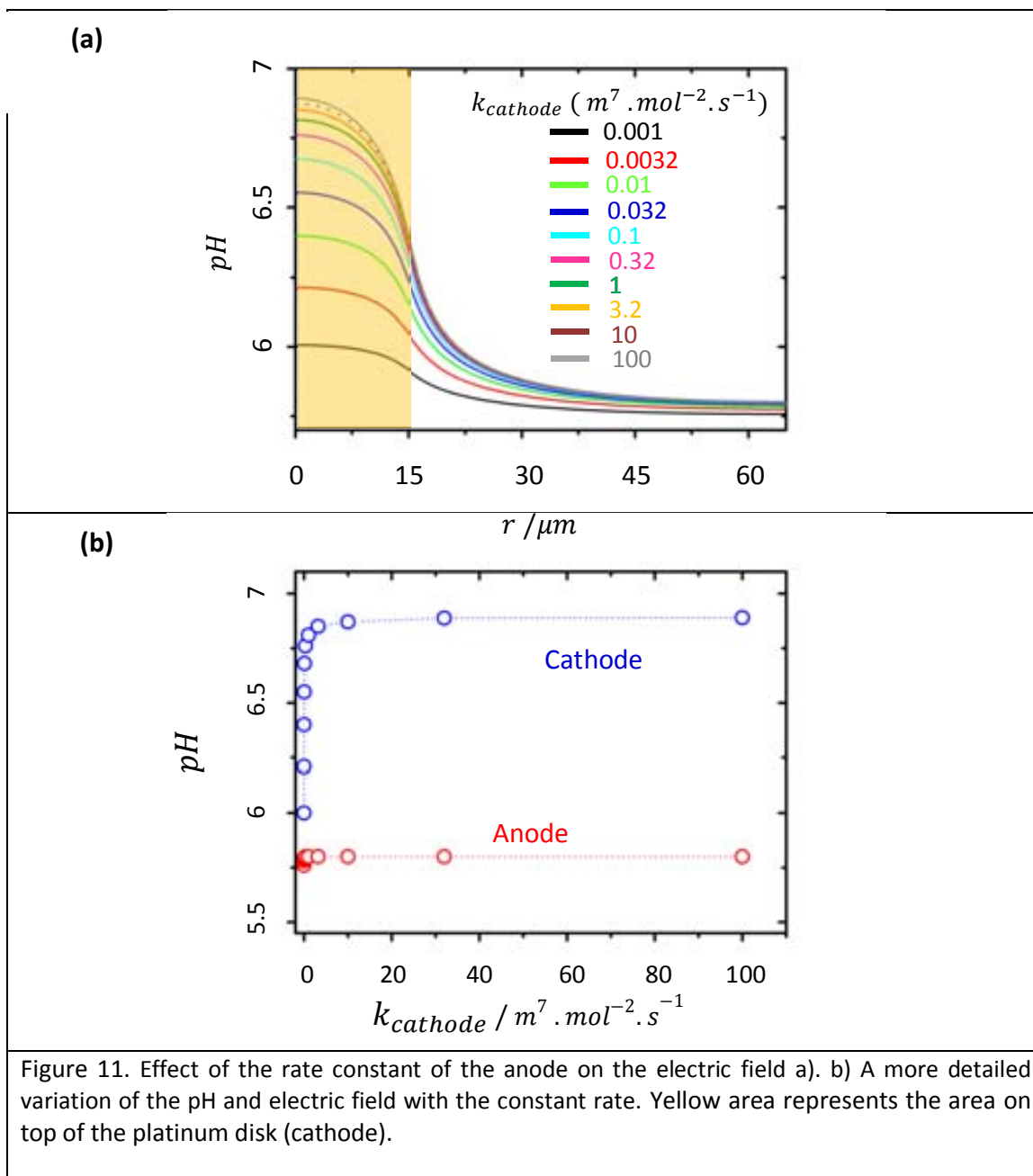


Figure 11. Effect of the rate constant of the anode on the electric field a). b) A more detailed variation of the electric field with the constant rate. Yellow area represents the area on top of the platinum disk (cathode).



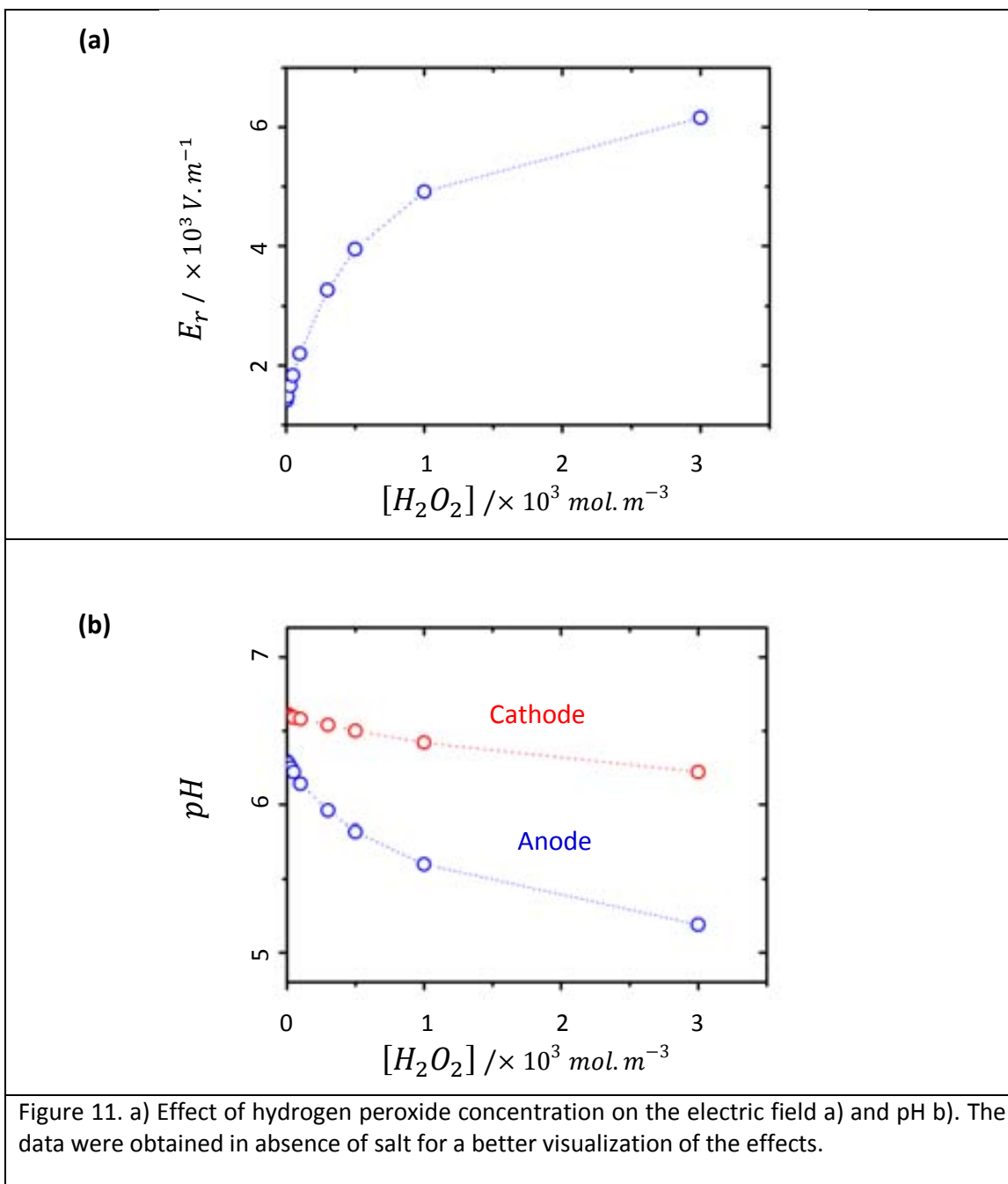
Effect of the hydrogen peroxide and the bulk proton concentration

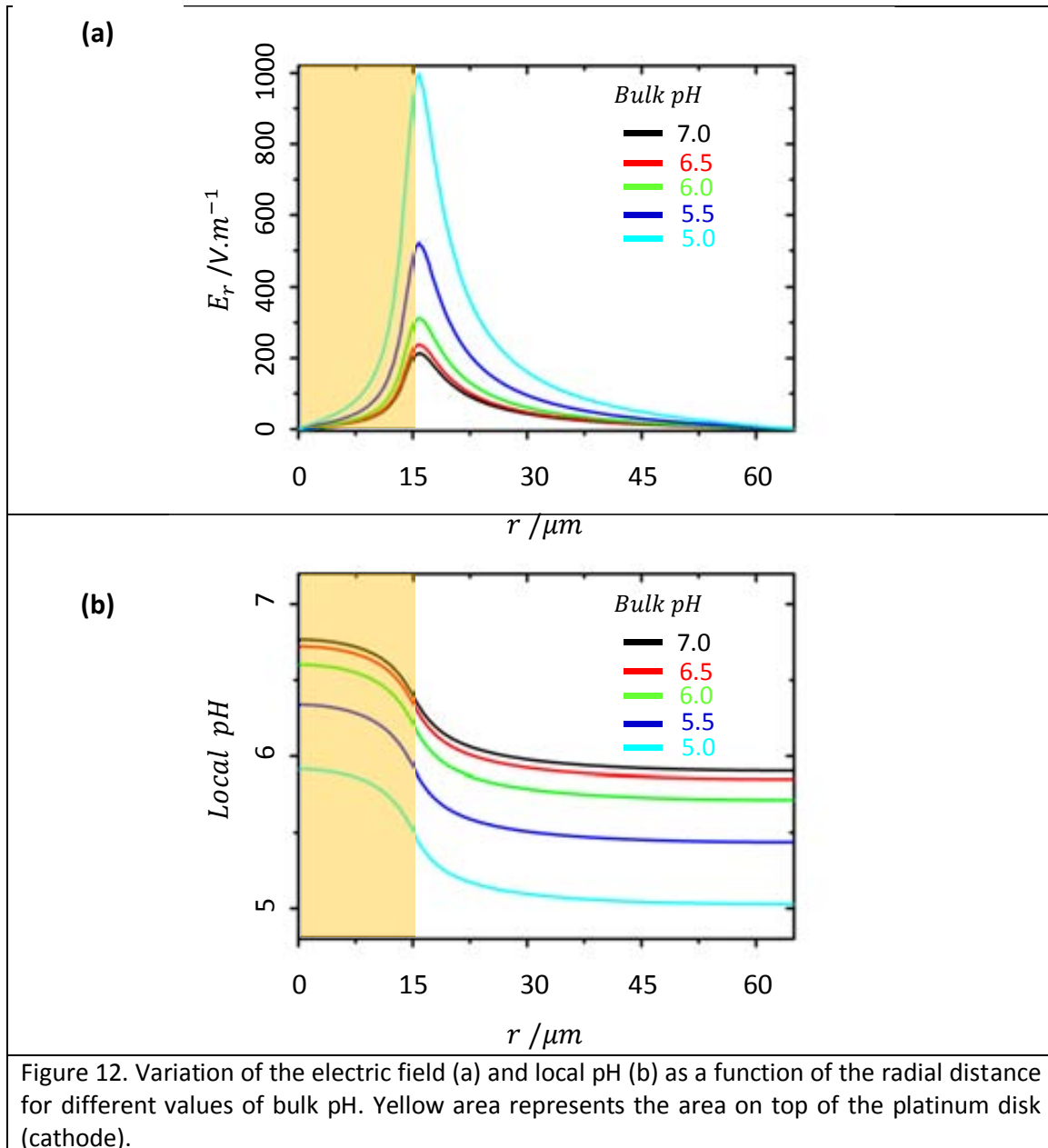
Hydrogen peroxide greatly affects the electric field and proton concentration since its concentration influences the rate of the electrochemical reaction at the anode and cathode⁸⁷. Figure 11 b and c shows that effect. The electric field and fluid velocity can increase over 20 times their values when the hydrogen peroxide concentration is changed by three orders of magnitude. However such increase is not linear in the whole range. For instance at higher hydrogen peroxide concentrations the parameters change in a smaller extent reaching a saturation. That is an agreement with the theoretical findings of Seifert et al. [5] and the experimental data. An interpretation of this saturation has been given in the framework of a Michaelis-Menten like surface kinetics [5].

On the other side the increase of H₂O₂ increases the local proton concentration at both metals shifting the pH towards lower values at both sides but being more dramatic on the anode which is indeed the source of proton generation. The pH can decrease up to one unit when increasing H₂O₂.

The initial concentration of protons at the bulk also impacts on the electrokinetic parameters. The electric field increases as the bulk concentration of protons increase (Fig. 12 a). The proton concentration at the bulk can specially affect the electrochemical reaction rate of the cathode since it depends on the concentration of protons (note 2). The increase of the electric field with the decrease of bulk pH could be related with an increment of the electrochemical reaction rate at the cathode. On the other hand the pH range is shifted towards lower values as the bulk pH is decreased but keeping almost the same pH change between anode and cathode (Fig. 12 b).

⁸⁷ Just to recall, the electrochemical current associated with the hydrogen peroxide decomposition at the anode can be expressed as $J_{\text{anode}} = k_{\text{anode}} [\text{H}_2\text{O}_2]$ and at the cathode as $J_{\text{cathode}} = k_{\text{cathode}} [\text{H}_2\text{O}_2] [\text{H}^+]^2$



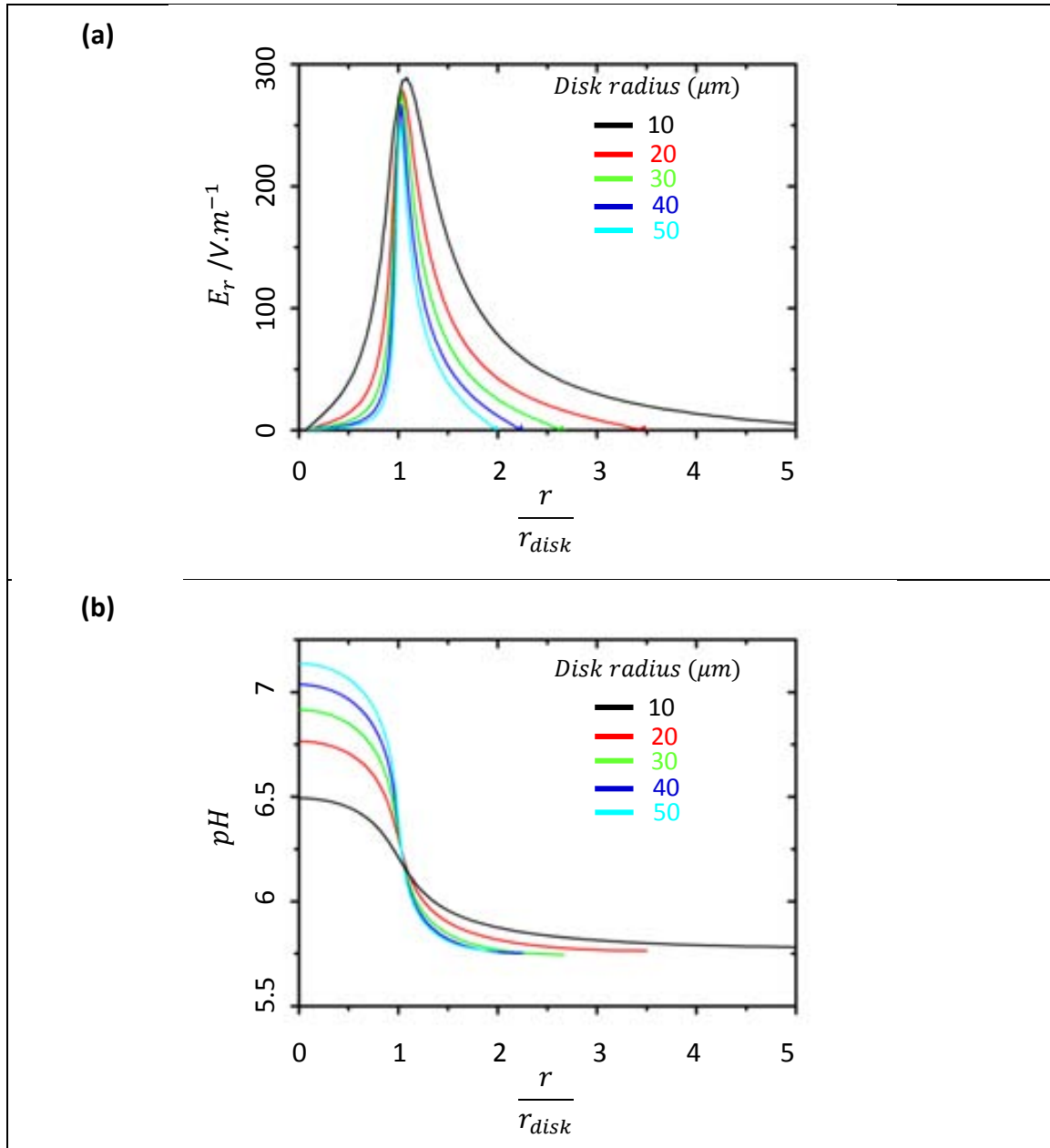


Effect of the geometry: size of the cathode and anode

The typical design of the micropump presented in this thesis is a smaller metal disk with the role of cathode which is patterned on a bigger radius disk acting as anode. For design purposes, it turns out very interesting to follow the impact of the electrode sizes on the electrokinetic parameters. Firstly it will be addressed the impact of changing the radius of the cathodic disk and then the effect of changing the size of the anode.

Indeed the size of the anode and cathode affects directly the reaction rates at both electrodes. Figure 13 shows the effect of the cathode disk size on the electric field. The electric field is not so much affected by the size of the cathode disk when its radius is changed from 10 to 50 μm

while keeping the anode radius at a constant value of 50 μm . However it can affect the electrochemical reaction at the cathode. Figure 13 c and b show how the consumption of protons increases on the cathode as the radius of the disk becomes bigger, producing a larger change in the pH from anode to cathode. The proton concentration remains almost the same at the anode side.



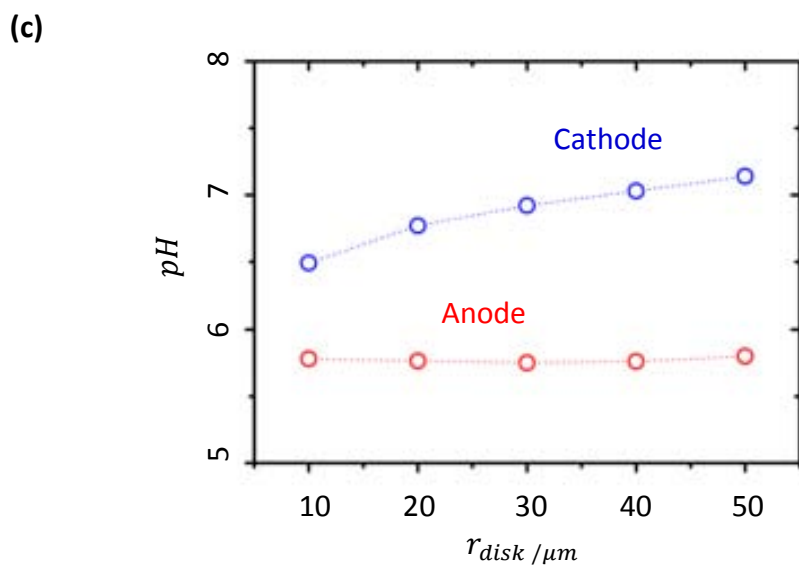
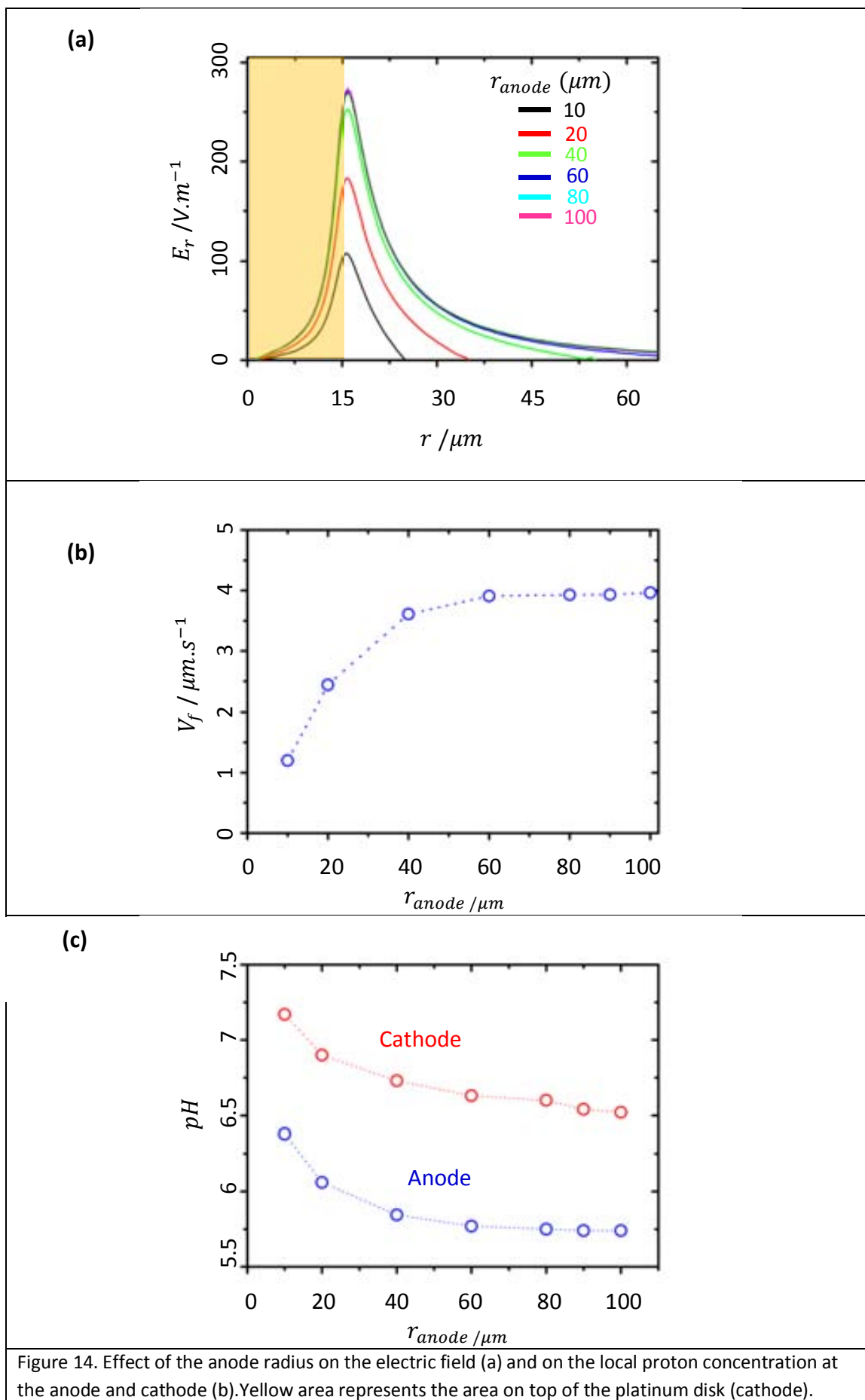


Figure 13. Effect of cathode disk size on the electric field (a) and on the proton production at the anode and cathode (b and c). For better visualization the multiple plots of the electric field and pH as a function of the radial distance were normalized with respect to the disk size.



The radius of the anode affects the electrokinetic parameters up to a certain value. Figures 14 a, b and c show the effect of varying the anode radius on the electric field and on the local concentration of protons. In these simulations the radius of the cathode disk was maintained at 15 μm and the anode radius was changed from 10 to 100 μm . Only remarkable changes in the electrokinetic parameters can be observed if the anode radius is below 50 μm . The electric field decreases almost three times when decreasing the radius from 50 μm up to 10 μm . The diminution of the area of the anode decreases the electrochemical reactions which are responsible to switch on the electrokinetic processes. The decrease of proton generation at the anode is reflected in the pH distribution. An increase of the pH is observed at both metallic sites.

Conclusions

In this part, a systematic analysis of the influence of the different parameters involved in the chemomechanical actuation has been performed. This theoretical approach can help to acquire a better understanding of the micropumps and to provide clues for optimizing the devices. The evaluated parameters were the surface potential, the salt concentration, charge and ion diffusion coefficients, the electrochemical rate constants at the anode and cathode, the hydrogen peroxide concentration, the bulk pH and the side of anode and cathode. The focus has been put on the changes that these parameters can exert on the electric field and local proton concentration. The behavior of the fluid flow has been only highlighted when analyzing the effect of surface potential. The fluid velocity was omitted in the rest of the analysis because it was shown that it is mainly controlled by the electric field and changes accordingly with the electric field.

The surface potential is a very important ingredient to switch on the electrokinetic phenomenon. It greatly affects the electric field, fluid velocity and pH. The surface charge is crucial to build up the double layer and to control the charge asymmetry along the anode and cathode which finally exerts a crucial role in the electrohydrodynamic process.

The salt concentration and the charge of its ions dramatically affect the electric field and the fluid flow due to screening effects. However they do not affect the local proton concentration at the anode and cathode. The diffusion coefficients of the ionic species play a minor role in the electric field and do not modify the local pH.

The variables involved in the electrochemical reactions, especially the rate constants at the anode and hydrogen peroxide, remarkably alter the electric field profile and the local proton concentration. Interestingly the rate constant of the cathode only presents a more secondary role.

The bulk pH can modify the electric field and the proton distribution in a more moderate way. Finally, the anode and cathode sizes exert a minor role on the electrokinetic process. The electric field and pH at the anode are insensitive to the cathode disk size, being the pH at the cathode more sensitive to the size changes. In the case of the anode, only small anode sizes have impact on the electrokinetic variables.

- [1] T. R. Kline, J. Iwata, P. E. Lammert, T. E. Mallouk, A. Sen, and D. Velegol, "Catalytically Driven Colloidal Patterning and Transport", *The Journal of Physical Chemistry B*, vol. 110, pp. 24513-24521, 2006.
- [2] J. L. Moran, P. M. Wheat, and J. D. Posner, "Locomotion of electrocatalytic nanomotors due to reaction induced charge autoelectrophoresis", *Physical Review E*, vol. 81, p. 065302, 2010.
- [3] J. L. Moran and J. D. Posner, "Electrokinetic locomotion due to reaction-induced charge auto-electrophoresis", *Journal of Fluid Mechanics*, vol. 680, pp. 31-66, 2011.
- [4] E. Yariv, "Electrokinetic self-propulsion by inhomogeneous surface kinetics," *Proceedings of the Royal Society A: Mathematical, Physical and Engineering Science*, vol. 467, pp. 1645-1664, 2011.
- [5] B. Sabass and U. Seifert, "Nonlinear, electrocatalytic swimming in the presence of salt," *The Journal of Chemical Physics*, vol. 136, 214507, 2012.

Chapter 10

Conclusions

This thesis has been able to successfully address all the goals that were set at the beginning of the work. A more comprehensive scenario of the physico-chemical processes behind the catalytic actuation in bimetallic pumps has been accomplished by complementing experimental and theoretical tools. In turn, these achievements have motivated the search of novel micropump devices based on alternative bimetallic structures or metal/semiconductor structures. Many promising findings encourage the continuity of the research widening the scope of this field to novel pumps with strong implications in the field of chemically driven actuators or nanomotors. Finally it has been possible to probe one of the potential applications of this kind of systems that could have important impact in many technological fields. Below a more detailed description of the conclusions in straightforward relation with the objectives will be covered.

Recalling what mentioned in chapter 2, four major goals were defined in the scope of this research. So, the achievements can be summarized and categorized under four main parts.

These parts are

- I. **Understanding the physical details of the chemochemical mechanism behind bimetallic catalytic micropump using as a model system Au-Pt in hydrogen peroxide solution.**

As expected, a complicated electrohydrodynamic process is in charge of the performance of bimetallic catalytic micropump. Many chemical and physical parameters are involved in the fluid pumping. The surface chemistry plays a key role in Au-Pt system. The surface plasma treatment oxidizes and modifies the electrochemical properties of the gold and platinum which enhances the hydrogen peroxide electrochemical reactions on the metal. It has been proved that the catalytic reactions take place on platinum and gold acting as cathode and anode respectively. The gold surface produces proton that are consumed at the platinum side. The redox role of the metals was predicted by Tafel measurements and confirmed by Confocal fluorescence Microscopy. The latter technique allows the 2D imaging and quantification of the proton gradient generation around the Au-Pt device as a consequence of the electrochemical reactions. It was found a higher concentration of protons on the gold side and a proton concentration depletion at the platinum surface. Thus, the electrochemical reaction can self-generate an electric field pointing from the gold to the platinum. Quantification of such gradient showed that the pH is changed about one unit along the Au/Pt device during the process. The spatial imaging and quantification of this relevant parameter constitutes the first reported study in the field of catalytic motors

Observing the interaction between differently charged tracers and the devices provided valuable information about the spatial distribution and quantification of the electric field and fluid velocity around the devices.

It has been found that the electric field strength and the fluid velocity are maximal just at the Au/Pt border. The findings also confirm an electric field pointing toward the Pt and a fluid flow in the same direction.

II. **Implementation of simulations based on finite elements to support experimental data.**

The simulation results of the fluid flow, electric field, proton concentration and proton flow were in agreement with experimental results.

The simulations have also shown that due to the chemical reaction a net positive charge was confined inside the double layer with a charge distribution asymmetry along the radial distance. Such asymmetry can induce an electric field. It was also observed the existence of electric field above the electric double layer at distances in which the fluid is electroneutral. That could be explained as a consequence of the motion of protons from the anode to cathode beyond the double layer.

Besides reproducing experiment results, the numerical analysis provided information about the effect of some physical and chemical parameters which affect the efficiency of the electrohydrodynamic processes. It was performed a systematic analysis of the influence of the surface potential, the salt concentration, charge and ion diffusion coefficients, the electrochemical rate constants at the anode and cathode, the hydrogen peroxide concentration, the bulk pH and the size of anode and cathode.

It was found that the electric field and fluid velocity are greatly affected by the salt concentration and charge, the surface potential and the parameters involved in the production of protons such as the constant rate of the anode and the hydrogen peroxide concentration. Other variables that could alter these parameters, but in a more moderate way, were the diffusion coefficient of extra ionic species and the initial pH value at the bulk.

The proton distribution was dictated mainly by the electrochemical reaction (especially the anodic rate constant of the peroxide decomposition and the peroxide concentration). Interestingly, the rate constant of the cathode only presented a more secondary role. Finally, it was found that the anode and cathode sizes exerted a minor role on the electrokinetic process. This study helped not only to have a better understanding of the whole scenario behind this process but also provided important clues of how to design more efficient catalytic actuators.

III. **Proposing alternative catalytic micropumps based on other bimetallic (X-Y) or semiconductor/metallic structures.**

TAFEL measurements represent a reliable tool to predict the behavior of bimetallic X-Y devices. Many different bimetallic structures were fabricated on the basis of Tafel predictions: Au-Rh, Au-Ru, Cu-Ag, Cu-Ni, Ni-Cu, Ni-Ru and Ni-Ag devices. Although some of the chosen materials were less noble than the Au-Pt system and could degrade with time, they can represent a lower cost alternative in applications which do not require extended lifetimes. These pumps show interesting interactions with differently charged tracers which require further investigation

Regarding semiconductor- metal systems, these novel systems provide the highest achieved fluid velocity among the studied systems. The catalytic actuation of these devices is triggered by the photo-activation of the catalytic reactions. Light

absorption produces hole/electron pairs at the semiconductor. The holes oxidize the chemical fuel whereas the photoexcited electrons are transferred to the metal favoring the cathodic reduction of the fuel on the metal surface. These semiconductor/metal devices can become promising candidates of a new generation of catalytic micropumps or swimmers.

IV. Studying the self-generated electrohydrodynamic process to guide colloidal self – assembly as a potential application of these devices.

A Au-Pt catalytic pump was used to demonstrate guided colloidal self-assembly as a potential application of these active devices. The local self-generated electrohydrodynamic forces triggered by the electrochemical reactions at both metals together with the nature of the colloidal charge and the surface treatment are the basic ingredients for tailoring the patterning process. The use of negative particles allowed patterning the gold surface starting from the Pt edge and forming a more 2D ordered colloidal crystal. Instead, the use of positive particles allowed patterning unordered but stable 3D colloidal aggregates on the platinum disks. In the case of negatively charged particles it was possible to monitor in real time many unexpected features during the patterning process: electrostatic repulsion, silica clustering, silica transport to the Pt edges and the fascinating dynamics of silica crystallization at the gold surface from the platinum edge. These self-guiding processes may become a very versatile tool to approach technological important challenges in nanofabrication. The autonomous accumulation of material to precise locations can have impact in the design of photonic crystals, smart nanostructured surfaces for sensing or catalysis, photovoltaics, corrosion protection, self-healing systems among others.

Outlook

One of the challenges of catalytic actuation either in pumps or micro/nanoswimmers is to improve their efficiency. Although there is still a long way to compete with the high efficient biological machinery, the exploration of new materials, layouts and fuels are important issues that should continue being addressed in the future in order to increase efficiency and also compatibility with different fluid environments. This research work has achieved the proof-of-concept of novel photochemical-electrohydrodynamic switches which have demonstrated to greatly amplify the electrohydrodynamic effects. We believe there is a lot of room for exploration and exploitation of this kind of systems which can open new and promising research activities in the field of catalytic actuators and nanomotors.

This thesis has also demonstrated the deposition of material in an autonomous fashion at pre-defined locations and with control of the aggregate structure. That is another important aspect that can be exploited in future research driven by the high impact that could bring in many technological areas such as nanophotonics , smart (bio)chemical sensing , catalysis , matter transport and separation, corrosion protection or adaptive(self-healing) systems.

Finally, and more importantly from the fundamental point of view, these catalytic pumps, which can be rationalized as immobilized potential swimmers, can become a very useful and practical model system for the design or first exploration of novel self-propelled nanomotors. With this kind of system new effective experimental methods could be more easily implemented and control to comprehend and spatially quantify the parameters involved in the complex process of actuation, a task which is not so easy to accomplish in free-suspending nanomotors. Moreover these pumps could also help to understand many interesting phenomena related with hydrodynamic interactions such as collective dynamics, complex self-organization, or the emergence of large-scale coherent structures. These are topics that are having a strong growing interest nowadays and whose understanding could greatly benefit from the experimental techniques and results of this thesis.

Appendixes

Appendix 4.1 : Ru and Rh voltammograms

Cyclic voltammetry is a powerful electrochemical characterization technique which is widely used for acquiring information of the electrochemical reactions taken place in a system and for assessing kinetics information of the electron transfer process. It provides a fast way to locate redox potentials of electroactive species. In this thesis, this technique was used to determine the cathodic potential (E_{pc}) against Ag/AgCl/KCl reference electrode for Ru and Rh deposition [1-4]. Experimental setup and electrolytes were described in 4.1.1b.

Cycle voltammetry is based on applying a potential cycle (figure 1.a) between a working electrode and a reference electrode. Applied potential generates current which passes through the electrolyte between counter electrode and working electrode. The response is an I-V curve (figure 1.b), the so called voltammogram. The applied potential is linear. The instrument applies an increasing voltage from E_1 to E_2 with a constant voltage sweep rate and afterwards it is reversed to E_1 with the same rate. The voltage range can be selected to cover the oxidation and reduction reactions that may occur in the electrochemical system under study. The redox signals generally appear in a peaked shaped form (depending on the dimensions of the electrodes). According to the European convention, the potential at which a positive peak current appears when applied positive voltages corresponds to the anodic or oxidation potential (E_{pa}) of the species and the potential at which negative peak current comes up when more negative voltages are applied is the cathodic (E_{pc}) or reduction potential (Figure 1.b) [5-9]. As mentioned above the technique was used to determine the cathodic waves corresponding to the electrochemical reduction of the Rh and Ru as shown in figure 2.

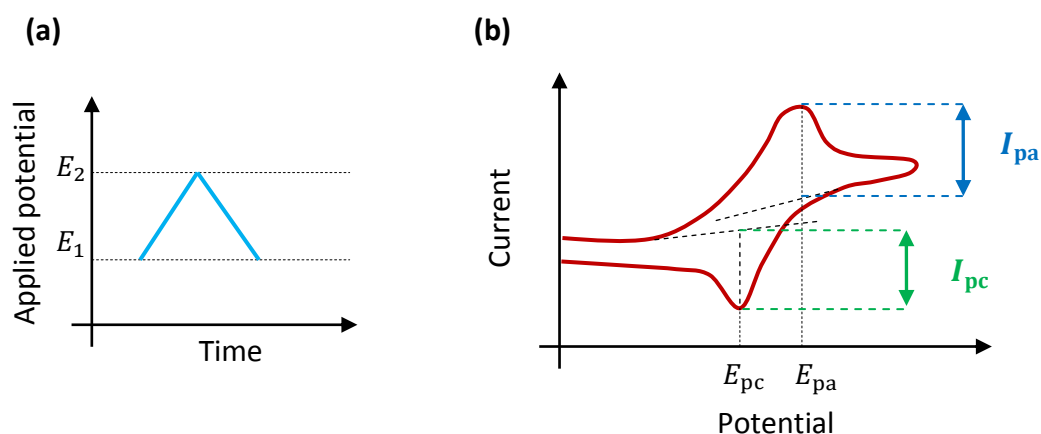


Figure 1: schematic illustration of a) applied potential cycle between E_1 and E_2 , b) a voltammogram indicating the cathodic (E_{pc}) and anodic (E_{pa}) potentials and their corresponding cathodic (I_{pc}) and anodic (I_{pa}) currents

The Ru deposition is taken place in three cathodic waves. The first two reduction waves at E_{pc} of 0.29 V and 0.03 V correspond to the deposition of thin Ru adlayers whereas the one at E_{pc} of -0.68 V corresponds to the massive or bulk deposition of Ru. In the case of Rh deposition it was only possible to capture one deposition peak at E_{pc} of -0.32 V. The fact that some metals can be deposited in different steps is quite common for some metals and depends on the binding interaction between the substrate and the metal to be deposited.

After having identified the cathodic potentials, the electrodeposition process is taken place by using chronocoulometry and applying a potential more negative than the cathodic peak potential (-0.85 V and -0.4 V for ruthenium and rhodium respectively).

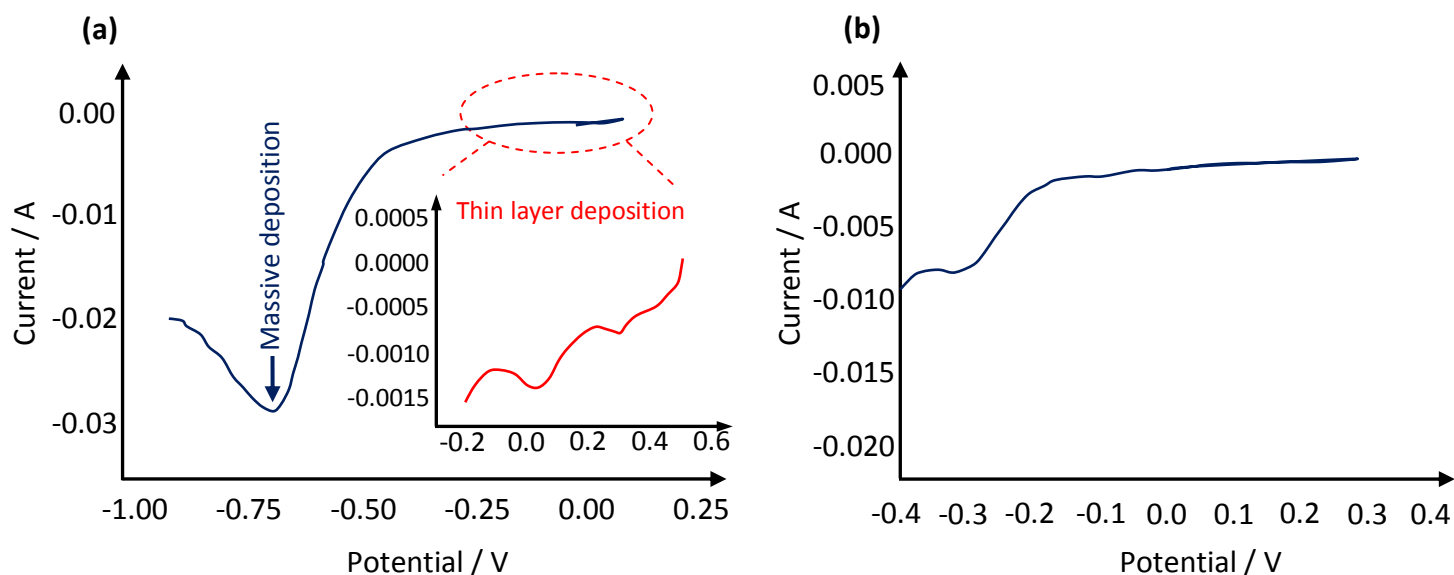


Figure 2: Voltammograms for Ru (a) and Rh (b) deposition taken at a scan rate of 100 $\text{mV}\cdot\text{s}^{-1}$.

References

- [1] L. A. Kibler, M. Kleinert, and D. M. Kolb, "The initial stages of rhodium deposition on Au(111)," *Journal of Electroanalytical Chemistry*, vol. 467, pp. 249-257, 6/7/ 1999.
- [2] R. T. S. Oliveira, M. C. Santos, L. O. S. Bulhões, and E. C. Pereira, "Rh electrodeposition on Pt in acidic medium: a study using cyclic voltammetry and an electrochemical quartz crystal microbalance," *Journal of Electroanalytical Chemistry*, vol. 569, pp. 233-240, 8/1/ 2004.
- [3] W. Chrzanowski and A. Wieckowski, "Ultrathin Films of Ruthenium on Low Index Platinum Single Crystal Surfaces: An Electrochemical Study," *Langmuir*, vol. 13, pp. 5974-5978, 1997/10/01 1997.
- [4] O. Raz, G. Cohn, W. Freyland, O. Mann, and Y. Ein-Eli, "Ruthenium electrodeposition on silicon from a room-temperature ionic liquid," *Electrochimica Acta*, vol. 54, pp. 6042-6045, 10/30/ 2009.
- [5] N. V. Cvetkovic, *Organic Electronics and Stencil Lithography Fabrication Methods: Organic Thin-Film Transistors and Circuits Fabricated by Stencil Lithography on Full-Wafer Flexible Substrates*: LAP Lambert Academic Publishing, 2012.

- [6] D. M. Mattox, *Handbook of Physical Vapor Deposition (PVD) Processing*: Elsevier Science, 2010.
- [7] O. V. Mena, *Development of Stencil Lithography for Nanopatterning and for Electronic and Biosensing Applications*: EPFL, 2010.
- [8] K. A. Pataky, *Stencil Lithography and Inkjet Printing as New Tools for Life Sciences Research*: Hartung-Gorre, 2011.
- [9] M. A. F. Van den Boogaart, *Stencil Lithography: An Ancient Technique for Advanced Micro- and Nano-patterning*: Hartung-Gorre, 2006.

Appendix 4.2: Measuring particle velocity toward disk center as a function of radial distance

As an important part of quantitative evaluation of particle behavior, the measurement of the particle velocity toward the disk center as a function of radial distance provides important data for further calculations. The data processing method is briefly described in this appendix. After recording a movie in which the directional motion of particles is observed, the movie is converted to a batch of image files. Image files are analyzed with a tracking software. Extracted raw data are subjected to calculation.

Assume that motion of k particles ($P_1, P_2, P_3, \dots, P_{i-1}, P_i, P_{i+1}, \dots, P_{k-1}, P_k$) were observed and recorded. To track the particles, DiaTrack software⁸⁸(Ver 3.03) is used. Proper input for the tracking software is the batch of BMP or JPEG files extracted from the movie with iWisoft Free Video Convert software⁸⁹ (Version:1.2 Build 091127). When motion of particle P_i is detected between numbers f_{1,P_i} and $f_{c_{P_i},P_i}$, the output of tracking software is a $3 \times c_{P_i}$ matrix (A_{P_i}) containing coordinates of particles for each frame between f_{1,P_i} and $f_{c_{P_i},P_i}$:

$$A_{P_i} = \begin{bmatrix} x_{1,P_i} & x_{2,P_i} & x_{3,P_i} & \cdots & x_{n-1,P_i} & x_{n,P_i} & x_{n+1,P_i} & \cdots & x_{c_{P_i}-1,P_i} & x_{c_{P_i},P_i} \\ y_{1,P_i} & y_{2,P_i} & y_{3,P_i} & \cdots & y_{n-1,P_i} & y_{n,P_i} & y_{n+1,P_i} & \cdots & y_{c_{P_i}-1,P_i} & y_{c_{P_i},P_i} \\ f_{1,P_i} & f_{2,P_i} & f_{3,P_i} & \cdots & f_{n-1,P_i} & f_{n,P_i} & f_{n+1,P_i} & \cdots & f_{c_{P_i}-1,P_i} & f_{c_{P_i},P_i} \end{bmatrix} \quad \text{Equation 1}$$

Where x_{n,P_i} and y_{n,P_i} are cartesian coordinates of particle P_i when it is tracked at frame number f_{n,P_i} . Coordinates are in pixel values. c_{P_i} and n are positive integer number. A_{P_i} content is illustrated in Figure 1.

For particle P_i observed at frame number f_{n,P_i} , the distance from disk center (r_{n,P_i}) is:

$$r_{n,P_i} = m^* \sqrt{(x_{n,P_i} - x_0)^2 + (y_{n,P_i} - y_0)^2} \quad \text{Equation 2}$$

Where m^* is a coefficient which shows actual length equal to one pixel. Its unit is micrometer per pixel. (x_{n,P_i}, y_{n,P_i}) and (x_0, y_0) are cartesian coordinates of particle and disk center respectively. Data in matrix A_{P_i} is subjected to the radial distance calculation (Equation 2). Therefore new set of data in a $2 \times c_{P_i}$ matrix (B_{P_i}) is achieved:

$$B_{P_i} = \begin{bmatrix} r_{1,P_i} & r_{2,P_i} & r_{3,P_i} & \cdots & r_{n-1,P_i} & r_{n,P_i} & r_{n+1,P_i} & \cdots & r_{c_{P_i}-1,P_i} & r_{c_{P_i},P_i} \\ f_{1,P_i} & f_{2,P_i} & f_{3,P_i} & \cdots & f_{n-1,P_i} & f_{n,P_i} & f_{n+1,P_i} & \cdots & f_{c_{P_i}-1,P_i} & f_{c_{P_i},P_i} \end{bmatrix} \quad \text{Equation 3}$$

⁸⁸ Semasopht Website: <http://www.semasopht.com>

⁸⁹ iWisoft Website: <http://www.easy-video-converter.com>

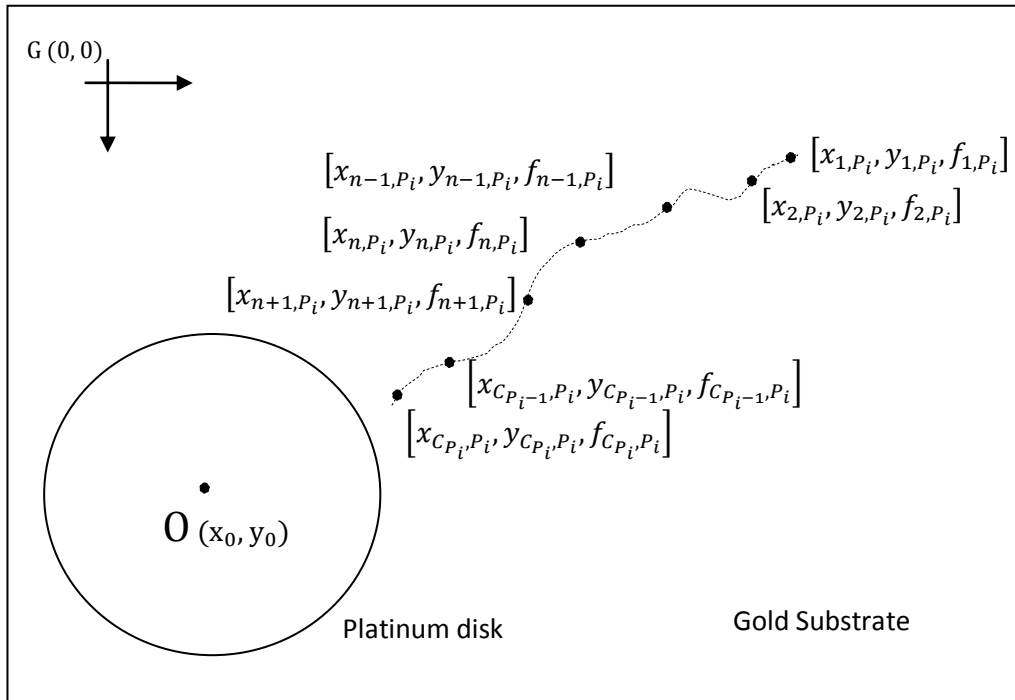


Figure 1: Tracking of particle P_i moving toward a platinum disk

When particle P_i moves from radial distance r_{n, P_i} at frame number f_{n, P_i} to radial distance r_{n+1, P_i} at frame number f_{n+1, P_i} , particle velocity at distance r_{n, P_i} from disk center is estimated as follows:

$$V_{r, n, P_i} \approx k^* \frac{r_{n, P_i} - r_{n+1, P_i}}{f_{n+1, P_i} - f_{n, P_i}} \quad \text{Equation 4}$$

Where k^* is the movie recording rate (frames per second). Appendix 4.2 shows how the above equation is obtained. After processing data stored in B_{P_i} by Equation 4, a $2 \times (C_{P_i} - 1)$ matrix (D_{P_i}) emerges:

$$D_{P_i} = \begin{bmatrix} r_{1, P_i} & r_{2, P_i} & r_{3, P_i} & \cdots & r_{n-1, P_i} & r_{n, P_i} & r_{n+1, P_i} & \cdots & r_{C_{P_i}-2, P_i} & r_{C_{P_i}-1, P_i} \\ V_{r, 1, P_i} & V_{r, 2, P_i} & V_{r, 3, P_i} & \cdots & V_{r, n-1, P_i} & V_{r, n, P_i} & V_{r, n+1, P_i} & \cdots & V_{r, C_{P_i}-2, P_i} & V_{r, C_{P_i}-1, P_i} \end{bmatrix} \quad \text{Equation 5}$$

Figure 2 shows the schematically result of data processing

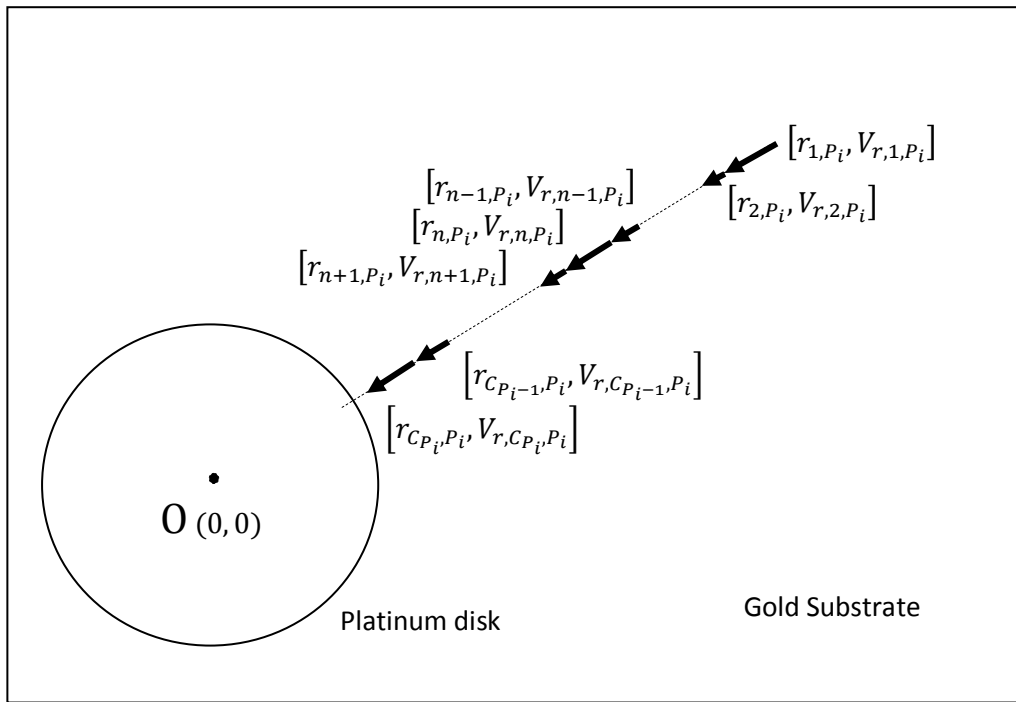


Figure 2: Radial velocity of particle P_i for different radial distances from platinum disk center

As illustrated in Figure 2, the radial velocity of any particle can be calculated as a function of the radial distance. To compare and evaluate the velocities of the different particles, the average velocities of particle P_i at specific distance ranges from disk center are calculated and reported. So, it is necessary to define specific distance ranges ($T_1, T_2, T_3, \dots, T_s$). As shown in Figure 3, the distance range T_j is the distance between r_{1, T_j} and r_{2, T_j} which are the radial distances from disk center. $L_1, L_2, L_3, \dots, L_{j-1}, L_j, L_{j+1}, \dots, L_{s-1}$ and L_s are the radial distances from middle the point of distance ranges $T_1, T_2, T_3, \dots, T_{j-1}, T_j, T_{j+1}, \dots, T_{s-1}$ and T_s respectively. Δ is a positive constant and d is the distance of an arbitrary point from disk center. Equations 6, 7 and 8 show the relations between L_j, L_{j-1}, Δ and d for consecutive distance ranges T_j and T_{j-1} :

$$\forall L_j: 0 < 3\Delta < L_j \quad \text{Equation 6}$$

$$\forall d: d \in T_j, \quad \forall d: L_j - \Delta < d \leq L_j + \Delta \quad \text{Equation 7}$$

$$L_j \in T_j, \quad L_{j-1} \in T_{j-1}, \quad \forall L_j, L_{j-1}: L_j - L_{j-1} = 2\Delta \quad \text{Equation 8}$$

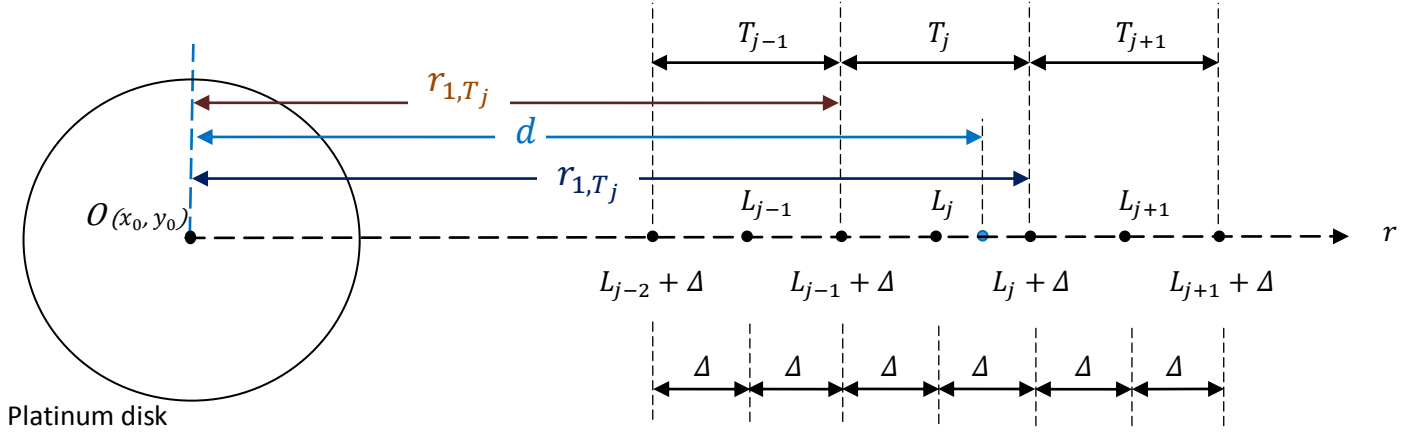


Figure 3: Illustration of the distance ranges T_{j-1} , T_j and T_{j+1}

For particle P_i , the matrix D_{P_i} (Equation 5) is processed to calculate the average velocity ($\bar{V}_{r,P_i(L_j)}$) for the distance range T_j around a point at the radial distance L_j . As it is shown in Appendix 4.3, the velocity can be calculated as follows:

$$\bar{V}_{r,P_i(L_j)} = \frac{\sum_{n=1}^{c_{P_i}-1} \left[\left\lfloor \frac{r_{n,P_i}}{L_j - \Delta} \right\rfloor \cdot \left\lfloor \frac{L_j + \Delta}{r_{n,P_i}} \right\rfloor \cdot \left(1 - \left\lfloor \frac{r_{n,P_i}}{L_j - \Delta} \right\rfloor \cdot \left\lfloor \frac{L_j - \Delta}{r_{n,P_i}} \right\rfloor \right) \cdot V_{r,n,P_i} \right]}{\sum_{n=1}^{c_{P_i}-1} \left[\left\lfloor \frac{r_{n,P_i}}{L_j - \Delta} \right\rfloor \cdot \left\lfloor \frac{L_j + \Delta}{r_{n,P_i}} \right\rfloor \cdot \left(1 - \left\lfloor \frac{r_{n,P_i}}{L_j - \Delta} \right\rfloor \cdot \left\lfloor \frac{L_j - \Delta}{r_{n,P_i}} \right\rfloor \right) \right]} \quad \text{Equation 9}$$

Where " $\lfloor \cdot \rfloor$ " is symbol of floor function. After applying Equation 9 to matrix D_{P_i} (Equation 5), the result is a $2 \times s$ matrix (E_{P_i}):

$$E_{P_i} = \begin{bmatrix} L_1 & L_2 & L_3 & \cdots & L_{s-1} & L_s \\ \bar{V}_{r,P_i(L_1)} & \bar{V}_{r,P_i(L_2)} & \bar{V}_{r,P_i(L_3)} & \cdots & \bar{V}_{r,P_i(L_{s-1})} & \bar{V}_{r,P_i(L_s)} \end{bmatrix} \quad \text{Equation 10}$$

Figure 4 illustrates the result (Equation 10). Red dots represent positions with radial distance values equal to L_1, L_2, L_3, \dots and L_s . The distance between two consecutive red dots is equal to 2Δ .

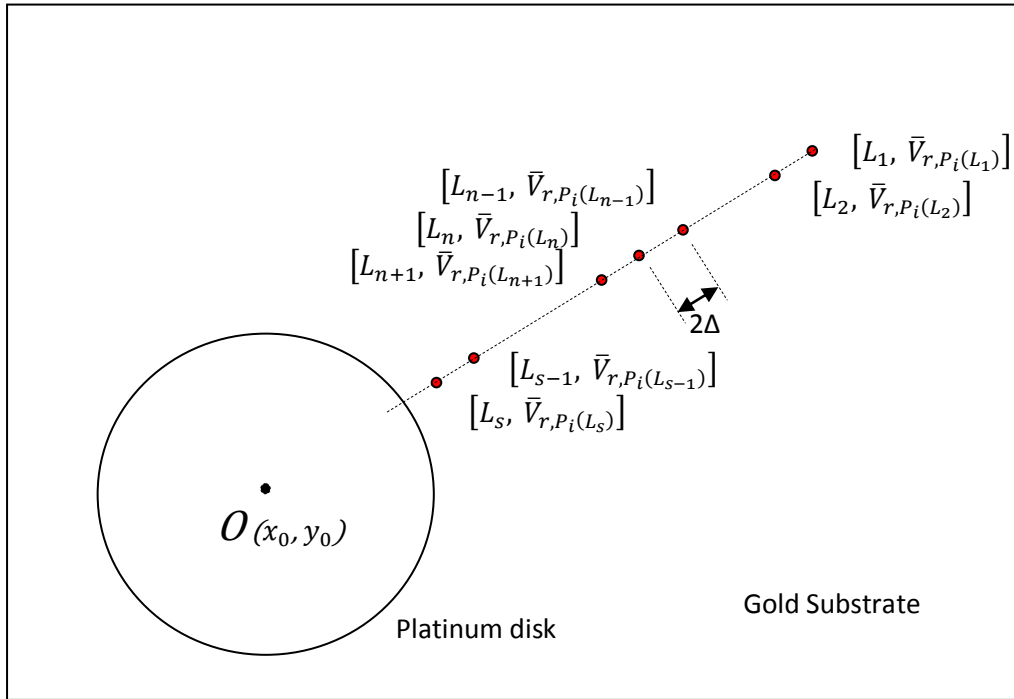


Figure 4: Radial velocity of particle P_i at specific radial distances $L_1, L_2, L_3, \dots, L_{j-1}, L_j, L_{j+1}, \dots, L_{s-1}$ and L_s from platinum disk center

The radial velocity of the particle as a function of certain distances from the disk center is available now.

This method can be applied individually to calculate the velocity as a function of distance for all particles $P_1, P_2, P_3, \dots, P_{i-1}, P_i, P_{i+1}, \dots, P_{k-1}$ and P_k .

Matrixes $E_{P_1}, E_{P_2}, E_{P_3}, \dots, E_{P_{k-1}}$ and E_{P_k} are achieved for particles $P_1, P_2, P_3, \dots, P_{k-1}$ and P_k respectively. To report the experimental results, the average of the particle velocities at each distance range is calculated. Average velocity of particles at radial distance L_j is:

$$\bar{V}_{rL_j}^* = \frac{\bar{V}_{r,P_1}(L_j) + \bar{V}_{r,P_2}(L_j) + \dots + \bar{V}_{r,P_{n-1}}(L_j) + \bar{V}_{r,P_n}(L_j) + \bar{V}_{r,P_{n+1}}(L_j) + \dots + \bar{V}_{r,P_{k-1}}(L_j) + \bar{V}_{r,P_k}(L_j)}{k} \quad \text{Equation 11}$$

If Equation 11 is applied for the radial distance L_1, L_2, L_3, \dots and L_s , the final result is a $2 \times s$ matrix (G):

$$G = \begin{bmatrix} L_1 & L_2 & L_3 & \cdots & L_{S-1} & L_S \\ \bar{V}_{rL_1}^* & \bar{V}_{rL_2}^* & \bar{V}_{rL_3}^* & \cdots & \bar{V}_{rL_{S-1}}^* & \bar{V}_{rL_S}^* \end{bmatrix} \quad \text{Equation 12}$$

Matrix G can be obtained from matrices $E_{P_1}, E_{P_2}, E_{P_3}, \dots, E_{P_{k-1}}$ and E_{P_k} :

$$G = \begin{bmatrix} \frac{1}{k} & 0 \\ 0 & \frac{1}{k} \end{bmatrix} \cdot (E_{P_1} + E_{P_2} + E_{P_3} + \dots + E_{P_{k-1}} + E_{P_k}) \quad \text{Equation 13}$$

Assuming that m similar and independent experiments were conducted, matrices $G_1, G_2, G_3, \dots, G_{m-1}$ and G_m are the results of these experiments. To merge the results and report the final radial velocity of particle for certain radial distances, the $2 \times s$ matrix (F) is calculated as follows:

$$F = \begin{bmatrix} \frac{1}{m} & 0 \\ 0 & \frac{1}{m} \end{bmatrix} \cdot (G_1 + G_2 + G_3 + \dots + G_{m-1} + G_m) \quad \text{Equation 14}$$

Matrix F is the final result. If it is required to normalize L_1, L_2, L_3, \dots and L_z values by dividing them to the disk radius (R_0), matrix F is modified to meet the requirement:

$$F^* = \begin{bmatrix} \frac{1}{R_0 m} & 0 \\ 0 & \frac{1}{m} \end{bmatrix} \cdot (G_1 + G_2 + G_3 + \dots + G_{m-1} + G_m) \quad \text{Equation 15}$$

Appendix 4.3: Derivation of Appendix 4.2-Equation 9

As a first step to derive Appendix 4.2-Equation 9, function $F(x)$ is defined as follows:

$$F(x) = \left\lfloor \frac{x}{a} \right\rfloor \cdot \left\lfloor \frac{b}{x} \right\rfloor \cdot \left(1 - \left\lfloor \frac{x}{a} \right\rfloor \left\lfloor \frac{a}{x} \right\rfloor\right) \quad \text{Equation 1}$$

Where $\lfloor \cdot \rfloor$ is Symbol of floor function ⁹⁰. a and b are positive numbers which satisfy Equations 3 and 4:

$$0 < a < b \quad \text{Equation 3}$$

$$b < 2a \quad \text{Equation 4}$$

Function $F(x)$ becomes zero when $x \geq b$ or $x < a$. Otherwise it is equal to 1:

$$F(x) = \begin{cases} x \leq a & 0 \\ a < x \leq b & 1 \\ x > b & 0 \end{cases} \quad \text{Equation 5}$$

Assuming that matrix V (Equation 6) contains velocities of a particle at different radial distances.

$$V = \begin{bmatrix} r_1 & r_2 & r_3 & \cdots & r_{z-1} & r_z \\ V_1 & V_2 & V_3 & \cdots & V_{z-1} & V_z \end{bmatrix} \quad \text{Equation 6}$$

$V_1, V_2, V_3, \dots, V_{z-1}$ and V_z are the velocities of the particle at the radial distances $r_1, r_2, r_3, \dots, r_{z-1}$ and r_z respectively. The average velocity (\bar{V}) of the particle when it moves in radial distance between a and b (Equation 7), is calculated by Equation 8:

$$a < r \leq b \quad \text{Equation 7}$$

$$\bar{V} = \sum_{d=1}^z [F(r_d) \cdot V_d] \quad \text{Equation 8}$$

$$\sum_{d=1}^z F(r_d)$$

Function $F(x)$ acts like a filter and any out of range data is omitted from the calculation. Considering Equation 8 as a fraction, the denominator provides the number of points at which the radial distance of the particle satisfies the Equation 7. The numerator is the sum of the particle velocities corresponding to the radial distances which meet the requirement mentioned in Equation 7. As a key part, equation 8 is simply applied to derive Appendix 3.2- Equation 9. If matrix D_{P_i} (Appendix 3.2 - Equation 5) of particle P_i is subjected to average velocity ($\bar{V}_{r,P_i(L_j)}$) calculation for distance range T_j (illustrated in Appendix 3.1– Figure 3), the velocity is:

$$\sum_{n=1}^{c_{p_i-1}} \left[\left[\frac{r_{n,P_i}}{L_j - \Delta} \right] \cdot \left[\frac{L_j + \Delta}{r_{n,P_i}} \right] \cdot \left(1 - \left[\frac{r_{n,P_i}}{L_j - \Delta} \right] \cdot \left[\frac{L_j - \Delta}{r_{n,P_i}} \right] \right) \cdot V_{r,n,P_i} \right]$$

$$\bar{V}_{r,P_i(L_j)} = \frac{\sum_{n=1}^{c_{p_i-1}} \left[\left[\frac{r_{n,P_i}}{L_j - \Delta} \right] \cdot \left[\frac{L_j + \Delta}{r_{n,P_i}} \right] \cdot \left(1 - \left[\frac{r_{n,P_i}}{L_j - \Delta} \right] \cdot \left[\frac{L_j - \Delta}{r_{n,P_i}} \right] \right) \right]}{\sum_{n=1}^{c_{p_i-1}} \left[\left[\frac{r_{n,P_i}}{L_j - \Delta} \right] \cdot \left[\frac{L_j + \Delta}{r_{n,P_i}} \right] \cdot \left(1 - \left[\frac{r_{n,P_i}}{L_j - \Delta} \right] \cdot \left[\frac{L_j - \Delta}{r_{n,P_i}} \right] \right) \right]} \quad \text{Equation 8}$$

Appendix 3.4: Calculation of particle radial velocity

This appendix shows how to calculate the radial velocity of a particle toward specific point O (Figure 1.a) which in this case is the platinum disk center. It is assumed that a particle moves from point A at frame number f_i to point B at frame number f_{i+1} . If cylindrical coordinates are set to solve the problem, O is considered as the origin. Coordinates of points A, B and O are $(r_i, \theta_i, 0)$, $(r_{i+1}, \theta_{i+1}, 0)$ and $(0,0,0)$ respectively (Figure 1.a). Particle velocity (\vec{V}) can be written as a combination of unit vectors (\hat{r} and $\hat{\theta}$):

$$\vec{V} = V_r \hat{r} + V_\theta \hat{\theta} \quad \text{Equation 1}$$

V_r and V_θ are the velocities in the direction of \hat{r} and $\hat{\theta}$ respectively (Figure 1.b). For a moving object, it is possible to express the velocity vector as a function of the radial distance (r) and the derivative of the coordinates with respect to time (\dot{r} and $\dot{\theta}$)⁹¹[1]:

$$\vec{V} = \dot{r} \hat{r} + r \dot{\theta} \hat{\theta} \quad \text{Equation 2}$$

Considering the particle displacement illustrated in figure 1.a, the velocity (Equation 2) can be estimated as follows:

$$\vec{V} \approx \frac{\Delta r}{\Delta t} \hat{r} + r \frac{\Delta \theta}{\Delta t} \hat{\theta} \quad \text{Equation 3}$$

Δt is the time which takes for a particle to move from A to B between two frames f_i and f_{i+1} :

$$\Delta t = \frac{f_{i+1} - f_i}{k} \quad \text{Equation 4}$$

Where k is the movie recording rate (frames per second). Incorporating equation 4 and coordinates of points A and B in equation 3, the velocity can be written as follows :

$$\vec{V} \approx k \frac{r_{i+1} - r_i}{f_{i+1} - f_i} \hat{r} + k \cdot r_i \frac{\theta_{i+1} - \theta_i}{f_{i+1} - f_i} \hat{\theta} \quad \text{Equation 5}$$

Comparing equations 1 and 5, V_r can be obtained:

$$V_r \approx k \cdot \frac{r_{i+1} - r_i}{f_{i+1} - f_i} \quad \text{Equation 6}$$

If particle moves toward the disk, V_r has a negative value. After rearranging the indexes, the following equation is applied:

$$V_r \approx k \cdot \frac{r_i - r_{i+1}}{f_{i+1} - f_i} \quad \text{Equation 7}$$

The directionality coefficient (Π_r) shown in equation 8 is defined to evaluate particle movement. It is a dimensionless coefficient between 0 and 1. Directionality coefficient shows

⁹¹ Reference: Kleppner, D.; Kolenkow, R. J., An Introduction to Mechanics. Cambridge University Press: 2010.

how much a moving particle tends to move toward disk center. It is the ratio of $|\vec{V}_r|$ (length of particle velocity vector projection on $-\hat{r}$) to $|\vec{V}|$ (length of particle velocity vector).

$$\Pi_r = \frac{|\vec{V}_r|}{|\vec{V}|} \quad \text{Equation 8}$$

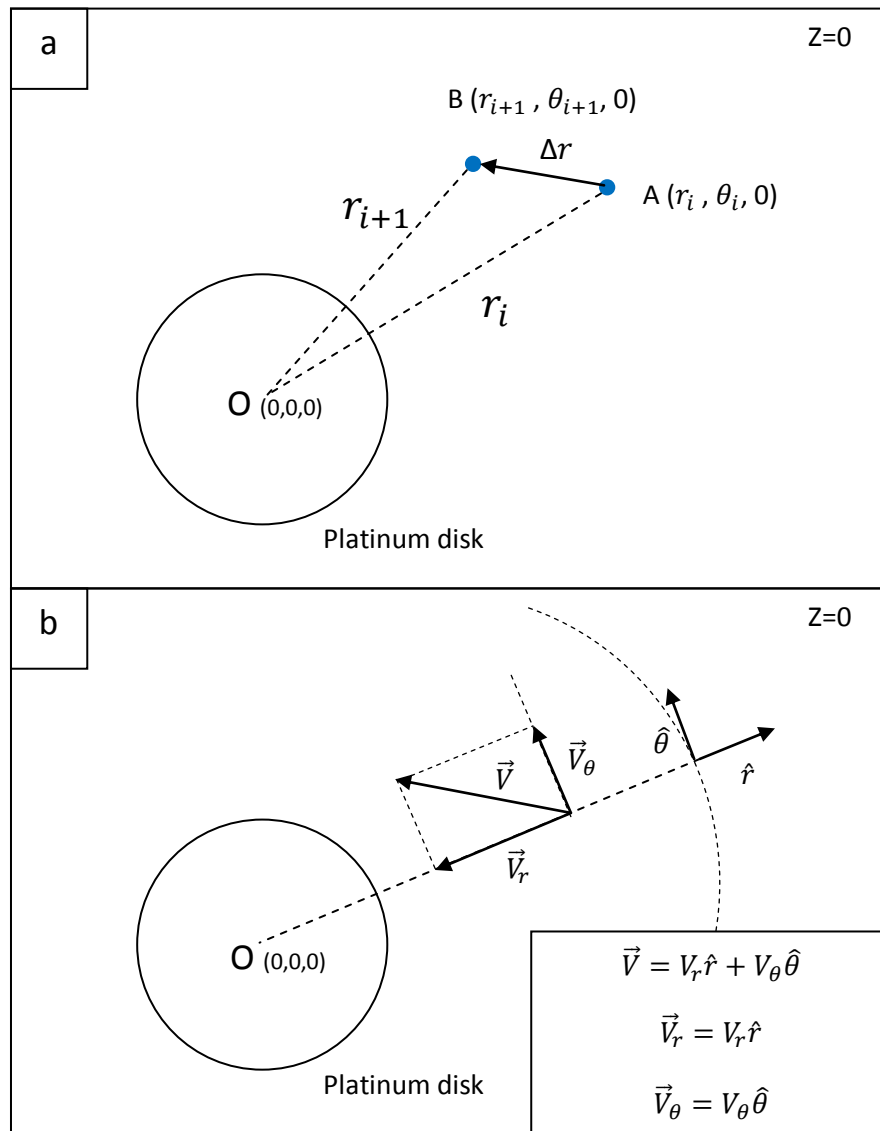
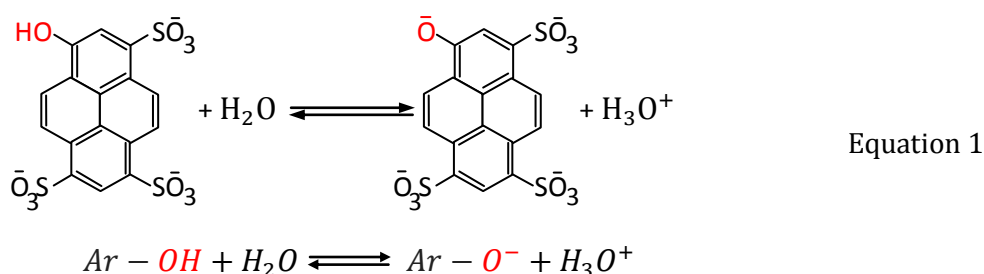


Figure 1: a) Movement of particle from point A to point B, b) Arrangement of velocity and unit vectors in cylindrical coordinate system

[1] D. Kleppner and R. J. Kolenkow, *An Introduction to Mechanics*: Cambridge University Press, 2010.

Appendix 3.5 Fluorescence confocal microscopy- Calculation

Pyranine (trisodium 8-hydroxypyrene-1,3,6-trisulfonate) was the fluorescence molecule selected for the experiments. When a fluorescence molecule like pyranine, absorbs photons with specific wavelength(s), the light brings it into the electronic excited-state. After passing lifetime of excited-state, de-excitation occurs with photon emission, it is so called, photoluminescence. The phenol group of this molecule undergoes reversible protonation/deprotonation (equation 1) depending on the pH of the environment which makes its absorption and emission spectra change with the pH. The absorption spectra of the deprotonated pyranine ($Ar - O^-$) and protonated one ($Ar - OH$) exhibit maximum signals at about 405 and 456 nm respectively (figure 1 a).[1-5]



The pK_a of this molecule is around 7. Therefore at pHs above pK_a the basic form of the molecule ($Ar - O^-$) dominates over the protonated one and inversely when the pH is below pK_a . Figure 1a shows the absorption spectra shift with pH. At pH=6 a more intense peak is located at about 405 nm which corresponds to the protonated form of the molecule whereas at about 456 nm the smaller peak corresponds to its conjugated base. At pH=8, a big absorption peak of the basic form appears at around 456 nm whereas the protonated species displays a very weak signal at 405 nm. Although in the excitation spectra of pyranine one can observe the absorption of both species the protonated and deprotonated ones, the emission spectra is only sensitive to the basic form of pyranine whose emission wavelength is located between 510-516 nm (figure 1 b). That is because a photo-induced proton transfer takes place during the lifetime of the excited molecule. The excitation enhances the acidic character of the OH group favoring the deprotonated form of the molecule (the pK_a of pyranine in the excited state is much lower than pK_a of 7 in the ground state). Thus, the emitting form is always the basic form since the acidic form is followed by such excited-state deprotonation. [6]

For reliable fluorescence sensing and quantification it is very recommendable to use ratiometric measurements which are applicable when fluorescent probes exhibit dual excitation or dual emission. Since pyranine presents dual excitation it becomes an ideal molecule for pH sensing under ratiometric measurements. Ratiometric measurements are based on the ratio of fluorescence signals intensities.

This methodology eliminates possible artifacts making the fluorescence measurements independent from dye concentration, dye destruction or photobleaching, intensity fluctuation of light source, instrument sensitivity, etc.

For imaging and quantification of pH of the samples the following protocol was used. First of all the excitation and emission conditions were adjusted by using pH solutions of extreme

values (in this case pH of 4 and 9) in presence of the bimetallic device. The molecule was excited at 405 and 458 nm and the emission was collected from 480 to 580 nm. Then, a series of pH solutions between pH 4 and 9 were tested in presence of device in order to get a pH calibration curve and be sure that the fluorescent dye acts in a reliable way in presence of the samples when varying the pH. The fluorescence signal at both excited wavelengths was collected as shown in chapter 5. At 405 nm the fluorescence intensity decreases as the pH increases, whereas the fluorescence signal increases as the pH increases when the dye is excited at 458 nm. Then the fluorescence signal was collected for the sample in presence of the chemical fuel (hydrogen peroxide).

The pH of the samples was extracted by applying equation 2, the standard calibration equation in terms of the ratio of the fluorescence signals

$$pH = pK_a + \log \left(\frac{R - R_A}{R_B - R} \times \frac{I_A(\lambda_2)}{I_B(\lambda_2)} \right) \quad \text{Equation 2}$$

Where R , R_A and R_B are defined as follow (equation 3, 4 and 5) [6]:

$$R = \frac{I(\lambda_1)}{I(\lambda_2)} \quad \text{Equation 3}$$

$$R_A = \frac{I_A(\lambda_1)}{I_A(\lambda_2)} \quad \text{Equation 4}$$

$$R_B = \frac{I_B(\lambda_1)}{I_B(\lambda_2)} \quad \text{Equation 5}$$

pK_a : Acid dissociation constant on the ground state

$I(\lambda_1)$: Fluorescence intensity at excitation wavelength $\lambda_1 = 405 \text{ nm}$

$I(\lambda_2)$: Fluorescence intensity at excitation wavelength $\lambda_2 = 458 \text{ nm}$

$I_A(\lambda_1)$: Fluorescence intensity of extreme acidic solution at excitation wavelength λ_1

$I_A(\lambda_2)$: Fluorescence intensity of extreme acidic solution at excitation wavelength λ_2

$I_B(\lambda_1)$: Fluorescence intensity of extreme basic solution at excitation wavelength λ_1

$I_B(\lambda_2)$: Fluorescence intensity of extreme basic solution at excitation wavelength λ_2

As mentioned, basic and acidic extremes were at pH=9 and pH=4 respectively. For all measurements, fluorescence intensity was normalized with respect to the area and expressed in arbitrary units.

The pH image was achieved by applying eq. 2 to every pixel of the fluorescence images that were acquired. Proton concentration image was obtained by applying equation 6 [7]:

$$[H^+] = 10^{-pH} \quad \text{Equation 6}$$

Derivation of equation 2⁹²

Equation 2 is obtained from the Henderson-Hasselbach equation (equation 7) which is used for calculating pH in presence of the acid form (protonated species, A) and the basic one (deprotonated species, B) of molecules or buffer solutions.[6]

$$pH = pK_a + \log \left(\frac{[B]}{[A]} \right) \quad \text{Equation 7}$$

At a given wavelength where both acidic form (A) and basic form (B) absorb or emit, the absorbance or the fluorescence intensity (*I*) are given by

$$I = a[A] + b[B] \quad \text{Equation 8}$$

a and *b* are the molar absorption coefficients (at the excitation wavelength) and the fluorescence quantum yields of A and B, respectively.

When the indicator is only in the acidic form or only in the basic form, the values of *I* are:

$$I_a = a c_0 \quad \text{Equation 9}$$

$$I_b = b c_0 \quad \text{Equation 10}$$

Where *c*₀ is the total concentration of the dye indicator such that

$$c_0 = [A] + [B] \quad \text{Equation 11}$$

Combination of the preceding relations yields

$$\frac{[B]}{[A]} = \frac{I - I_a}{I_b - I} \quad \text{Equation 12}$$

The Henderson-Hasselbach equation (Equation 7) can be written as

$$pH = pK_a + \log \left(\frac{I - I_a}{I_b - I} \right) \quad \text{Equation 13}$$

⁹² Reproduced with written permission from John Wiley and Sons Inc. website: www.wiley.com
 Source: Bernard Valeur, Mário Nuno Berberan-Santos, Molecular Fluorescence: Principles and Applications, 2nd Edition ISBN: 3527650024 Chapter 10 - Appendix A
 License Number: 3276440441565 License Date :Nov 26, 2013

Equation 13 corresponds to the situation when absorbance or fluorescence intensity is measured at a given wavelength. When there are dual-wavelength measurements (at λ_1 and λ_2), the absorbance or fluorescence intensities can be written in a form analogous to equation 8,

$$I_{(\lambda_1)} = a_1[A] + b_1[B] \quad \text{Equation 14}$$

$$I_{(\lambda_2)} = a_2[A] + b_2[B] \quad \text{Equation 15}$$

As mentioned before in this case one can do ratiometric measurements consisting in monitoring the ratio of intensities $I(\lambda_1)/I(\lambda_2)$ which can be expressed as

$$R = \frac{a_1[A] + b_1[B]}{a_2[A] + b_2[B]} \quad \text{Equation 16}$$

When the indicator is only in the acidic form or only in the basic form, the values of R are, respectively

$$R_A = \frac{a_1}{a_2} \quad \text{Equation 17}$$

$$R_B = \frac{b_1}{b_2} \quad \text{Equation 18}$$

Taking account of equation 11, equation 12 can be replaced by

$$\frac{[B]}{[A]} = \frac{a_2}{b_2} \frac{R - R_A}{R_B - R} \quad \text{Equation 19}$$

Hence

$$pH = pK_a + \log \left(\frac{R - R_A}{R_B - R} \right) + \log \left(\frac{a_2}{b_2} \right) \quad \text{Equation 20}$$

The ratio a_2/b_2 represents the ratio of the absorbances or fluorescent intensities of the acidic form alone and the basic form alone at the wavelength λ_2 yielding directly to equation 2 used for extracting the pH with pyranine.

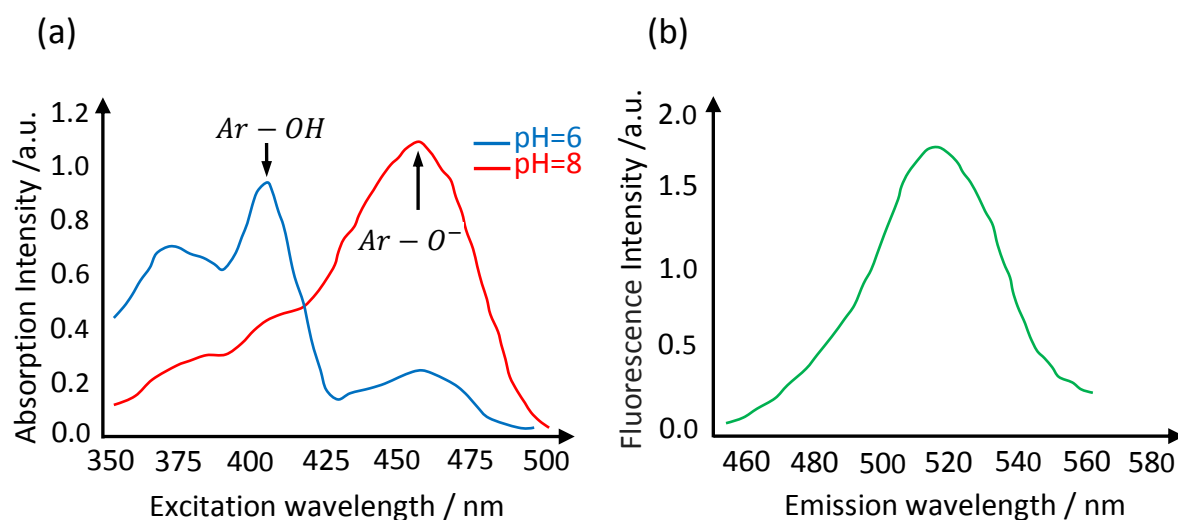


Figure 1: schematic illustration of the a) absorption and b) emission spectra of Pyranine. The molecule exhibits dual excitation at 405 and 456 nm whereas the emission takes place at a wavelength between 510 and 516 nm. Fig. 1a also shows the excitation shift with pH.

Reference

- [1] Y. Avnir and Y. Barenholz, "pH determination by pyranine: Medium-related artifacts and their correction," *Analytical Biochemistry*, vol. 347, pp. 34-41, 12/1/ 2005.
- [2] A. Hakonen and S. Hulth, "A high-precision ratiometric fluorosensor for pH: Implementing time-dependent non-linear calibration protocols for drift compensation," *Analytica Chimica Acta*, vol. 606, pp. 63-71, 1/7/ 2008.
- [3] J. Han and K. Burgess, "Fluorescent Indicators for Intracellular pH," *Chemical Reviews*, vol. 110, pp. 2709-2728, 2010/05/12 2009.
- [4] P. Herman, H. Drapalova, R. Muzikova, and J. Vecer, "Electroporative Adjustment of pH in Living Yeast Cells: Ratiometric Fluorescence pH Imaging," *Journal of Fluorescence*, vol. 15, pp. 763-768, 2005/09/01 2005.
- [5] H. R. Kermis, Y. Kostov, P. Harms, and G. Rao, "Dual Excitation Ratiometric Fluorescent pH Sensor for Noninvasive Bioprocess Monitoring: Development and Application," *Biotechnology Progress*, vol. 18, pp. 1047-1053, 2002.
- [6] B. Valeur and M. N. Berberan-Santos, *Molecular Fluorescence: Principles and Applications*: Wiley, 2013.
- [7] J. W. Moore, C. L. Stanitski, and P. C. Jurs, *Principles of Chemistry: The Molecular Science: The Molecular Science*: Cengage Learning, 2009.

Appendix 4.6 Surface zeta potential measurement

An experiment was designed to measure zeta potential of metallic (Au or Pt) surfaces. When a positively charged particle close to the metallic surface, is subjected to the external electric field (figure 1), the particle starts moving in the direction of external electric field. The motion of the particle can be explained by considering the electrophoresis and electro-osmosis processes (Chapter 3). Therefore particle velocity is:

$$V_{p^+} = V_{ep} + V_{eo} \quad \text{Equation 1}$$

V_{p^+} : Velocity of positively charged particle [$\text{m}\cdot\text{s}^{-1}$]

V_{ep} : Fraction of total particle velocity caused by electrophoresis [$\text{m}\cdot\text{s}^{-1}$]

V_{eo} : Fraction of total particle velocity caused by electro-osmosis [$\text{m}\cdot\text{s}^{-1}$]

Considering 3.58 and 3.46, equation 1 is re-written as follow:

$$V_{p^+} = \frac{\epsilon_r \epsilon_0}{\eta} E \cdot \zeta_{p^+} - \frac{\epsilon_r \epsilon_0}{\eta} E \cdot \zeta_s \quad \text{Equation 2}$$

ϵ_r : Dielectric constant of the medium

ϵ_0 : Free space permittivity (8.854×10^{-12} [$\text{F}\cdot\text{m}^{-1}$])

η : Dynamic viscosity [$\text{Pa}\cdot\text{s}$]

E : Electric field strength [$\text{V}\cdot\text{m}^{-1}$]

ζ_{p^+} : Zeta potential of positively charged particle [mV]

ζ_s : Zeta potential of metallic surface [mV]

Figure 2 shows the experimental setup for tracking the particle motion over gold and platinum patterns under same constant electric field. The sample (figure 2.b) included gold-coated surface, platinum-coated surface and two gold contacts to apply the electric field. Stencil lithography and e-beam evaporation were used to deposit Au and Pt patterns. The sample was cleaned following cleaning process C5 (table 3.3). It was exposed to aqueous solution containing positively charged particles ($2 \mu\text{m}$ polystyrene spheres functionalized with amidine groups⁹³, $\zeta_{p^+} = 46 \pm 1$ mV) and subjected to external electric field (E).

Considering equation 2, the velocities of particles over platinum and gold surface (figure 1) are:

⁹³Supplier: Life Technologies Corporation Website: <http://www.invitrogen.com>

$$V_{\frac{p^+}{Au}} = \frac{\varepsilon_r \varepsilon_0}{\eta} E \cdot \zeta_{p^+} - \frac{\varepsilon_r \varepsilon_0}{\eta} E \cdot \zeta_{Au} \quad \text{Equation 3}$$

$$V_{\frac{p^+}{Pt}} = \frac{\varepsilon_r \varepsilon_0}{\eta} E \cdot \zeta_{p^+} - \frac{\varepsilon_r \varepsilon_0}{\eta} E \cdot \zeta_{Pt} \quad \text{Equation 4}$$

$V_{\frac{p^+}{Au}}$: Velocity of positively charged particle over gold surface [m.s⁻¹]

$V_{\frac{p^+}{Pt}}$: Velocity of positively charged particle over platinum surface [m.s⁻¹]

ζ_{Au} : Zeta potential of gold surface [V]

ζ_{Pt} : Zeta potential of platinum surface [V]

According equations 3 and 4 , ζ_{Au} and ζ_{Pt} are :

$$\zeta_{Au} = \zeta_{p^+} - \frac{\eta}{\varepsilon_r \varepsilon_0 E} V_{\frac{p^+}{Au}} \quad \text{Equation 5}$$

$$\zeta_{Pt} = \zeta_{p^+} - \frac{\eta}{\varepsilon_r \varepsilon_0 E} V_{\frac{p^+}{Pt}} \quad \text{Equation 6}$$

Considering equations 5 and 6, the difference between the particle velocities over gold and platinum is proportional to difference between the gold and platinum surface zeta potentials:

$$\zeta_{Au} - \zeta_{Pt} = -\frac{\eta}{\varepsilon_r \varepsilon_0 E} (V_{\frac{p^+}{Au}} - V_{\frac{p^+}{Pt}}) \quad \text{Equation 7}$$

Strength of external electric field is simply calculated as follow:

$$E = \frac{V}{x} \quad \text{Equation 8}$$

V : The potential difference between two gold contacts [V]

x : Distance between two gold contacts [m]

By considering equations 3 and 4, other relation between ζ_{Au} and ζ_{Pt} is :

$$\left(\frac{V_{p^+}}{Au} - \frac{V_{p^+}}{Pt}\right) \cdot \zeta_{p^+} = \frac{V_{p^+}}{Au} \cdot \zeta_{Pt} - \frac{V_{p^+}}{Pt} \cdot \zeta_{Au}$$

Equation 9

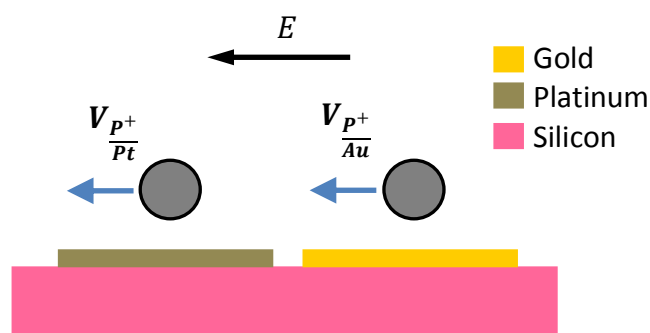


Figure 1: Motion of positively charged particles over gold and platinum surface under external electric field (parameters were described in the text.)

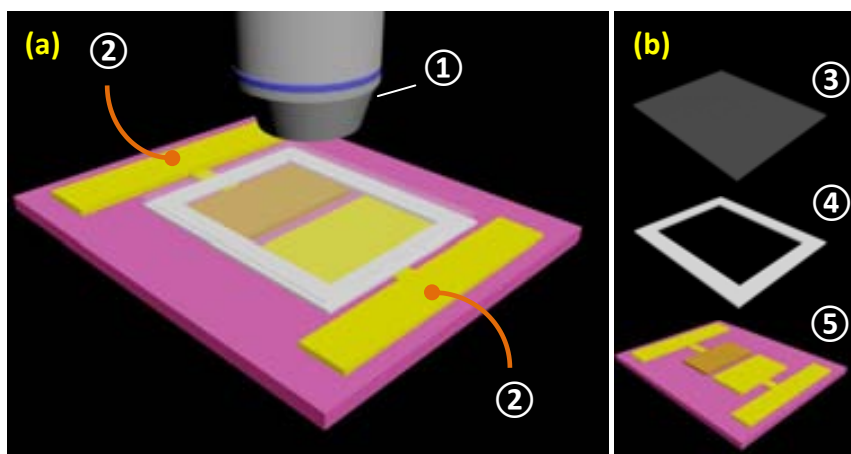


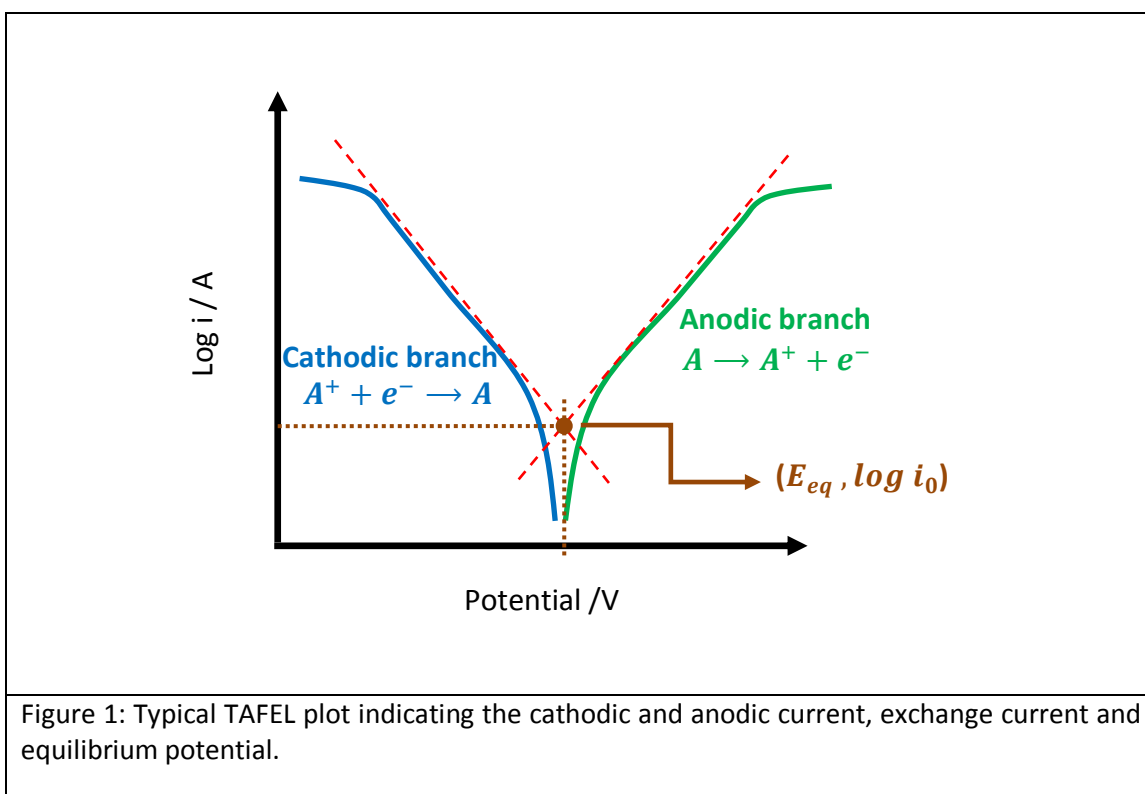
Figure 2: Experimental setup for tracking the particles under constant electric field a) assembled view, b) exploded view ① Microscope objective ② Wires to connect gold contacts to the power supply ③ Cover glass ④ Spacer ⑤ Sample . Two separate platinum (brown) and gold (yellow) areas are connected to the gold contacts.

Appendix 5.1 : A guideline to TAFEL plots

TAFEL plots are very useful curves to characterize the kinetics of an electrochemical reaction and have been very useful to evaluate corrosion rates, the passivity of electrodes, etc. The curves represent the log of the electrochemical current as a function of the electrode potential and are taken at steady state conditions (or with low scan rates). The TAFEL representation exhibits an almost V shaped characteristic (Figure 1). In general there are an anodic branch (electrochemical current at more positive voltages) which represents the oxidation behavior of an electrochemical species at the electrode and a cathodic branch (electrochemical current at more negative voltages) corresponding to the reduction of the electroactive species. The important segments in the TAFEL plots are the linear ones (dashed lines) in which the TAFEL equation is satisfied⁹⁴. The extrapolation of both segments intercepts in $\log i_0$ (the exchange current) and E_{eq} (the equilibrium potential). The exchange current is the current at equilibrium (absence of net electrochemical reaction), which means that the anodic and cathodic reaction progress at the same rates. Thus, the TAFEL curves allow evaluating the charge transfer coefficient α (see note below) and i_0 , the latter being related with the charge transfer resistance (R_{CT}) of the reaction process (equation 1). Both are very important parameters to evaluate the electrode kinetics.

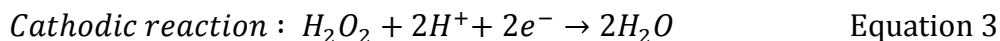
$$i_0 = \frac{RT}{F \cdot R_{CT}}$$

Equation 1



⁹⁴ TAFEL equation $E - E_{eq} = \left(\frac{RT}{\alpha F}\right) \ln i_0 - \left(\frac{RT}{\alpha F}\right) \ln i$, where E_{eq} is the equilibrium potential of the electroactive species, α is the so-called charge transfer coefficient, i_0 is the exchange current, R is the universal gas constant, T is the temperature and F is the Faraday constant.

Apart from such valuable kinetic information, TAFEL plots can provide additional clues. For instance it is possible to predict the role of the electrodes when facing electroactive species which is the case in this work. For illustration one can consider the typical reactions taking place on a metal electrode M1.



Just notice that the reaction taking place at the cathode is not exactly the backward reaction at the anode. Such detail makes that the equilibrium potential cannot be called like that. In this case is named mixed potential. A mixed potential is also a kind of equilibrium potential in which the net electrochemical reaction is also zero but the anodic and cathodic current are not the forward and backward reaction of an electroactive species (figure 2a).

The measurement of the mixed potentials in presence of the electroactive H_2O_2 with different metals can help to predict which metal would act as anode or cathode when both metals are connected. Figure 2b illustrates such situation. It shows the TAFEL plot for the redox reaction of H_2O_2 in metal 1 (M1) and metal 2 (M2). The metal which exhibits a higher mixed potential for the reaction will act as cathode (M2) and the one which lower mixed potential will act as anode (M1). For verifying that, one can just concentrate on the region that the TAFEL branches of the different metals are mixed (region enclosed by the circle). In this region a kind of TAFEL plot is also formed with the mixed electrochemical branches coming from the different metal electrodes. The intersection of both branches provides the bimetallic potential and the current that would result if the metals were connected electrically. The electrochemical current at more negative potentials from such intersection is related with the cathodic branch of M2 and at more positive voltages of such point the electrochemical current is related to the anodic branch of M1. Accordingly it indicates that M1 would favor the anodic reaction of H_2O_2 (anode) and M2 the cathodic one (cathode) when short-circuited. Moreover the higher is the difference of the mixed potential difference between both metals, the higher is the current at the intersection of both metals and consequently increased driving force for the electrochemical reaction and catalytic pumping are expected.

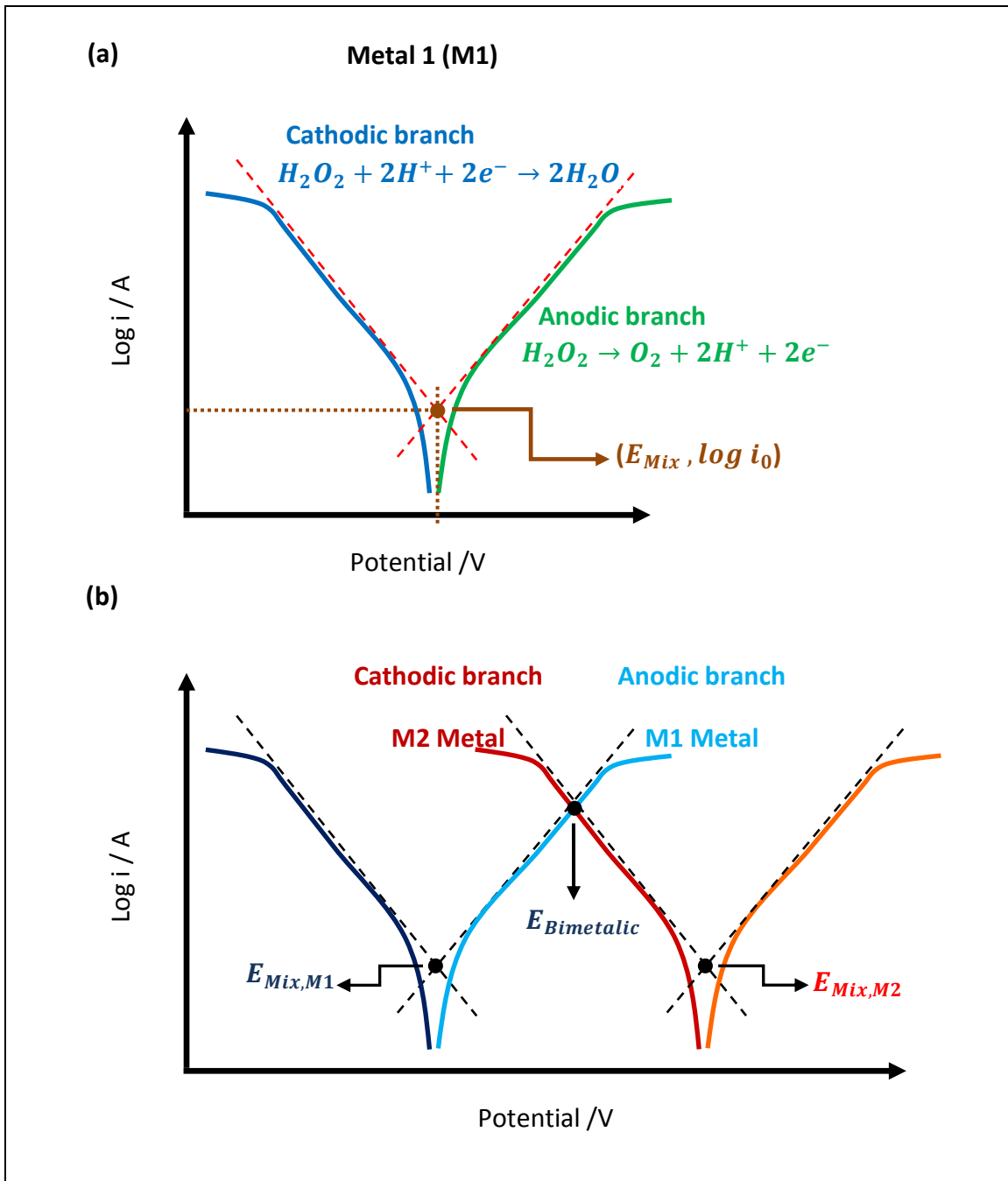


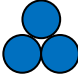
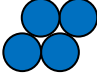
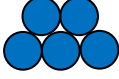
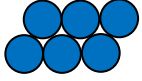

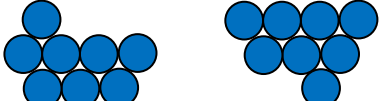
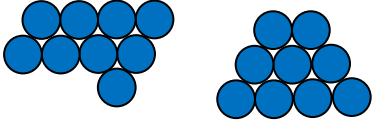
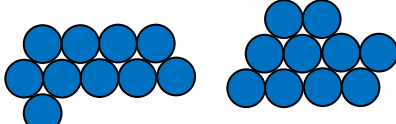
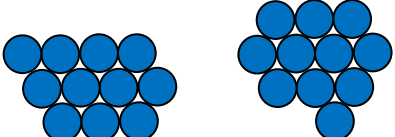
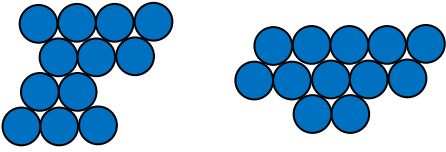
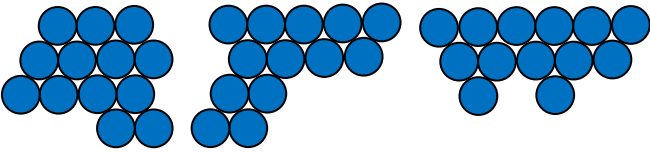
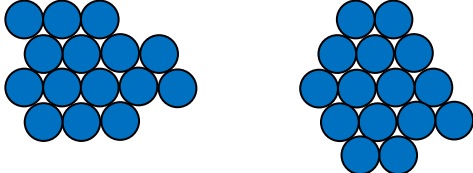
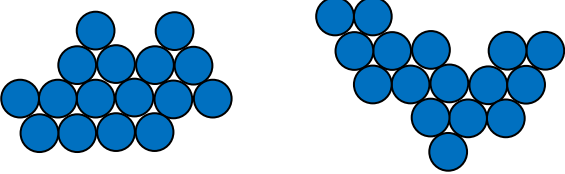
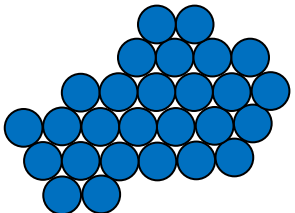
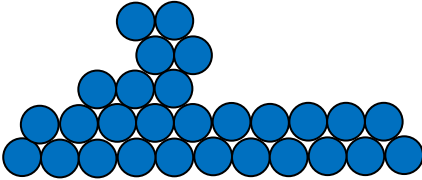
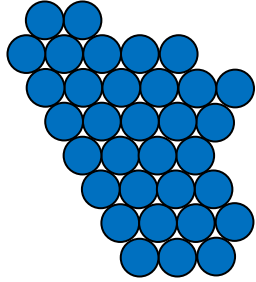


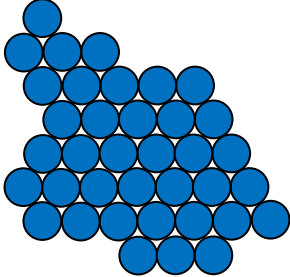
Figure 2: a) TAFEL plot for H_2O_2 redox reactions at metal 1 indicating the mixed potential. b) TAFEL plots for H_2O_2 for two metals. The illustration shows the mixing of redox branches of the two metals. The metal which exhibits a more positive mixed potential acts as cathode whereas the one that has more negative mixed potential acts as anode. The intersection of the cathodic of M2 and anodic branch of M1 provides the potential and the current that would have the system when both metals are electrically connected.

Appendix 6.1 configuration of adjoining clusters

Table 1 contains the information about configuration of adjoining clusters to the device shown in the figure 6.2.

| Table 1: configuration of adjoining clusters | | |
|--|---|----------------|
| size | Observed configuration(s) | Percentage (%) |
| 1 |  | 38.16 |
| 2 |  | 13.74 |
| 3 |  | 11.45 |
| 4 |  | 9.92 |
| 5 |  | 7.63 |
| 6 |  | 0.76 |
| 7 |  | 3.81 |
| 8 |  | 1.52 |
| 9 |  | 1.52 |
| 10 |  | 1.52 |
| 11 |  | 1.52 |

| Table 1: continue | | |
|-------------------|---|----------------|
| size | Observed configuration(s) | Percentage (%) |
| 12 |  | 1.52 |
| 13 |  | 2.29 |
| 15 |  | 1.52 |
| 16 |  | 1.52 |
| 27 |  | 0.76 |
| 28 |  | 0.76 |
| 33 |  | 0.76 |

| Table 1: continue | | |
|-------------------|---|----------------|
| size | Observed configuration(s) | Percentage (%) |
| 37 |  | 0.76 |